Microdamage Accumulation in Bovine Trabecular Bone

by

Tara L. Arthur Moore

B.Eng., Aerospace Engineering (1994)
Carleton University

S.M., Mechanical Engineering (1996)
Massachusetts Institute of Technology

Submitted to the Harvard-MIT Division of Health Sciences and Technology
in Partial Fulfillment of the Requirements for the Degree of

Doctor of Philosophy in Medical Engineering

at the

Massachusetts Institute of Technology

June 2001

© 2001 Massachusetts Institute of Technology
All rights reserved.

ARCHIVES

MASSACHUSETTS INSTITUTE OF TECHNOLOGY
AUG 1 4 2001
LIBRARIES

Signature of Author_____
Harvard-MIT Division of Health Sciences and Technology
May 4, 2001

Certified by_____
Lorna J. Gibson
Matoula S. Salapatas Professor of Materials Science and Engineering
Thesis Supervisor

Accepted by_____
Martha Gray
Edward Hood Taplin Professor of Medical Engineering and Electrical Engineering
Director, Harvard-MIT Division of Health Sciences and Technology

Microdamage Accumulation in Bovine Trabecular Bone

by

Tara L. Arthur Moore

Abstract

When bone is loaded beyond its failure point, it develops damage in the form of microcracks. Normally, microcracks are repaired by the remodeling process, limiting the number of *in vivo* microcracks. However, if the rate of microdamage accumulation increases or the rate of remodeling slows, microdamage can accumulate, reducing bone stiffness and strength and may lead to stress fractures or fragility fractures.

A new technique for visualizing microdamage *in vitro* has been developed that uses chelating fluorochromes to label microcracks. Sequential staining is used to distinguish between microdamage that occurred before testing and damage created during testing. Microdamage parameters quantified include the total number of microcracks, total length of microcracks, damaged area, the number of trabeculae containing microcracks, the pattern of microcracking, the extent of microdamage across the thickness of the trabeculae, and the size of the damage-containing region in the specimen.

The chelating fluorochrome marker technique was used to label and quantify microdamage in specimens of bovine trabecular bone damaged in uniaxial compression and compressive fatigue, and relationships between microdamage parameters and changes in mechanical properties (maximum compressive strain, modulus reduction) were quantified. The progressions of damage accumulation during a single compression cycle and during fatigue to failure were determined. Comparisons were made between specimens tested in different loading modes, including uniaxial compression, compressive fatigue, and compressive creep (Pierce, 1999). Microdamage accumulation increases with increasing specimen strain and with increasing stiffness loss.

A model was developed to predict modulus reductions based on observed microdamage using cellular solid principles. The predictions were compared to experimentally measured changes in mechanical properties during uniaxial compressive loading and compressive fatigue. There was good agreement between model predictions and experimental results for specimens tested in uniaxial compression. The model predictions were less accurate when applied to specimens tested in compressive fatigue.

Thesis Supervisor: Lorna J. Gibson, Ph.D.
Thesis Committee: Brian D. Snyder, M.D., Ph.D.
Subra Suresh, Ph.D.

Biography

Tara LeeAnne Arthur attended Carleton University in Ottawa, Ontario, Canada from 1990-1994. In 1991, she participated in research at Carleton University, studying the fatigue of offshore structures. In 1991, she was accepted to the National Research Council of Canada's Women in Engineering and Science program, including one summer work term at the Dominion Astrophysical Observatory and two terms in the Structures and Materials Laboratory at the Institute for Aerospace Research. She received a Bachelor of Engineering degree in Aerospace Engineering in 1994 and was awarded a Senate Medal for Outstanding Academic Achievement. She was also awarded a NSERC 1967 Fellowship for graduate study from the Natural Sciences and Engineering Research Council of Canada.

From 1994-1996, she attended the Massachusetts Institute of Technology and worked in the Three Dimensional Printing Lab under Professor Emanuel Sachs in the Department of Mechanical Engineering. Her master's thesis, awarded in 1996, was titled "Factors Limiting the Surface Finish of Three Dimensional Printed Parts".

After completing her master's degree, she joined the Harvard-MIT Division of Health Sciences and Technology for a doctorate in Medical Engineering/Medical Physics. Her thesis work was conducted with Professor Lorna J. Gibson in the Department of Materials Science and Engineering and at the Orthopedic Biomechanics Laboratory at Beth Israel Deaconess Medical Center. In 1999-2000 and 2000-2001, she was partially supported by the Sir James Lougheed Award of Distinction from the Alberta Heritage Scholarship Fund.

Acknowledgements

Funding for this work was provided by the National Institutes of Health (AR41894-0182), the Natural Sciences and Engineering Research Council of Canada, the Alberta Heritage Scholarship Fund, the Harvard-MIT Division of Health Sciences and Technology (Becton Dickinson Fellowship in Health Sciences and Technology), and the Matoula S. Salapatas Professorship in Materials Science and Engineering at MIT. Dr. Clive Lee's work at the Orthopedic Biomechanics Lab was supported by the Fulbright Scholarship program and the Health Research Board of Ireland.

Professor Lorna Gibson has been a wonderful advisor over the past five years. She called me one afternoon in 1996 and asked if I would like to work on a project of hers involving fatigue testing of trabecular bone. Since this was the third time in my life I was asked, out of the blue, to work on a fatigue-related project, I decided that my destiny somehow involved fatigue and said yes. I've never regretted it.

I owe a lot to Dr. Clive Lee, of the Royal College of Surgeons in Ireland, for taking me under his wing when I started this project, for developing the staining protocols, applying them to observing microdamage in trabecular bone, and getting my project started. The assistance and advice of Clive and his student, Fergal O'Brien, since then, has been a great help, both for the project and my morale.

Professor Subra Suresh and Dr. Brian Snyder were both great assets as committee members. Brian's knowledge of the bone literature and his comments over the years were particularly helpful.

Ryan Pierce deserves a lot of credit for developing the idea that microdamage might be seen in creep specimens and making it his bachelor's thesis. His ideas and help were invaluable over the two years he worked on the project.

This work could not have been done without the support of students and staff at both the Orthopedic Biomechanics Lab at Beth Israel Deaconess Medical Center and the Cellular Solids Lab at MIT. Aaron Hecker kept the early mechanical testing running smoothly, and Steve Bowman was a great resource while I was learning about trabecular bone behavior. Debbie Chachra's proofreading and advice on thesis preparation was a great help. The friendship and support of Sara Wilson and Cecile Smeesters was particularly appreciated.

Finally, I'd like to acknowledge the support of my family, who gave me a love of learning and much support over the years. My husband, Peter, cannot be thanked enough for his patience support, and proofreading, and for keeping our life running smoothly during the past few months.

Table of Contents

Biography **5**

Acknowledgements **7**

List of Figures **13**

List of Tables **23**

List of Symbols **27**

Chapter 1: Introduction **29**

1.1 Motivation 29
1.2 Research Questions 32
1.3 Literature Review 33
1.3.1 Bone Biology 33
1.3.1.1 Bone Structure 33
1.3.1.2 Bone Remodeling 34
1.3.2 Contributors to Mechanical Properties 35
1.3.3 Mechanical Properties of Trabecular Bone 37
1.3.3.1 Elastic and Plastic Behavior 37
1.3.3.2 Fatigue 38
1.3.3.3 Creep 40
1.3.4 Microdamage 40
1.3.4.1 *In vivo* Observations - Natural History 41
1.3.4.2 Microdamage and Remodeling 41
1.3.4.3 Microdamage and Mechanical Testing 42
1.3.4.4 Microdamage and Mechanical Properties 43
1.3.4.5 Modeling of Microdamage 44
1.3.5 Staining of Microdamage 44
1.3.5.1 Basic Fuchsin 44
1.3.5.2 Chelating Fluorochromes 45
1.3.6 Cellular Solids 46
1.4 Outline of Thesis 47

Chapter 2: Stain Concentration and Stain Optimization **49**

2.1 Introduction 49
2.2 Materials and Methods 50
2.3 Results 53
2.4 Discussion 59

Chapter 3: Microdamage Accumulation in Bovine Trabecular Bone in Compression 61

3.1 Introduction 61
3.2 Materials and Methods 62
3.3 Results 69
3.4 Discussion 82

Chapter 4: Modeling Microdamage in Bovine Trabecular Bone in Compression ... 87

4.1 Introduction 87
4.2 Modeling 90
4.2.1 Trabeculae Level 92
4.2.2 Cellular Solid Level 101
4.2.3 Specimen Level 108
4.3 Comparison with Experiments 111
4.4 Parametric Study 114
4.5 Discussion 122

Chapter 5: Fatigue Microdamage of Trabecular Bone 125

5.1 Introduction 125
5.2 Materials and Methods 130
5.3 Results 139
5.4 Model Predictions 166
5.5 Discussion 172

Chapter 6: Comparison of Microdamage Accumulation in Specimens Tested in Different Loading Modes 179

6.1 Introduction 179
6.2 Materials and Methods 181
6.3 Results 186
6.4 Discussion 206

Chapter 7: Conclusions 211

7.1 Summary of Results 211
7.2 Strengths and Limitations 214
7.2.1 Strengths 214
7.2.2 Limitations 215
7.3 Future Work 216
7.4 Overall Conclusions 219

References 223

Appendix A: Sampling Issues in Quantifying Microdamage Accumulation 241

A.1 Introduction 241
A.2 Methods 241
A.3 Results 243
A.4 Discussion 251

Appendix B: Low Cycle Fatigue Testing of Trabecular Bone 253

B.1 Introduction 253
B.2 Materials and Methods 254
B.3 Results 256
B.4 Discussion 263

Appendix C: Monotonic Testing 267

Appendix D: Fatigue Testing 273

List of Figures

Figure 2.1: Bone specimen stained with a low concentration of oxytetracycline (0.003%) producing insufficient staining: the crack, indicated by arrows, is not distinct. 55

Figure 2.2: Bone specimen stained with medium concentration of oxytetracycline (0.03%) giving sufficient staining: the crack is well labeled (arrows). 55

Figure 2.3: Bone specimen stained with a high concentration of oxytetracycline (0.03%) leading to overstaining: diffuse staining is seen around the crack edges (arrows). .. 56

Figure 2.4: Bone specimen stained with a high concentration of xylenol orange (0.9%) with extensive staining: it is difficult to distinguish individual cracks. 56

Figure 2.5: Crack stained with alizarin complexone (red, white arrow) followed by calcein (green, black arrow), showing crack growth 57

Figure 2.6: Crack stained with oxytetracycline (yellow) followed by calcein (green). The two stains cannot be distinguished. 57

Figure 2.7: Cortical bone specimen showing an uncracked specimen edge stained with calcein blue followed by alizarin complexone (red). The calcein blue has been displaced by the alizarin complexone, and the edge appears reddish. 58

Figure 3.1: Stress-strain curves for bovine trabecular bone in compression. (a) Specimen unloaded to zero strain. The initial Young's modulus, E_0, the secant modulus, E_{sec}, the reloading modulus, E_r, the unloading modulus, E_{unload}, the maximum strain, ε_{max}, the residual strain, ε_{res}, and the region of residual tension (gray shading) are indicated. (b) Specimen unloaded to zero stress. 67

Figure 3.2: Schematic of types of microdamage in trabecular bone. (a) single crack (b) parallel cracks (c) cross-hatched cracks (equal cross-hatching) (d) complete fracture (e) damaged band across section (average of five measurements). 68

Figure 3.3: Examples of machining damage seen on the outer edges of specimens. Specimens were stained in 0.03% alizarin complexone (red) before testing, and 0.01% calcein (green) after testing. (a) Untested specimen. (b) Specimen loaded to ε_{max} = -4.0% 73

Figure 3.4: Observed patterns of microdamage in trabecular bone. All images are taken from a single specimen tested to -4.0%. (a) single crack, (b) parallel cracks, (c) cross-hatch: equal cross-hatching, (d) cross-hatch: unequal cross-hatching, one primary crack with minor secondary cracks, (e) cross-hatch (white arrow): diffuse damage (black), (f) complete fracture. 74

Figure 3.5: Breakdown of number of damaged trabeculae, normalized by section area, by damage pattern for each strain level. The -2.5% strain level was not plotted because only two specimens were tested to that level. 75

Figure 3.6: Breakdown of number of damaged trabeculae, normalized by section area, by extent of damage through the trabecular thickness for each strain level. The -2.5% strain level was not plotted because only two specimens were tested to that level. . 75

Figure 3.7: (a) Crack length frequency distribution for a single specimen (tested to ε_{max} = -4.0%). (b) Average crack number frequency distribution for each strain level (n = 5 for each strain level). Distributions for strain levels below ε_{max} = -1.1% are very small and are not plotted. 76

Figure 3.8: (a) Crack number, *Cr.Num.*, normalized by section area plotted against damage ($1 - E_{sec}/E_0$). (b) Total crack length, *Cr.Len.*, normalized by section area plotted against damage ($1 - E_{sec}/E_0$) 77

Figure 3.9: Composite images of typical gauge lengths showing the damaged band. Both specimens were stained in alizarin complexone before testing and calcein (green) after testing. (a) Specimen compressed to ε_{max} = -1.3%. Small regions of damage are visible (middle, about one third of the height from the top), but no distinct band is seen. (b) Specimen compressed to ε_{max} = -4.0%. A distinct damage band is visible. 78

Figure 3.10: Images of section gauge lengths, with location of damaged trabeculae marked. Images are typical for the strain level. (a) Untested specimen, little damage present. (b) Specimen tested to ε_{max} = -0.4%, not significantly different from untested specimen. (c) Specimen tested to ε_{max} = -0.8%, some damage seen. Damage is not localized. (d) Specimen tested to ε_{max} = -1.1%, damage occurs locally, but does not extend across the specimen. (e) Specimen tested to ε_{max} = -1.3%, localized region of damage extends across the specimen, forming a damage band. (f) Specimen tested to ε_{max} = -2.0%, damage band has increased in length. (g) Specimen tested to ε_{max} = -4.0%, damage band is not significantly longer than in (f), but damage density within the band has increased. 81

Figure 4.1: Schematic of trabecular bone, showing different levels of structure. Individual trabeculae may have microcracks, reducing their stiffness, or be fractured. A region of trabecular bone may have trabeculae with no damage, with microcracks, or with fractures. As strain increases, the damage is concentrated in a band, indicated by the darker area on the whole specimen view, within the specimen. The model described in the text considers all three scales. 91

Figure 4.2: An idealized two-dimensional representation of a single trabecula. The trabecular width b is either thickness t (rod model) or length l (plate model). (a) An idealized undamaged trabecula of modulus E_s. (b) The damaged area is delineated as containing the local damage. (c) The damaged area is represented as a new material with a reduced modulus, $\overline{E}$ 97

Figure 4.3: Each damaged trabeculae is replaced by an intact trabeculae of the same initial modulus but a new effective thickness, t'. The effective thickness, t', is chosen such that the intact trabecula of thickness t' has the same stiffness as the damaged trabecula of thickness t_0. 98

Figure 4.4: General form of a beam with a segment missing. The beam may be deformed in bending (rod model) or by axial stretching (plate model). 99

Figure 4.5: Damage location and depth across the thickness, as measured in Chapter 3. Damage depth across the thickness is rounded to the nearest 25%. Schematic showing damage occurring (a) in the middle of a trabecula, 50% depth across the thickness, and (b) at one end of a trabecula, 25% depth across the thickness. 100

Figure 4.6: Trabeculae organized into a cellular solid network. (a) Entire network, showing trabeculae with no damage (black), trabeculae with partial damage (dark gray), and fractured trabeculae with a crack or cracks through the entire thickness (light gray). (b) Fractured trabeculae have been removed from the model. (c) Partially damaged trabeculae have been reduced in thickness. (d) The thickness reduction is averaged over all the remaining trabeculae, to give an average thickness of $\overline{t}$ 106

Figure 4.7: Plot of modulus reduction vs. density fraction reduction (Valhalla, private communication) for random removal of rod-like struts random open-cell cellular solid (black). An estimate for the modulus reduction for random removal of plate-like struts has also been included; the dashed portion of the line indicates the interpolation between the two limits (gray). 107

Figure 4.8: Damage within trabecular bone specimens is localized. (a) Image of a specimen tested to -4.0% compressive strain, stained after testing with calcein green. (b) Schematic representation of localized damage. 110

Figure 4.9: Typical stress-strain curve of a trabecular bone specimen, loaded to a strain of -3.0%, then unloaded to zero strain. Initial modulus, E_0, and secant modulus, E_{sec}, are shown. 112

Figure 4.10: Comparison of model predictions with experimentally determined modulus loss. Experimental modulus loss is the secant modulus divided by the initial loading modulus. (a) Closed-cell model based on plate-like trabeculae ($Y = 0.995X + 0.01$, $R^2 = 0.82$, $R_c^2 = 0.81$. (b) Open-cell model based on rod-like trabeculae ($Y = 1.13X - 0.16$, $R^2 = 0.83$, $R_c^2 = 0.75$). 113

Figure 4.11: Effects of changes in input variables on the specimen reduced modulus. Closed symbols represent a specimen tested to -4.0% strain, with considerable damage. Black diamonds represent the closed-cell model (plate); gray squares represent the open-cell model (rod). The other symbols represent a specimen tested to -1.1% strain, with little damage. The open triangles represent the closed-cell (plate model), while the solid gray line represents the open-cell (rod) model. Input parameters varied include (a) reduced modulus due to removal of fractured struts, E_{strut_loss}/E_0, (b) width of the localized damage band, (c) total damaged area in the specimen, A_{total}, (d) estimate of depth of damage through the thickness, t_{damage}/t_0, (e) fraction of undamaged struts, f_0, and (f) ratio of middle damage to end damage, plotted on a log scale. 120

Figure 4.12: Effects of changing the distribution of damage on predicted modulus reduction. Black diamonds represent an even distribution of areas; black circles represent damage concentrated in fractured struts (no partial damage). The error bars represent the range of created by different distributions. (a) Open-cell model. (b) Closed-cell model. 121

Figure 5.1: S-N curve for 61 waisted cylindrical specimens of bovine trabecular bone tested in compression (Appendix B). An endurance limit is seen at a normalized stress of $\Delta\sigma/E_0 \approx 0.0035$. The cut off between high and low cycle fatigue occurs at approximately 3000 cycles. Regressions for high and low cycle fatigue (Appendix B) are shown. 129

Figure 5.2: Experimental setup, including specimen geometry. An unwaisted cylinder is glued into brass end caps to minimize end effects. The specimen is loaded in compression between two platens (one fixed, one self-aligning) in a servohydraulic testing machine. An extensometer is attached to the specimen endcaps. 134

Figure 5.3: Typical fatigue test. Specimen was loaded at $\Delta\sigma/E_0 = 0.007$ to $\varepsilon_{max} = -2.5\%$. The specimen shows both cycle-dependent fatigue damage (modulus reduction, E_{sec}/E_0, with increasing cycles) and time-dependent creep damage (increase in residual or plastic strain, ε_{res}, with increasing number of cycles, N). 135

Figure 5.4: Modulus reduction, E_{sec}/E_0 (black), and maximum strain, ε_{max} (gray), are plotted as a function of number of cycles, N. Specimens stopped at a given maximum strain will have similar modulus reductions, but those stopped at a preset number of cycles may have different modulus reductions. Each symbol (square, triangle, diamond) represents a different specimen. (a) Two specimens from a previous study (Appendix B) tested at the same normalized stress ($\Delta\sigma/E_0 = 0.0085$). Data from the current fatigue tests shows that modulus reduction and maximum strain follow similar paths for (b) $\Delta\sigma/E_0 = 0.008$. (c) $\Delta\sigma/E_0 = 0.007$. (d) $\Delta\sigma/E_0 = 0.006$. (e) $\Delta\sigma/E_0 = 0.005$. 138

Figure 5.5: S-N curve for specimens at -1.3% strain. Open diamonds represent tests stopped at -1.3% strain; filled triangles represent specimens tested to strains greater than -1.3%. The data points plotted indicate the cycle number where -1.3% strain was exceeded. There is a power law relationship between normalized stress and number of cycles ($N = 7.47 \times 10^{-22} (\Delta\sigma/E_0)^{-10.4}$, $R^2 = 0.62$)..... 150

Figure 5.6: Bovine trabecular bone follows the Coffin-Manson law at low cycle numbers. There is a power law relationship between the change in the change in plastic strain in a single cycle, $\Delta\varepsilon_{pl}$, and number of cycles for specimens tested to less than 100 cycles (filled diamonds) ($\Delta\varepsilon_{pl} = 0.691\ N^{-1.10}$, $R^2 = 0.82$)..... 151

Figure 5.7: Plot of modulus reduction, E_r/E_0, as a function of maximum compressive strain, ε_{max}. (a) Data plotted by normalized stress. Data at each strain level spread for clarity. (b) Pooled fatigue data. The data are linearly related ($Y = 0.27X + 1.12$, $p < 0.05$, $R^2 = 0.48$). The regression intersects the line $E_r/E_0 = 1$ at $\varepsilon_{max} = -0.44\%$. 152

Figure 5.8: Plot of modulus reduction, E_{sec}/E_0, as a function of maximum compressive strain, ε_{max}. (a) Data plotted by normalized stress. Data at each strain level spread slightly for clarity. (b) Pooled fatigue data. The regression intersects the line $E_{sec}/E_0 = 1$ at $\varepsilon_{max} = -0.64\%$..... 153

Figure 5.9: Plot of residual strain, ε_{res}, as a function of maximum compressive strain, ε_{max}. (a) Data plotted by normalized stress. Data at each strain level spread slightly for clarity. (b) Pooled fatigue data. There is a linear relationship between residual strain and maximimum strain ($\varepsilon_{res} = 0.71\varepsilon_{max} + 0.39$, $p < 0.001$, $p < 0.05$, $R^2 = 0.76$). The regression intersects the axis $\varepsilon_{res} = 0$ at $\varepsilon_{max} = -0.55\%$..... 154

Figure 5.10: Examples of damage patterns observed, including (a) diffusely stained area, without visible cracks, (b) single crack, (c) parallel cracks, (d) cross-hatching, (e) complete trabecular fracture, and (f) local region of damage in the specimen.. 155

Figure 5.11: Examples of damage patterns observed. All images are taken from a single specimen tested to -2.0% strain at $\Delta\sigma/E_0 = 0.007$. (a) diffusely stained area, without visible cracks, (b) single crack, (c) parallel cracks, (d) cross-hatching, and (e) complete trabecular fracture. 158

Figure 5.12: Plot of total number of (a) damaged trabeculae and (b) damaged area fraction vs. maximum compressive strain, ε_{max}. The numbers in the legend represent the normalized stress level. Data at each strain level spread slightly for clarity. Microdamage increases with increasing maximum strain, ε_{max}, after yield. 159

Figure 5.13: Microdamage parameters increased with increasing modulus reduction (decreasing E_r/E_0). The data plotted shows number of damaged trabeculae per unit area, but results are similar for other microdamage parameters. 160

Figure 5.14: Plots of damage parameters showing the relationship between damage parameters, normalized stress, $\Delta\sigma/E_0$, and number of cycles, N. The damage parameter, D, is: (a) number of damaged trabecular per unit area. ($D/N = 5.26\times10^{16}(\Delta\sigma/E_0)^{8.7}$, $R^2 = 0.39$). (b) damaged area fraction. ($D/N = 1.06\times10^{11}(\Delta\sigma/E_0)^{6.84}$, $R^2 = 0.22$) A weak but significant relationship is seen in both cases. 161

Figure 5.15: Patterns of microdamage observed in bone specimens, tested to two normalized stress levels. Number of specimens = 5 for each column. The numbers above each column represent the average number of cycles, N, needed to reach the maximum strain. (a) $\Delta\sigma/E_0 = 0.008$. No specimens were tested to strain levels less than $\varepsilon_{max} = -1.3\%$ at this normalized stress. (b) $\Delta\sigma/E_0 = 0.005$ 162

Figure 5.16: Plot of fraction of total trabeculae containing complete fractures. There is a threshold number of cycles needed for fractures to form. This threshold increases with decreasing maximum specimen strain, ε_{max} (arrows). 163

Figure 5.17: Extent of damage across the trabecular strut, rounded to the nearest one-quarter for specimens tested at a normalized stress of $\Delta\sigma/E_0 = 0.005$. Values were estimated to the nearest quarter. The trabecular damage extends all the way across the specimen approximately half the time. Relatively few cracks extend 75% of the distance across the trabecula. Results are typical for other normalized stress levels. 164

Figure 5.18: Progression of damage in typical sections. Each mark represents a damaged trabecula. All specimens shown here were tested (when applicable) at the same normalized stress level of $\Delta\sigma/E_0 = 0.006$. (a) untested control, (b) $\varepsilon_{max} = -0.8\%$, (c) $\varepsilon_{max} = -1.1\%$, (d) $\varepsilon_{max} = -1.3\%$, (e) $\varepsilon_{max} = -1.65\%$, (f) $\varepsilon_{max} = -2.0\%$, (g) $\varepsilon_{max} = -2.5\%$. 165

Figure 5.19: Comparison of model parameters with experimental results. Values for the monotonic tests (open triangles) are included for comparison. The solid line represents perfect agreement between the predicted and experimentally measured values. The correlation coefficient, R^2, and the concordance correlation, R_c^2, of the line Y = X were determined. (a) Closed-cell, plate model. ($Y = 0.74X + 0.17$, $R^2 = 0.39$, $R_c^2 = 0.38$) (b) Open-cell rod model. ($Y = 1.03X - 0.20$, $R^2 = 0.41$, $R_c^2 = 0.23$). 168

Figure 5.20: (a) General case of localized damage from an unwaisted fatigue specimen. Usually, damage forms (b) a band ($L_3 = 0$) or (c) a patch of damage ($L_2 = 0$). Compressive loading occurs in the vertical direction. 169

Figure 5.21: An improvement in model predictions was seen when the general equation was used to determine modulus reduction due to localized damage (closed symbols). The initial calculation (open symbols) assumed that damage always formed a distinct band. The solid line represents perfect agreement between the predicted and experimentally measured values. (a) Closed-cell, plate model ($Y = 0.74X + 0.21$, $R^2 = 0.39$, $R_c^2 = 0.38$). (b) Open-cell rod model ($Y = 1.02X - 0.11$, $R^2 = 0.42$, $R_c^2 = 0.31$). 170

Figure 5.22: Breakdown of model predictions by normalized stress level for the (a) closed-cell and (b) open-cell model. The model predictions do not improve when each normalized stress is examined separately. 171

Figure 6.1: Typical creep test, specimen 65E, loaded at $\Delta\sigma/E_0 = 0.0082$ to $\varepsilon_{max} = -2.5\%$ strain. The specimen shows typical creep behavior, with a primary, secondary, and tertiary regime. A residual strain, ε_{res}, was present on unloading. 185

Figure 6.2: (a) Plot of modulus reduction, E_r/E_0, as a function of maximum strain. Data points have been separated for clarity. The same figure, without the monotonic data, is seen as Figure 5.4. (a) Fatigue data separated by normalized stress. (b) Pooled fatigue data. The equations of the regression lines are: fatigue, $Y = 0.27X + 1.12$, $p < 0.05$, $R^2 = 0.48$; monotonic, $Y = 0.23X + 1.02$, $p < 0.05$, $R^2 = 0.77$, monotonic without $\varepsilon_{max} = -3.0\%, -4.0\%$: $Y = 0.34X + 1.18$, $p < 0.05$, $R^2 = 0.74$. 194

Figure 6.3: Residual strain after loading, ε_{res}, as a function of maximum strain, ε_{max}, for various loading modes. (a) Specimens plotted individually. The slope of the regression for the fatigue data ($Y = 0.71X + 0.39$, $p < 0.05$, $R^2 = 0.76$) was significantly different from the slope of the monotonic data ($Y = 0.43X + 0.33$, $p < 0.05$, $R^2 = 0.83$), the creep data ($Y = 0.26X - 0.003$, $R^2 = 0.65$, not plotted in (a)), and the monotonic data excluding data points at strains greater than $\varepsilon_{max} = -2.5\%$ ($Y = 0.31X + 0.17$, $p < 0.05$, $R^2 = 0.74$). (b) Pooled strain data. Data points have been separated for clarity. 195

Figure 6.4: Plot of residual strain vs. modulus reduction for specimens tested in monotonic compression (stars) and compressive fatigue (diamonds). The fatigue specimens tested at different strain levels were not significantly different, so the data were pooled. The slopes and intercepts of the two regression lines were: monotonic compression, $Y = 1.43X - 1.36$, $p < 0.05$, $R^2 = 0.64$; fatigue, $Y = 1.04X - 1.50$, $p < 0.05$, $R^2 = 0.25$). 196

Figure 6.5: Plot of total number of damaged trabeculae vs. maximum compressive strain, ε_{max}. The numbers in the legend represent the normalized stress level. The damage increases with increasing strain. Microdamage parameters from monotonic compression tests and creep tests are lower than microdamage from fatigue-tested specimens loaded to the same strain, particularly near yield. Data points have been separated for clarity. The same plot, without monotonic and creep data, is seen as Figure 5.10(a). (a) Fatigue specimens separated by normalized stress. (b) Pooled fatigue data. 197

Figure 6.6: Plot of total damaged area fraction vs. maximum compressive strain, ε_{max}. The numbers in the legend represent the normalized stress level. Microdamage parameters from monotonic compression tests and creep tests are smaller than microdamage from fatigue-tested specimens loaded to the same strain, particularly near yield. Data points have been separated for clarity. The same plot, without monotonic and creep data, is seen as Figure 5.10(b). (a) Fatigue specimens separated by normalized stress. (b) Pooled fatigue data. 198

Figure 6.7: Damage parameters as a function of modulus reduction. Damage parameters increased with increasing modulus loss (decreasing E_r/E_0). (a) Number of damaged trabeculae per unit area. (b) Damaged area fraction. 199

Figure 6.8: Crack length histogram for a typical creep specimen, 85B, tested to $\varepsilon_{max} = -2.0\%$ at a normalized stress level of $\Delta\sigma/E_0 = 0.0055$. The solid line represents the average value of five specimens tested to $\varepsilon_{max} = -2.0\%$ in monotonic compression. 200

Figure 6.9: Damage band comparisons for specimens tested in compression and creep. Damage band length increased with increasing maximum strain, ε_{max}. No significant differences were seen between groups tested to the same strains. 201

Figure 6.10: Comparison of crack number and length for specimens tested in monotonic compression and compressive creep. Both crack numerical density and crack length density increased with increasing maximum strain, ε_{max}. No significant differences were seen between groups tested to the same maximum strain. 202

Figure 6.11: Breakdown of number of damaged trabeculae by damage pattern, normalized by section area, for the various loading modes. Low cycle fatigue (LCF) is represented by specimens tested at $\Delta\sigma/E_0$ = 0.008; high cycle fatigue (HCF) is represented by specimens tested at $\Delta\sigma/E_0$ = 0.005 203

Figure 6.12: Fraction of damaged trabeculae containing complete fractures, with separated ends. Creep specimens contained almost no fractures and, for clarity, are not plotted. No fractures were observed in specimens tested in monotonic compression at strains below -2.0%. Specimens fatigued at low normalized stresses (high number of cycles) had an increased proportion of fractures compared to specimens tested at higher normalized stresses (lower number of cycles) and specimens tested in monotonic compression and creep. Data points have been spread out for clarity. 204

Figure 6.13: Breakdown of number of damaged trabeculae by damage pattern for the various loading modes. Low cycle fatigue (LCF) is represented by specimens tested at $\Delta\sigma/E_0$ = 0.008; high cycle fatigue (HCF) is represented by specimens tested at $\Delta\sigma/E_0$ = 0.005. 205

Figure A.1: Images showing running averages of crack number, *Cr.Num.*, as more images are used to compute the average in a specimen with a substantial amount of damage (89D, 159 images of damage). The shaded band indicates the range within ten percent of the final estimate. 245

Figure A.2: Images showing running averages of crack length, *Cr.Len.*, as more images are used to compute the average in a specimen with a substantial amount of damage (89D, 159 images of damage). The shaded band indicates the range within ten percent of the final estimate. 246

Figure A.3: Images showing running averages of damaged area as more images are used to compute the average in a specimen with a substantial amount of damage (89D, 159 images of damage). The shaded band indicates the range within ten percent of the final estimate. 247

Figure A.4: Images showing running average of crack number, *Cr.Num.*, as more images are used to compute the average in a specimen with a small amount of damage (55D, 40 images of damage). The shaded band indicates the range within ten percent of the final estimate. 248

Figure A.5: Images showing running averages of crack length, *Cr.Len.*, as more images are used to compute the average in a specimen with a small amount of damage (55D, 40 images of damage). The shaded band indicates the range within ten percent of the final estimate. 249

Figure A.6: Images showing running averages of damaged area as more images are used to compute the average in a specimen with a small amount of damage (55D, 40 images of damage). The shaded band indicates the range within ten percent of the final estimate. 250

Figure B.1: Normalized stress, $\Delta\sigma/E_0$, versus number of cycles to failure, N_f, for 61 fatigue specimens. 260

Figure B.2: Normalized stress, $\Delta\sigma/E_0$, versus number of cycles to failure, N_f, of 27 specimens tested in low cycle fatigue (cutoff, N = 100). 261

Figure B.3: Normalized stress, $\Delta\sigma/E_0$, versus number of cycles to failure, N_f, of 34 specimens tested in high cycle fatigue (cutoff, N = 100). 261

Figure B.4: Normalized stress, $\Delta\sigma/E_0$, versus number of cycles to failure, N_f, of 39 specimens tested in low cycle fatigue (cutoff, N = 3000). 262

Figure B.5: Normalized stress, $\Delta\sigma/E_0$, versus number of cycles to failure, N_f, of 22 specimens tested in high cycle fatigue (cutoff, N = 3000). 262

Figure B.6: Comparison of fatigue tests performed by three operators, as indicated in the legend. No differences were apparent. 265

List of Tables

Table 2.1: Excitation and emission maxima of chelating fluorochromes (Rahn, 1977; Lee, 1997) 51

Table 2.2: Concentration results for five chelating fluorochromes. 53

Table 2.3: Acceptable two-stain sequences of chelating fluorochromes. 54

Table 2.4: Potentially acceptable three, four, and five stain sequences of chelating fluorochromes. 60

Table 3.1: Mechanical properties of trabecular bone specimens tested in monotonic compression to various strains. Numbers in parentheses represent standard deviations. 69

Table 3.2: Microdamage parameters of trabecular bone specimens tested in monotonic compression. Numbers in parentheses are standard deviations. 70

Table 4.1: Comparison of components contributing to modulus reduction in the localized damaged region. The overall modulus reduction, E_2/E_0, is the product of modulus loss due to strut loss, E_{strut_loss}/E_0, and the modulus loss due to damage, E_{damage}/E_0. Values are shown for both open- and closed-cell models. All values decrease with increasing strain. E_{strut_loss}/E_0 has a greater effect on E_2/E_0 for both models, with E_{damage}/E_0 having only a minor effect in the closed-cell model. 117

Table 5.1: Combinations of normalized stress, $\Delta\sigma/E_0$, and maximum strain, ε_{max}, tested. Specimens loaded to the two highest normalized stress levels were not tested to the two lowest strains because the high load levels would cause the maximum strains to be exceeded within one cycle. 131

Table 5.2: Average mechanical property (± standard deviation) of all fatigue tests..... 140

Table 5.3: Average area measurements for 110 fatigue tests. 144

Table 5.4: Average microdamage parameters of 110 fatigue tests. 145

Table 5.5: Specimens tested to the same modulus reductions, with different maximum strains, ε_{max}, and numbers of cycles, N. 147

Table 5.6: Groups of specimens tested to the same normalized stress, $\Delta\sigma/E_0$, and maximum compressive strain, ε_{max}, with different numbers of cycles, N. 148

Table 5.7: Summary of model fit parameters for a variety of different cases discussed in the text. Numbers in parentheses represent standard deviations. Data from monotonic compression tests are included for comparison..... 167

Table 6.1: Overview of all tested specimens, including monotonic compression, compressive creep, and compressive fatigue tests. 182

Table 6.2: Mechanical property data for all creep tests (Pierce, 1999)..... 186

Table 6.3: Microdamage data for all creep tests. 187

Table 6.4: Breakdown of number of damaged trabecula for all creep tests, by patterns of damage and by the extent of the damage across the trabeculae thickness, rounded to the nearest quarter. 188

Table A.1: Dehydration schedule for trabecular bone cores. 242

Table A.2: Fraction of total available images of microdamage required for microdamage parameter estimates to approach within 10% of final estimates. 244

Table B.1: Low cycle fatigue test results. Failure occurred at ten percent modulus loss or at fracture, whichever occurred first..... 257

Table B.2: Summary of all fatigue results to date. Tests were performed by three different operators, as indicated by the specimen prefix..... 258

Table C.1: Mechanical properties measured for 38 monotonic tests unloaded to zero strain. 268

Table C.2: Microdamage parameters measured for 38 monotonic tests unloaded to zero strain. 269

Table C.3: Damaged trabeculae in each of 38 monotonic tests unloaded to zero strain, classified by pattern of damage and by extent of damage across the trabeculae, rounded to the nearest quarter. 270

Table C.4: Mechanical properties measured for 6 monotonic tests unloaded to zero load. 271

Table C.5: Microdamage parameters measured for 6 monotonic tests unloaded to zero load. 271

Table C.6: Damaged trabeculae in each of for 6 monotonic tests unloaded to zero load, classified by pattern of damage and by extent of damage across the trabeculae, rounded to the nearest quarter. 271

Table D.1: Mechanical properties measured for 20 fatigue tests tested to a normalized stress of $\Delta\sigma/E_0 = 0.008$, plus 10 control specimens. 274

Table D.2: Mechanical properties measured for 20 fatigue tests tested to a normalized stress of $\Delta\sigma/E_0 = 0.007$. 275

Table D.3: Mechanical properties measured for 20 fatigue tests tested to a normalized stress of $\Delta\sigma/E_0 = 0.006$. 276

Table D.4: Mechanical properties measured for 30 fatigue tests tested to a normalized stress of $\Delta\sigma/E_0 = 0.005$. 277

Table D.5: Microdamage parameters measured for 30 fatigue tests tested to a normalized stress of $\Delta\sigma/E_0 = 0.008$, plus 10 control specimens. 278

Table D.6: Microdamage parameters measured for 20 fatigue tests tested to a normalized stress of $\Delta\sigma/E_0 = 0.007$. 279

Table D.7: Microdamage parameters measured for 30 fatigue tests tested to a normalized stress of $\Delta\sigma/E_0 = 0.006$. 280

Table D.8: Microdamage parameters measured for 30 fatigue tests tested to a normalized stress of $\Delta\sigma/E_0 = 0.005$. 281

Table D.9: Damaged trabeculae in each of 20 fatigue tests tested to a normalized stress of $\Delta\sigma/E_0 = 0.008$, plus 10 control specimens, classified by pattern of damage and by extent of damage across the trabeculae, rounded to the nearest quarter. 282

Table D.10: Damaged trabeculae in each of 20 fatigue tests tested to a normalized stress of $\Delta\sigma/E_0 = 0.007$, classified by pattern of damage and by extent of damage across the trabeculae, rounded to the nearest quarter. 283

Table D.11: Damaged trabeculae in each of 20 fatigue tests tested to a normalized stress of $\Delta\sigma/E_0 = 0.006$, classified by pattern of damage and by extent of damage across the trabeculae, rounded to the nearest quarter. 284

Table D.12: Damaged trabeculae in each of 30 fatigue tests tested to a normalized stress of $\Delta\sigma/E_0$ = 0.005, classified by pattern of damage and by extent of damage across the trabeculae, rounded to the nearest quarter. 285

List of Symbols

A_{crack}	area of the crack-containing region
A_{damage}	area of damage in a single rod or plate
$A_{section}$	cross-sectional area of the strut
A_{total}	total damaged area in a specimen
b	width of rod or plate
Cr.Len.	total length of cracks observed in a specimen
Cr.Num.	total number of cracks observed in a specimen
D	generalized damage parameter
d_1	width of specimen containing damage in a partially formed band
d_2	width of specimen containing no damage in a partially formed band
E	Young's modulus
E'	reduced modulus in a damage-containing specimen
E_0	modulus of the intact cellular solid or trabecular bone specimen
E_2	local reduced modulus due to fractured and damaged struts
$\overline{E}$	reduced modulus of the crack-containing region
E_{damage}	modulus of the damaged cellular solid
E_r	Young's modulus measured during specimen reloading
E_s	Young's modulus of the rod or plate material
E_{sec}	secant Young's modulus
E_{strut_loss}	reduced modulus due to the removal of fractured struts
E_{unload}	Young's modulus measured during specimen unloading
F	applied force
f	number of plates (faces) per unit cell
f_0	fraction of trabeculae with no damage
$f(l_n)$	crack length frequency at length l_n
$f_{n\%,i}$	fraction of struts with damage through n% of the thickness in location i (m – middle, e – end)
h	height of damaged region in a trabecula
HCF	high cycle fatigue
i	number of plates removed due to fracture
I'	moment of inertia of strut with effective thickness t'
I_0	moment of inertia of the intact section
I_{damage}	moment of inertia of the damage containing region
I_i	moment of inertia of section i
k	damage formation rate coefficient
LCF	low cycle fatigue
L_0	length of specimen that is stressed during testing
L_1	length of undamaged region in the specimen, with modulus E_0
L_2	length of damaged region in the specimen, with modulus E_2
L_3	length of specimen containing a partially formed band
l_0	original length of rod or plate
M	applied moment
$m(l)$	moment of crack length distribution per unit area
N	number of cycles during fatigue loading

N_{damage}	number of struts containing damage or fracture
N_f	number of cycles to failure (10% modulus loss)
$N_{fracture}$	number of cycles to fracture
$N_{remaining}$	number of trabeculae remaining after removal of fractured struts
N_{total}	total number of plates in a cellular solid
q	exponent
t	rod or plate thickness
t'	effective strut thickness accounting for reduced stiffness due to damage
t_0	original thickness of rod or plate
$\bar{t}$	mean strut effective thickness after accounting for damage
t_{damage}	thickness of the damaged region
t_i	thickness of section i
$t'_{n\%,i}$	effective thickness of a trabeculae with damage through n% of the thickness in location i (m – middle, e – end)
t_{stop}	duration of creep tests (sec)
x_{damage}	length of the damage containing section
x_i	length of section i
δ	deflection of individual rod or plate
ε	strain
ε'	parameter used to calculate local modulus reduction in a trabecula
ε_{max}	maximum applied strain
ε_{res}	residual strain after unloading
λ	wavelength (nm)
ρ	density
ρ^*	cellular solid bulk density
ρ_s	density of the solid material making up the cellular solid
(ρ^*/ρ_s)	relative density of a cellular solid
$(\rho^*/\rho_s)_0$	original relative density of bone
$(\rho^*/\rho_s)_{damage}$	relative density of bone due to damaged struts
$(\rho^*/\rho_s)_{fracture}$	relative density of bone after removal of fractured struts
σ	applied stress
$\Delta\sigma$	change in stress
$\Delta\varepsilon_{pl}$	change in plastic strain in a single fatigue cycle
$\Delta\sigma/E_0$	normalized stress, or effective applied strain
$\bar{\nu}$	reduced Poisson's ratio

Chapter 1: Introduction

1.1 Motivation

Microdamage, in the form of small cracks, is present in healthy human bone. Microdamage may occur due to a single overload (at loads below those required to fracture the bone) or due to fatigue loading (repetitive loading during the activities of daily living). In the case of an overload, such as a fall, significant amounts of microdamage are created without causing a clinically apparent fracture. During fatigue, relatively small loads may cause initiation and propagation of cracks over many cycles, although the load levels are not sufficient to cause damage during a single cycle.

Microdamage is thought to be a stimulus for bone remodeling (Burr *et al.*, 1985, 1997; Mori and Burr, 1993; Bentolila *et al.*, 1998), so areas of bone that contain microdamage are preferentially targeted for replacement with new, intact bone. Current estimates suggest that at least 30% of remodeling activity is targeted remodeling of damaged areas (Burr, 2000), rather than stochastic modeling of randomly selected regions. In healthy individuals, bone is continually removed and replaced by the bone remodeling process and few microcracks are present *in vivo*.

Microdamage accumulates when microdamage formation exceeds the body's capacity for repair, leading to reductions in bone stiffness and strength (Keaveny *et al.*, 1994c; Fyhrie and Vashishth, 2000) and increased fracture risk (Burr *et al.*, 1997). If microdamage continues to accumulate, the damage may coalesce and lead to an overt fracture. Two relatively common situations may result in pathologic microdamage accumulation. In the first case, the increase in microdamage formation is due to abnormal stresses on the bone, usually caused by a new or different type of strenuous, repetitive exercise in an otherwise healthy individual (Daffner and Pavlov, 1992). This is particularly common in elite athletes, dancers, and military recruits, but may also occur in individuals beginning an intensive exercise program. Fractures resulting from increased loads on a normal bone are termed stress fractures.

In the second case, microdamage is created at normal rates, but damage accumulates due to decreased remodeling ability. Bone remodeling rates decrease naturally with increasing age, and an exponential increase in microdamage is seen after

age 70 (Schaffler *et al.*, 1995b; Mori *et al.*, 1997; Fazzalari *et al.*, 1998b). A suppression of bone remodeling may also occur as a side effect of some drugs, including a resorption-inhibiting class of drugs, bisphosponates, used to treat osteoporosis (McClung, 1996; Parfitt *et al.*, 1996). Fractures that occur due to decreased remodeling are termed age-related fragility fractures, or insufficiency fractures (Daffner and Pavlov, 1992). In the case of elderly individuals, the reductions in bone stiffness and strength due to microdamage accumulation are compounded by stiffness and strength reductions due to the naturally occurring decrease in bone mass with age. This decrease in bone strength increases fracture risk, sometimes enough that a fracture may occur during activities of daily living, such as lifting moderate loads, reaching, or coughing. Current studies estimate that 10% of all hip fractures and 50% of vertebral fractures are so-called spontaneous fractures, occurring at load levels less than the expected strength of the bone (Lane and Myers, 1996). These fractures represent a serious public health concern (Dargent-Molina, 1998), as associated health care costs due to osteoporotic fractures were estimated at $13.8 billion in 1995 (Fox Ray *et al.*, 1997) and insufficiency fractures represent a significant fraction of these.

Microdamage in bone can be observed by histologic examination of thin sections of bone specimens that have been bulk stained prior to sectioning to label microcracks. A new technique using chelating fluorochromes has been developed to label microdamage in bone (Lee *et al.*, 2000). Chelating fluorochromes bind directly to calcium and can be used in sequence to determine when microdamage occurred. For example, specimens can be stained before and after mechanical testing to distinguish between microdamage present before testing and that created during testing.

Microdamage is present in both solid cortical bone and porous trabecular bone as small cracks that are usually less than 1 mm in length in cortical bone and somewhat shorter in trabecular bone. Cracks may be present individually or may be grouped together on a single trabecular strut. As well, damage is present in localized regions in the specimen, with other regions remaining intact. Because the organization of microdamage in trabecular bone occurs on several levels, a number of parameters can be used to quantify microdamage accumulation. They include crack number and length, crack surface density, damaged area fraction, damaged volume fraction, and number of

damaged trabeculae. Damage can also be classified by the pattern of cracking, including diffuse damage, single cracks (longitudinal and transverse), regions of cross-hatching, and complete trabecular fracture. We have also used two new microdamage parameters: the extent of damage across the trabecular thickness and the length the specimen containing damage.

Microdamage has been observed in mechanically tested specimens of cortical and trabecular bone that have been subjected to known loads and strains, but microdamage is not present in significant amounts until the specimen has been loaded beyond yield (Zioupos *et al.*, 1995; Wachtel and Keaveny, 1997). A number of studies have shown an increase in microdamage accumulation with increasing specimen stress (Zioupos *et al.*, 1995) or increasing specimen strain (Wachtel and Keaveny, 1997; Reilly and Currey, 1999) in monotonic tests. Microdamage also increases with increasing modulus reduction during fatigue loading (Forwood and Parker, 1989; Schaffler *et al.*, 1989; Zioupos *et al.*, 1996a; Hoshaw *et al.*, 1997; Boyce *et al.*, 1998; Burr *et al.*, 1998; Jepson *et al.*, 1999; O'Brien, 2001). A recent study (Burr *et al.*, 1998) determined mathematical relationships between microdamage accumulation and changes in mechanical properties in cortical bone. We are not aware of any studies of this sort using trabecular bone.

The work presented here assessed mechanical property changes and microdamage accumulation in mechanically tested bovine trabecular bone that has been loaded in uniaxial compression and in compressive fatigue. Relationships between mechanical property changes (maximum strain and modulus reduction), and microdamage parameters were examined and the progression of microdamage during loading to failure was determined.

Recently, researchers have begun to study the mechanistic relationships between microdamage and mechanical properties, and have developed models to explain these relationships. Guo *et al.* (1994) modeled modulus reduction due to random trabecular strut removal, as well as mechanistic removal of trabecular struts that failed due to growth of pre-existing microcracks during fatigue loading. Yeh and Keaveny (2000) used finite element modeling to simulate microdamage and microfractures in trabecular bone and found that microdamage affects bone mechanical properties more than microfractures, due to the relatively small number of microfractures present. Taylor

(1998b) has developed a model that predicts crack growth in cortical bone during fatigue loading based on measured stiffness reductions throughout the test. This thesis develops a cellular solid model that predicts modulus reductions for specimens tested in uniaxial compression based on observations of microdamage in experiment specimens and compares the predictions to experimentally measured values.

1.2 Research Questions

In this study, we related microdamage accumulation to changes in mechanical properties in mechanically tested bovine trabecular bone specimens, and developed cellular solid models to relate changes to bone modulus to observed microdamage. Both the overloading (post-yield) and fatigue damage cases were studied, and the two cases were compared to each other and to specimens loaded in compressive creep in a separate study (Pierce, 1999). Specifically, we asked the following research questions:

1. What are the best concentrations and sequences of chelating fluorochrome stains for visualizing microdamage in bovine trabecular bone?

2. Can microdamage created prior to testing be distinguished from that created during mechanical testing?

3. How does microdamage accumulate in bovine trabecular bone loaded to increasing strain during compression?

4. Is there a relationship between microdamage accumulation parameters and changes in mechanical properties for trabecular bone specimens loaded in uniaxial compression?

5. Can changes in stiffness in bovine trabecular bone tested in uniaxial compression be explained by a cellular solid model based on observed microdamage?

6. How does microdamage accumulate in bovine trabecular bone during compressive fatigue from zero load to fracture?

7. Can the cellular solid models developed for bovine trabecular bone tested in monotonic compression be used to explain changes in stiffness caused by fatigue loading?

8. Is the microdamage accumulation during fatigue different from that created during uniaxial compression and compressive creep, and does microdamage accumulation differ in specimens tested in fatigue at different normalized stresses?

1.3 Literature Review

1.3.1 Bone Biology

1.3.1.1 Bone Structure

Bone serves several purposes in the body. As well as acting as a rigid structural support and providing lever arms for muscles, tendons, and ligaments, bone protects internal organs, bone marrow within the bone provides hematopoesis, and bone itself serves as a reservoir for calcium and phosphorus (Nordin and Frankel, 1989). Bone is a living organ that is constantly being removed and replaced or "turned over" by the bone remodeling process, and the adult skeleton is replaced approximately every ten years. Bone mineral is a composite structure, consisting of small (~50 nm (Schaffler and Jepsen, 2000)) hydroxyapatite crystals (65 - 70% of dry weight) in a collagen matrix (25 - 30%) (Nordin and Frankel, 1989).

Normal bone is classified into two types: cortical, or compact, bone and trabecular, or cancellous, bone. Cortical bone is nearly solid (porosity ranging from 5% to approximately 30%) and is found in the shafts of long bones and as the outer layer of all bones. The interior of some bones, including vertebral bodies and the ends of the long bones, is filled with a porous, spongy-looking bone, termed trabecular or cancellous bone. This interior of porous bone increases the weight-bearing capacity of the bone with a relatively small increase in mass. Trabecular bone is generally considered to have a relative density, ρ^*/ρ_s, of less than 0.70. The structure of trabecular bone varies widely between different species, different anatomical sites (Amling *et al.*, 1996), and between individuals. Low-density trabecular bone, such as that seen in osteoporotic human vertebral bodies, consists of rod-like elements in an open-celled structure. Denser trabecular bone, such as that seen in the bovine proximal tibia, is usually composed of plate-like elements, forming a nearly closed-cell foam.

Some of the differences in structure of trabecular bone in different locations can be explained using Wolff's Law (Woo *et al.*, 1981; Cowin, 1986), which states that bone will adapt to optimally carry the loads placed on it. Bones with increased loading

increase in mass, while disuse causes a reduction in bone mass. As well, the architecture of the bone adapts to optimally carry the loads placed on it.

With age, several factors affect the skeleton. The most apparent of these changes is a reduction in bone mass. Bone mass reaches a peak by the age of 25, then decreases at a rate of 1-2% per year (Lane and Myers, 1996). In women, the rate of bone loss increases more dramatically with the cessation of estrogen production at menopause (occurring at approximately age 50). This results in the development of osteopenia or osteoporosis, depending on the degree of bone loss, with osteoporosis defined as bone mass 2.5 standard deviations below the young normal mean (Alexeera *et al.*, 1994). As bone mass is lost, the trabecular structure changes as trabecular plates are perforated and evolve into trabecular rods (Mosekilde *et al.*, 1987), and as some trabecular struts thin and others are lost completely (Bergot *et al.*, 1988). This loss of trabeculae increases the slenderness ratio of the remaining trabeculae, decreasing their buckling resistance (Snyder *et al.*, 1993). As well, the bone tissue becomes more mineralized (Grynpas, 1993) and the rate of remodeling slows (Daffner and Pavlov, 1992). This results in reductions in bone stiffness, strength, and failure energy (toughness) with increasing age (Ding *et al.*, 1997; Zioupos and Currey, 1998; Zioupos, 2001). These mechanical property reductions are beyond those expected due to changes in bone mass alone (Mosekilde *et al.*, 1987). All of these factors result in an increased fracture risk. This risk is turn is compounded by other factors, such as the risk of falling, which also increase with age.

1.3.1.2 Bone Remodeling

Bone remodeling begins when a region of bone is resorbed by osteoclastic activity and replaced by new bone laid down by osteoblasts. Remodeling occurs gradually, with only a few percent of the total bone volume undergoing remodeling at any given time. The remodeling process takes approximately 6-9 months to complete: 3-6 months to make the new bone packet, and a further 3 months the new bone to be completely mineralized (Frost, 1989).

Bone is thought to contain sensor cells that measure strain, compare the strain to acceptable values, and activate when the strain is not within that range. Many theories

(Turner, 1998, 1999; Martin, 2000) hypothesize that osteocytes in the bone matrix are able to sense strain, possibly through stretch-activated ion channels, interstitial fluid flow, electric potentials, or another phenomenon. A direct link exists between microdamage and the initiation of remodeling in cortical bone (Burr *et al.*, 1985, 1997; Mori and Burr, 1993; Bentolila *et al.*, 1998), and the same relationship is assumed to be true for trabecular bone (Martin, 2000).

An interesting development in bone remodeling involves the bisphosphonate class of drugs, which have been approved for the treatment of osteoporosis. Bisphosphonates help increase bone mass by suppressing bone resorption while allowing bone deposition to proceed (Parfitt *et al.*, 1996). Specifically, bisphosphonate use suppresses the targeted portion of bone remodeling (Li *et al.*, 2001). The use of bisphosphonates have been shown to increase bone mass in humans and in animal models (Schneider *et al.*, 1999). However, if a significant portion of the bone to be resorbed is targeted remodeling, i.e. remodeling initiated to repair microdamage, then suppressing remodeling will cause microdamage accumulation. While most recent studies of animals treated with bisphosphonates show an increase in microdamage accumulation (Forwood *et al.*, 2000a; Forwood *et al.*, 2000b; Hirano *et al.*, 2000; Mashiba *et al.*, 2000), others do not (Forwood *et al.*, 1995). Mechanical property reductions are also associated with high doses of bisphosphonates, but this may be due to poor mineralization rather than microdamage accumulation (Hirano *et al.*, 2000; Mashiba *et al.*, 2000).

1.3.2 Contributors to Mechanical Properties

The mechanical properties of trabecular bone are affected by several factors. Trabecular bone strength and modulus are strongly correlated with bone relative density, ρ^*/ρ_s (Carter and Hayes, 1977c; Rice *et al.*, 1988; Keaveny *et al.*, 1993b). In general, trabecular bone stiffness is related to the relative density by a linear or power law relationship (Gibson, 1985; Keaveny and Hayes, 1993b). Variations in trabecular bone relative density account for approximately 75 - 85% of the variation in trabecular bone modulus (Mosekilde, 1993; Goulet *et al.*, 1994).

A number of studies have been performed to determine what factors other than relative density affect bone modulus. These factors, collectively termed bone quality (Heaney, 1993; Schnitzler, 1993), include bone architecture, amount of microdamage, effect of local damage, amount of bone mineralization, and the structural organization of mineral and collagen within the bone matrix (Martin, 1991). Bone quality is of particular interest in the elderly, where multiple factors that reduce stiffness may be present, and their combined influence and interactions may reduce bone strength to below that required to prevent fractures during daily activities. For example, microdamage has been shown to accumulate more rapidly in patients with low bone density (Mori *et al.*, 1997).

The major secondary contributor to trabecular bone modulus is bone architecture, or the distribution of bone material in the trabecular structure. Studies of bone architecture have used histomorphometry, micro-computed tomography, and micro-MRI to investigate the effects of connectivity, trabecular number, trabecular thickness, trabecular separation, and fabric on mechanical properties (Turner *et al.*, 1990; Goldstein *et al.*, 1993; Recker, 1993; van Rietbergen *et al.*, 1996; Kinney and Ladd, 1998). Finite element models have shown that increases in trabecular thickness variations can have large effects on the bulk modulus (Yeh and Keaveny, 1999).

Recently, micro-finite element models have been developed based on computer reconstructions of trabecular bone specimens, and the effects of architecture on mechanical properties were studied for individual structures (Mueller and Ruegsegger, 1995; van Rietbergen *et al.*, 1995; Ladd *et al.*, 1998; van Rietbergen *et al.*, 1998a; van Rietbergen *et al.*, 1998b). As well, micro-finite element models can be modified to determine the effects of changes in density and architecture on a specific trabecular bone structure (Mueller and Ruegsegger, 1996).

Other factors shown to affect the mechanical properties of bone include amount of mineralization (Hvid *et al.*, 1985; Martin, 1991; Martin and Boardman, 1993; Landis, 1995), the collagen-hydroxyapatite interface in the bone material (Mammone and Hudson, 1993), collagen structure (Dunn *et al.*, 1995) and organization (Martin *et al.*, 1996a), and the presence of microdamage (Fazzalari *et al.*, 1998b). Changes in the hard tissue tensile yield strain have been shown to affect the proportion of bone that fails in

tension and in compression in trabecular bone, which can change the overall failure mode of trabecular bone (Nieber *et al.*, 2000).

1.3.3 Mechanical Properties of Trabecular Bone

Considerable work has been done to characterize the mechanical behavior of trabecular bone. Young's modulus, yield strength, yield strain, and ultimate strength have been measured for trabecular bone specimens in tension, compression, shear, and torsional loading situations. The mechanical behavior of trabecular bone damaged in an overload has also been characterized. Creep and fatigue studies have characterized the time-dependent properties of trabecular bone. Animal models, specimen geometries, and loading protocols vary considerably, making it difficult to directly compare results (Keaveny *et al.*, 1993b).

1.3.3.1 Elastic and Plastic Behavior

A number of studies have been performed to characterize the modulus of trabecular bone (Linde *et al.*, 1992; Keaveny *et al.*, 1993a, 1993b, 1994c; Ding *et al.*, 1997). Trabecular bone modulus was strongly related to apparent density ($E = 613\rho^{1.44}$, across a number of anatomic locations and species and over a range of moduli, (Keaveny and Hayes, 1993b; Rice *et al.*, 1988)). There is a weak power law relationship between both bone stiffness and loading strain rate and bone strength and loading strain rate, with an exponent of approximately 0.05 - 0.07 in both cases (Carter and Hayes, 1977c; Linde *et al.*, 1991).

Analytic (Gibson, 1985) and finite element models (Beaupré and Hayes, 1985; Kasra and Grynpas, 1998) have been used to predict stiffness behavior based on relative density. Recently, micro-finite element models based on reconstructions of actual specimens have been developed to predict stiffness (Mueller and Ruegsegger, 1995; van Rietbergen *et al.*, 1995, 1996; Ladd *et al.*, 1998).

The yield behavior of trabecular bone from different species and anatomic locations was measured in a number of studies (Turner, 1989; Keaveny *et al.*, 1993c, 1994c; Kopperdahl and Keaveny, 1998). Failure strains were both isotropic (Chang *et*

al., 1999) and independent of density in the bovine proximal tibia (Ford and Keaveny, 1996) and weakly correlated with density in the bovine proximal femur (Turner, 1989), but failure stress was linearly related to apparent density in both cases. Later studies in human bone found no relationship between tensile yield strain and apparent density but found that compressive yield strain was linearly related to apparent density (Kopperdahl and Keaveny, 1998). The yield strain can be considered independent of density at a given anatomic site (Morgan and Keaveny, 2001).

Bone that has been loaded beyond the yield point shows reductions in modulus and strength in subsequent loading cycles (Keaveny *et al.*, 1994d, 1999). They found a strong inverse correlation between modulus reduction and damaging strain level and a linear relationship between strength reduction and damaging strain level. In this case, the reloading modulus is approximately equal to the secant modulus and can be used as an estimate for the reloading modulus.

Considerable local strain inhomogeneity has been measured during compression tests, and local strains can be difficult to predict (Odgaard *et al.*, 1989; Guo *et al.*, 1995; Bay *et al.*, 1997). Two new methods to predict local loading include homogenization theory (Hollister *et al.*, 1991, 1994) and micro-finite element models (van Rietbergen *et al.*, 1995).

Specimen geometry can affect the measured mechanical properties of trabecular bone. End effects (caused by unsupported trabeculae at the cut ends of the specimen), which tend to underestimate modulus measurements, have also been observed (Odgaard and Linde, 1991; Keaveny *et al.*, 1993a, 1997). Specimen size effects have also been observed in trabecular bone specimens; the stiffness is nearly linearly related to the length of the specimen and positively correlated to the specimen cross-sectional area (Linde *et al.*, 1992). Stiffness also increased when specimens were side-constrained (Linde and Hvid, 1989).

1.3.3.2 Fatigue

Time-dependent loading, specifically fatigue, was studied to determine the effect of repetitive motions of daily living on the skeleton. Physiologic fatigue loading on

bones consists of a static compressive component representing the weight of the body, and a varying component consisting of the dynamic loads placed on the bones during movement.

The fatigue behavior of bone has been characterized in bovine cortical bone (Carter and Hayes, 1976, 1977a, b; Schaffler *et al.*, 1989, 1990; Zioupos *et al.*, 1996b), bovine trabecular bone (Guo, 1993; Michel *et al.*, 1993; Guo *et al.*, 1994; Cheng, 1995), human cortical bone (Pattin *et al.*, 1996; Zioupos *et al.*, 1996a), and human trabecular bone (Haddock *et al.*, 2000). In the case of trabecular bone, the specimens were loaded to loads normalized by modulus, rather than by load alone, since bone strength is related to modulus. Dividing by modulus, which is also related to density by a similar relationship, removes much of the density component from the fatigue results. During most *in vitro* tests, fatigue of bone causes a progressive loss of stiffness with increasing cycles, with a dramatic drop in stiffness immediately prior to failure. However, bone specimens fatigued at physiologic levels displayed an initial stiffness loss, after which the modulus remained stable for the remainder of loading (Schaffler *et al.*, 1990). Zioupos *et al.* (1995, 1996a) found that the damage parameter ($1 - E/E_0$) was linearly related to the life fraction, N/N_f, and the slope of the relationship increased with increasing specimen stress. Initial studies have shown that the behavior of bone tested in multi-level fatigue depends on both the magnitudes of the applied stress and the order they were applied (Zioupos and Casinos, 1998).

Taylor (1998a) examined the size effect on the fatigue behavior of bones and has developed a stressed volume approach for comparing fatigue data from specimens with different specimen geometries. He estimated that the fatigue strength of whole bones is up to 2-3 times lower than that of smaller machined specimens because of the increased probability of including a weak region in the larger stressed volume.

Guo *et al.* (1994) developed a finite element model for the failure of trabecular bone during fatigue loading. The model assumed that bone had a regular honeycomb structure with pre-existing cracks. During fatigue loading, the cracks grew and eventually reached a critical length that caused strut fracture. Local loads surrounding the fractured strut increased, causing additional failures in regions surrounding the previously broken trabeculae. Similar results were found when the model was extended

to three dimensions; however, the three-dimensional models had an increased number of cycles to failure when loaded to the same normalized stress (Vajjhalla, 1999).

The work of Carter and Caler determined that damage during cortical bone fatigue was composed of both cycle-dependent (fatigue) and time-dependent (creep) components, with creep damage dominating at low numbers of cycles to failure (high stress) and fatigue damage dominating at high numbers of cycles to failure (low stress) (Carter and Caler, 1983, 1985; Caler and Carter, 1989). This model was later further developed by Bowman, who found that creep was a significant contributor to fatigue damage in trabecular bone at all load levels (Bowman *et al.*, 1998).

1.3.3.3 Creep

Bone behaves as a viscoelastic material (Fondrk *et al.*, 1988; Deligianni *et al.*, 1994), due to creep of the collagen matrix (Bowman *et al.*, 1999). The creep behavior of bovine cortical (Rimnac *et al.*, 1993b; Archdeacon *et al.*, 1997), human cortical (Rimnac *et al.*, 1993a), and bovine trabecular bone (Bowman *et al.*, 1994) has been characterized. As well, the creep behavior of bovine trabecular bone has been modeled based on models developed for metal matrix composites (Bowman, 1997). Microdamage has been observed in specimens loaded in creep to strains above the yield strain (Pierce, 1999).

1.3.4 Microdamage

Microdamage exists in healthy human bone. It occurs as a result of overloading, or due to the repetitive motions of the activities of daily living. It is thought that a portion of bone remodeling, at least 30%, is targeted remodeling (Burr, 2000), meaning that damaged bone is preferentially selected for replacement by a signaling mechanism that is not yet completely understood. Microdamage plays a role in initiating the signaling mechanism, but its exact role is unclear. Generally, microdamage is repaired by the bone remodeling process and the number of *in vivo* microcracks is limited.

When microdamage is created faster than it is repaired, the damage accumulates, leading to a loss of stiffness and strength. Eventually, microdamage accumulation may lead to an overt fracture, either a stress fracture (due to excessive microdamage

production) or a fragility fracture (due to decreased ability to repair) (Daffner and Pavlov, 1992).

Microdamage has been observed and quantified in human and animal subjects. Naturally occurring microdamage has been studied, as has microdamage resulting during *in vivo* or *in vitro* controlled loading. These observations of microdamage can then be related to changes in bone strength and stiffness.

1.3.4.1 *In vivo* Observations - Natural History

Frost (1960) first identified microcracks in human ribs. He hypothesized that the cracks occurred due to fatigue loading of the ribs during breathing. Later studies confirmed the presence of microdamage in human cortical bone and observed an exponential increase in microdamage accumulation with age (Mori *et al.*, 1997; Fazzalari *et al.*, 1998b), with a greater increase in females (Schaffler *et al.*, 1995b). The number of trabecular microfractures, consisting of a repair callus around an area of presumed microdamage (Frost, 1989), also increases with age in otherwise healthy subjects (Fazzalari *et al.*, 1987) and has been implicated in hip fractures (Freeman *et al.*, 1974). Vashishth *et al.* (2000a) characterized diffuse damage, seen as large numbers of submicroscopic cracks, in human vertebral bone and determined that this type of damage contributes to the microdamage content of bone.

Increased crack densities were observed in greyhounds with stress fractures, compared to contralateral controls (Muir *et al.*, 1999). *In vivo* microdamage accumulation has also been observed in the cannon bones of thoroughbred racehorses, who are prone to stress fractures at this anatomic site (Stover *et al.*, 1993). However, crack densities observed in human metatarsals at common stress fracture sites were not significantly different from those observed at sites unlikely to sustain a fracture (Donahue *et al.*, 2000).

1.3.4.2 Microdamage and Remodeling

Resorption spaces, which are evidence of bone remodeling, have been observed in association with linear microcracks in canine (Burr *et al.*, 1985; Mori and Burr, 1993)

and rat (Bentolila *et al.*, 1998) models after fatigue loading. The osteocyte network may detect cracks and signal for repair, and changes in osteocyte integrity have been noticed in association with fatigue damage and microdamage accumulation (Mori *et al.*, 1997; Verborgt *et al.*, 2000). Osteocyte lacunar density decreases with age (Vashishth *et al.*, 2000b), suggesting that the increases in microdamage with age are associated with a decrease in microdamage detection by the osteocyte network.

The bisphosphonate class of drugs has been used to treat osteoporosis by inhibiting bone remodeling. Specifically, bisphosphonate use suppresses the targeted portion of bone remodeling (Li *et al.*, 2001). Recent models predict an increase in microdamage with long term suppression of bone remodeling (Martin *et al.*, 2000). Bisphosphonates have been shown to increase microdamage accumulation in some studies (Forwood *et al.*, 2000a, 2000b; Hirano *et al.*, 2000; Mashiba *et al.*, 2000) although not in others (Forwood *et al.*, 1995). Mechanical property reductions are also associated with high doses of bisphosphonates, but this may be due to poor mineralization in bisphosphonate-treated bones rather than microdamage accumulation (Hirano *et al.*, 2000; Mashiba *et al.*, 2000).

1.3.4.3 Microdamage and Mechanical Testing

Much of what is known about microdamage has been determined from mechanical testing, where microdamage accumulation is created under known loading conditions. *In vivo* loading of bone results in an increase in microdamage accumulation and indicates that a relationship between microdamage accumulation and bone remodeling exsits (Mori and Burr, 1993; Burr and Hooser, 1995; Bentolila *et al.*, 1998). Zioupos and Currey (1994) noted increased microcracking in regions of high strain, particularly surrounding machined stress concentrators. Wachtel and Keaveny (1997) observed microdamage in bovine trabecular bone after post-yield loading. Pierce (1999) showed that microdamage was created in bovine trabecular bone during compressive creep loading to strains beyond yield. The amount of microdamage decreases with decreasing strain rate, but fatigue loading at physiological strain rates has been shown to create microdamage (Schaffler *et al.*, 1989).

Microdamage has been observed in bone as diffuse damage, single cracks, regions of cross-hatched cracks, or complete fractures. Diffuse damage has been observed surrounding microcracks in cortical bone loaded *in vitro*, corresponding to small cracks in the damage process zone surrounding macrocracks in toughened materials (Schaffler *et al.*, 1994). Cracks in cortical bone specimens have been observed in two and three dimensions, and were found to be elliptical in shape, with an aspect ratio of approximately 4.5:1 (Taylor and Lee, 1998; O'Brien *et al.*, 2000). Microcracks frequently terminate at osteocyte lacunae (Reilly, 2000), suggesting that the lacunae may serve as stress concentrators, crack arrestors, or both. The type of microdamage has been related to the loading mode (diffuse damage in tensile loading, linear microcracks in compression) for cortical bone (Boyce *et al.*, 1998; Reilly and Currey, 1999), but we know of no experiments that independently measure local stress state and microdamage in trabecular bone.

1.3.4.4 Microdamage and Mechanical Properties

A number of studies have been performed to relate microdamage accumulation to changes in bone mechanical properties, including stiffness and strain levels. Microdamage has been shown to increase significantly when the bone is loaded past its yield point (Zioupos *et al.*, 1994; Wachtel and Keaveny, 1997; Reilly and Currey, 1999). Microdamage also increases during loading to increasing compressive strain levels (Wachtel and Keaveny, 1997) or increasing torsional deformation (Forwood and Parker, 1989). Decreased stiffness and strength have been associated with microdamage accumulation during fatigue (Schaffler *et al.*, 1989, 1990; Hoshaw *et al.*, 1997; Bentolila *et al.*, 1998). However, several studies have noted that significant amounts of microdamage accumulation are not seen until modulus reductions of more than 15 - 30% were observed (Schaffler *et al.*, 1996; Burr *et al.*, 1998).

Recently, several studies have quantified the relationship between mechanical properties and microdamage accumulation. Stiffness loss in whole canine femurs tested in bending fatigue was found to be approximately linearly related to the damaged area fraction, but the relationship between crack numerical density and stiffness loss was approximately quadratic (Burr *et al.*, 1998). A positive correlation was seen between

damage and secant stiffness reduction ($R^2 = 0.22$) in human cortical bone tested in torsion (Jepson *et al.*, 1999). Studies of human vertebral bone found *in vivo* microdamage to be a reasonable predictor of strength (linear regression, $R^2 = 0.26$, $p < 0.0005$; nonlinear, $R^2 = 0.40$) (Burr *et al.*, 1997).

1.3.4.5 Modeling of Microdamage

Mathematical models of microdamage have been developed to explain how microdamage relates to mechanical testing observations. Zioupos *et al.* (1995) found that the Tsai-Wu failure criteria predicted the pattern of cracking near stress concentrators (holes) in loaded bovine bone specimens. Yeh and Keaveny (2000) developed a finite element model that determined that microdamage (strut thinning) affects modulus reductions more than microfractures (strut removal) in trabecular bone, possibly because relatively few microfractures were seen. Taylor (1998b) has developed a model that predicts microcrack growth in cortical bone based on measured changes in stiffness during fatigue testing.

1.3.5 Staining of Microdamage

Microdamage is observed by bulk staining a specimen after microdamage has been created, then sectioning the bone into thin slices and observing microdamage histologically in the two-dimensional planes. Without staining, cracks are very difficult to visualize, and there is no way to differentiate between cracks created during testing and artifactual cracks created during the slide preparation process. Trabecular bone must be embedded in poly(methyl methacrylate) or another embedding agent prior to sectioning to maintain the three-dimensional structure of the bone in the sections.

1.3.5.1 Basic Fuchsin

The "gold standard" method used to label microdamage in bone is brightfield examiniations of thin sections that have been bulk stained with basic fuchsin. The method was developed by Frost (1960) then later validated and modified (Burr and

Stafford, 1990; Burr and Hooser, 1995). Basic fuchsin diffuses into cracks, lacunae, and other spaces in bone, which then appear red under visible light. Cracks created during slide preparation are unstained and can be differentiated from experimentally created cracks.

Recent work has investigated fluorescence microscopy of basic fuchsin-stained specimens. Lee *et al.* (1998) found no significant differences between brightfield and fluorescent observations, but Huja *et al.* (1999) found a significant increase in microdamage detected using the fluorescent technique when compared to the brightfield technique.

1.3.5.2 Chelating Fluorochromes

Several fluorochromes have been developed for staining in bones, including oxytetracycline (yellow) (Frost *et al.*, 1961), calcein blue (Rahn and Perren, 1970), calcein (green), alizarin complexone (red) (Rahn and Perren, 1972), and xylenol orange (Rahn and Perren, 1971). Chelating fluorochromes emit different wavelengths when exposed to fluorescent light, appearing as different colors. The fluorochromes are site-specific; that is, they bind directly to exposed calcium. Two or more stains can be used sequentially to differentiate between damage created at different time points. For example, specimens can be stained before and after mechanical testing to distinguish between damage created before testing (damage that was present in the animal and damage created during specimen preparation) and damage created during testing.

Chelating fluorochromes have been used *in vivo* to measure bone deposition and resorption as single stains (Frost *et al.*, 1961; Frost, 1963, 1969) and as multiple stain sequences (Suzuki and Mathews, 1966; Oleru' and Lorenzi, 1970; Aaron *et al.*, 1984). Chelating fluorochromes have also been used to label microdamage *in vivo* in racehorses (Stover *et al.*, 1993).

Recently, chelating fluorochromes have also been used to label microdamage in *in vitro* specimens (Vashishth *et al.*, 1994; Lee *et al.*, 2000). Several stains can also be used in sequence during fatigue loading to monitor crack growth during a fatigue test (Lee, 1997; O'Brien, 2001).

1.3.6 Cellular Solids

A cellular solid refers to any porous material, including many natural materials such as trabecular bone (Gibson and Ashby, 1997). As well, cellular solids have been developed for structural use as cement, polymer, and metal foams. These foams have applications as cores in structural sandwich panels and as lightweight structures. Cellular solid theories have been used to show the dependence of mechanical properties of cellular materials, including trabecular bone, on relative density, ρ^*/ρ_s, and cell geometry. Experimental tests have shown that the mechanical behavior of closed-cell foams is more closely predicted by open-cell foam models, indicating that there are microstructural defects in the cell walls that compromise the strength of the foam (McCullough *et al.*, 1999b; Olurin *et al.*, 1999).

The progression of damage during compression in aluminum foams has been characterized, including the formation of a damage band (Bart-Smith *et al.*, 1998; Sugimura *et al.*, 1998; McCullough *et al.*, ; Bastawros *et al.*, 2000). Size effects were examined and revealed that a minimum specimen dimension of approximately nine cells are needed to minimize size effects in experimental tests (Zhu *et al.*, 1994; Andrews *et al.*, 2001; Onck *et al.*, 2001).

Finite element models have been developed to predict the behavior of cellular materials. Early models used a two-dimensional honeycomb representation of a cellular solid. Later models used two-dimensional (Silva and Gibson, 1997a) and three-dimensional (Vajjhalla, 1999) semi-random Voronoi structures to better represent the irregular structure of some cellular solids.

The cellular solid model has been applied to the mechanical behavior of trabecular bone (Gibson, 1985). Initial finite element models used a two-dimensional honeycomb to represent trabecular bone structure (Guo *et al.*, 1994); more recent models have used two-dimensional (Silva and Gibson, 1997b; Schaffner *et al.*, 2000) and three-dimensional (Vajjhala *et al.*, 2000) semi-random Voronoi structures that more closely represent the structure of trabecular bone. These models determined that density lost by removing trabecular struts has a greater effect on stiffness than similar density reductions caused by thinning the trabeculae in the structure (Silva and Gibson, 1997b; Vajjhala *et al.*, 2000). The effects of fatigue crack growth on the stiffness behavior of trabecular

bone have been modeled in two-dimensional (Guo *et al.*, 1994) and three-dimensional (Vajjhalla, 1999; Makiyama and Gibson, unpublished data) finite element models.

1.4 Outline of Thesis

This work studied the accumulation of microdamage in experimental specimens of bovine trabecular bone tested in compression and related the observed microdamage to measures of damage, such as modulus reduction, maximum strain, and residual (plastic) strain. A cellular solid model was developed to predict modulus reductions in mechanically tested specimens based on microdamage observations. The experiments and modeling were done for two clinically relevant loading conditions: monotonic compression and compressive fatigue. Finally, we compared microdamage accumulation in bones tested in different loading modes.

The first section of this work, Chapter 2, provides an overview of the staining procedure and discusses experiments to determine acceptable stain concentrations and stain sequences for bovine bone. The next two chapters describe the experimental (Chapter 3) and analytical (Chapter 4) work based on microdamage accumulation during a single compression cycle to various strains. The progression of microdamage accumulation from zero load to fracture occurred in a series of steps that were consistent between specimens. Microdamage increased with increasing specimen strain and with increasing modulus reduction. The cellular solid model predicted the modulus loss based on observations of microdamage in histologic sections.

The second part of the thesis describes a series of experiments to determine the effect of fatigue loading on microdamage accumulation (Chapter 5). The model developed in Chapter 4 to predict modulus reductions based on observed microdamage was applied to fatigue data. Microdamage increased with increasing normalized stress in specimens tested to a constant number of cycles, and with increasing number of cycles in specimens tested to a constant normalized stress level. As with the tests using a single compression cycle, microdamage increased with increasing strain and with increasing modulus loss. There was considerably more scatter in the model predictions for fatigue-tested specimens than for monotonic compression-tested specimens.

The final section of the thesis discusses the results of the previous sections. Chapter 6 compares microdamage accumulation for different types of loading, including monotonic compression, compressive fatigue, and preliminary results for compressive creep (Pierce, 1999). Chapter 7 presents overall conclusions for this work and discusses future directions.

Chapter 2: Stain Concentration and Stain Optimization

Abstract

Microdamage, in the form of microcracks, occurs in cortical and trabecular bone during day-to-day activities. Recently, a new method of labeling microdamage in bone using chelating fluorochromes has been developed that allows damage created at different time points to be identified. Five fluorochrome stains were used: alizarin complexone (red), xylenol orange, oxytetracycline (yellow), calcein (green), and calcein blue. We asked the question: what concentrations and sequences of fluorochrome stains are acceptable for labeling and visualizing microcracks? To determine acceptable concentrations, cortical bone beams were damaged and stained in one of three stain concentrations. To test stain sequence, cortical bone beams were damaged, stained in one stain, damaged again, and stained with a second stain. Observations of cracks stained with different concentrations of fluorochromes were classified as understained, adequately stained, or overstained. Microcracks in sequentially stained specimens were observed to ensure that the two colors were distinguishable and to ensure that the second stain did not displace the first one. The optimal stain concentrations were: alizarin complexone (red), 0.03%; calcein blue, 0.03%; calcein (green), 0.01%; oxytetracycline (yellow), 0.03%; and xylenol (orange), 0.09%. Sequential staining was able to distinguish crack growth using eight of the twenty possible two-stain sequences, the best of which was alizarin complexone (red)/calcein (green).

2.1 Introduction

Microdamage, in the form of microcracks, occurs in both cortical and trabecular bone during day-to-day activities (Schaffler *et al.*, 1995a; Mori *et al.*, 1997). Microdamage was first examined histologically using the basic fuchsin bulk staining technique to separate microdamage created *in vivo* from any damage that occurred during the slide preparation process (Frost, 1960; Burr and Stafford, 1990; Burr and Hooser, 1995).

Recently, a new method of labeling microdamage in bone using chelating fluorochromes, developed by Lee (1997), has been shown to be as effective as basic fuchsin staining. Lee examined microcrack number, length and density of human ribs stained with 1.0% solutions of basic fuchsin and five chelating fluorochromes (**Table 2.1**). He found that the five chelating fluorochrome stains were as effective as basic fuchsin in detecting microcracks in human ribs. The fluorochrome molecules attach directly to exposed calcium; therefore, contrasting fluorochromes can be used to distinguish features stained at different times (Suzuki and Mathews, 1966; Aaron *et al.*, 1984). For example, a fluorochrome of one color can be used to stain pre-existing damage before mechanical testing and a second fluorochrome of a different color can be used after testing, to stain damage created during the test (Lee *et al.*, 2000). Several fluorochromes of different colors can be used in sequence to monitor crack growth during a test.

Five fluorochrome stains have been used in bone: alizarin complexone (red), xylenol orange, oxytetracycline (yellow), calcein (green), and calcein blue (Rahn, 1977; Lee, 1997). In this study we asked the question: what concentrations and sequences of these five chelating fluorochromes are acceptable for labeling microcracks in bovine cortical bone?

2.2 Materials and Methods

All stain optimization specimens were made from bovine cortical bone taken from the diaphysis of the tibia (Bertolino Beef Co., South Boston MA). Cortical bone was chosen rather than trabecular bone because thin sections of cortical bone can be mounted directly on microscope slides (Frost, 1958) and do not require an embedding step. The diaphysis of the tibia was sectioned radially into eighths on a band saw (1 HP #C.92 H, Food Machinery of America, Buffalo NY) and then cut into beams with nominal dimensions of 5 mm x 5 mm x 25 mm on a diamond saw (Extec Labcut 1010, L. B. Bennett Ltd., Leicaster UK) under continuous irrigation with water. One specimen was used for each concentration of stain used in the evaluation procedure.

Prior to staining, specimens were damaged by hitting them with a hammer at the ends of the beams. This causes cracking and splintering without fracture. Parameters that affect the quality of the staining include stain concentration, staining time, temperature, and pressure. All tests were done at a constant time of four hours, at room temperature and at atmospheric pressure. We used three concentrations of each stain, differing by a factor of 10. The highest level was comparable to the concentrations used by Lee (1997). Because different fluorochromes have different affinities for calcium, solutions of different fluorochromes at the same concentration will stain microcracks to different intensities. Rahn (1977) compared five fluorochrome stains and determined *in vivo* dosages (in mg/kg) that stained to equal intensities. We have applied the relative ratios developed by Rahn but used concentrations similar to those developed by Lee (1997) for the aqueous concentrations used for *in vitro* staining in this work (**Table 2.1**). The concentrations used in this study were: calcein blue, alizarin complexone and oxytetracycline (0.3, 0.03, 0.003%); xylenol orange (0.9, 0.09, 0.009%) and calcein (0.1, 0.01, 0.001%).

Fluorochrome	Excitation Wavelength (nm)	Emission Wavelength (nm)	Color	Highest Concentration This Study (%)
Calcein blue	375	435	blue	0.30
Xylenol Orange	377	615	orange	0.90
Calcein	495	540	green	0.10
Alizarin complexone	580	625	red	0.30
Oxytetracycline	390	520	yellow	0.30

Table 2.1: Excitation and emission maxima of chelating fluorochromes (Rahn, 1977; Lee, 1997)

The same type of bovine cortical bone specimens was used to determine the optimal dye sequence. Specimens were cut to nominal dimensions, damaged, stained in one fluorochrome stain for two hours, then damaged again and stained with a second fluorochrome for a further two hours. All two-stain combinations of the five fluorochromes were tested.

Slide preparation was performed using the method developed by Frost (1958). Specimens were cut into thin sections (~250 μm thick) on a diamond saw and then hand ground to approximately 50 μm thick using fine silicon carbide grinding paper (Buehler, Lake Bluff IL). Specimens were kept wet during all steps of specimen preparation. A few initial sections were polished without rinsing the grinding paper between sections. Dye contamination was then seen as long, faint streaks of consistent width across the surface of the specimen. Dye contamination could be distinguished from the diffuse staining associated with microcracks as the latter tended to be local and have variations in width. Washing the grinding paper with soapy water and thoroughly rinsing between sections eliminated the problem.

After slide preparation, the thin sections were washed with soapy water and air-dried. The dried specimens were mounted on glass slides with Eukitt's mounting medium (O. Kindler, Germany) and covered with glass cover slips. In general, 3 or 4 sections were examined for each stain concentration, but, in a small number of cases, as few as 2 or as many as 6 sections were examined.

All specimens were observed under ultraviolet epifluorescence with a wavelength of 365 nm. Using this high-energy illumination allowed all five fluorochromes to be excited at the same time. Images of damaged bone were captured using a CCD camera (HRT060-CMT and DEI-750, Optronics Engineering, Goleta CA) attached directly to a computer (Dell Optiplex GXMT 5166, Dell Computer Corp., Austin TX) using an image capture program (Snappy Software 1.0, Play Incorporated, Rancho Cordova CA).

Several criteria were used to evaluate the effectiveness of the concentration and sequence of the stains. In understained specimens the cracks were not clearly visible, while in overstained specimens, diffuse staining was seen in the bone surrounding the crack, blurring the extent of the crack. Microcracks in sequentially stained specimens were observed to ensure that the two colors were distinguishable under epifluorescence and to ensure that the second stain did not displace the first one, making it difficult to identify which loading created the crack.

2.3 Results

Observations of cracks stained with different concentrations of fluorochromes were classified as understained (typical example, shown with oxytetracycline, **Figure 2.1**), adequately stained (**Figure 2.2**), or overstained (**Figure 2.3**). The pattern for all five stains was similar: the lowest concentration labeled cracks, but stains were sometimes too faint to be easily distinguished under fluorescence. The middle concentration labeled cracks well, with occasional slight diffuse staining into surrounding bone. The highest concentration used (ranging from 0.1% to 0.9%) consistently produced diffusely stained areas surrounding a crack in the bone, blurring the extent of the crack (**Table 2.2**) and occasionally obscuring all underlying features (**Figure 2.4**). Regions of bone with more damage tended to have more diffuse staining surrounding the cracks than regions with a single microcrack. Several sections had parallel scratches across the surface consistent with sandpaper scratches. It is assumed that these specimens were not polished sufficiently. Otherwise, staining observations were consistent for sections from the same specimen.

Stain	Low Concentration	Middle Concentration	High Concentration
Calcein Blue	Good contrast/ Some Faint Cracks	Some Diffuse Staining*	Diffuse Staining
Xylenol Orange	No cracks seen	Good Contrast/ Some Diffuse Staining	Diffuse Staining
Calcein	No cracks seen	Good contrast	Some bleeding
Alizarin Complexone	Less Bleeding	Some Diffuse Staining*	Diffuse staining
Oxytetracycline	Good contrast/ Some Faint Cracks	Good Contrast/ Some Diffuse Staining	Diffuse staining

*Diffuse staining only seen in regions of heavy damage

Table 2.2: Concentration results for five chelating fluorochromes.

Sequential staining was able to distinguish crack growth using eight of the twenty possible two-stain combinations (**Table 2.3**). For example, distinct crack growth was observed using alizarin complexone (red) followed by calcein (green) (**Figure 2.5**).

Stain Sequence	Colors
Alizarin Complexone/Calcein*	red/green
Alizarin Complexone/Calcein Blue	red/blue
Alizarin Complexone/Oxytetracycline	red/yellow
Xylenol Orange/Calcein	orange/green
Oxytetracycline/Xylenol Orange	yellow/orange
Calcein Blue/Calcein**	blue/green
Calcein Blue/Xylenol Orange**	blue/orange
Xylenol Orange/Calcein Blue**	orange/blue

* best sequence
** poor sequence

Table 2.3: Acceptable two-stain sequences of chelating fluorochromes.

Crack growth could not be observed using the other twelve two-stain sequences for two reasons. Stains that fluoresce at similar colors cannot be distinguished from one another: this occurs with oxytetracycline (greenish yellow) and calcein (green) (**Figure 2.6**) and with alizarin complexone (red) and xylenol orange. A fluorochrome with a high affinity for calcium may displace a previously deposited stain with a lower affinity: in particular, alizarin complexone (red) has the highest affinity for calcium and will displace all other stains. For example, the sample in **Figure 2.7** was stained first with calcein blue, damaged, and then stained with alizarin complexone (red). All initially exposed surfaces, including any cut edges of the specimen, should be stained blue, while crack growth from the imposed damage should be stained red. However, the edges of the bone have been stained red, indicating that the calcein blue has been displaced.

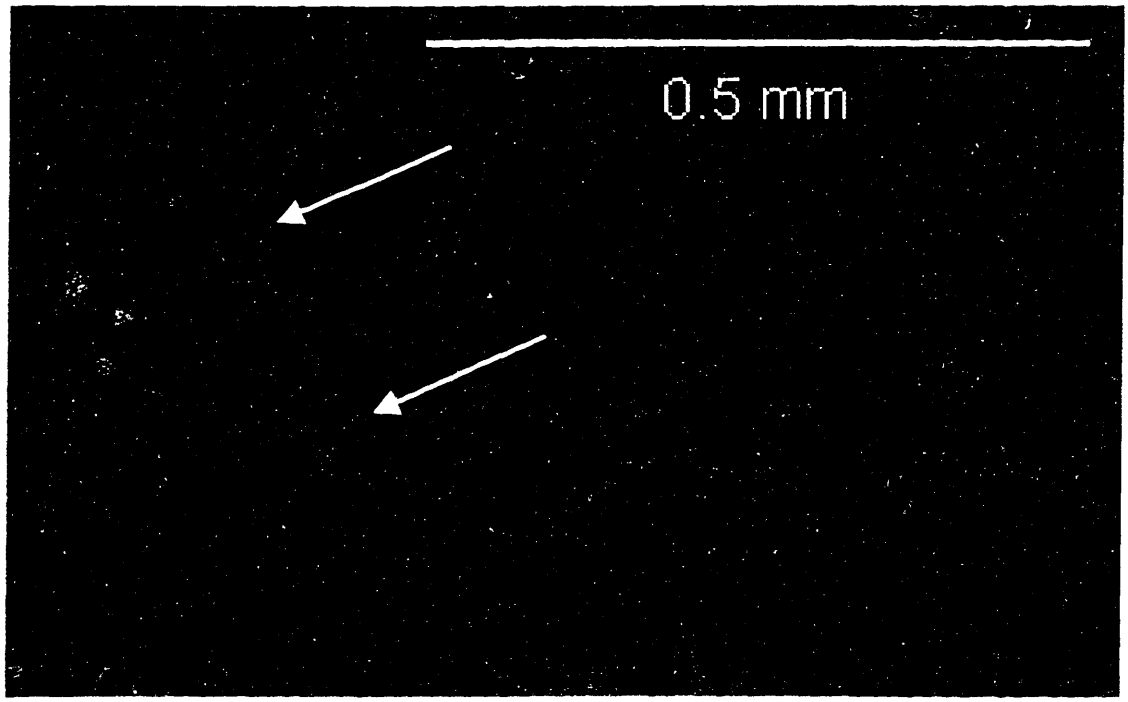

Figure 2.1: Bone specimen stained with a low concentration of oxytetracycline (0.003%) producing insufficient staining: the crack, indicated by arrows, is not distinct.

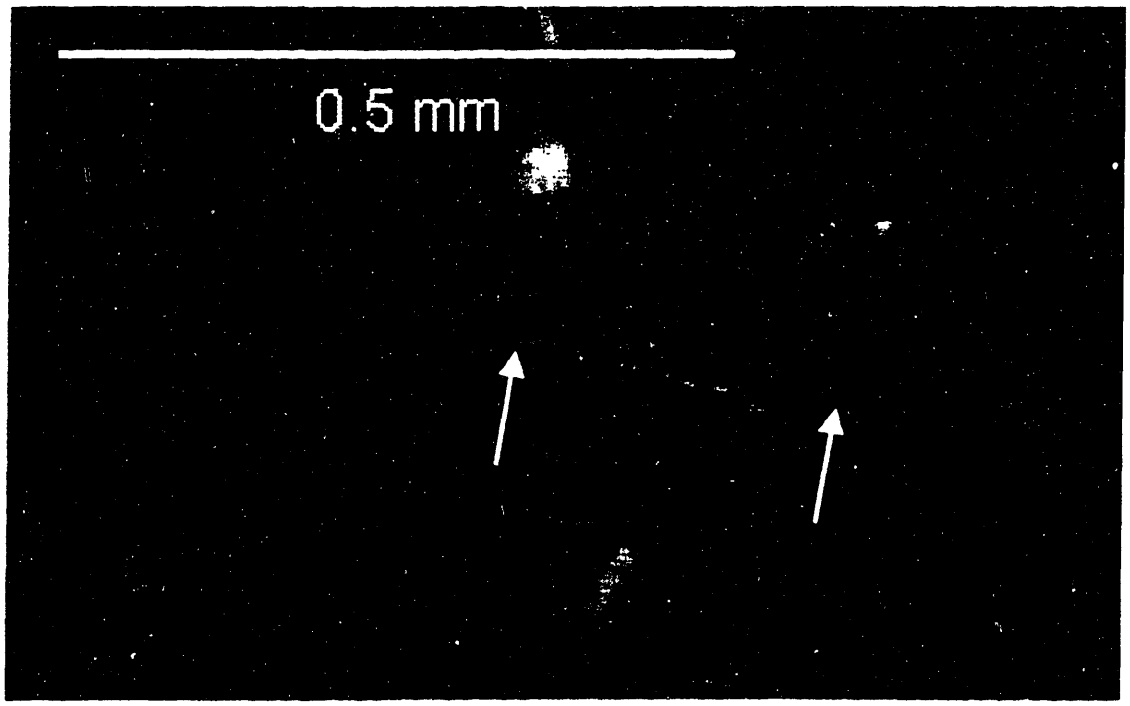

Figure 2.2: Bone specimen stained with medium concentration of oxytetracycline (0.03%) giving sufficient staining: the crack is well labeled (arrows).

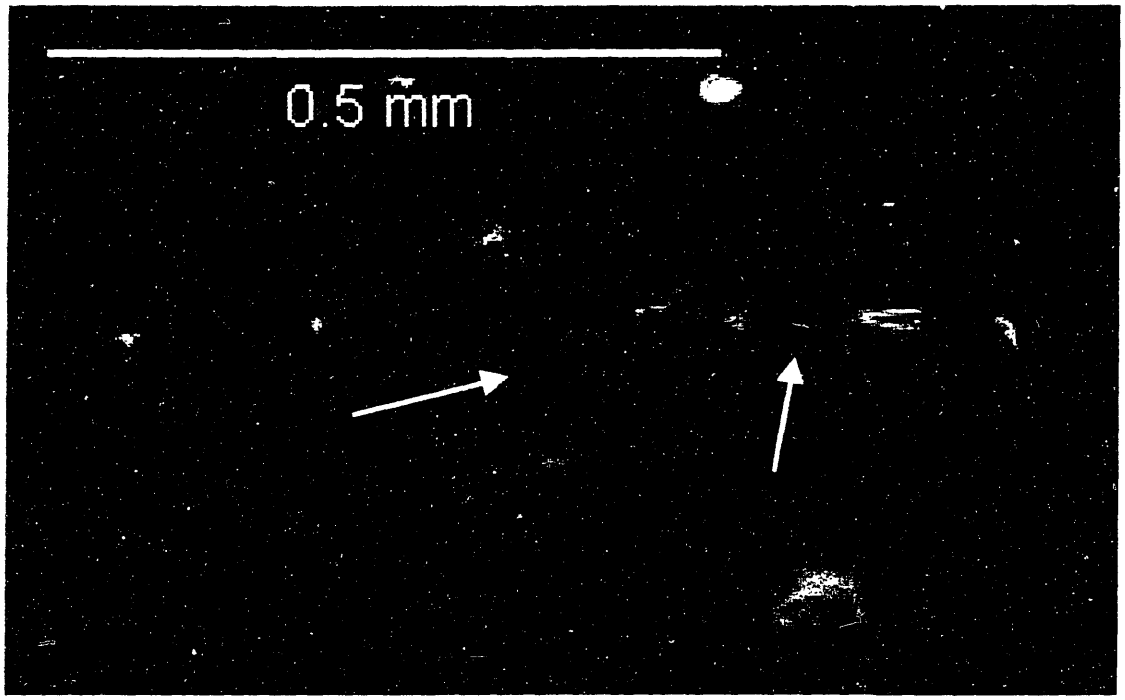

Figure 2.3: Bone specimen stained with a high concentration of oxytetracycline (0.03%) leading to overstaining. diffuse staining is seen around the crack edges (arrows)

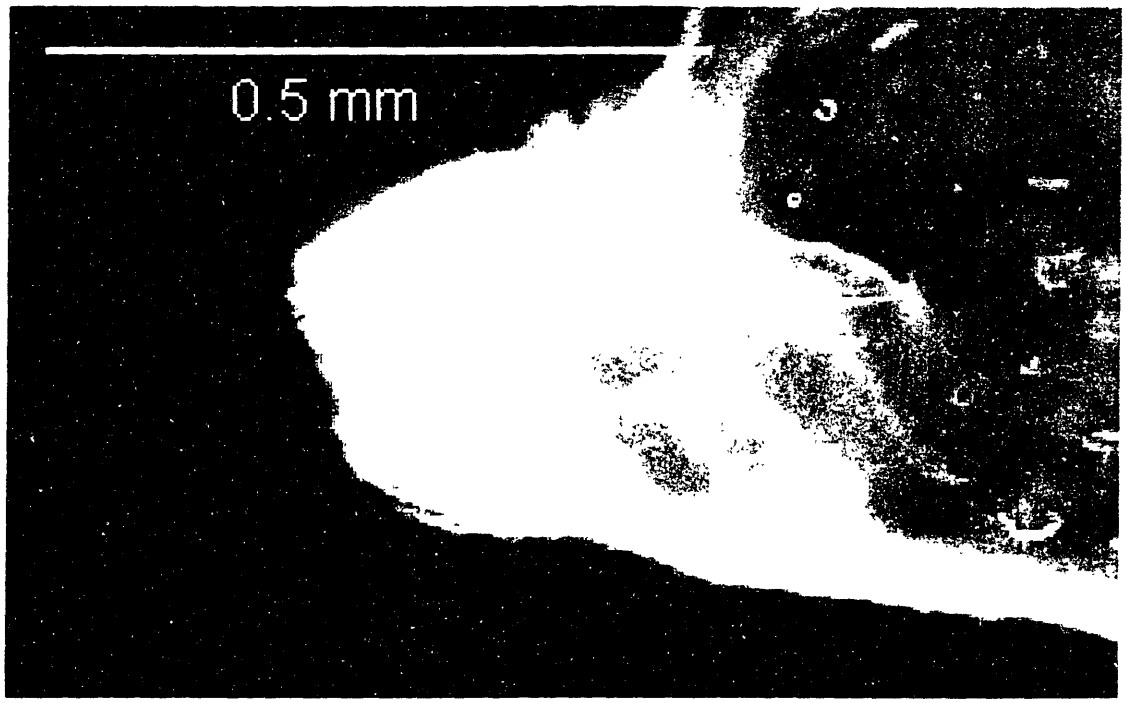

Figure 2.4: Bone specimen stained with a high concentration of xylenol orange (0.9%) with extensive staining it is difficult to distinguish individual cracks

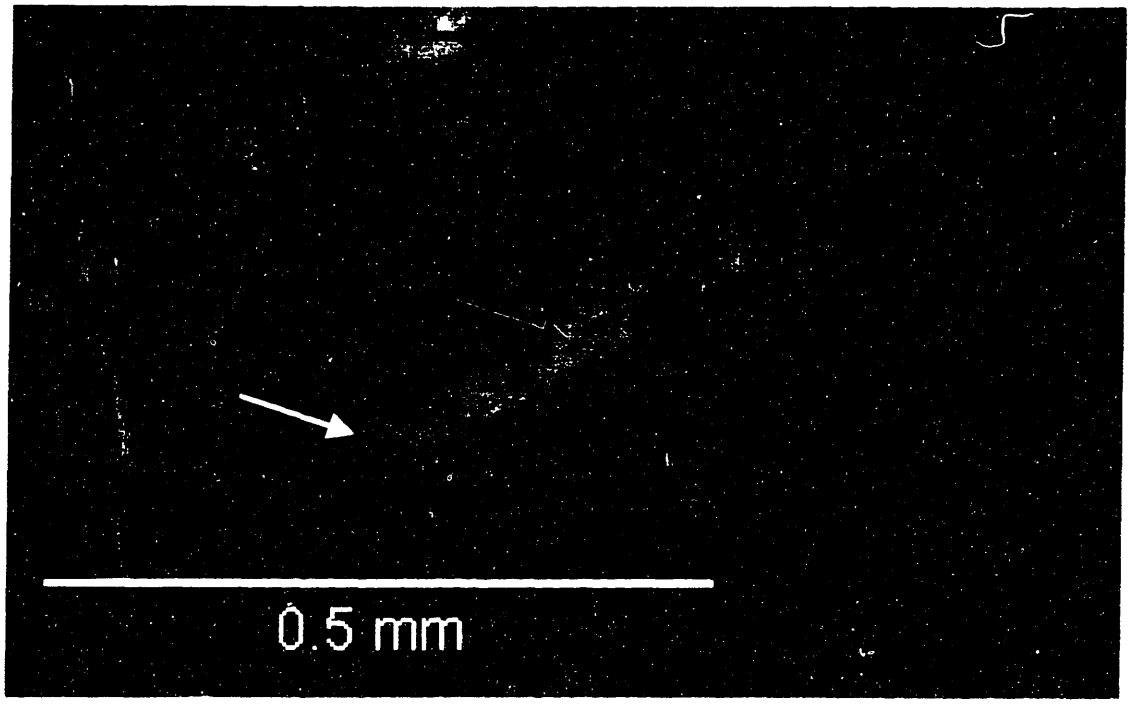

Figure 2.5: Crack stained with alizarin complexone (red, white arrow) followed by calcein (green, black arrow), showing crack growth

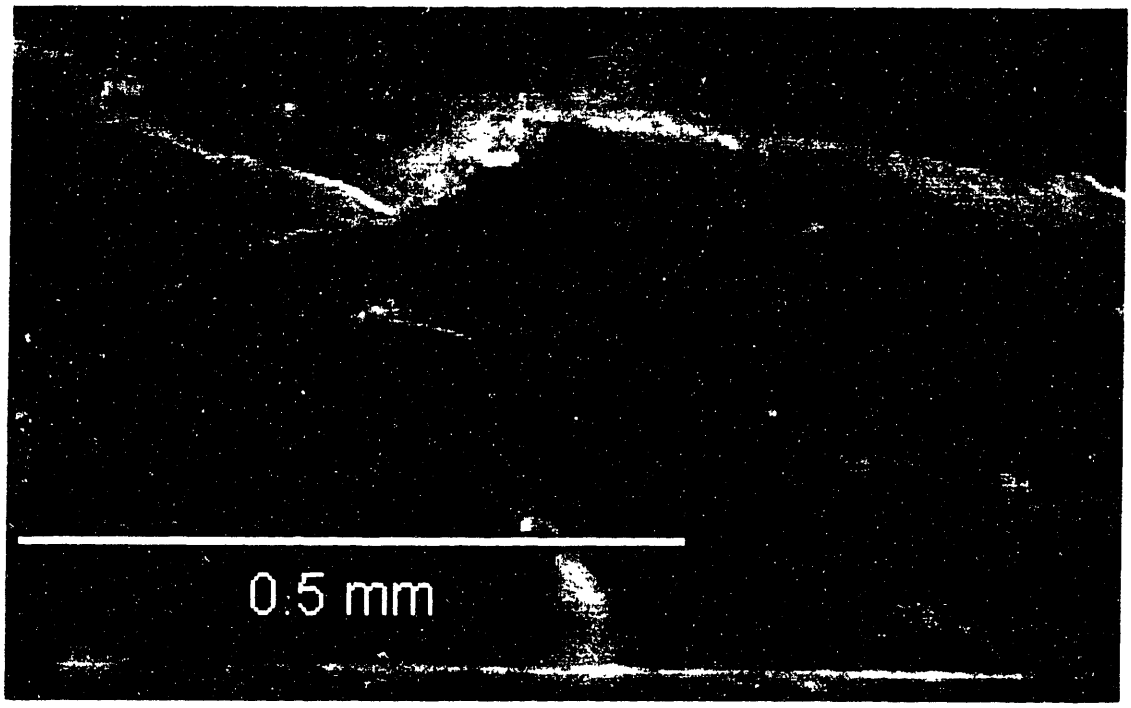

Figure 2.6: Cracks stained with oxytetracycline (yellow) followed by calcein (green). The two stains cannot be distinguished

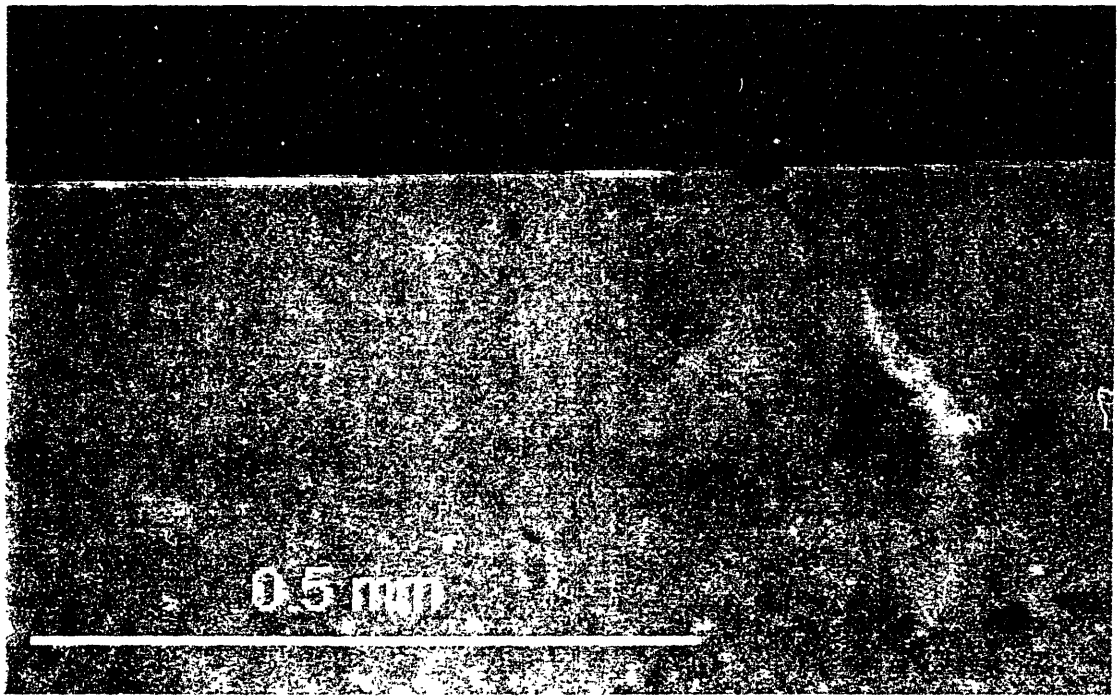

Figure 2.7: Cortical bone specimen showing an uncracked specimen edge stained with calcein blue followed by alizarin complexone (red). The calcein blue has been displaced by the alizarin complexone, and the edge appears reddish.

2.4 Discussion

Acceptable concentrations and two-stain sequences of fluorochromes to label microcracks in bone were found. The optimal concentrations for each stain were found to be: alizarin complexone (red), 0.03%; calcein blue, 0.03%; calcein (green), 0.01%; oxytetracycline (yellow), 0.03%; and xylenol orange (0.09%). The optimal sequence of stains was found to be alizarin complexone (red)/calcein (green). This accords well with ion chromatography studies of binding strengths of the chelating fluorochromes (O'Brien *et al.*, 1999a; O'Brien *et al.*, 1999b).

We report areas of diffusely stained damage surrounding cracks in sections with high concentrations of stain. These areas may represent bleeding of excess stain into the surrounding bone or they may represent diffuse damage at a finer scale (Zioupos *et al.*, 1994, 1995; Schaffler *et al.*, 1995b; Fazzalari *et al.*, 1998a; Fazzalari *et al.*, 1998b; Vashishth *et al.*, 2000a). In either case, high concentrations of stain causes regions with large amounts of damage to be completely obscured, preventing identification of microcracks that may be present (**Figure 2.4**).

Future applications of sequential staining include monitoring crack growth during fatigue testing, using sequences of more than two stains (Lee *et al.*, 2000; O'Brien, 2001). The two-stain sequences were extrapolated into potential three-, four-, and five-stain sequences using the criterion used to identify two-stain sequences: (1) adjacent stains must fluoresce in contrasting colors and (2) later stains must not displace previously deposited stains (**Table 2.4**); this preliminary list should be tested directly. Our results differ from the stain order suggested by Rahn (1977) (as ordered in **Table 2.1**) and used by Lee et al. (2000). There is also evidence that some stains can alter the appearance of previously deposited stains. For example, alizarin complexone followed by xylenol orange cannot be distinguished; however, following xylenol orange with calcein changed the color of the xylenol to a different shade of orange that could be distinguished from alizarin (O'Brien *et al.*, 1999a).

Number of Stains	Stains	Colors
3	Alizarin Complexone/Oxytetracycline/ Xylenol Orange	red/yellow/orange
3	Oxytetracycline/Xylenol Orange/Calcein	yellow/orange/green
3	Oxytetracycline/Xylenol Orange/Calcein Blue	yellow/orange/blue
3	Calcein Blue/Oxytetracycline/ Xylenol Orange	blue/yellow/orange
3	Alizarin Complexone/Calcein Blue/Calcein	red/blue/green
4	Alizarin Complexone/ Oxytetracycline/ Xylenol Orange/Calcein	red/yellow/orange/green
4	Alizarin Complexone/ Oxytetracycline/ Xylenol Orange/Calcein Blue	red/yellow/orange/blue
4	Alizarin Complexone/Calcein Blue/ Xylenol Orange/Calcein	red/blue/orange/green
5	Alizarin Complexone/ Oxytetracycline/ Xylenol Orange/Calcein Blue/Calcein	red/yellow/orange/blue/green

Table 2.4: Potentially acceptable three, four, and five stain sequences of chelating fluorochromes.

During fatigue testing, crack surfaces may come into contact with each other as the load is cycled. If this occurs, shear forces on the crack surface may remove a previously attached fluorochrome which can then reattach elsewhere, labeling a crack as pre-existing damage when it is really damage created during testing. As well, a new fluorochrome may attach where the first one was removed and label the pre-existing damage site as damage created during testing. This issue needs to be investigated further before using this technique to characterize crack growth during compressive fatigue testing.

Chapter 3: Microdamage Accumulation in Bovine Trabecular Bone in Compression

Abstract

In this study we investigated how microdamage accumulated with increasing compressive strain in bovine trabecular bone. Microdamage increased with increasing compressive strain on the specimen and with decreasing secant modulus. We found that little damage was created in the linear elastic region, up to -0.4% strain. At an average strain of about -0.7% ± 0.2%, the stress-strain curve became non-linear and peaked at about -1.85% ± 0.56% strain. Microdamage increased rapidly during this stage, and a localized band of damage formed. At higher strains, the damaged band widened and the density of damage within the band increased. The data obtained in this study was used in the following chapter to develop a model relating the microdamage parameters to the associated modulus loss.

3.1 Introduction

Microdamage, in the form of microcracks, occurs in both cortical and trabecular bone *in vivo* during day-to-day activities (Frost, 1960; Forwood and Parker, 1989; Schaffler *et al.*, 1989; Schaffler *et al.*, 1995b; Martin *et al.*, 1996b; Wenzel *et al.*, 1996; Burr *et al.*, 1997; Mori *et al.*, 1997; Fazzalari *et al.*, 1998a; Muir *et al.*, 1999; Vashishth *et al.*, 2000a) and *in vitro* during overloading (Fyhrie and Schaffler, 1994; Zioupos and Currey, 1994; Zioupos *et al.*, 1994; Wachtel and Keaveny, 1997; Reilly and Currey, 1999). The presence of microcracks decreases the stiffness of bone, allowing the reduced modulus to be used as a measure of the amount of damage (Keaveny *et al.*, 1994d, 1999; Hoshaw *et al.*, 1997). A number of recent studies have begun to quantify the relationship between damage and a number of mechanical properties measured during testing (Zioupos *et al.*, 1995; Burr *et al.*, 1998).

Wachtel and Keaveny (1997) loaded specimens of bovine trabecular bone in strain control to one of three different strains. They found no significant difference

between microdamage measures in pre-yield specimens (ε_{max} = -1.0%) and control specimens (ε_{max} = -0.4%), but found significant differences in amount of total damage and in the numbers of individual cracks types (except transverse cracks) between pre-yield and yielded specimens (ε_{max} = -2.5%). Yeh and Keaveny (2000) used a finite element model of low-density human vertebral bone to determine the bulk modulus loss due to trabecular microdamage and microfractures during compressive strains up to -2.0%.

Bulk specimen staining with basic fuchsin has been the method of choice to observe microdamage (Frost, 1960; Burr and Stafford, 1990; Burr and Hooser, 1995). Recently, a new method of labeling microdamage in bone using chelating fluorochromes was developed that labels microdamage as effectively as basic fuchsin (Lee, 1997). This staining method is site-specific and allows pre-existing damage to be differentiated from that created during a test (Lee *et al.*, 2000). In this study we used this technique to characterize microdamage accumulation in specimens of trabecular bone compressed to varying strains, using the optimal stain sequences determined in an earlier study (Lee *et al.*, 1997a). This work observed microdamage accumulation in bovine trabecular bone during compression to various strain levels and determined how microdamage progresses with increasing compressive strain.

In this study we asked two research questions: (1) how does microdamage accumulate in trabecular bone under increasing strain in uniaxial compression? To answer this question we measured several microdamage accumulation parameters in specimens tested to various strains, and (2) is there a relationship between microdamage accumulation parameters and changes in mechanical properties of bovine trabecular bone tested in compression? In the chapter that follows (Chapter 4), we model the reduction in modulus with increasing damage and compare the results with the measured modulus reduction.

3.2 Materials and Methods

Trabecular bone specimens were damaged by monotonic uniaxial compressive loading to varying strain levels. All tests were performed using waisted cylindrical

specimens of trabecular bone taken from the bovine proximal tibia using the machining protocol developed by Keaveny *et al.* (1994a). Details of specimen preparation can be found in Appendix B. Specimens were excised from relatively homogeneous regions of trabecular bone and machined so that the specimen loading axis was aligned with the axis of the trabecular structure. The test specimens had a nominal diameter of 6 mm and a nominal gauge length of 5 mm. This geometry was chosen to minimize specimen heterogeneity while maintaining continuum behavior in the specimen (Keaveny *et al.*, 1994a). We note that edge effects in cellular materials become small (< 10%) if the specimen size is larger than 8 times the cell size (Andrews *et al.*, 2001; Onck *et al.*, 2001). Our specimen diameters were typically 8-9 cells, so edge effects should not be significant.

Before testing, the specimen diameter within the gauge length was measured six (6) times at different locations with digital calipers (Model 500-531, Mitutoyo Corp., Japan). Each specimen was loaded in an Instron servo-hydraulic testing machine (Model 1331 Instron, Canton MA with a series 3200 controller, Interlaken Technology Corp., Eden Prairie MN; Model 8511/8500, Instron Corp., Canton MA; Instron 1321/8500 Plus, Instron Corp., Canton MA) under strain control to a prescribed compressive strain at a rate of 0.5%/second (Keaveny *et al.*, 1999), unloaded to zero strain at the same rate, and removed from the testing machine. A miniature extensometer (Model 632-29C-30, MTS, Eden Prairie MN) was mounted centrally in the waisted section. All tests were performed at room temperature (22 - 24°C). Specimens were kept moist with a physiological saline drip (0.9% NaCl) throughout testing.

Load and strain data were collected for each specimen, and stress-strain plots were created. The initial modulus, E_0, was measured from the linear portion of the loading curve (from -0.1% to -0.4% (Keaveny *et al.*, 1994d)), and the damaged modulus was measured as the secant modulus, E_{sec} (**Figure 3.1a**) (Jepson *et al.*, 1999; Wilson *et al.*, 2000). The maximum compressive strain, ε_{max}, and residual strain, ε_{res}, at zero load were also recorded. Thirty-four specimens were tested to 9 strain levels: 4 at ε_{max} = 0.0%, 2 each at ε_{max} = -0.4% and -0.8%, 4 at ε_{max} = -1.1%, 5 each at ε_{max} = -1.3% and ε_{max} = -2.0%, 2 at ε_{max} = -2.5%, and 5 each at ε_{max} = -3.0% and ε_{max} = -4.0%.

The testing protocol produced some residual tension in the specimen at the end of the test (at zero strain) (**Figure 3.1a**). To determine if residual tension at zero strain affected the amount of microdamage, additional specimens were tested to strains of -2.0% and -4.0% (n = 3 for each strain). Testing was done under the same conditions as the previous tests except that the tests were stopped when the test reached zero stress on unloading, rather than stopping at zero strain (**Figure 3.1b**).

After specimen preparation but before mechanical testing all specimens were stained 16 hours (overnight) at atmospheric pressure. The first specimens were stained in oxytetracycline (1.0% concentration) (n = 3), but later, specimens (n = 31) were stained with alizarin complexone (0.03% concentration) as the stain optimization study indicated that alizarin was a preferred initial stain (Lee *et al.*, 1997a; O'Brien, 2001; Chapter 2). Marrow was removed from the specimens before staining to improve dye penetration into the bone; the removal of marrow is not expected to affect the mechanical properties of the bone at the strain rates used here (Pugh *et al.*, 1973; Carter and Hayes, 1977c).

After mechanical testing, the waisted section of the specimen was removed by cutting with a diamond saw (Isomet Low Speed Saw, Buehler, Lake Bluff IL) and stained with a second fluorochrome, either xylenol orange (1.0%) (for specimens initially stained with oxytetracycline (n = 3)) or calcein (0.01%) (for specimens initially stained with alizarin complexone (n = 31)). Removing the waisted section allowed better stain penetration. All specimens were supported during cutting to minimize damage created during the cutting process. Specimens were again stained for 16 hours (overnight) at atmospheric pressure.

After staining, the specimens were gradually dehydrated in ethanol and embedded in transparent poly(methyl methacrylate) (PMMA) (Lee *et al.*, 2000; Appendix A). The embedded cores were sectioned into longitudinal slices, 100-150 μm thick, with a diamond saw (Isomet Low Speed Saw, Buehler, Lake Bluff IL). The slices were mounted on glass slides using Eukitt's mounting medium (Electron Microscopy Sciences, Fort Washington PA) and glass cover slips. Thresholded greyscale images of the sections taken with a CCD camera (Optronics Engineering DEI-750, Goleta CA) and image capture program (Snappy 1.0, Play Incorporated, Rancho Cordova CA) were used to

measure the total area of the sections and the area fraction of bone (ImageTool 1.25, UTHSCSA, San Antonio TX).

Slides were observed under ultraviolet epifluorescence with an excitation wavelength of 365 nm. The type of damage (single crack, parallel cracks, cross-hatch, or complete fracture **(Figure 3.2a-e)** (Fyhrie and Schaffler, 1994; Wachtel and Keaveny, 1997; Fazzalari *et al.*, 1998b)) and extent of damage across the trabecular thickness (25%, 50%, 75%, or 100% of trabecular thickness) were marked on the corresponding trabeculae on an image of the section. The cross-hatch pattern consisted of several subtypes, including uniform cross-hatching (**Figure 3.2d**), where cracks form at ±45° and unequal cross-hatching where a single primary crack is crossed by minor cracks in the second direction. Some regions of cross-hatching consisted of what has been termed "diffuse damage" (Burr *et al.*, 1998; Fazzalari *et al.*, 1998b; Vashishth *et al.*, 2000a), where the damage consisted of flame-shaped cracks. All types of cross-hatching were classified together due to the difficulty in differentiating between the subtypes. The length of the damage band was taken as the average of five (5) measurements of the damage band across an image of the specimen with individual damaged trabeculae marked (**Figure 3.2e**).

Images of cracked areas within individual trabeculae were captured using a CCD camera attached directly to a personal computer. The damaged area was determined using stereological point counting techniques with a ten-by-ten grid. A custom Matlab (Matlab 5.0, The Math Works, Natick MA) program was developed to quantify crack numerical density (*Cr.Num.*/section area) and length density (*Cr.Len.*/section area). The program displays all images from a particular specimen sequentially. On each image, the user traces visible microcracks with the computer mouse. The program assigns a number to each traced crack and records the length of that crack. The cracks are assumed to be sheet-like in three dimensions (Fazzalari *et al.*, 1998a; Taylor and Lee, 1998), and we assume a one-to-one correspondence between three-dimensional cracks and the cracks visible in the two-dimensional slide. Once all of the images for a specific specimen have been displayed, the program displays the total number of cracks, the total length of cracks, and a frequency distribution of crack lengths. The number of cracks, the total crack length, the number of damaged trabeculae and the damaged area were normalized

by the total area of the image. Section area could be measured more accurately than bone area because the projected bone area overestimated the surface bone area due to the finite section thickness. There was no significant difference in the area fractions of bone for the different strain levels tested (**Table 3.1**), so section area scaled with bone area.

Total crack number, *Cr.Num.*, and total crack length, *Cr.Len.*, normalized by section area, were plotted against the damage parameter, defined as $1 - E_{sec}/E_0$, where E_{sec} is the secant modulus at the point of maximum strain and E_0 is the initial modulus. Microdamage parameters at different strain levels were compared using t-tests. The average frequency distribution for each strain level was plotted to show microdamage accumulation with increasing strain.

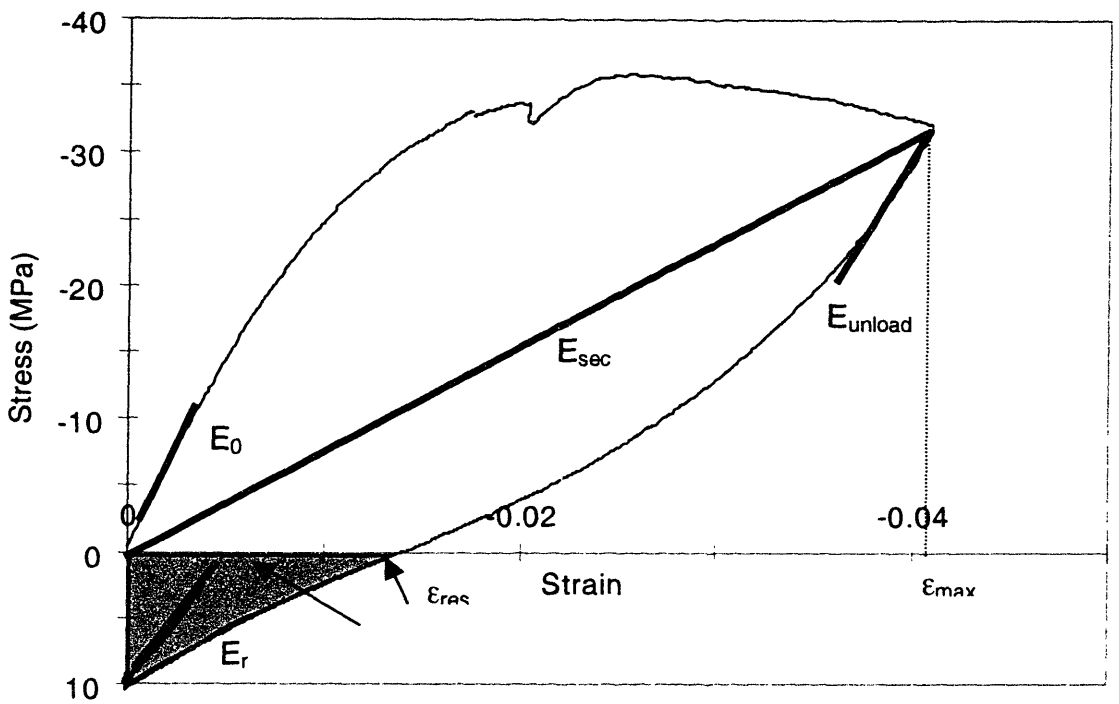

(a)

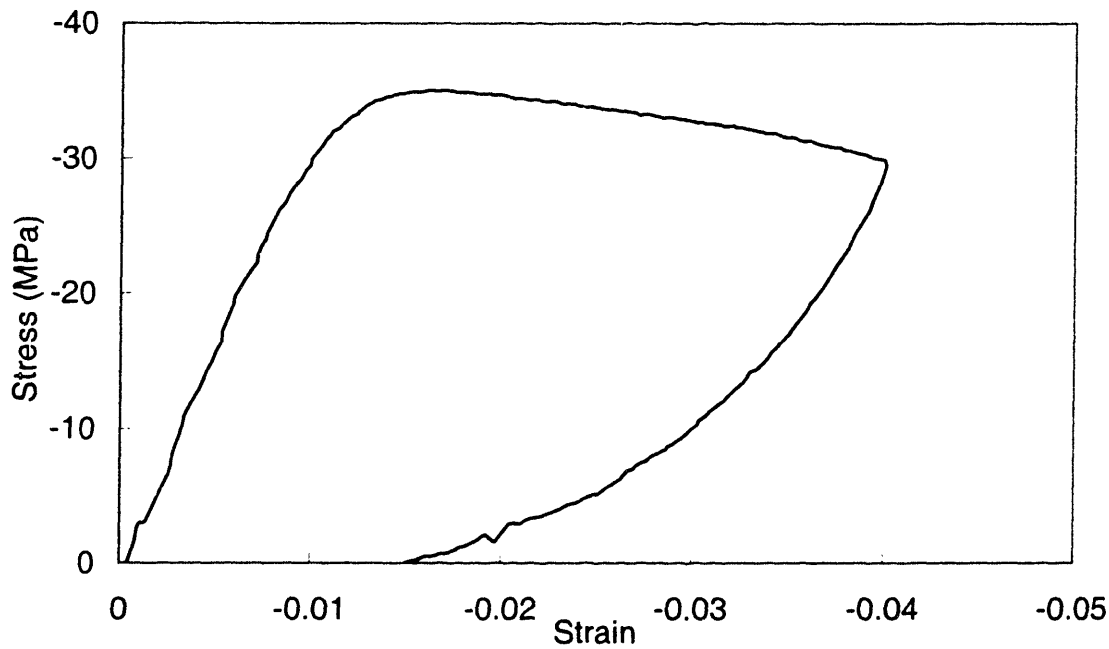

(b)

Figure 3.1: Stress-strain curves for bovine trabecular bone in compression. (a) Specimen unloaded to zero strain. The initial Young's modulus, E_0, the secant modulus, E_{sec}, the reloading modulus, E_r, the unloading modulus, E_{unload}, the maximum strain, ε_{max}, the residual strain, ε_{res}, and the region of residual tension (gray shading) are indicated. (b) Specimen unloaded to zero stress.

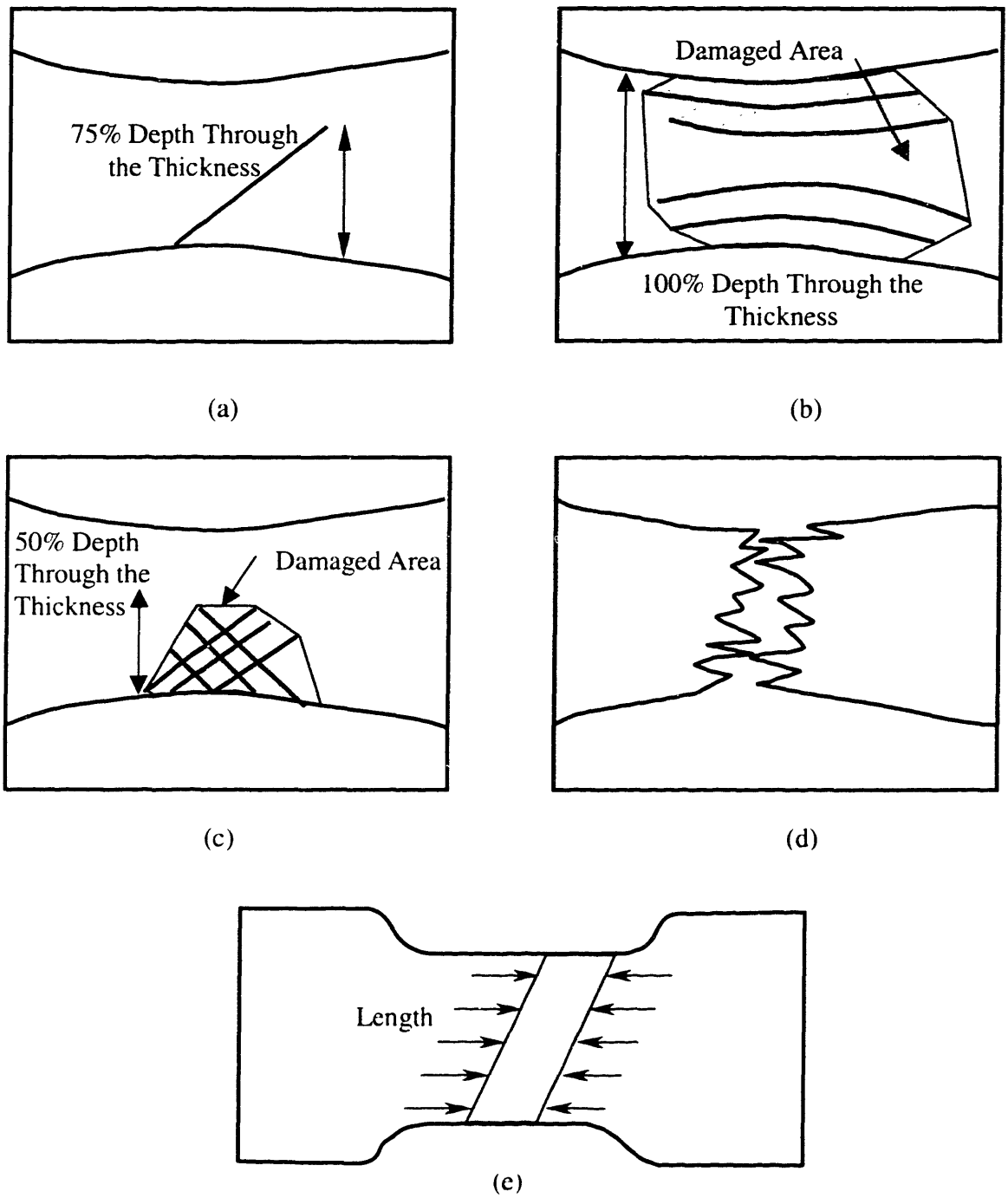

Figure 3.2: Schematic of types of microdamage in trabecular bone. (a) single crack (b) parallel cracks (c) cross-hatched cracks (equal cross-hatching) (d) complete fracture (e) damaged band across section (average of five measurements).

3.3 Results

Typical stress-strain curves for specimens loaded to -4.0% strain are shown in **Figure 3.1**. Stress-strain curves for specimens loaded to lower strains were similar, up to the strain at which loading was stopped. Examination of all the stress-strain curves indicated that they became visibly non-linear at an average strain of -0.7% (SD = 0.2%). The peak, or ultimate, stress occurs at a strain of -1.85% (SD = 0.56%). Inelastic strain on unloading was observed all but four of the specimens loaded to –0.8% strain or higher, but not in those loaded to -0.4% strain. Damage, $1 - E_{sec}/E_0$, and residual strain, ε_{res}, increased with increasing maximum strain, ε_{max} (**Table 3.1**).

ε_{max} (%)	E_0 (GPa)	E_{sec} (GPa)	Damage ($1-E_{sec}/E_0$)	ε_{res} (%)	Relative Density[a]
Zero Strain Tests					
0.0	N/A	N/A	0.000	0.0	0.426 (0.070)
-0.4	2.38 (0.37)	2.39 (0.41)	-0.004 (0.017)	0.001 (0.007)	0.414 (0.032)
-0.8	2.42 (0.54)	2.08 (0.64)	0.146 (0.076)	-0.05*	0.450 (0.017)
-1.1	2.40 (1.28)	1.82 (0.98)	0.229 (0.084)[1,2,3]	-0.148 (0.087)	0.410 (0.090)
-1.3	2.07 (0.72)	1.49 (0.41)	0.255 (0.169)[1,2]	-0.277 (0.104)[1,2]	0.399 (0.040)
-2.0	2.53 (0.99)	0.95 (0.45)	0.617 (0.115)[1-5]	-0.514 (0.169)[1,2,5]	0.397 (0.046)
-2.5	4.16 (2.94)	1.06 (0.16)	0.644 (0.289)	-0.525 (0.177)	0.510 (0.018)
-3.0	2.85 (1.15)	0.95 (0.51)	0.681 (0.083)[1-5]	-0.960 (0.181)[1,2,4-7]	0.461 (0.139)
-4.0	2.89 (1.84)	0.54 (0.37)	0.812 (0.079)[1-8]	-1.468 (0.437)[1,2,4-7]	0.466 (0.171)
Zero Load Tests					
-2.0	3.48 (1.23)	1.75 (0.90)	0.522 (0.112)[1]	-0.460 (0.078)[1]	0.543 (0.106)
-4.0	2.16 (1.13)	0.52 (0.23)	0.754 (0.019)[1]	-1.283 (0.202)[1]	0.457 (0.058)

Significantly different from ($p < 0.05$): [1]0.0%, [2]–0.4%, [3]–0.8%, [4]–1.1%, [5]–1.3%, [6]–2.0%, [7]–2.5%, [8]–3.0%

* Only one residual strain was measured at –0.8% strain due to a data acquisition error, so no statistical comparisons were made.

[a]bone area divided by section area

Table 3.1: Mechanical properties of trabecular bone specimens tested in monotonic compression to various strains. Numbers in parentheses represent standard deviations.

34 tests were performed to nine strain levels. Three to five sections were obtained for characterization of damage in each specimen, and the mean section area was 301 ± 64 mm^2 per specimen. The pooled area fraction of bone in the specimens was

0.43 ± 0.10. Prior to testing ($\varepsilon = 0.0\%$), specimens have relatively little damage (**Table 3.2**). The damage that is present occurs on the outer surface of the machined specimen and does not extend more than one trabecular length into the specimen (**Figure 3.3**). This damage usually consists of broken trabecular struts and is assumed to occur during specimen preparation. The damage on the outer edges is stained with the first stain, either oxytetracycline or alizarin complexone, indicating that the damage occurred prior to testing.

ε_{max} (%)	Cr.Num./Area (mm^{-2})[a]	Cr.Len./Area ($\mu m/mm^2$)[b]	Damaged Trabeculae/Area (mm^{-2})[c]	Damaged Area Fraction (mm^2/mm^2)[d]	Band Length (mm)[e]
Zero Strain Tests					
0.0	0.015 (0.014)	1.4 (1.5)	0.007 (0.006)	0.000	0.0
-0.4	0.012 (0.005)	0.9 (0.5)	0.007 (0.002)	0.000	0.0
-0.8	0.033 (0.002)	3.6 (0.3)[2]	0.010 (0.001)	0.000[2]	0.0
-1.1	0.21 (0.10)[1,2,3]	13.4 (7.8)[1,2,3]	0.046 (0.014)[1,2,3]	0.001 (0.001)[2]	0.6 (0.6)
-1.3	1.2 (1.1)	98.9 (90.4)	0.144 (0.124)[1]	0.006 (0.005)	1.7 (1.5)
-2.0	2.4 (1.2)[1-4]	179 (86)[1-4]	0.256 (0.100)[1-4]	0.010 (0.005)[1-4]	3.7 (1.5)[1-4]
-2.5	6.6 (7.2)	490 (544)	0.284 (0.161)	0.021 (0.023)	3.1 (2.2)
-3.0	8.7 (7.9)	574 (510)	0.419 (0.272)[1-4]	0.018 (0.013)[1-4]	4.0 (1.8)[1-4]
-4.0	13.7 (9.5)[1-5]	917 (582)[1-6]	0.462 (0.151)[1-7]	0.028 (0.014)[1-6]	4.3 (1.2)[1-5]
Zero Load Tests					
-2.0	7.1 (5.8)	562 (527)	0.362 (0.233)	0.016 (0.011)	3.4 (1.3)[1]
-4.0	13.3 (7.7)	965 (596)	0.560 (0.120)[1]	0.030 (0.019)	4.9 (0.1)[1]

Significantly different from ($p < 0.05$): [1]0.0%, [2]-0.4%, [3]-0.8%, [4]-1.1%, [5]-1.3%, [6]-2.0%, [7]-2.5%

[a]total number of cracks in the specimen, normalized by specimen section area

[b]total length of cracks in the specimen, normalized by specimen section area

[c]total number of trabeculae containing damage in the section, normalized by specimen section area

[d]total area of the localized regions of damage, normalized by specimen section area

[e]length of the section of the specimen containing damage

Table 3.2: Microdamage parameters of trabecular bone specimens tested in monotonic compression. Numbers in parentheses are standard deviations.

Both stain sequences allowed microdamage resulting from the mechanical loading to be identified under UV epifluorescence. Specimens stained with oxytetracycline followed by xylenol orange showed comparable amounts of damage to specimens stained

with alizarin complexone/calcein. Microcracks of length greater than approximately 10 μm could be resolved. The different patterns of microstructural damage observed are shown in **Figure 3.4**. Diffuse staining and single cracks occurred throughout the damaged region. In general, parallel cracks occur at junctions between trabeculae and often followed the curvature of the trabecula. Regions of equal cross-hatching occurred in the middle of trabeculae aligned parallel to the loading axis. Unequal cross-hatching, where regions of cross-hatching had one major crack surrounded by minor cracks occurred mainly in trabeculae that were perpendicular to the loading axis. Complete trabecular fracture was only observed in specimens with compressive strains greater than or equal to -2.0%.

Microdamage parameters were obtained for each specimen, and average values were obtained for each strain level (**Table 3.2**). All microdamage parameters showed an increase with increasing strain and increasing damage ($1 - E_{sec}/E_0$). The distribution of the various patterns of damage with increasing strain are shown in **Figure 3.5**. Regions of cross-hatching and trabecular fracture were seen more frequently in highly strained specimens. The number of damaged trabeculae per unit area could also be broken down by the extent of damage across the trabecular thickness (**Figure 3.6**). Nearly one half of all observed damaged trabeculae had cracks extending completely across the trabecular thickness. Crack density levels for individual specimens ranged widely, from 0.004 cracks per unit area to 23.8 cracks per unit area.

Frequency distribution histograms (**Figure 3.7a** illustrates a typical example) were created for specimens with a damage density greater than 1.0 cracks/mm^2. The peaks of the average frequency distribution for each strain level increase with increasing strain on the specimen (**Figure 3.7b**). The location of the peak of the crack length frequency distribution remained constant at a length of approximately 40 μm with increasing strain, and the mean crack length of all the specimens is constant at 65.3 μm, with little variation (slope of *Cr.Len.* vs. *Cr.Num.* = 65.3 ± 1.3 μm, $p < 0.001$, $R^2 = 0.99$). The crack numerical density and the crack length density for the 31 specimens stained with alizarin/calcein are exponentially related to the damage ($1 - E_{sec}/E_0$) (numerical density: $p < 0.001$, $R^2 = 0.85$, **Figure 3.8a;** length density: $p < 0.001$, $R^2 = 0.84$, **Figure**

3.8b). Adding the 3 specimens stained with oxytetracycline/xylenol orange did not affect the results significantly.

Composite images of individual specimens revealed that microdamage was localized in a band (**Figure 3.9**). The band began to form at a strain of about -1.3% and was distinct at the highest strain applied (ε_{max} = -4.0%). The progress of damage accumulation within a single damage band for specimens loaded to increasing levels of strain is further illustrated in **Figure 3.10**, in which individual damaged trabeculae are indicated by a bar. The damage band begins to form at a strain of -1.3% and increases in length and in density of damage as the strain is increased further.

Microdamage parameters in specimens stopped at zero load (n = 3) were similar to the microdamage parameters in specimens stopped at zero strain (n = 5) for specimens tested to -2.0% and -4.0% strain (**Table 3.2**). A power analysis revealed that more than 25 specimens would be needed to show statistical significance for the differences observed.

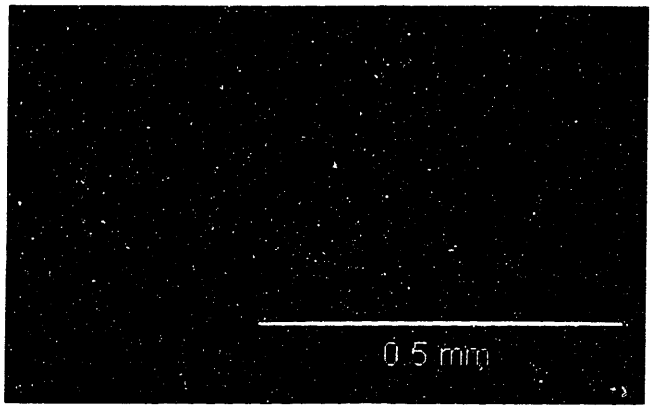

(a)

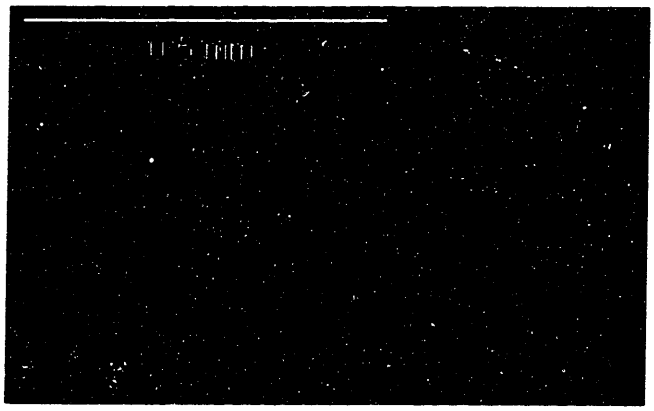

(b)

Figure 3.3: Examples of machining damage seen on the outer edges of specimens. Specimens were stained in 0.03% alizarin complexone (red) before testing, and 0.01% calcein (green) after testing. (a) Untested specimen. (b) Specimen loaded to ε_{max} = -4.0%

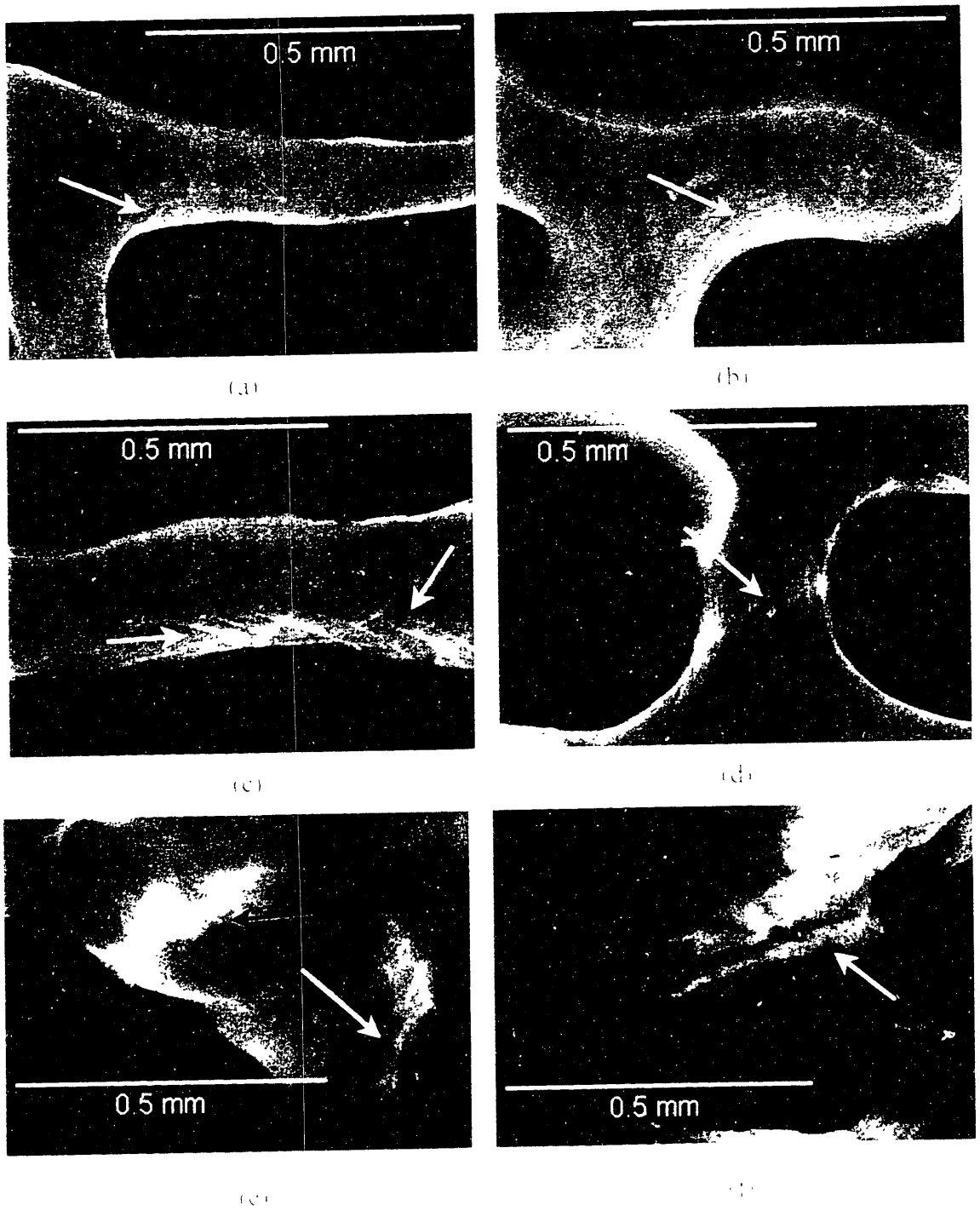

Figure 3.4: Observed patterns of microdamage in trabecular bone. [illegible] from a single specimen tested [illegible] (a) single crack (b) parallel cracks [illegible] (c) cross hatch equal cross hatching (d) cross hatch unequal cross hatching one primary crack with minor secondary cracks (e) cross hatch [illegible] diffuse damage (black) (f) complete fracture

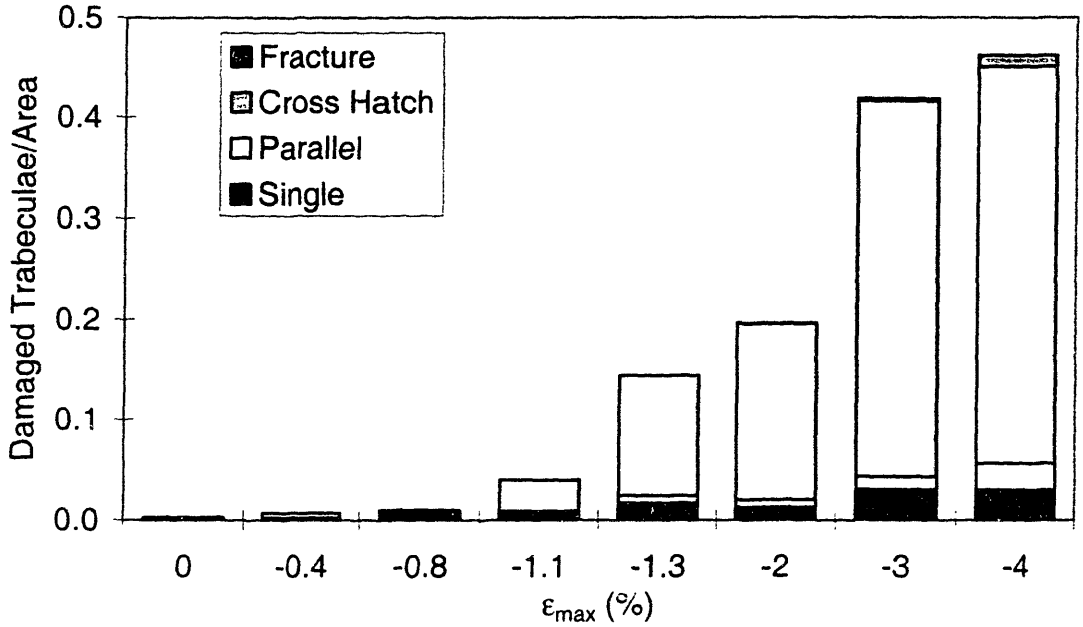

Figure 3.5: Breakdown of number of damaged trabeculae, normalized by section area, by damage pattern for each strain level. The -2.5% strain level was not plotted because only two specimens were tested to that level.

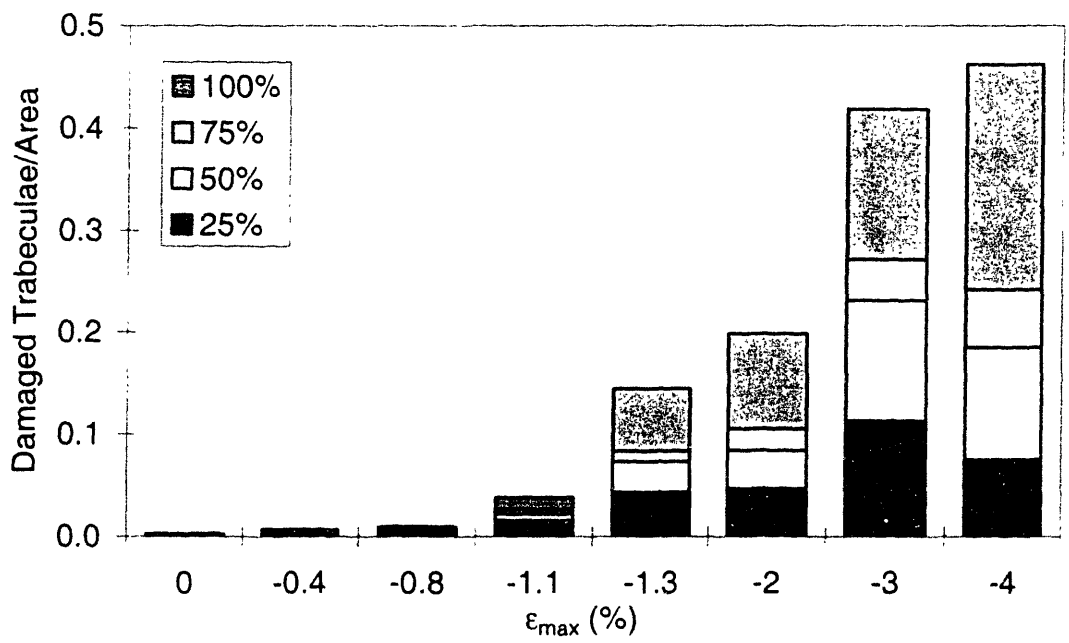

Figure 3.6: Breakdown of number of damaged trabeculae, normalized by section area, by extent of damage through the trabecular thickness for each strain level. The -2.5% strain level was not plotted because only two specimens were tested to that level.

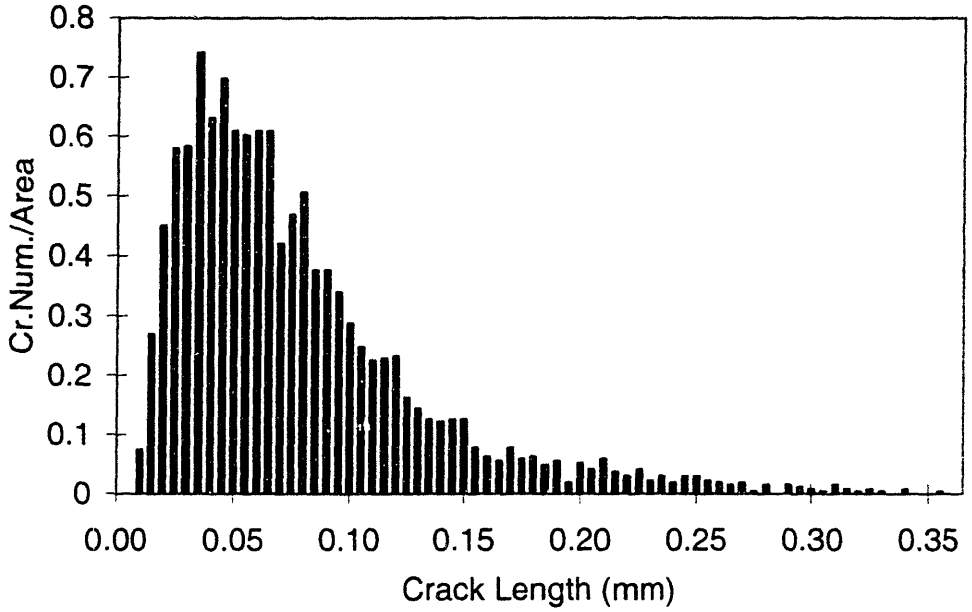

(a)

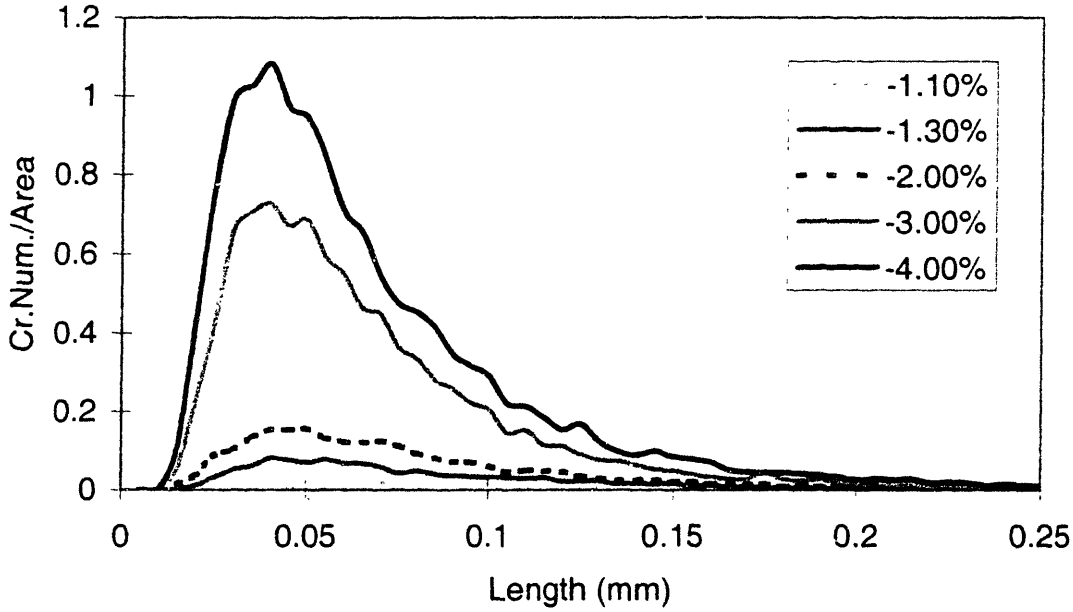

(b)

Figure 3.7: (a) Crack length frequency distribution for a single specimen (tested to ε_{max} = -4.0%). (b) Average crack number frequency distribution for each strain level (n = 5 for each strain level). Distributions for strain levels below ε_{max} = -1.1% are very small and are not plotted.

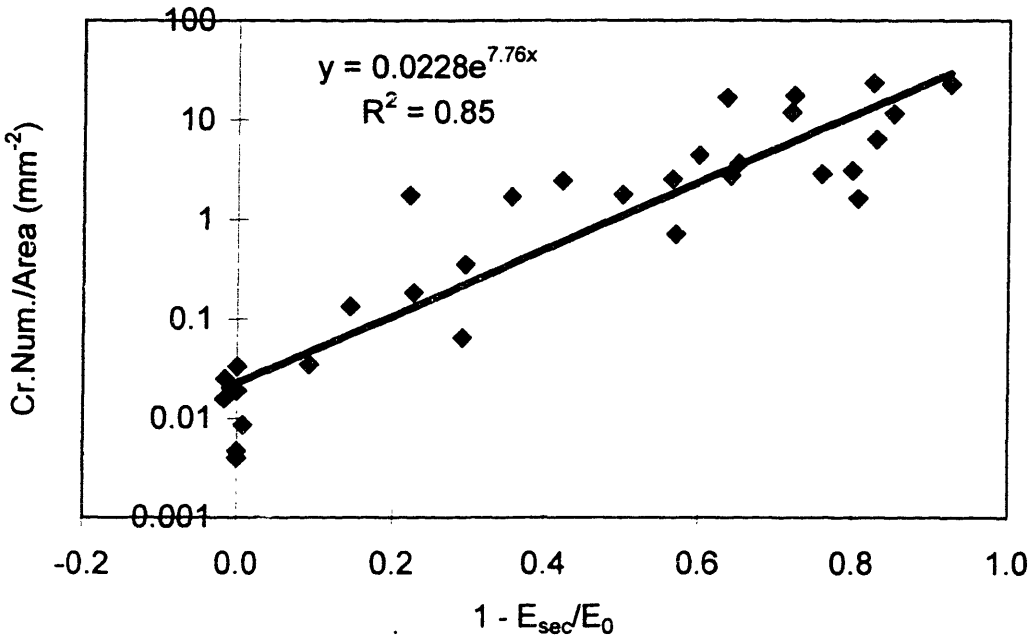

(a)

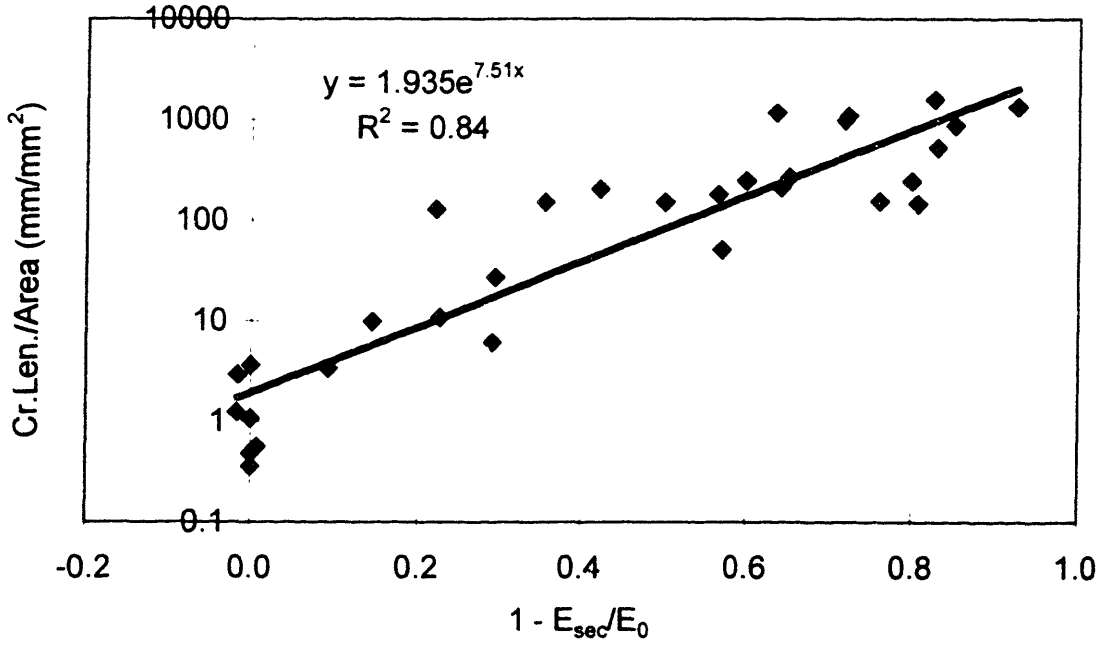

(b)

Figure 3.8: (a) Crack number, *Cr.Num.*, normalized by section area plotted against damage ($1 - E_{sec}/E_0$). (b) Total crack length, *Cr.Len.*, normalized by section area plotted against damage ($1 - E_{sec}/E_0$).

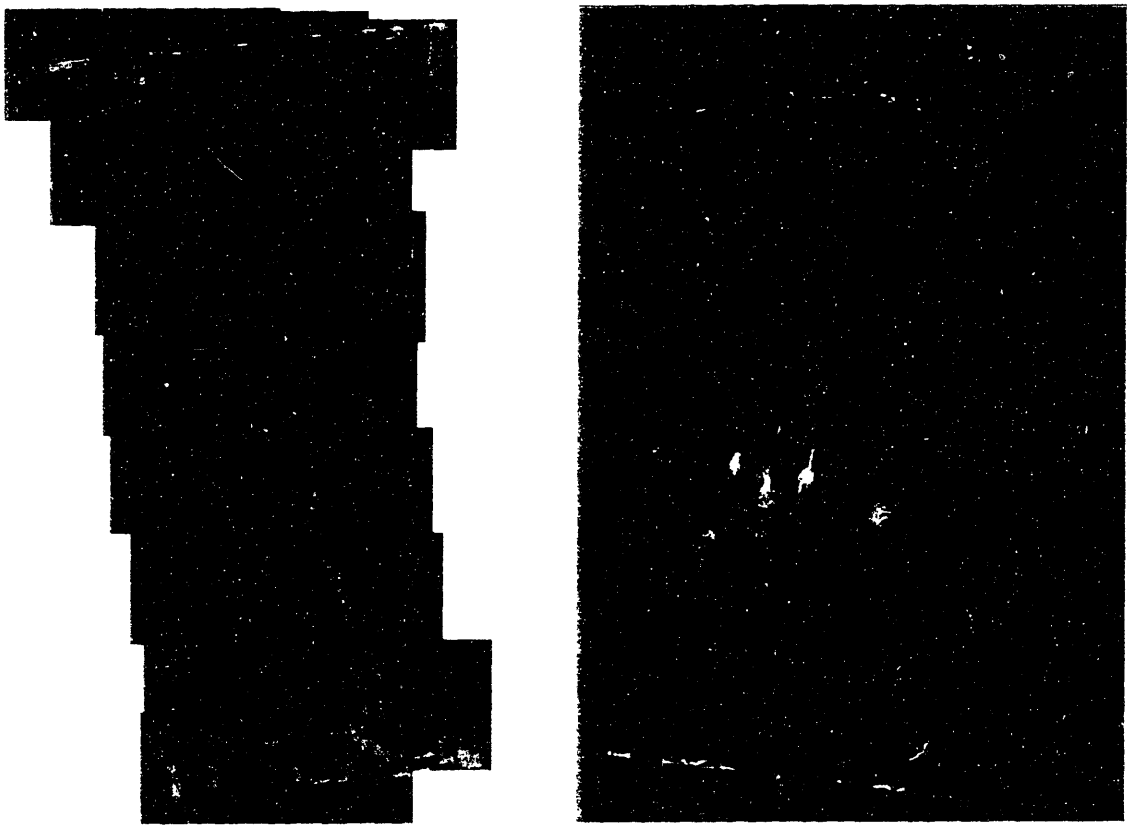

(a) (b)

Figure 3.9: Composite images of typical gauge lengths showing the damaged band. Both specimens were stained in alizarin complexone before testing and calcein (green) after testing. (a) Specimen compressed to [illegible] -1.3%. Small regions of damage are visible (middle, about one third of the height from the top) but no distinct band is seen. (b) Specimen compressed to [illegible] -4.0%. A distinct damage band is visible.

(a) Untested specimen, little damage present.

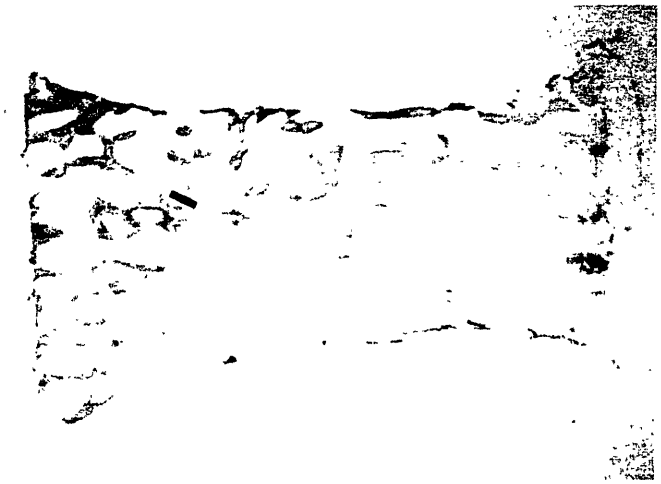

(b) Specimen tested to ε_{max} = -0.4%, not significantly different from untested specimen.

(c) Specimen tested to ε_{max} = -0.8%, some damage seen. Damage is not localized.

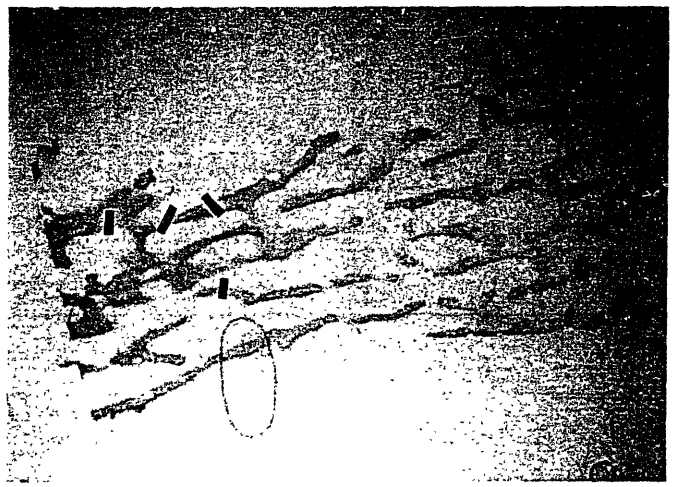

(d) Specimen tested to ε_{max} = -1.1%, damage occurs locally, but does not extend across the specimen.

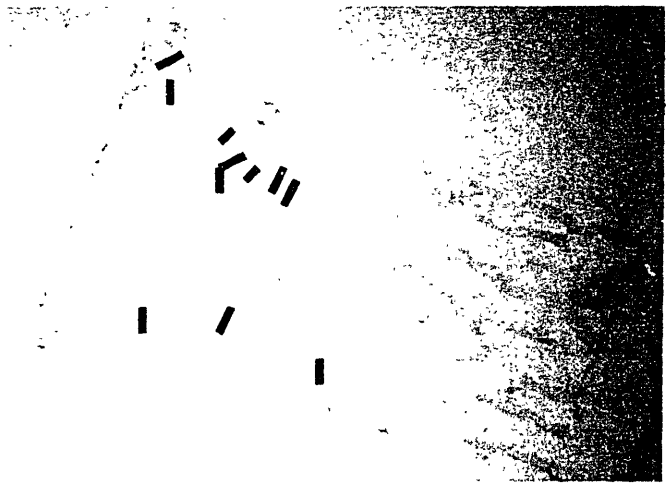

(e) Specimen tested to ε_{max} = -1.3%, localized region of damage extends across the specimen, forming a damage band.

(f) Specimen tested to ε_{max} = -2.0%, damage band has increased in length.

(g) Specimen tested to ε_{max} = -4.0%, damage band is not significantly longer than in (f), but damage density within the band has increased.

Figure 3.10: Images of section gauge lengths, with location of damaged trabeculae marked. Images are typical for the strain level. (a) Untested specimen, little damage present. (b) Specimen tested to ε_{max} = -0.4%, not significantly different from untested specimen. (c) Specimen tested to ε_{max} = -0.8%, some damage seen. Damage is not localized. (d) Specimen tested to ε_{max} = -1.1%, damage occurs locally, but does not extend across the specimen. (e) Specimen tested to ε_{max} = -1.3%, localized region of damage extends across the specimen, forming a damage band. (f) Specimen tested to ε_{max} = -2.0%, damage band has increased in length. (g) Specimen tested to ε_{max} = -4.0%, damage band is not significantly longer than in (f), but damage density within the band has increased.

3.4 Discussion

The observations of microstructural damage can be related to the stress-strain behavior as follows. Prior to testing, specimens have relatively little damage. The damage that is present is likely due to machining: broken struts on the outer surface of the machined region and does not extend more than one trabecular length into the specimen (**Figure 3.3**).

On loading, the stress-strain curves are linearly elastic up to a strain of at least -0.5%. Accordingly, microdamage parameters in the two specimens tested to -0.4% strain are not significantly different from untested specimens ($p > 0.05$ for all microdamage parameters). The stress-strain curve becomes nonlinear when the strain reaches about -0.5% to -0.8% (mean, -0.7% ± 0.2%). Stress continues to increase until about -1.85% strain (SD = 0.56%), when it peaks. From -0.8% strain, through -1.1%, and -1.3%, all microdamage parameters increase rapidly (**Table 3.2**). This level corresponds to the yield strain of bovine trabecular bone in compression measured using the same specimen geometry (-1.09% ± 0.12%) (Keaveny *et al.*, 1994c). For example, the crack numerical density at a strain level of -1.3% is 1.2 ± 1.1 mm^{-2}, compared to a numerical density of 0.033 ± 0.002 mm^{-2} for specimens at a strain level of -0.8%, an increase of nearly two orders of magnitude. The damage band also begins to form at strains of about -1.3%. No damage bands were observed in specimens loaded to -0.8% or below. At -1.1% strain, all specimens show small amounts of damage confined to localized regions, but a distinct band cannot be defined. At strain levels of –1.3%, some specimens (n = 3 of 5 total) have formed a distinct band (**Figure 3.9, 3.10; Table 3.2**).

At strain levels beyond about -1.5%, the stress-strain curve becomes roughly flat. The strain peaks at about -1.85% ± 0.56%. As the strain increases, the damage band widens. At strain levels of -2.0%, the average damage band length is 3.7 mm, approaching the gauge length (5.0 mm). At higher strain levels, the damage band length remains approximately constant and damage progresses by increasing the number of damaged trabeculae and the area fraction of damage within the band. The mean crack length remains constant with increasing strain, so damage accumulates by increasing the number of cracks, not their length. For example, the crack numerical density at a strain

level of -4.0% is 13.7 ± 9.5 mm^{-2}, an increase of an order of magnitude from specimens at a strain level of -1.3% (1.2 ± 1.1 mm^{-2}). At high strains (at and above -2.0%), individual trabeculae fracture.

Damage progression continues until the specimen cannot carry the applied load and the specimen fractures. The likelihood that a specimen can carry the load required to reach a given strain decreases with increasing strain levels. One specimen was lost during loading to -2.0% strain, and two specimens were lost during loading to -4.0%. Microdamage parameters could not be obtained from fractured specimens, but qualitative observations show large amounts of damage, including a specimen with two damage bands.

In this study, microdamage was present as large numbers of small cracks, consistent with earlier studies (Zioupos and Currey, 1994) and supporting the notion that it is more important to prevent crack growth than prevent crack formation. The consistency of the mean crack length at all strain levels tested (*Cr.Len.* vs. *Cr.Num.*: slope = 65.3 ± 1.3 μm, $p < 0.001$, $R^2 = 0.99$) suggests that it is related to a microstructural feature of the trabecular bone. The mean crack length is similar to the distance between lacunae (center to center distance = 85.8 ± 21.2 μm, n = 117 from 35 specimens). Lacunae spacing was measured by determining the mean free path through the bone matrix (DeHoff and Rhines, 1968). We hypothesize that the lacunae serve as crack arrestors or stress concentrators. We have observed cases of cracks intersecting lacunae; however, these observations are near the maximum resolution of our imaging equipment. Reilly and Currey (1999) and Reilly (2000) report increased microcracking in regions surrounding osteocyte lacunae in equine cortical bone, consistent with the damage expected at stress concentrations.

We observe several patterns of microdamage in the specimens. We are not aware of literature on trabecular bone that directly relates microcrack damage patterns to local stresses in individual trabeculae. Fyhrie and Schaffler (1994) hypothesize that cross-hatch cracks in trabecular bone occur due to shear stresses from direct compression, based on similar observations in cortical bone. Regions of diffuse damage have been associated with tensile loading in cortical bone specimens (Boyce *et al.*, 1998; Reilly and Currey, 1999). The cortical bone literature suggests that the crack patterns observed in

trabecular bone may result from the same loading types, but we have no means of determining local stresses in individual trabeculae.

This study is the first to characterize microstructural damage in trabecular bone in detail, allowing the progress of damage accumulation to be related to the applied strain. This work extends the study of microdamage in trabecular bone to higher strain levels (up to -4.0%) than previous studies, allowing observation of damage to near the fracture point. The use of a specimen geometry that is well established in the literature (Bowman *et al.*, 1994; Keaveny *et al.*, 1994a; Ford and Keaveny, 1996; Oden *et al.*, 1998) allows comparison of our results with those of other groups. We observed the same patterns of damage and a similar increase in the amount of damage with increasing maximum strain as that reported in other studies (Fazzalari *et al.*, 1998a, 1998b), including that of Wachtel and Keaveny (1997) using the same specimen geometry. However, we report a lower damage density for pre-yield specimens and a higher damage density for post-yield specimens tested to the same strain levels.

Several damage moduli have been described and used in other studies (**Figure 3.1a**) (Keaveny *et al.*, 1993b, 1994a, 1994d, 1999; van Rietbergen *et al.*, 1995; Rho *et al.*, 1997; Zysset *et al.*, 1998; Jepson *et al.*, 1999; Morgan *et al.*, 2000). In this study, we used the secant modulus, as it was the easiest to measure consistently. The secant modulus can be taken as an upper limit of the reloading modulus, since the linear portion of the reloading stress-strain curve approaches the secant modulus of the previous curve in compression studies using the same specimen geometry (Keaveny *et al.*, 1994d). Attempts to use the reloading modulus (Keaveny *et al.*, 1994d, 1999) were not successful, since the specimens were in tension when unloaded to zero strain (**Figure 3.1a**). There is also concern that reloading could create additional microdamage. The unloading modulus, used in nanoindentation studies (Rho *et al.*, 1997; Zysset *et al.*, 1998) was difficult to define because the initial unloading curve (immediately after the maximum strain) is nonlinear.

A limitation of the study is the possible introduction of additional damage due to the residual tension on the specimen at the end of the loading curve (**Figure 3.1a**). This residual tension could open cracks created during the compression portion of the loading cycle and lengthen existing cracks. Values of the microdamage parameters in specimens

that were never loaded in tension were not significantly different from those of specimens tested to the same maximum strains that were exposed to residual tension. This degree of residual tension on a specimen at zero strain does not appear to increase microdamage.

A second limitation of the study is the small number of specimens used. We used five specimens for most high strain categories, and three specimens for the zero load tests. Power analyses indicate that more than twenty-five specimens would be required in each group to show statistical significance at the differences we observe. Microdamage analysis of a large number of specimens would be prohibitive; we feel that the numbers of specimens used adequately describe the progression of damage in bovine trabecular bone.

This study uses bovine trabecular bone, which is denser, on average, than human trabecular bone, especially osteoporotic human bone. Although it is difficult to extrapolate particular results from bovine to human bone, we expect that the sequence of events in the accumulation of damage in human trabecular bone will be similar to that in bovine trabecular bone (Keaveny *et al.*, 1999).

The characterization of damage during monotonic compression is obtained from observations of a number of trabecular bone specimens compressed to various strains. The overall description of damage accumulation is a composite of the events seen in different specimens. Ideally, it would be desirable to observe the accumulation of damage with increasing strain in a single trabecular bone specimen.

The data obtained in this study can be used to develop a micromechanical model relating the microstructural damage parameters to the loss in modulus. The chapter that follows describes such a micromechanical model to calculate $(1 - E_{vol}/E_0)$ using the microstructural damage parameters reported here. The model gives a good description of the measured values of $(1 - E_{vol}/E_0)$, suggesting that the observed microstructural damage can be related to the associated modulus loss.

Chapter 4: Modeling Microdamage in Bovine Trabecular Bone in Compression

Abstract

Loading bone beyond its yield point creates microdamage, leading to reduction in stiffness. Previously, we related microdamage accumulation to changes in mechanical properties. We developed a model that predicts stiffness loss based on the presence of microdamage. Modeling was done at three levels: (1) single trabeculae, (2) a cellular solid consisting of intact, damaged, and fractured trabeculae, and (3) a specimen with a localized damage band. Predictions of reduced modulus agreed well with experimental measured modulus reductions of post-yield compression of bovine trabecular bone. The predicted reduced modulus was relatively insensitive to changes in the input parameters, with changes in the damage band length having the greatest effect on the predicted modulus reduction.

4.1 Introduction

Loading bone beyond its yield point is known to cause a loss of both stiffness and strength (Keaveny *et al.*, 1994d, 1999). Post-yield loading also causes microdamage (Wachtel and Keaveny, 1997), in the form of microcracks and also as diffusely damaged areas that cannot be resolved into individual microcracks at the resolution of the light microscope. Recently, empirical relationships have been developed to quantify the relationship between mechanical property parameters and microdamage.

Burr *et al.* (1998) found mathematical relationships between stiffness loss and microcrack areal density and between stiffness loss and damaged area density in cortical bone, suggesting that similar correlations may also exist in trabecular bone. Wachtel and Keaveny (1997) showed an increase in the number of damaged trabecular struts with increasing strain in a single compression cycle in bovine tibial trabecular bone. Yeh and Keaveny (2000) have used finite element modeling to estimate the number of damaged trabeculae and the number of fractured trabeculae in a cube of human vertebral trabecular bone compressed to strains up to 2.0%. They used strain-based yield and fracture criteria

to model damage and fracture in the trabeculae. Microdamage and microfractures were modeled separately. The model predicted that microdamage led to greater reductions in modulus than microfractures. The microdamage model overpredicted the measured modulus reduction at small strains (< 1%), but gave a reasonable estimate of the measured modulus reductions at higher strains; however, the microfracture model underpredicted the measured modulus reductions at all strains.

Modulus reduction due to fatigue or resorption of trabeculae has been modeled in several studies. Using finite element simulations, Guo *et al.* (1992) and Schaffner *et al.* (2000) modeled crack growth during fatigue of two-dimensional honeycombs representing trabecular bone. The Young's modulus of a single trabecula was considered to remain constant during crack growth. When the crack reached a critical length, it was assumed to propagate, fracturing the trabecula. The broken trabecula was eliminated from the model and the modulus recalculated. This process was repeated the modulus was reduced by 10%. The effect of resorption of trabeculae on modulus has been modeled by Silva and Gibson (1997a, b) and Vajjhalla *et al.* (2000). These studies analyzed the reduction in modulus in a random two-dimensional honeycomb and in a two-dimensional representation of vertebral bone. In both cases, there was a dramatic reduction in modulus: elimination of ten percent of the struts reduced the modulus by approximately forty percent. In the vertebral bone simulation, elimination of the horizontal struts was more damaging than eliminating vertical struts. Vajhalla (1999) determined the loss of stiffness as a function of reduced density as struts were removed from a three-dimensional Voronoi foam representing the structure of trabecular bone. This work extended the relationship between modulus reduction and strut removal to a generalized three-dimensional cellular structure representative of trabecular bone but did not account for modulus loss in partially cracked, but unfractured, trabeculae. Taylor (1998b) has used measurements of loss of stiffness in a single cycle of cortical bone fatigue to predict crack growth in the bone material during that cycle.

A significant amount of work has been done to show how the presence of cracks and voids affect the modulus of a continuous solid. Much of this work is in the fields of composite materials and geology, which considers macroscopic cracks in rocks. Budiansky and O'Connell (1976), for instance, found that the effective moduli of an

isotropic material with randomly distributed flat cracks decreased linearly with the crack density, and that this result was insensitive to the details of the crack shape.

In the previous chapter, we characterized damage in compression specimens of bovine trabecular bone at the microstructural level by measuring microdamage parameters (number of cracks per unit area, total length of cracks per unit area, damaged area fraction, and number of struts damaged). We also measured mechanical properties (modulus reduction and maximum strain reached) at the continuum level. We found that at strains less than -0.7%, the stress-strain curve was linear and there was no detectable increase in damage. Stress then increased non-linearly up to a peak value at a strain of about -1.85%; in this range of strain all microdamage parameters increased dramatically. At a strain of about -1.3%, a localized band of damage became apparent. At strains beyond -1.85% the stress-strain curve leveled off and damage accumulated in a widening band. Once the length of the damage band was roughly equal to the gauge length of the specimen, damage progressed by increasing the number of damaged trabeculae and the area fraction of damage within the band. The mean crack length remained constant with increasing strain, indicating that damage progression occurs by increasing the number of cracks, not their length. At strains beyond -2.0%, individual trabeculae fractured. Damage progression continued until the specimen could not support the applied load. This was seen as a reduction in stress with increasing strain or sudden fracture.

This work seeked to develop relationships between microcrack parameters (number of cracks per unit area, total length of cracks per unit area, damaged area fraction, number of struts damaged, etc.) and continuum mechanical properties (modulus reduction and maximum strain reached) using cellular solid models. We developed a model that explained mechanistically how the presence of microcracks affects bone stiffness loss. In this study, we asked: can the modulus reduction in bovine trabecular bone damaged in a single compression cycle be explained by a model based on measured microdamage parameters?

4.2 Modeling

Modeling microdamage was performed in three steps (**Figure 4.1**). First, microdamage within a single trabecula was modeled and we determined how microcracking reduces the stiffness of the trabecula. Individual trabeculae were assumed to be either rods or plates. Second, the network of individual trabeculae was modeled as a cellular solid, accounting for the effective loss of fractured trabeculae and for the reduced stiffness in damaged trabeculae. A reduced modulus was determined for the local damaged region. Finally, the effect of the damaged region, in the form of a shear band, on the modulus of the entire specimen was estimated.

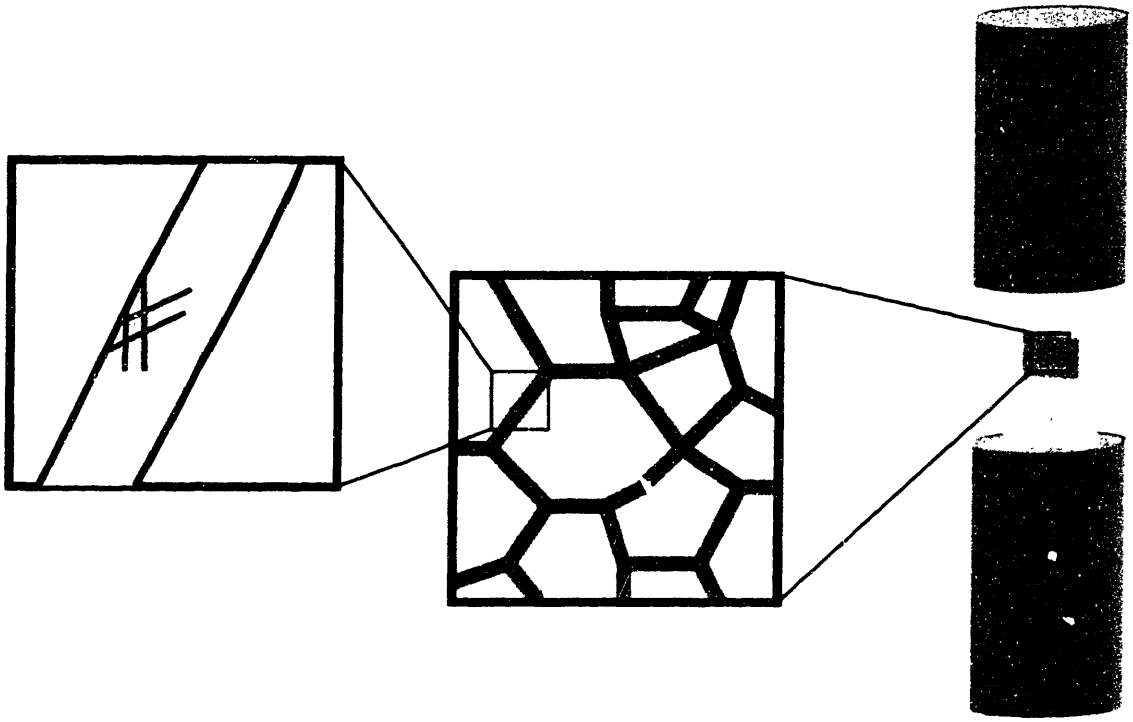

Figure 4.1: Schematic of trabecular bone, showing different levels of structure. Individual trabeculae may have microcracks, reducing their stiffness, or be fractured. A region of trabecular bone may have trabeculae with no damage, with microcracks, or with fractures. As strain increases, the damage is concentrated in a band, indicated by the darker area on the whole specimen view, within the specimen. The model described in the text considers all three scales.

4.2.1 Trabeculae Level

Damage is present in a number of trabeculae within a bone specimen. We idealized each trabecula as a rod or a plate with length, l_0, thickness, t_0, width, b, and initial undamaged modulus, E_s (**Figure 4.2a**). A rod-like trabecula was assumed to have width, b, equal to the thickness, t_0, while a plate-like trabecula was assumed to have a width b equal to the length, l_0. Microdamage occurred as microcracks in a localized region of the trabecula of thickness, t_{damage} (**Figure 4.2b**). The damage was assumed to be uniform into the depth of the trabecula. The presence of microcracks reduced the modulus of the damaged area to a new modulus, $\bar{E}$ (**Figure 4.2c**).

Budiansky and O'Connell (1976) used a self-consistent method to calculate the reduction in the elastic moduli of an isotropic material associated with a given distribution of random microcracks. The decrease in Young's modulus with increasing crack numerical density was approximately linearly. At crack densities typical of the damaged area in a single trabecula, the stiffness of the damaged area was approximately zero, allowing it to be effectively eliminated.

We considered the case of a cracked solid containing circular cracks. Although cracks in bone have been observed to be elliptical (Taylor and Lee, 1998), the assumption of circular cracks was made since the final value of the modulus reduction, $\bar{E}/E_s$, was relatively independent of the crack aspect ratio. The modulus reduction was given as (Budiansky and O'Connell, 1976):

$$\frac{\bar{E}}{E_s} = 1 - \frac{16}{45} \cdot \frac{\left(1-\bar{\nu}^2\right)\left(10-3\bar{\nu}\right)}{\left(2-\bar{\nu}\right)} \varepsilon' \tag{4.1}$$

where

$$\varepsilon' = \frac{45}{16} \frac{\left(\nu-\bar{\nu}\right)\left(2-\bar{\nu}\right)}{\left(1-\bar{\nu}^2\right)\left[10\nu-\bar{\nu}\left(1+3\nu\right)\right]} = \frac{3}{4\pi} M\left\langle l^2 \right\rangle \tag{4.2}$$

when

$$M\left\langle l^2 \right\rangle = \frac{1}{A_{crack}} \sum_{n=0}^{\infty} l_n^2 \cdot f\left(l_n\right) \tag{4.3}$$

From the plot of modulus reduction versus the parameter ε' in the original paper (Budiansky and O'Connell, 1976), we noted that for a dry crack

$$\frac{\bar{E}}{E} \to 0, \quad \frac{\bar{\nu}}{\nu} \to 0, \quad \varepsilon' \to 0.563, \quad M\left\langle l^2 \right\rangle \to 2.356 \tag{4.4}$$

and for a wet crack

$$\frac{\bar{E}}{E} \to 0, \quad \frac{\bar{\nu}}{\nu} \to 0.5, \quad \varepsilon' \to 1.4, \quad M\left\langle l^2 \right\rangle \to 5.86 \tag{4.5}$$

To determine the reduction in modulus a damaged area, we considered cases corresponding to the patterns of damaged observed in various studies (diffuse damage, single crack, parallel cracks, equal cross-hatch, unequal cross-hatch, and fracture) (Wachtel and Keaveny, 1997; Fazzalari *et al.*, 1998b). In the case of complete fracture, the trabecula had been effectively removed from the structure and there was no region of reduced modulus. For single cracks and parallel cracks, the damaged area was taken to be only the edges of the crack, and the modulus was assumed to go to zero in that region. The unequal cross-hatch pattern was essentially a single crack with accompanying small cracks; we assumed that the long crack dominates, so an unequal cross-hatch was treated like a single crack.

For the case of equal cross-hatching, we considered a typical case. A review of twelve specimens loaded to or beyond a strain of -2.0% gave an average of 22.4 ± 14.5 cracks per image. Since most damage in this region was seen as cross-hatching, we assumed that the average number of cracks per image estimated the number of cracks in a region of cross-hatching. Stereological point counting only identified areas very close to the actual damage, so we assumed that the entire region was filled with cracks. We also assumed that the cracks extended to 70% of the height, h, of the damaged area. For example, if the area of damage was twice as long as it was high,

$$M\left\langle l^2 \right\rangle = \frac{1}{2h \cdot h}(0.7h)^2 \cdot 22.4 = 5.49 \tag{4.6}$$

which reduced $\bar{E}$ to near zero for completely saturated cracks and to zero for dry cracks.

Diffuse damage usually occurred as regions adjacent to clearly distinguishable microcracks. We assumed that diffuse damage was composed of fine microcracks too small to distinguish individually under a light microscope. In this case, the presence of

fine cracks extended the area of reduced modulus. It was difficult to estimate the number of fine cracks in a region of diffuse damage; however, the presence of diffuse staining implied a high crack density and a significantly reduced modulus.

To account for the effective loss of material caused by the presence of microdamage, we replaced the damaged trabecula by one that was thinner but intact, with effective strut thickness t' (**Figure 4.3**). Cellular solid models indicated that a rod in an open-cell foam is loaded in bending, with the displacement under load proportional to $1/t^3$, and that a plate in a closed-cell foam is loaded in axial tension or compression, and its displacement would be proportional to $1/t$ (Gibson and Ashby, 1997).

To determine the effective thickness corresponding to each damage location and depth through the thickness for a rod model, we considered the general case of a beam loaded in pure bending (**Figure 4.4**). Shear forces were assumed to be negligible.

$$\delta = \frac{M}{2E_s}\left[\frac{x_3^2}{I_3} + \frac{x_2^2}{I_2} + \frac{x_1^2}{I_1} + \frac{2x_2x_3}{I_2} + \frac{2x_1(x_2+x_3)}{I_1}\right] \tag{4.7}$$

For an intact beam,

$$I_1 = I_2 = I_3 \tag{4.8}$$

$$\delta = \frac{l_o^2 M}{2E_s I_1} \tag{4.9}$$

In this model, the effective thickness was chosen so that the deflections of the two beams under the same loading conditions were equal.

$$\frac{l_o^2 M}{2E_s I'} = \frac{M}{2E_s}\left[\frac{x_3^2}{I_3} + \frac{x_2^2}{I_2} + \frac{x_1^2}{I_1} + \frac{2x_2x_3}{I_2} + \frac{2x_1(x_2+x_3)}{I_1}\right] \tag{4.10}$$

where I' is the moment of inertia of the effective beam

Equation (4.10) can be simplified for the three cases of damage used in this model: for example, for the case of damage in the middle of the beam, $x_1 = x_3$, $I_1 = I_3$, and

$$\frac{l_o^2}{I'} = \left[\frac{x_2^2}{I_2} + 4\frac{x_1^2}{I_1} + \frac{2x_1x_2}{I_2} + \frac{2x_1x_2}{I_1}\right] \tag{4.11}$$

$$I_1 = I_3 = \frac{bt_0^3}{12}, \quad I_2 = \frac{b\left(t_0 - t_{damage}\right)^3}{12} \tag{4.12}$$

The amount of damage has been measured as a total damaged area, A_{total}, and as a depth of damage through the thickness of the beam, t_{damage}/t_0, rounded to the nearest one quarter. The area of damage for each trabecula was estimated by dividing the total damaged area by the number of trabeculae containing damage.

$$A_{damage} = \frac{A_{total}}{N_{damage}} \tag{4.13}$$

The intact thickness and the length of damage were determined from the area and the depth through the thickness.

$$x_{damage} = \frac{A_{damage}}{t_{damage}} \tag{4.14}$$

Therefore,

$$I_{damage} = I_0 \cdot \left(1 - \frac{t_{damage}}{t_0}\right)^3 \tag{4.15}$$

Trabeculae that had damage through the entire thickness were considered to have fractured and were eliminated from the matrix. Eqn. 4.10 to Eqn. 4.15 were combined and solved to determine the effective moment of inertia, and thus an effective thickness, for the beam.

In a cellular solid composed of plates, the individual members deform by stretching of the cell walls. In the general case, the deflection were calculated as the sum of the deflections of each component.

$$\delta = \delta_1 + \delta_2 + \delta_3 + \cdots = \frac{F}{E_s \cdot l_0}\left(\frac{x_1}{t_1} + \frac{x_2}{t_2} + \frac{x_3}{t_3} + \ldots\right) \tag{4.16}$$

To calculate the effective thickness, Eqn. 4.16 was set equal to the case of a plate with constant thickness, t', and we solved for t'.

$$t' = \frac{t_0 - t_{damage}}{1 - \frac{t_{damage}}{t_0} - \frac{A_{damage}}{t_0 \cdot l_0}} \tag{4.17}$$

To model an individual specimen, several experimental parameters were required. The location of the damage on the strut (middle or end, **Figure 4.5**) and the depth through the thickness of damage, t_{damage}/t_0, (25%, 50%, 75% or 100% of the trabeculae, **Figure 4.5**) were measured for each specimen. The location of damage affected the deflection of the trabeculae in bending, in the open-cell model, as the deflection depends on the distribution of the moment, Young's modulus, and the thickness along the length of the member. For plate stretching in the closed-cell model, the deflection was unaffected by the distribution of the thickness along the length of the member. It was assumed that any crack visible in two dimensions is a sheet-like crack (Fazzalari *et al.*, 1998a) that extends through the depth of the strut in the third dimension. Finally, the damaged area, A_{damage}, was measured for each cracked region and a total damaged area, A_{total}, for a given specimen was available.

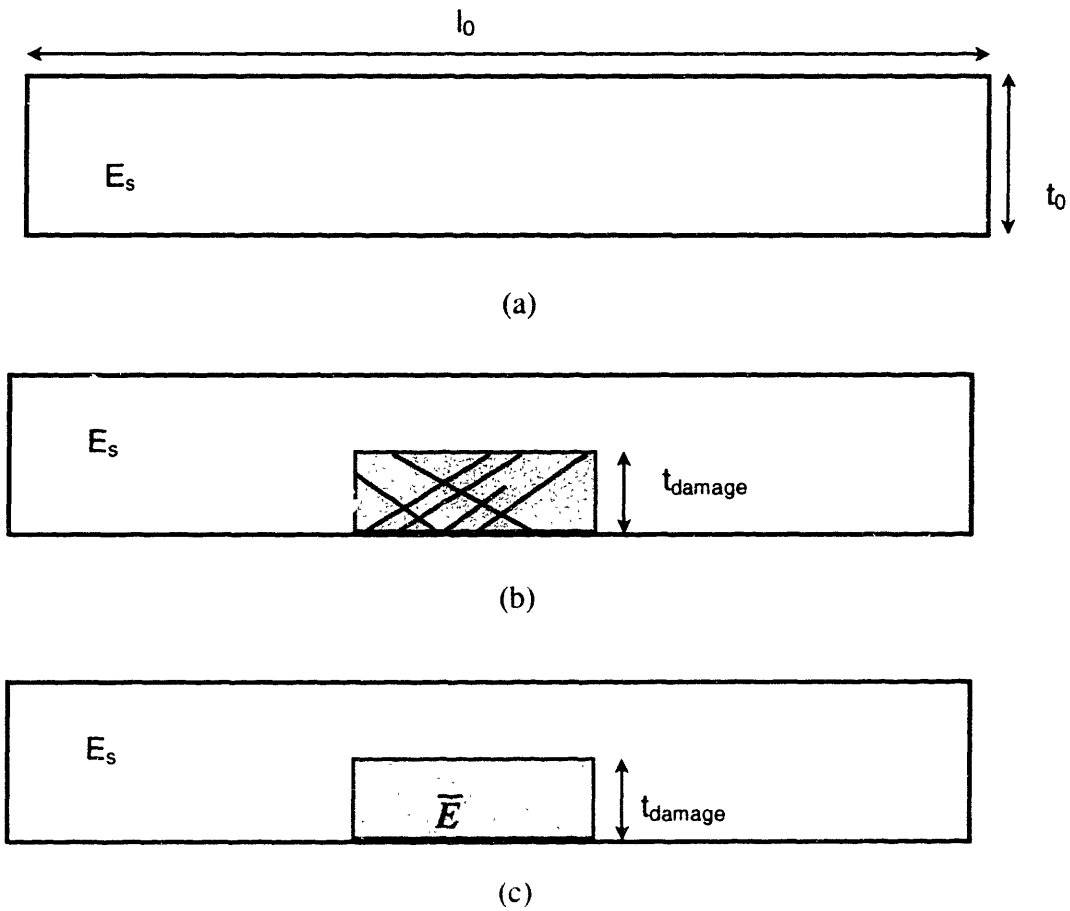

Figure 4.2: An idealized two-dimensional representation of a single trabecula. The trabecular width b is either thickness t (rod model) or length l (plate model). (a) An idealized undamaged trabecula of modulus E_s. (b) The damaged area is delineated as containing the local damage. (c) The damaged area is represented as a new material with a reduced modulus, $\bar{E}$.

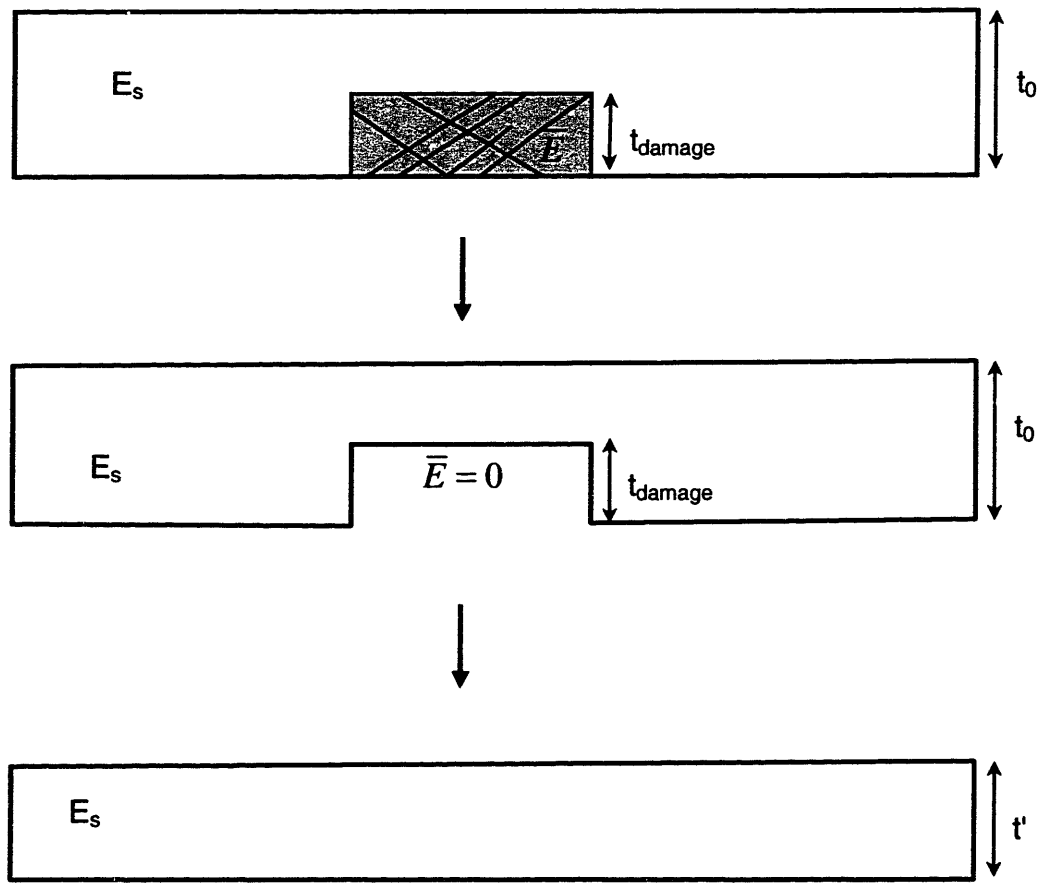

Figure 4.3: Each damaged trabeculae is replaced by an intact trabeculae of the same initial modulus but a new effective thickness, t'. The effective thickness, t', is chosen such that the intact trabecula of thickness t' has the same stiffness as the damaged trabecula of thickness t_0.

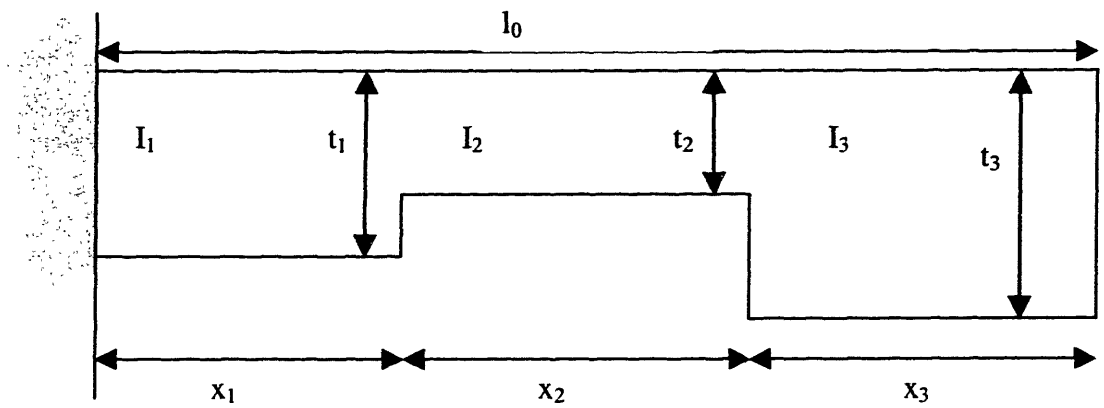

Figure 4.4: General form of a beam with a segment missing. The beam may be deformed in bending (rod model) or by axial stretching (plate model).

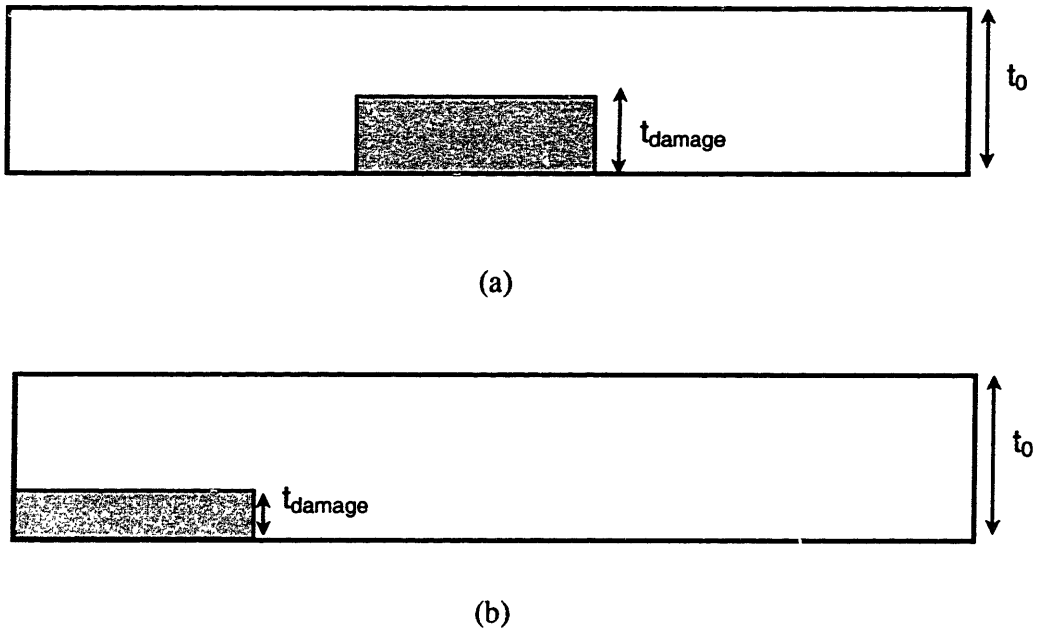

Figure 4.5: Damage location and depth across the thickness, as measured in Chapter 3. Damage depth across the thickness is rounded to the nearest 25%. Schematic showing damage occurring (a) in the middle of a trabecula, 50% depth across the thickness, and (b) at one end of a trabecula, 25% depth across the thickness.

4.2.2 Cellular Solid Level

To develop a model for damage of trabecular bone in compression, the damaged and fractured trabeculae were incorporated into a three-dimensional network of struts that represented the structure of trabecular bone. Within a region of damaged trabecular bone there were intact trabeculae with no microcracks, trabeculae with microcracks that were modeled as intact trabeculae of reduced effective thickness, and fractured trabeculae with a through-thickness crack, which had no load-bearing capacity (**Figure 4.6a**).

The fractured struts were eliminated from the network (**Figure 4.6b**) creating a more open network with a reduced modulus, E_{strut_loss}/E_0. The modulus of a random three dimensional, open-cell network with struts randomly removed has been calculated (**Figure 4.7**) (Vajjhala *et al.*, 2000). This random network is similar to the structure of randomly oriented trabecular bone. Analyses of the effect of random strut loss in a variety of two-dimensional networks (regular hexagonal cells, random cells, two-dimensional vertebral bone model) suggested that the modulus reduction is insensitive to the exact geometry of the network (Silva and Gibson, 1997a, b).

A similar method was used to obtain the stiffness reduction due to strut removal in a closed-cell network of plates. There are currently no studies available that show how randomly removing plates affects the modulus of closed-cell foams. However, the modulus loss for the removal of small numbers of plates can be estimated, and a percolation threshold, where the cellular solid is no longer continuous, can also be estimated (Stauffer and Aharony, 1992). From this information, we interpolated the remainder of the curve. Initially, in the intact foam, all plates deform by stretching ($E \propto \rho^*/\rho_s$). When a plate was removed, a gap was created, and the surrounding plates deformed mainly by bending ($E \propto (\rho^*/\rho_s)^2$). Assuming that only plates within a one-cell distance of the removed plate were affected, the modulus reduction were calculated as follows:

$$\frac{E_{strut\_loss}}{E_0} = \frac{f \cdot i}{N_{total} - i} \cdot \left(\frac{\left(\rho^* / \rho_s \right)_{fracture}}{\left(\rho^* / \rho_s \right)_0} \right)^2 + \frac{N_{total} - f \cdot i - i}{N_{total} - i} \cdot \left(\frac{\left(\rho^* / \rho_s \right)_{fracture}}{\left(\rho^* / \rho_s \right)_0} \right) \tag{4.18}$$

where E_{strut_loss} is the modulus after the removal of trabeculae, E_0 is the initial modulus of the cellular solid, f is the number of plates per cell, i is the number of plates removed, N_{total} is the total number of plates, $(\rho^*/\rho_s)_{fracture}$ is the relative density after removal of fractured trabeculae, and $(\rho^*/\rho_s)_0$ is original relative density. This estimate was valid as long as the plates that were removed were far enough apart to not interact. Since there were typically 12-14 faces per unit cell in a three-dimensional cellular solid (Gibson and Ashby, 1997), and we assumed that removing a trabeculae only affects trabeculae within one cell, this approximation was valid until approximately 5% of the struts have been removed. At this point, removal of an additional plate was likely to be within the range of influence of a plate that had been removed previously.

At the other extreme, there is a limit to how many faces of a closed-cell cellular solid can be removed while keeping the cellular solid intact. The percolation threshold is defined as the fraction of struts that can be randomly removed before the structure is separated into two pieces, with resulting zero modulus. For a closed-cell cubic structure, the percolation threshold is approximately 75% (Stauffer and Aharony, 1992). The approximate reduced modulus was calculated for the two extreme cases, and an estimate for the intermediate region was obtained by interpolation (**Figure 4.7**).

The damaged rods or plates can be represented as intact rods (plates) with reduced thickness (**Figure 4.3, 4.6c**). The thickness reduction was then averaged over the remaining struts (**Figure 4.6d**)). Models suggest that the Young's moduli of closed-cell foams are relatively insensitive to the distribution of the wall thickness (Grenestedt and Bassinet, 2000) while those of open-cell foams are more sensitive (Yeh and Keaveny, 1999). This probably reflects the differing mechanisms in closed- and open-cell cellular solids: the local stiffness of each plate-like member in a closed-cell foam is related to its axial stiffness ($\propto t$) while that of each rod-like member in an open-cell foam is related to its bending stiffness ($\propto t^4$). The bovine trabecular bone used in this study had an average relative density of 0.43, with a more plate-like structure. Here, for simplicity, we used the average reduced thickness, $\bar{t}$, for both plate- and rod-like trabeculae, for subsequent density and modulus calculations.

$$\bar{t} = \frac{1}{N_{remaining}} \sum_{i=1}^{N_{remaining}} t_i' \tag{4.19}$$

To determine the average effective thickness, the model calculated the effective thickness for several general cases (middle and end damage at a percentage extent of damage across the thickness of 25%, 50%, or 75%) and applied those values according to the observed fraction of trabeculae with that type of damage.

$$\frac{\bar{t}}{t_0} = f_{0\%} \cdot 1 + f_{25\%,m} \cdot \frac{t'_{25\%,m}}{t_0} + f_{25\%,e} \cdot \frac{t'_{25\%,e}}{t_0} + f_{50\%,m} \cdot \frac{t'_{50\%,m}}{t_0} + f_{50\%,e} \cdot \frac{t'_{50\%,e}}{t_0} + f_{75\%,m} \cdot \frac{t'_{75\%,m}}{t_0} + f_{75\%,e} \cdot \frac{t'_{75\%,e}}{t_0} + f_{100\%} \cdot 0 \tag{4.20}$$

The ratio of the fraction of struts with middle damage to those with end damage was measured in the previous study: it was consistent and approximately 3:1. Therefore,

$$\frac{\bar{t}}{t_0} = f_{0\%} + \left(f_{25\%,m} + f_{25\%,e}\right) \cdot \left(\frac{3t_{25\%,m} + t_{25\%,e}}{4t_0}\right) + \left(f_{50\%,m} + f_{50\%,e}\right) \cdot \left(\frac{3t_{50\%,m} + t_{50\%,e}}{4t_0}\right) + \left(f_{75\%,m} + f_{75\%,e}\right) \cdot \left(\frac{3t_{75\%,m} + t_{75\%,e}}{4t_0}\right) \tag{4.21}$$

Considerable work has been done showing that trabecular bone modulus is strongly related to density (Carter and Hayes, 1977c; Ducheyne *et al.*, 1977; Hvid *et al.*, 1985; Ashman and Rho, 1988; Rice *et al.*, 1988; Hvid *et al.*, 1989; Ciarelli *et al.*, 1991; Goldstein *et al.*, 1993; Keaveny and Hayes, 1993b; Ding *et al.*, 1997). Thus, the effective density reduction was used to calculate the reduced modulus, E_{damage}/E_0, due to the presence of damaged regions. The reduced modulus, given by the reduced thickness, $\bar{t}$, was determined since the deflection of the beam, δ, remains constant. For a rod model (Gibson and Ashby, 1997),

$$E_{damage} \propto \frac{F}{l_0^2} \cdot \frac{l_0}{\delta} \cdot \frac{F}{l_0} \cdot \frac{E_s b \bar{t}^3}{F l_0^3} \propto E_s \frac{b \bar{t}^3}{l_0^4} \tag{4.22}$$

$$\frac{E_{damage}}{E_s} \propto \frac{\bar{t}^3 b}{l_0^4} \tag{4.23}$$

The deflection of the undamaged specimen is given by

$$\frac{E_0}{E_s} \propto \frac{t_0^3 b}{l_0^4} \tag{4.24}$$

so

$$\frac{E_{damage}}{E_0} = \left(\frac{\bar{t}}{t_0}\right)^3 \tag{4.25}$$

For a plate model (Gibson and Ashby, 1997),

$$\frac{E_{damage}}{E_s} \propto \frac{\bar{t}}{l_0} \tag{4.26}$$

and

$$\frac{E_0}{E_s} \propto \left(\frac{\rho^*}{\rho_s}\right)_{damage} \propto \frac{t_0}{l_0} \tag{4.27}$$

so,

$$\frac{E_{damage}}{E_0} = \frac{\bar{t}}{t_0} \tag{4.28}$$

The local modulus reduction, E_2/E_0, depended on both the modulus reduction due to fractures, E_{strut_loss}/E_0, and the modulus reduction due to microdamage, E_{damage}/E_0. Each modulus reduction was calculated separately, then the individual modulus reductions were multiplied to determine the overall modulus reduction.

$$\frac{E_2}{E_0} = \frac{E_{strut\_loss}}{E_0} \cdot \frac{E_{damage}}{E_0} \tag{4.29}$$

To model an individual specimen, we measured the fraction of struts with damage through 0%, 25%, 50%, 75%, and 100% of the thickness in the two-dimensional thin sections of the specimens. The fraction of damaged struts per unit area corresponds to the fraction per unit volume. The fraction of undamaged struts can be determined by obtaining a value of the fraction of struts per unit volume for bovine tibial trabecular bone and subtracting the number of damaged struts per unit volume. Currently, the fraction of undamaged struts was estimated from images of the damaged sections with damaged marked. Measuring the number of connected rods or plates using stereological methods was difficult because the struts are not distinct.

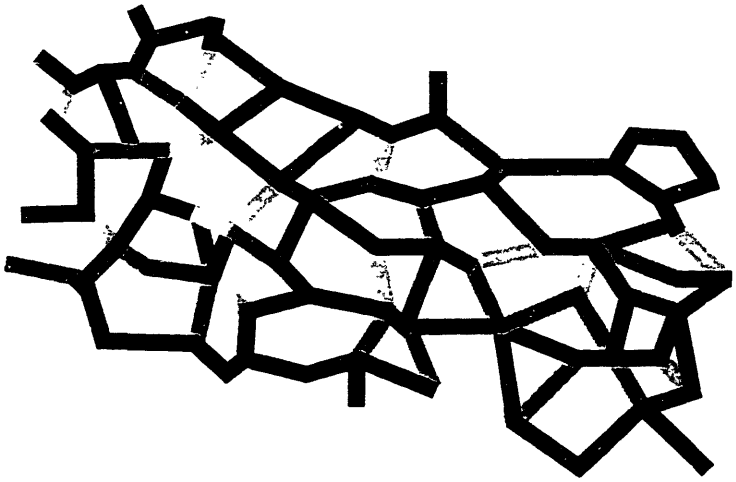

(a)

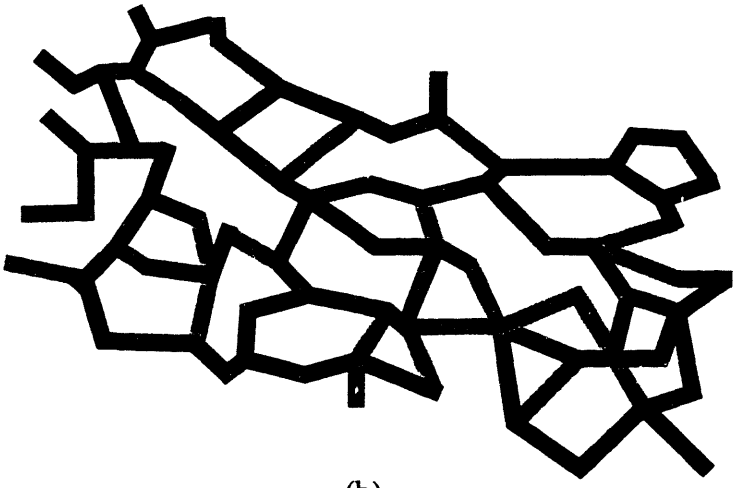

(b)

Figure 4.6: Trabeculae organized into a cellular solid network. (a) Entire network, showing trabeculae with no damage (black), trabeculae with partial damage (dark gray), and fractured trabeculae with a crack or cracks through the entire thickness (light gray). (b) Fractured trabeculae have been removed from the model. (c) Partially damaged trabeculae have been reduced in thickness. (d) The thickness reduction is averaged over all the remaining trabeculae, to give an average thickness of $\bar{t}$.

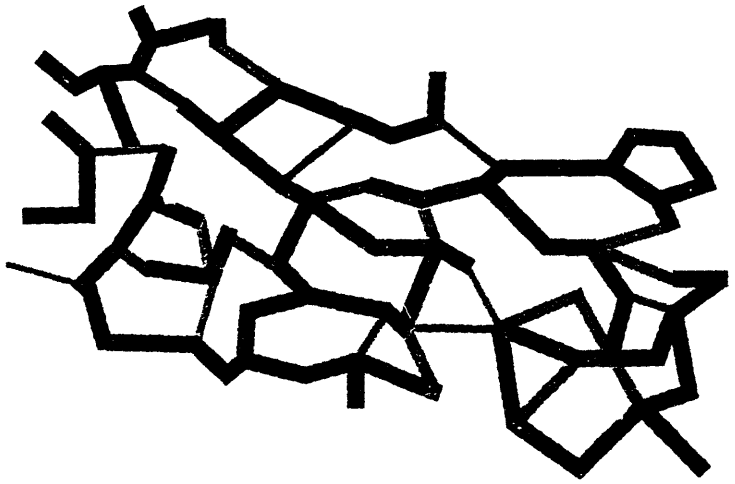

(c)

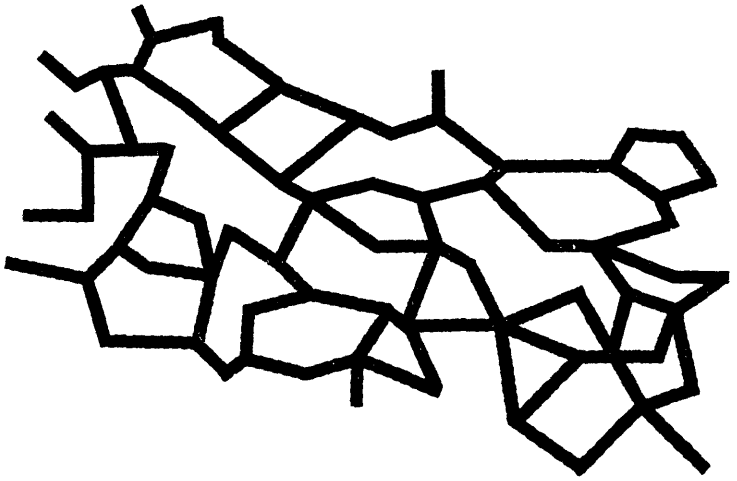

(d)

Figure 4.6: Trabeculae organized into a cellular solid network. (a) Entire network, showing trabeculae with no damage (black), trabeculae with partial damage (dark gray), and fractured trabeculae with a crack or cracks through the entire thickness (light gray). (b) Fractured trabeculae have been removed from the model. (c) Partially damaged trabeculae have been reduced in thickness. (d) The thickness reduction is averaged over all the remaining trabeculae, to give an average thickness of $\bar{t}$.

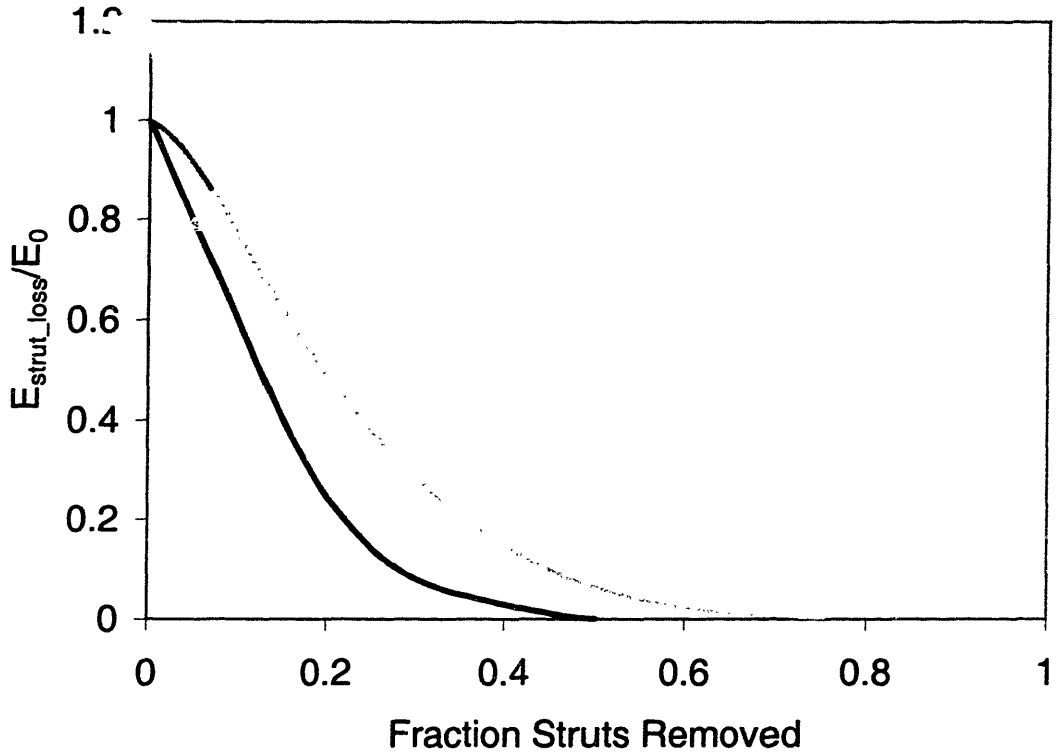

Figure 4.7: Plot of modulus reduction vs. density fraction reduction (Valhalla, private communication) for random removal of rod-like struts random open-cell cellular solid (black). An estimate for the modulus reduction for random removal of plate-like struts has also been included; the dashed portion of the line indicates the interpolation between the two limits (gray).

4.2.3 Specimen Level

Compression damage in trabecular bone, as in other cellular solids (Bart-Smith *et al.*, 1998; McCullough *et al.*, 1999; Bastawros *et al.*, 2000), occurs grossly in the form of localized damage bands. Initially, in cellular solids, damage occurs randomly with the weakest members (with the most vulnerable defects) failing first. Failure of the first few members produced local stress concentrations, making further strut failures more likely in the vicinity of the initial failures, and giving rise to a localized damaged band (Guo *et al.*, 1994; Bart-Smith *et al.*, 1998). Localized strut fractures, concentrated together as a result of this mechanism, reduce the modulus more than random strut fractures (Guo *et al.*, 1994; Yeh and Keaveny, 1999). We simulated this sequence of events by distributing damage, including fractures, randomly throughout the model at lower strains and concentrating the damage within a band at higher strains.

In trabecular bone, these bands were visible as large deformations in individual struts viewed using microcomputed tomography (micro-CT) (Mueller *et al.*, 1998; Tantillo, 1999) and as bright regions on thin histologic section after bulk fluorescent staining of a damaged specimen (**Figure 4.8a**). Our observations indicated that damage bands begin to form in bovine trabecular bone at compressive strains of -1.3% (Chapter 3). In this model, damage was distributed randomly at lower strains and concentrated within the damage band at higher strains. The damage band separated the specimen into two regions, with different moduli (**Figure 4.8b**). The damaged area of specimen, with length L_2, had a modulus E_2, as determined in the previous section. The remaining area, with initial modulus E_0, was of length $L_0 - L_2$, where L_0 is the gauge length of the extensometer used (5.0 mm). It was assumed that all damage occurred within the band, that the band extended across the specimen, and that all bone outside the band remained elastic.

We have estimated the length of the damage band from images of the entire section with the areas of damage marked on it. The localized region containing the damage was outlined, and the length of the localized region was measured at five (5) points parallel to the long axis of the specimen. The average lengths in each plane were

then averaged to obtain the average damage band length for the entire specimen, and the reduced modulus, E', was calculated as:

$$\frac{E'}{E_0} = \frac{1}{1 + \frac{L_2}{L_0}\left(\frac{E_0}{E_2} - 1\right)} \tag{4.30}$$

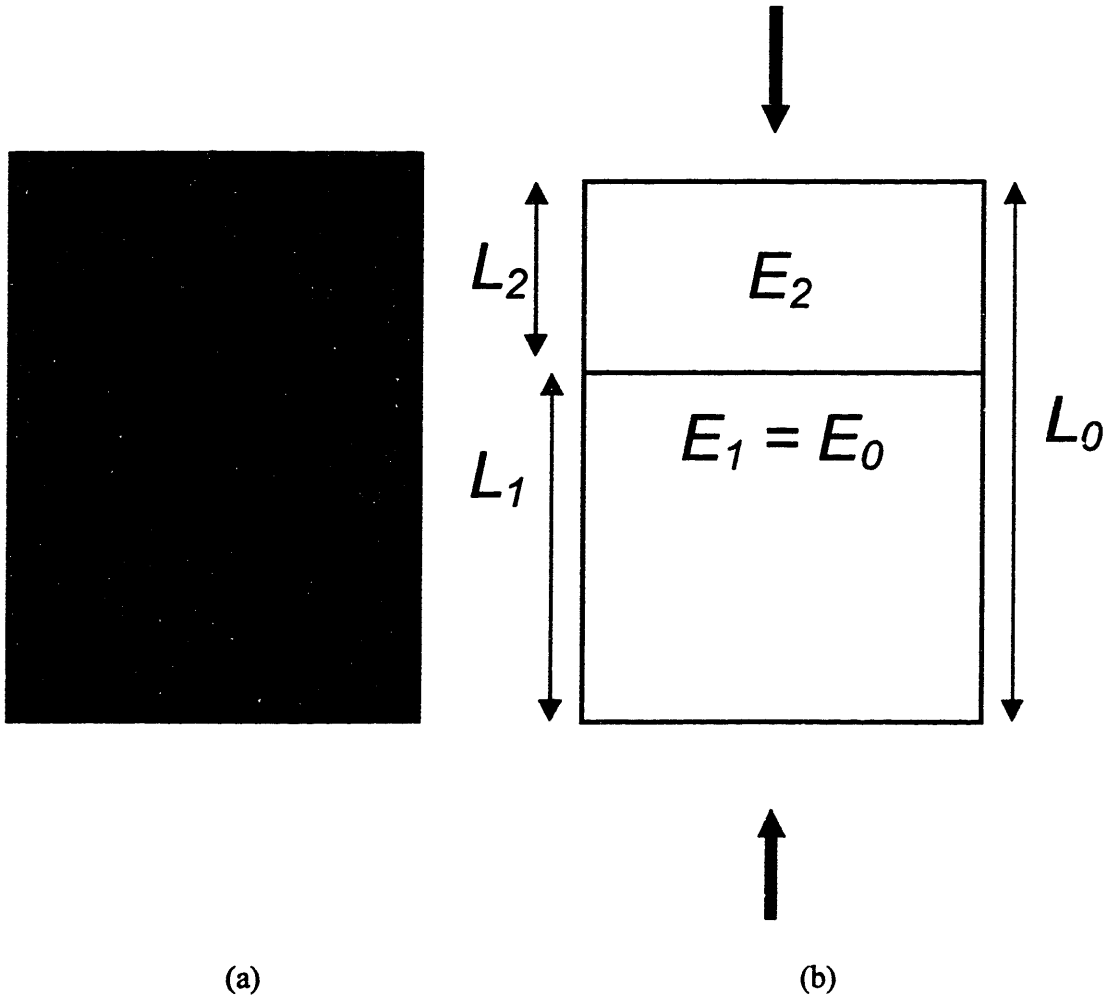

Figure 4.8: Damage within trabecular bone specimens is localized. (a) Image of a specimen tested to -4.0% compressive strain, stained after testing with calcein green. (b) Schematic representation of localized damage.

4.3 Comparison with Experiments

Previously, we tested 38 specimens in monotonic compression under strain control to maximum strains from 0.0% (untested) to ε_{max} = -4.0% (example, **Figure 4.9**). Experimental modulus reductions compared well with results reported in the literature (Keaveny *et al.*, 1994d). Microdamage parameters were analyzed for all specimens, and the data were applied to our model. The modulus reduction predicted by the model was compared to the modulus reduction determined using the secant modulus reduction for each specimen (**Figure 4.10**). There is a high correlation between the secant modulus, E_{sec}, and the reloading modulus, E_r, and the secant modulus has been used to estimate the reloading modulus in other studies (Keaveny *et al.*, 1994d, 1999). Values of the modulus reduction within the localized damaged area, E_2/E_0, varied widely between specimens (0.56 to 0.04 for plates, 0.42 to 0.01 for rods). Linear regressions for the rod model gave a slope of 1.129 ± 0.086 ($p < 0.001$, $R^2 = 0.83$), with an intercept of -0.159 ± 0.056 ($p < 0.005$); regressions for the plate model gave a slope of 0.995 ± 0.078 ($p < 0.001$, $R^2 = 0.82$) and an intercept of 0.010 ± 0.051 ($p = 0.84$). The concordance correlation was calculated for each model (rod $R_c^2 = 0.75$, plate $R_c^2 = 0.81$).

Microdamage was observed under UV epifluorescence in thin sections of bone that had been bulk stained in contrasting chelating fluorochromes before and after testing. Three stain combinations were used: oxytetracycline/xylenol orange ($n = 3$), oxytetracycline only ($n = 4$), and alizarin complexone/calcein ($n = 31$). When only specimens stained with the alizarin complexone/calcein combination were used in the analysis, the regressions improved (rod: $R^2 = 0.85$, $R_c^2 = 0.75$; plate: $R^2 = 0.85$, $R_c^2 = 0.84$).

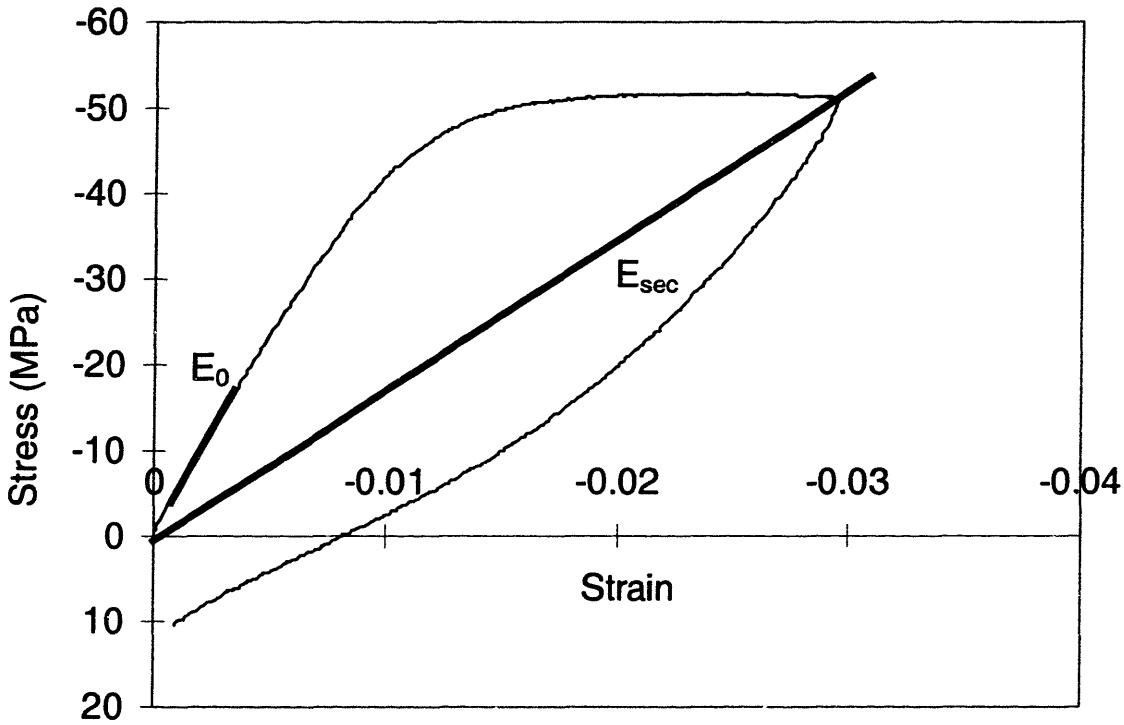

Figure 4.9: Typical stress-strain curve of a trabecular bone specimen, loaded to a strain of -3.0%, then unloaded to zero strain. Initial modulus, E_0, and secant modulus, E_{sec}, are shown.

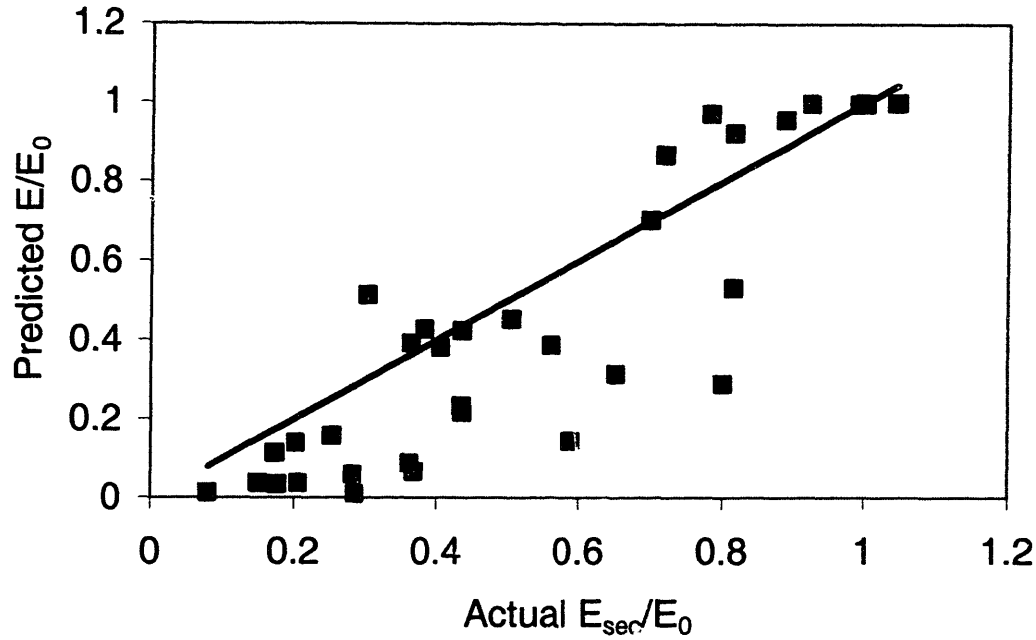

(a)

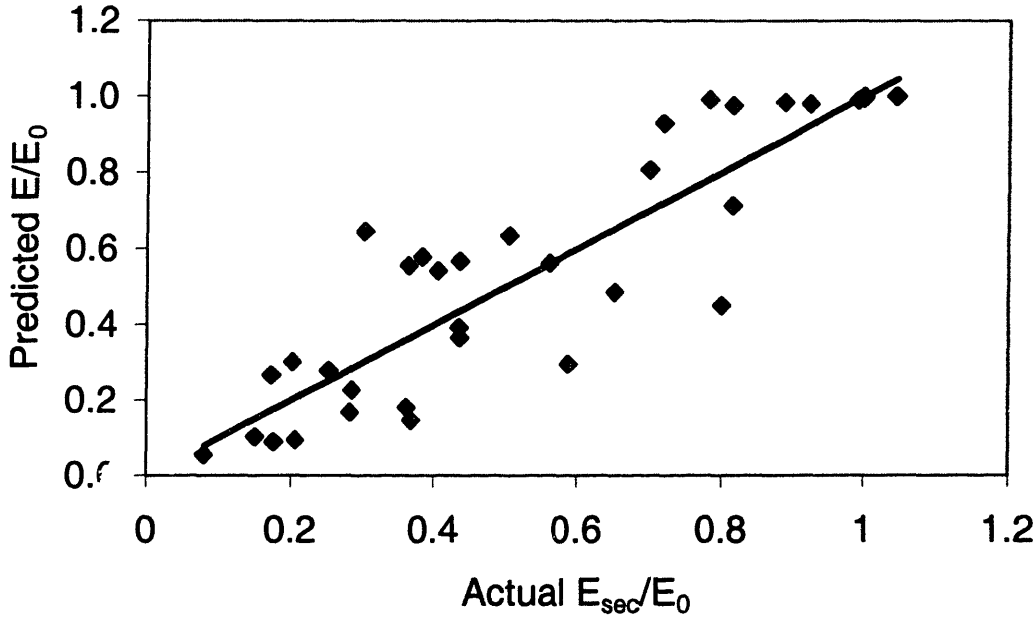

(b)

Figure 4.10: Comparison of model predictions with experimentally determined modulus loss. Experimental modulus loss is the secant modulus divided by the initial loading modulus. (a) Closed-cell model based on plate-like trabeculae ($Y = 0.995X + 0.01$, $R^2 = 0.82$, $R_c^2 = 0.81$. (b) Open-cell model based on rod-like trabeculae ($Y = 1.13X - 0.16$, $R^2 = 0.83$, $R_c^2 = 0.75$).

4.4 Parametric Study

A parametric study was performed to determine which variables have the greatest effect on the final value of modulus reduction. Variables tested included the total amount of damaged area, A_{total}, the length of the damage band, L_2, the depth of damage through the thickness, t_{damage}/t_0, the fraction of intact trabeculae, f_0, and the modulus reduction due to the removal of fractured trabeculae, E_{strut_loss}/E_0. These parameters were tested by varying one input parameter at a time and calculating the change in the overall modulus reduction, E'/E_0. The effect of distribution of damage between damage types (25%, 50%, 75%, or 100% depth through the thickness) and location (middle or end) was also calculated. This was tested by assigning all of the damage to a single type (e.g. all damage occurs in the middle and extends 50% of the depth through the thickness) and comparing that to the case where damage is evenly divided between the groups. For the rod model, the ratio of middle damage to end damage was also varied from the assumed ratio of 3:1. Damage location does not affect modulus reduction in the plate model, so no study was performed in this case.

The amount of variation in specimen modulus reduction depended on the specimen studied. In general, the closer the predicted specimen modulus reduction was to 1.0, the less variation was observed. The results presented here were calculated from data obtained from a specimen compressed to ε_{max} = -4.0%, with a modulus reduction of $0.176E_0$, and a specimen compressed to ε_{max} = -1.1% strain, with a modulus reduction of $0.886E_0$. Other specimens showed similar responses to changes in input parameters.

Both the open- and closed-cell models were most sensitive to changes in the modulus caused by the removal of struts (**Figure 4.11a**). The reduced modulus for an open-cell rod model was based on finite element studies (Vajjhala *et al.*, 2000); however, no studies exist of the effects of random plate removal on modulus. The values we used have been interpolated between known end points and may contain some error. There was an approximate one-to-one correspondence between changes in the input parameter and changes in the specimen reduced modulus, E'/E_0. For example, a ten percent decrease in the modulus loss due to strut removal results in a reduction of E'/E_0 by slightly less than ten percent. Similar results were observed for changes in the damage band length (**Figure 4.11b**); here, the closed-cell model was more sensitive than the

open-cell model. The damage band length was relatively straightforward to measure when the band was distinct at high compressive strains but was quite difficult to measure while the band was forming.

The reduced modulus was less sensitive to variations in the amount of damaged area, A_{total}, (**Figure 4.11c**), and to variations in the depth through the thickness, t_{damage}/t_0 (**Figure 4.11d**). In both cases, the open-cell model was more sensitive to variations in the input parameter than the closed-cell model. For example, a change in the amount of damaged area by ten percent changed E'/E_0 by about five percent for the open-cell model and less than 1.5% for the closed-cell model. Both models were relatively insensitive to changes in the fraction of undamaged struts, f_0 (**Figure 4.11e**); a change in this input parameter of ten percent varied E'/E_0 by two percent in the open-cell model and less than one percent in the closed-cell model. The open-cell model was quite insensitive to changes in the ratio of damage location (**Figure 4.11f**). As mentioned before, the closed-cell model did not use damage location as an input variable. Varying the ratio from 9:1 to 3:2 produced a change in E'/E_0 of less than four percent from the original E'/E_0 calculated using a ratio of 3:1.

The open-cell model was more sensitive to the distribution of damaged areas throughout the various depths through the thickness and damage locations than the closed-cell model. As mentioned earlier, the closed-cell model was not sensitive to the damage location. Both observations were consistent with deformation of the rod model by bending and that of the closed-cell model by stretching. In the open-cell model, the maximum modulus reduction occurred when damage was spread evenly between the different types of damage. Conversely, the minimum modulus reduction occurred when all the damaged area was concentrated in the fractured struts (**Figure 4.12a**). In the closed-cell model, the minimum reduced modulus occurred when all damage was assumed to concentrate in the fractured struts, but the maximum reduced modulus did not necessarily occur in the evenly distributed case (**Figure 4.12b**).

We also evaluated the relative contributions of fractured struts, E_{strut_loss}/E_0, and damaged struts, E_{damage}/E_0, to the modulus reduction in the localized band, E_2/E_0, for the open- and closed-cell models (**Table 4.1**). No microdamage accumulation or change in modulus was observed at strains below -1.1%, before yielding. After yield, the fraction

of fractured and damaged members increased, with corresponding decreases in E_{strut_loss}/E_0 and E_{damage}/E_0. The fraction of fractured members remained approximately constant after -2.0% strain. The value of E_{strut_loss}/E_0 reached a plateau about -2.0%, then decreased dramatically at ε_{max} = -4.0%. These plateaus approximately corresponded to the plateau in the stress-strain curve near the ultimate stress. E_{strut_loss}/E_0 was smaller in the open-cell model, and the differences between open- and closed-cell models increased with increasing strain.

The modulus change due to damaged members also increased with increasing maximum strain (**Table 4.1**). Modulus changes due to damaged trabeculae in the closed-cell model were about 15% in the worst case and average about 10% in post-yield specimens. However, modulus losses due to damaged trabeculae were considerable in the open-cell model, reducing the overall modulus by up to 40%. For example, at -2.0% strain, the modulus reduction for the closed-cell model due to fractured trabeculae, E_{strut_loss}/E_0, was 0.32 and the loss due to damaged trabeculae, E_{damage}/E_0, was 0.92, leading to an overall modulus reduction in the damaged region, E_2/E_0, of 0.29. We concluded that the modulus reduction due to fractured struts, E_{strut_loss}/E_0, was the major contributor to local overall modulus reduction, E_2/E_0, in both the open- and closed-cell models, and that the modulus reduction due to other types of damage, E_{damage}/E_0, was a significant contributor to E_2/E_0 only in the open-cell model.

ε_{max} (%)	Broken Struts			Damaged Struts		
	Average Fraction	E_{strut_loss}/E_0		Average Fraction	E_{damage}/E_0	
		Open-cell	Closed-cell		Open-cell	Closed-cell
0.0	0	1.00 (0)	1.00 (0)	0.01 (0)	1.00 (0)	1.00 (0)
-0.4	0	1.00 (0)	1.00 (0)	0.01 (0)	1.00 (0)	1.00 (0)
-0.8	0.004 (0.001)	1.00 (0)	0.99 (0.01)	0.006 (0.001)	1.00 (0)	1.00 (0)
-1.1	0.099 (0.043)	0.60 (0.17)	0.75 (0.18)	0.301 (0.189)	0.89 (0.08)	0.95 (0.03)
-1.3	0.199 (0.126)	0.33 (0.38)	0.41 (0.35)	0.194 (0.148)	0.84 (0.15)	0.94 (0.06)
-2.0	0.232 (0.083)	0.22 (0.15)	0.32 (0.19)	0.269 (0.047)	0.78 (0.09)	0.92 (0.03)
-2.5	0.215 (0.068)	0.24 (0.12)	0.34 (0.14)	0.430 (0.091)	0.77 (0.13)	0.91 (0.05)
-3.0	0.224 (0.056)	0.21 (0.13)	0.31 (0.14)	0.404 (0.084)	0.67 (0.15)	0.87 (0.07)
-4.0	0.291 (0.072)	0.08 (0.07)	0.18 (0.09)	0.309 (0.071)	0.59 (0.20)	0.83 (0.09)

Table 4.1: Comparison of components contributing to modulus reduction in the localized damaged region. The overall modulus reduction, E_2/E_0, is the product of modulus loss due to strut loss, E_{strut_loss}/E_0, and the modulus loss due to damage, E_{damage}/E_0. Values are shown for both open- and closed-cell models. All values decrease with increasing strain. E_{strut_loss}/E_0 has a greater effect on E_2/E_0 for both models, with E_{damage}/E_0 having only a minor effect in the closed-cell model.

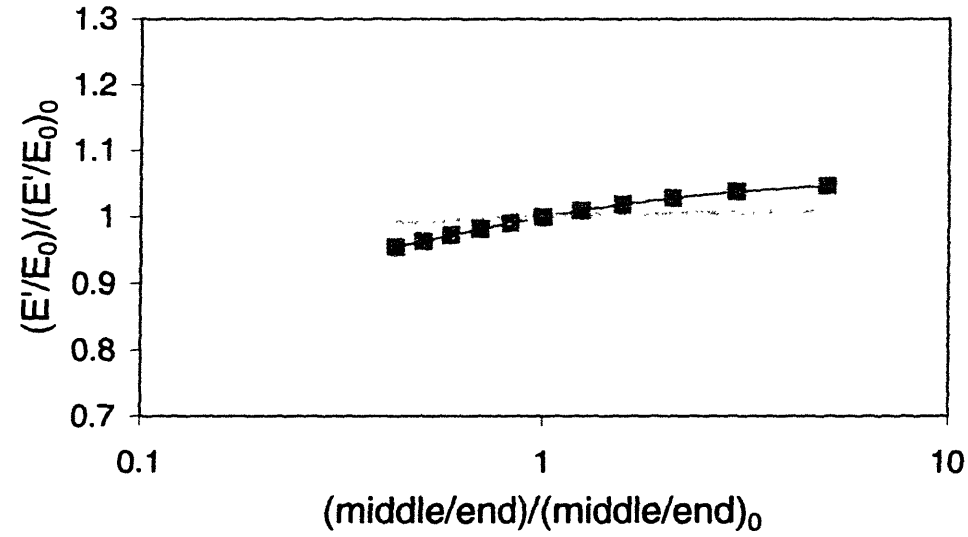

(a)

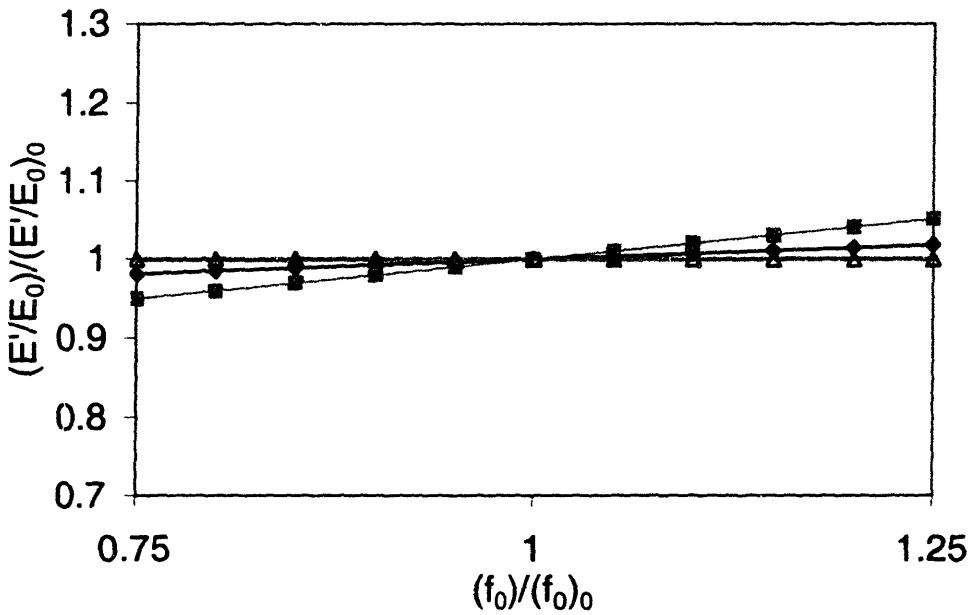

(b)

Figure 4.11: Effects of changes in input variables on the specimen reduced modulus. Closed symbols represent a specimen tested to -4.0% strain, with considerable damage. Black diamonds represent the closed-cell model (plate); gray squares represent the open-cell model (rod). The other symbols represent a specimen tested to -1.1% strain, with little damage. The open triangles represent the closed-cell (plate model), while the solid gray line represents the open-cell (rod) model. Input parameters varied include (a) reduced modulus due to removal of fractured struts, E_{strut_loss}/E_0, (b) width of the localized damage band, (c) total damaged area in the specimen, A_{total}, (d) estimate of depth of damage through the thickness, t_{damage}/t_0, (e) fraction of undamaged struts, f_0, and (f) ratio of middle damage to end damage, plotted on a log scale.

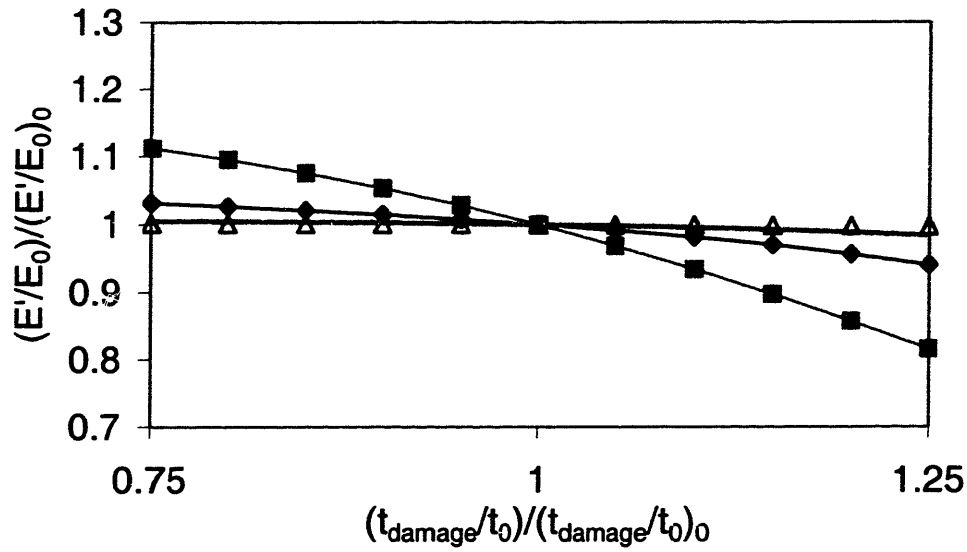

(c)

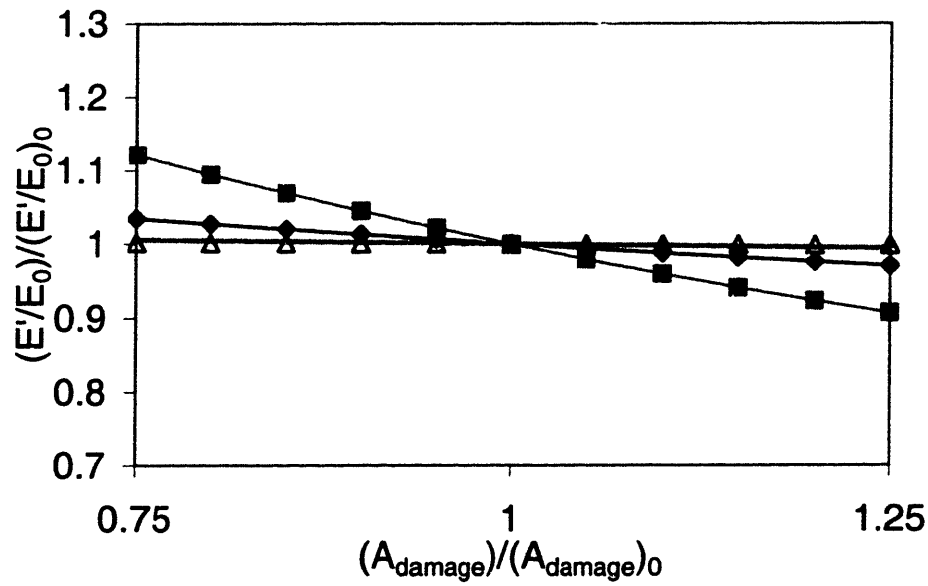

(d)

Figure 4.11: Effects of changes in input variables on the specimen reduced modulus. Closed symbols represent a specimen tested to -4.0% strain, with considerable damage. Black diamonds represent the closed-cell model (plate); gray squares represent the open-cell model (rod). The other symbols represent a specimen tested to -1.1% strain, with little damage. The open triangles represent the closed-cell (plate model), while the solid gray line represents the open-cell (rod) model. Input parameters varied include (a) reduced modulus due to removal of fractured struts, E_{strut_loss}/E_0, (b) width of the localized damage band, (c) total damaged area in the specimen, A_{total}, (d) estimate of depth of damage through the thickness, t_{damage}/t_0, (e) fraction of undamaged struts, f_0, and (f) ratio of middle damage to end damage, plotted on a log scale.

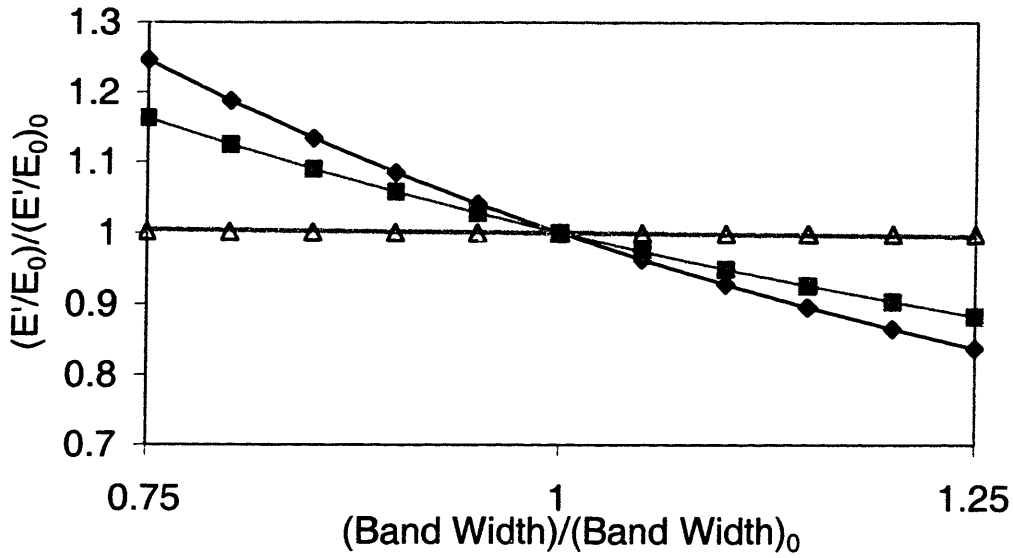

(e)

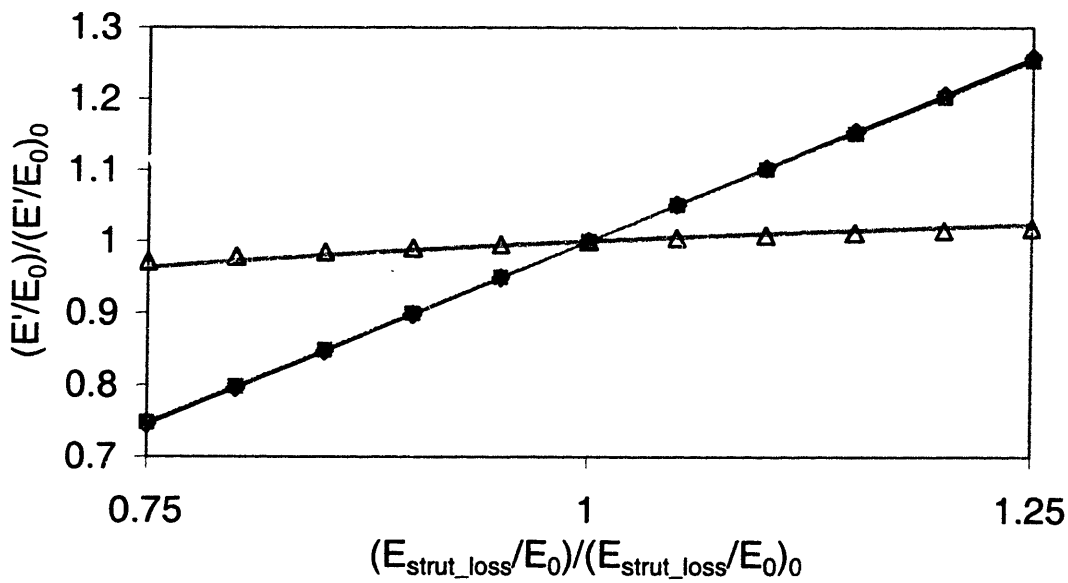

(f)

Figure 4.11: Effects of changes in input variables on the specimen reduced modulus. Closed symbols represent a specimen tested to -4.0% strain, with considerable damage. Black diamonds represent the closed-cell model (plate); gray squares represent the open-cell model (rod). The other symbols represent a specimen tested to -1.1% strain, with little damage. The open triangles represent the closed-cell (plate model), while the solid gray line represents the open-cell (rod) model. Input parameters varied include (a) reduced modulus due to removal of fractured struts, E_{strut_loss}/E_0, (b) width of the localized damage band, (c) total damaged area in the specimen, A_{total}, (d) estimate of depth of damage through the thickness, t_{damage}/t_0, (e) fraction of undamaged struts, f_0, and (f) ratio of middle damage to end damage, plotted on a log scale.

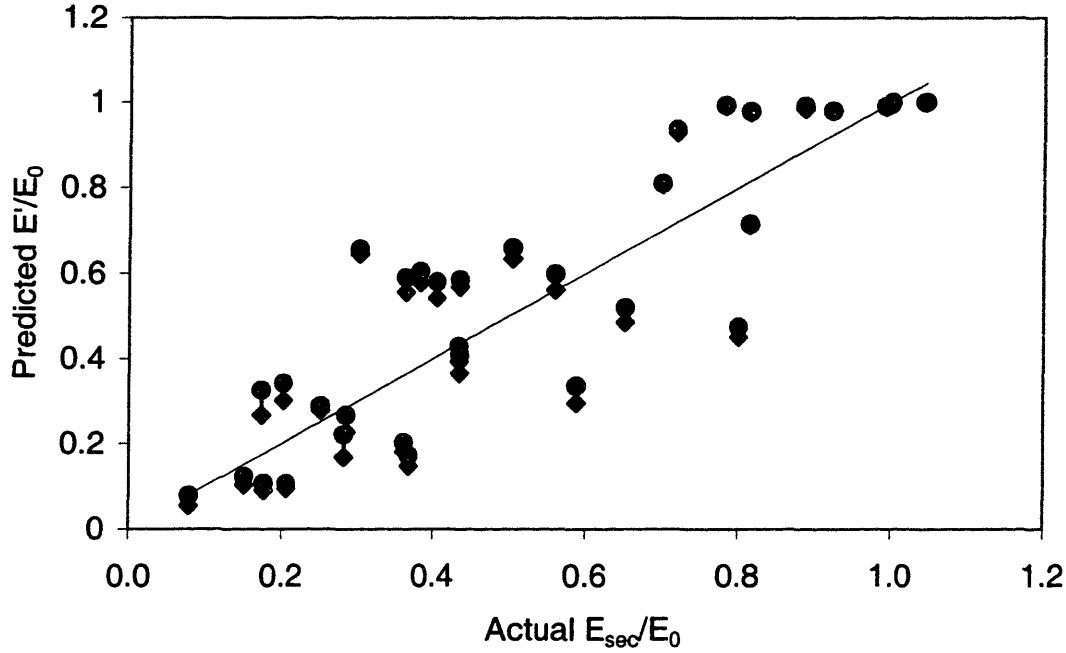

(a)

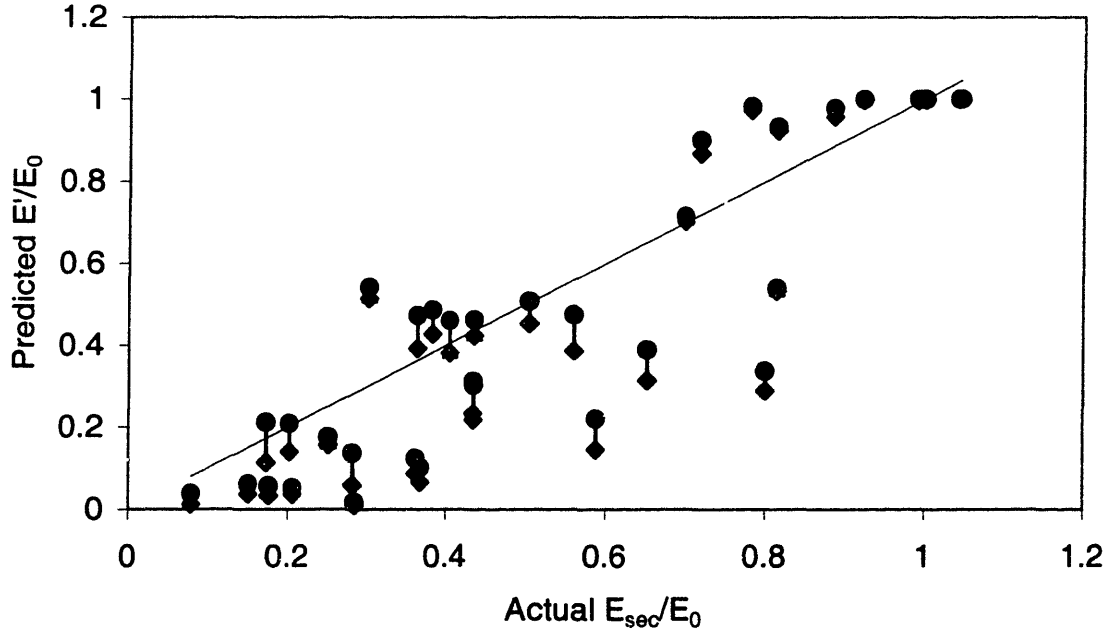

(b)

Figure 4.12: Effects of changing the distribution of damage on predicted modulus reduction. Black diamonds represent an even distribution of areas; black circles represent damage concentrated in fractured struts (no partial damage). The error bars represent the range of created by different distributions. (a) Open-cell model. (b) Closed-cell model.

4.5 Discussion

This study used an analytical model to predict the expected reduced modulus of a specimen of bovine trabecular bone based on observations of the microdamage and compared the predicted value to the experimentally measured secant modulus. The model explained the progression of microdamage accumulation based on mechanistic models. In general, the predictions agreed well with the measured values.

Two models were developed: an open-cell model (a rod-like structure) and a closed-cell model (with a plate-like structure). Bovine trabecular bone from the proximal tibiae is mostly a closed-cell structure, so, as expected, the closed-cell model performed better than the open-cell model. However, trabecular bone structure varies widely between species and anatomic locations, generally containing rod-like and plate-like elements. Developing both models will allow us to extend our work to other types of trabecular bone. Also, the rod and plate models can be combined to better represent trabecular bone structures that lie somewhere between the two extremes.

The model presented here represents a descriptive model, based on observations of microdamage after testing. In this model, the calculated reduced modulus is not a unique solution to a particular set of microdamage parameters, so this model cannot be used as a predictive one. There were approximately linear relationships between different microdamage parameters, but accurately predicting the sequence of microdamage accumulation in trabecular bone is beyond the scope of this work.

This model was much more effective at predicting reduced modulus due to damage accumulation at larger reduced modulus than at smaller reduced modulus. The model assumed that no changes in mechanical properties occurred without corresponding microdamage accumulation. Wide ranges in the modulus predictions occurred at strains near yielding when damage was present, but a distinct band had not formed. These small amounts of damage were distributed in three different ways: as randomly occurring damage, as a band extending part of the way across the specimen, or as a band extending across the specimen. Different distributions affected the modulus prediction. In this study, the case of the band extending across the entire specimen was used, since that case resulted in the greatest modulus reduction and was thus the worst case scenario.

When the damage band formed, it formed in the region surrounding the first instances of damage. In metallic foams, defects such as voids or kinking in the cell walls were identified in the cell structure that predispose that cell to collapse (Bart-Smith *et al.*, 1998; McCullough *et al.*, 1999b). No such defects have been definitively identified in trabecular bone, although it has been suggested that osteocytic lacunae may be stress concentrators points and therefore act as crack initiation sites (Reilly, 2000).

There are a number of limitations associated with the assumptions of the model. We assumed that the Young's modulus of trabecular bone was relatively insensitive to the distribution of trabecular thickness. Models indicate that this was more accurate for closed-cell cellular materials, with plate-like members (Grenestedt and Bassinet, 2000), than for open-cell materials, with rod-like members (Yeh and Keaveny, 1999). This assumption is probably more appropriate for high density trabecular bone such as the bovine bone used in this study than it would be for low density, osteoporotic human bone. Modification of the model to account for the effect of the distribution of trabecular thickness would be necessary to more closely model, open-cell, rod-like, low density trabecular bone.

The model predicted the new reloading modulus in a specimen that had damage present. However, the experimentally measured modulus was the secant modulus, which was related to, but not equal to, the reloading modulus (Keaveny *et al.*, 1994d, 1999). When we converted our measured secant modulus to a reloading modulus using the relationship $E_{sec} = 0.92E_r + 69.2$ (modulus in MPa) obtained for the same specimen geometry (Keaveny *et al.*, 1999), the slope of the regression line decreased by approximately six percent in both the open-cell and closed-cell case, and the correlation coefficients changed by less than one percent.

This model is isotropic; trabecular bone is known to be anisotropic (Turner *et al.*, 1990), and the amount of anisotropy depends on species and anatomic location. The degree of anisotropy for bovine proximal tibia has been measured at 1.42 ± 0.16 (Oden *et al.*, 1998). An isotropic structure was used here as an initial approach to relate changes in mechanical properties to microdamage accumulation.

The model developed here has been used to predict a modulus reduction based on measured microdamage parameters. The predictions agreed well with experimentally

measured modulus reductions in bovine trabecular bone. This model provided an initial step towards understanding the role of microdamage accumulation in stiffness degradation of trabecular bone.

Chapter 5: Fatigue Microdamage of Trabecular Bone

Abstract

Microdamage accumulation occurs when bones are loaded in fatigue during the repetitive motions of day-to-day activities. Specimens of bovine trabecular bone were mechanically tested in fatigue to one of four load levels and stopped at one of six maximum strains. The reloading modulus and secant modulus decreased and residual strains increased with increasing maximum compressive strain. The tested specimens were sectioned and examined histologically for microdamage. All microdamage parameters increased with increasing specimen strain at strains above a minimum threshold of approximately -0.5%. The progression of damage during loading was similar to that described for specimens loaded in uniaxial compression. Increases in the number of cycles resulted in an increase in the proportion of parallel cracks and trabecular fractures in the specimen. Trabecular fractures were seen at relatively low strains (-1.1%), compared to specimens tested in uniaxial compression. The cellular solid model developed to predict changes in modulus based on observed microdamage was applied to specimens tested in fatigue; the model did not predict modulus reductions as well in fatigue-tested specimens as it did for monotonic compression-tested specimens.

5.1 Introduction

Bones are loaded in fatigue as a result of the repetitive activities of daily life. Fatigue loading may result in the creation of microdamage, seen as small cracks in the bone. Usually microdamage is repaired by the bone remodeling process, and few microcracks are present *in vivo*. If it is not repaired, microdamage may accumulate, reducing bone stiffness. Eventually, microdamage accumulation and coalescence may lead to a stress fracture or a fragility fracture (Daffner and Pavlov, 1992; Burr *et al.*, 1997).

The fatigue behavior of bone has been characterized in cortical (Carter and Hayes, 1976, 1977a, b; Pattin *et al.*, 1996; Zioupos *et al.*, 1996a, 1996b) and trabecular bone

(Guo *et al.*, 1994; Cheng, 1995; Haddock *et al.*, 2000). Fatigue damage in cortical and trabecular bone is characterized by decreasing modulus throughout the test, with rapid modulus reductions near failure, and increasing plastic strain. Plastic strain development is similar to that seen during creep of engineering materials, with a primary, secondary, and tertiary regime (Bowman *et al.*, 1998). Bovine trabecular bone specimens tested in fatigue showed different slopes of the S-N curve for specimens tested in low cycle fatigue and high cycle fatigue (Guo, 1993; Cheng, 1995), using a cutoff of 3000 cycles between high and low cycle fatigue (Appendix B, **Figure 5.1**). Fatigue of bone has been modeled as a combination of cycle-dependent (fatigue) damage, consisting of modulus reduction, and time-dependent (creep) damage, consisting of increasing plastic strain (Carter and Caler, 1983, 1985; Caler and Carter, 1989; Bowman *et al.*, 1998).

Microdamage is observed by histologic examination of thin sections of bone that has been bulk stained to label microdamage. Brightfield observation of sections stained with basic fuchsin has been the method of choice (Burr and Stafford, 1990). Recently, new staining methods using chelating fluorochromes have been developed (Lee *et al.*, 2000). The chelating fluorochromes are site-specific, attaching to exposed calcium. They can be used sequentially to determine when the damage was created. For example, staining after specimen preparation but before testing will label all pre-existing microdamage that was present *in vivo* or created during specimen preparation.

Microdamage occurs naturally in bones that were loaded in fatigue (Frost, 1960; Nunamaker *et al.*, 1990; Muir *et al.*, 1999) and has also been observed in bones with artificial *in vivo* loading (Burr *et al.*, 1985; Mori and Burr, 1993; Bentolila *et al.*, 1998). Fatigue microdamage is thought to initiate bone remodeling (Burr *et al.*, 1985; Mori and Burr, 1993; Bentolila *et al.*, 1998; Verborgt *et al.*, 2000). Microdamage is not observed prior to specimen yield (Zioupos *et al.*, 1994), and after yield, microdamage accumulation leads to stiffness and strength losses (Forwood and Parker, 1989; Hoshaw *et al.*, 1997). Burr *et al.* (1998) found an approximately quadratic relationship between crack density and stiffness loss and a linear relationship between damaged area and stiffness loss in whole canine femora tested in bending fatigue. Microcracks were observed to accumulate during the initial portion of fatigue testing, then remained

constant prior to increasing again before failure (O'Brien, 2001). To our knowledge, no examination of microdamage in trabecular bone in fatigue has been performed.

Models have been developed to explain the relationship between mechanical properties, in the form of modulus reduction, and microcrack growth. Taylor (1998b) has developed a model to predict microcrack growth in cortical bone during fatigue using a fracture mechanics approach based on measured stiffness variation. Guo *et al.* (1994) modeled trabecular bone modulus reduction and failure due to growth of pre-existing microcracks using finite element models.

Microdamage has been characterized in bovine trabecular bone tested in uniaxial compression (Chapter 4; Wachtel and Keaveny, 1997) and compressive creep (Pierce, 1999). In these studies, specimens were loaded to a predetermined compressive strain, and various microdamage parameters were determined histologically and compared to mechanical properties (e.g. maximum strain, ε_{max}, and modulus reduction, E_r/E_0 or E_{sec}/E_0). Microdamage did not begin to accumulate until the specimen had exceeded the yield strain; after yield, microdamage increased with increasing specimen strain.

Martin (1992) developed a theory of damage repair in cortical bone which postulated that the amount of damage was related to the applied stress and the number of cycles, specifically

$$D = k\sigma^q N \tag{5.1}$$

where D is a measure of damage, in this case the total length of cracks, k is a damage rate coefficient, σ is applied stress, q is the exponent of the stress term, and N is number of cycles. Higher stresses are associated with greater strain rates (in a constant frequency series of tests), and damage formation increases with increased stress during fatigue of cortical bone (Schaffler *et al.*, 1989). If trabecular bone microdamage accumulates according to this relationship, then damage is expected to increase with increasing stress levels and increasing numbers of cycles.

Also, specimens loaded in fatigue have the potential for crack growth in all cycles beyond the first cycle, as well as the potential for crack initiation in all cycles. It was hypothesized that specimens loaded for greater numbers of cycles would have more or different microdamage (for example, greater crack lengths and a larger damaged area fraction) than specimens loaded to the same modulus reduction for fewer cycles.

In our previous study (Chapter 3), the progression of microdamage accumulation with increasing specimen strain was determined for bovine trabecular bone tested in uniaxial compression. We found that little to no microdamage was present initially, and few cracks were created prior to the yield strain. After yield, cracks formed in isolated trabeculae. The load from the damaged trabeculae was redistributed within a localized area, which was more likely to become damaged. The local region of damage expanded and coalesced with other regions to form a band extending across the trabeculae. A distinct band was usually visible by a strain of -2.0%. The size of the damaged band then increased until it approached the specimen gauge length. After that, the density of the damage within the band increased. As damage increased and during band formation, individual trabeculae began to fracture completely. When all trabeculae across the specimen were fractured, the specimen had broken.

This study observed the mechanical behavior of bovine trabecular bone in fatigue, related microdamage accumulation with changes in mechanical properties, and determined the progression of microdamage accumulation in fatigue in a similar manner to our earlier study (Chapter 3). The effects of changes in load levels, maximum strain reached, and number of cycles were studied, and the model developed to relate modulus reductions to microdamage observations was applied to the fatigue-tested specimens. Specifically, we asked the following research questions: (1) How does microdamage accumulate in bovine trabecular bone tested in fatigue; and (2) How is microdamage accumulation in fatigue affected by changes in load levels, maximum compressive strain, and number of cycles; and (3) Can the cellular solid model developed to predict changes in modulus based on observed microdamage be applied to specimens of bovine trabecular bone tested in compressive fatigue?

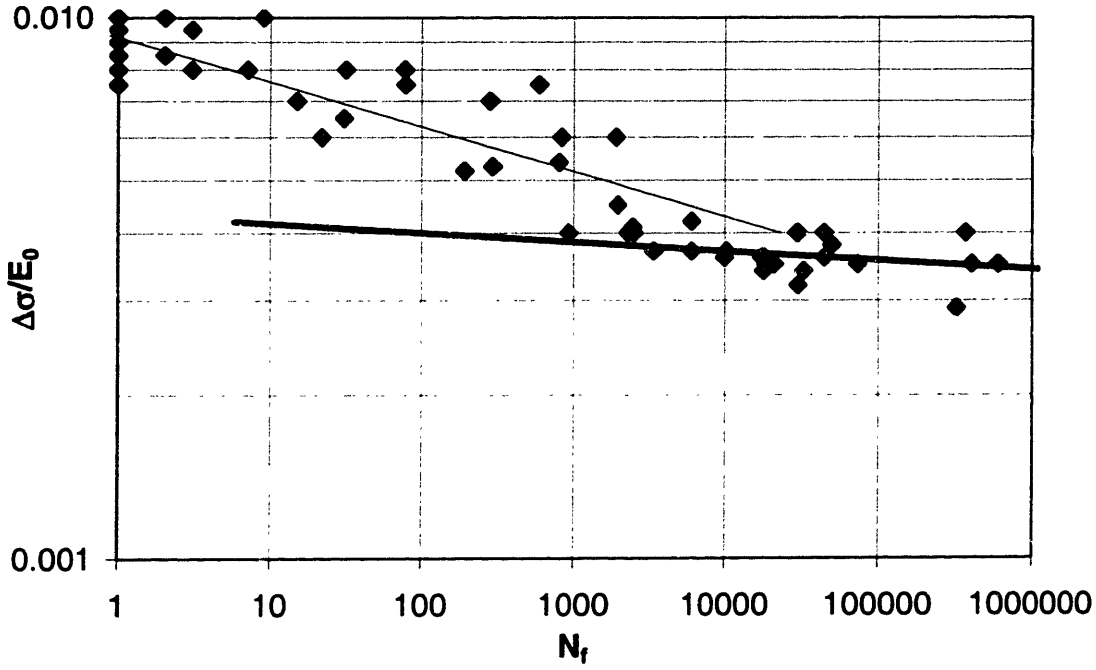

Figure 5.1: S-N curve for 61 waisted cylindrical specimens of bovine trabecular bone tested in compression (Appendix B). An endurance limit is seen at a normalized stress of $\Delta\sigma/E_0 \approx 0.0035$. The cut off between high and low cycle fatigue occurs at approximately 3000 cycles. Regressions for high and low cycle fatigue (Appendix B) are shown.

5.2 Materials and Methods

Trabecular bone specimens were damaged by compressive fatigue loading to various stress levels, with tests stopped at various maximum strains. All testing was performed using specimens of bovine trabecular bone taken from the proximal tibia (**Figure 5.2**), using specimens based on the design of Keaveny *et al.* (1997). Aligned sections of trabecular bone were identified on contact radiographs of sagittal slices of the bovine proximal tibia. 6.27 mm diameter cores were taken from the aligned regions using a diamond-tipped coring tool (Starlite, Rosemont PA). The cores were press-fit into brass end caps and glued in place using cyanoacrylate glue (910 Metal Bonding Adhesive, Permabond, Englewood NJ). Specimens were kept moist during all steps of specimen preparation and were kept frozen at -20°C between steps. The resulting specimens have a gauge diameter of 6.27 mm, and a length of approximately 9 mm between the end caps (**Figure 5.2**).

Before testing, the marrow was removed from the gauge length with a high pressure water jet and specimens were stained overnight at atmospheric pressure in 0.03% alizarin complexone to identify damage created *in vivo* and during specimen preparation (Chapter 2; Lee *et al.*, 2000). After staining, the specimens were rinsed well with distilled water. Specimen diameter was measured six (6) times with a digital calipers (Model 500-531, Mitutoyo Corp., Japan), and the average diameter and cross-sectional area was determined.

The specimen, was placed between a rigid upper platen and a self-aligning lower platen (**Figure 5.2**), in a servo-hydraulic testing machine (Instron 1321 with 8500 Plus controller, Instron Corp., Canton MA). A 0.5-inch (12.7 mm) extensometer (Instron 2620-826, Instron Corp., Canton MA) was attached to the end caps using elastic bands. A small compressive pre-load (< 50 N) was placed on the specimen to ensure contact between the platens. All testing was performed at room temperature, and specimens were kept moist with physiologic saline (0.9% NaCl) throughout testing. Prior to fatigue testing, the specimen was preconditioned by loading for ten cycles in strain control using a sinusoidal waveform from 0.0% strain to -0.3% strain at 2.0 Hz. The initial modulus,

E_0, was measured by taking the slope of the best linear fit of the tenth loading cycles from -0.1% to -0.3% strain. The preconditioning strain level is well below both the yield strain (approximately -0.7%) and the endurance limit (approximately -0.35%, see Appendix B) and was not expected to create damage in the specimen (Keaveny *et al.*, 1993c).

Fatigue tests were performed under load control at 2.0 Hz. Specimens were loaded from a nominal compressive preload (~ -50 N) to a predetermined load corresponding to one of four normalized stress levels, $\Delta\sigma/E_0$. When the specimen reached a predetermined maximum compressive strain, ε_{max}, the specimen was unloaded and the test was stopped (**Figure 5.3**). Maximum compressive strain was chosen as a stopping point as it was previously found to more closely correspond with the modulus reduction than the other possibility, which was N, the number of cycles (Appendix B; **Figure 5.4a**). Specimens were loaded to various combinations of four normalized stresses, $\Delta\sigma/E_0$, and six maximum strains (**Table 5.1**). Normalized stress was used to reduce the scatter in results based on large differences in specimen initial modulus. The normalized stresses chosen cover a range of expected numbers of cycles to failure, from less than ten cycles to failure ($\Delta\sigma/E_0$ = 0.008) to normalized stresses of $\Delta\sigma/E_0$ = 0.005, near the endurance limit of about $\Delta\sigma/E_0$ = 0.004 (Appendix B; Seireg and Kempke, 1969; Pattin *et al.*, 1996).

$\Delta\sigma/E_0$	ε = -0.8%	ε = -1.1%	ε = -1.3%	ε = -1.65%	ε = -2.0%	ε = -2.5%
0.008			5	5	5	5
0.007			5	5	5	5
0.006	5	5	5	5	5	5
0.005	5	5	5	5	5	5

Table 5.1: Combinations of normalized stress, $\Delta\sigma/E_0$, and maximum strain, ε_{max}, tested. Specimens loaded to the two highest normalized stress levels were not tested to the two lowest strains because the high load levels would cause the maximum strains to be exceeded within one cycle.

Five specimens were loaded to each combination of stress and maximum compressive strain (**Table 5.1**). Ten control specimens were also used: five control specimens were not tested, and five were preconditioned to measure the initial modulus,

but were not loaded in fatigue. The second set of control specimens were tested to ensure that the preconditioning protocol does not create damage in the specimens. The number of cycles, N, changes in plastic strain during a single cycle, $\Delta\varepsilon_{pl}$, secant modulus of the final cycle, E_{sec}, maximum strain, ε_{max}, and residual strain on unloading, ε_{res}, were measured for each specimen (**Figure 5.3**).

After testing, the specimen was loaded in strain control for one sinusoidal cycle in strain control from 0.0% to -0.3% strain at 2.0 Hz, and the reloading modulus, E_r, was measured as the slope of the loading curve between -0.1% and -0.3%. The specimen was removed from the testing machine, the bone section between the end caps was cut out with a diamond saw (Isomet Low Speed Saw, Buehler, Lake Bluff IL), and bone marrow at the cut ends was removed with a water jet. The specimen was stained overnight in 0.09% calcein green stain to label microdamage created during testing. The specimen was supported during removal of the gauge length to prevent further damage to the specimen. Specimens were dehydrated in a series of ethanol/water baths, embedded in transparent poly (methyl methacrylate), and cut into thin longitudinal sections (100 - 150 μm) on a diamond saw (Isomet Low Speed Saw, Buehler, Lake Bluff IL). The sections were mounted on microscope slides with Eukitt's mounting medium (Electron Microscopy Sciences, Fort Washington PA) and covered with glass cover slips.

Slide area was measured using digital images of the section taken through a dissecting microscope (Optronics Engineering, DEI-750, Goleta CA; Snappy 1.0, Play Incorporated, Rancho Cordova CA). The section area was measured and the bone area fraction was determined using thresholding techniques and used to calculate bone area fraction (ImageTool 1.25, UTHSCSA, San Antonio TX).

Slides were observed under ultraviolet epifluorescence with an excitation wavelength of 365 nm. Several microdamage parameters were measured in each specimen (Chapter 3). The size of the localized damage area was measured by stereological point counting or, if a distinct band existed, as the average of five measurements across an image of each section with the damage marked. The measurement was normalized by the total section area to account for changes in specimen length. The number of damaged trabeculae, including the pattern of damage (diffusely stained areas, single crack, parallel cracks, cross-hatching, or complete fracture (Wachtel

and Keaveny, 1997; Fazzalari *et al.*, 1998b)) and the extent of damage across the trabeculae (rounded to the nearest 25%), was measured for each specimen. Damaged area fraction of the section was measured using stereological point counting. All microdamage parameters were normalized by section area. T-tests were used to determine if there was a statistically significant difference in the microdamage parameters. Microdamage parameters were compared with the mechanical properties of the specimens to determine if relationships existed.

The relationship between damage, applied stress, and number of cycles suggested by Martin (1992) (Eqn. 5.1) was modified for trabecular bone. Applied stress was replaced by normalized stress, $\Delta\sigma/E_0$, and the number of damaged trabeculae and the damaged area fraction were used as measures of damage since crack numbers and lengths were not counted in the fatigue specimens. The modified equation thus became:

$$D = k\left(\frac{\Delta\sigma}{E_0}\right)^q N \tag{5.2}$$

where D is a measure of damage, either the number of damaged trabeculae per unit area or the damaged area fraction, k is a damage rate coefficient, $\Delta\sigma/E_0$ is applied stress, q is the exponent of the stress term, and N is number of cycles. Fatigue specimens were sorted by modulus reduction, E_r/E_0, and specimens with similar modulus reductions were compared to determine the effect of number of cycles on other mechanical properties and on microdamage accumulation. A more detailed study was made of specimens that were loaded at the same normalized stress to the same maximum strain to determine if the number of cycles or other mechanical properties affected microdamage accumulation. Specimens were also examined to determine the overall progression of damage with increasing normalized stress and increasing number of cycles.

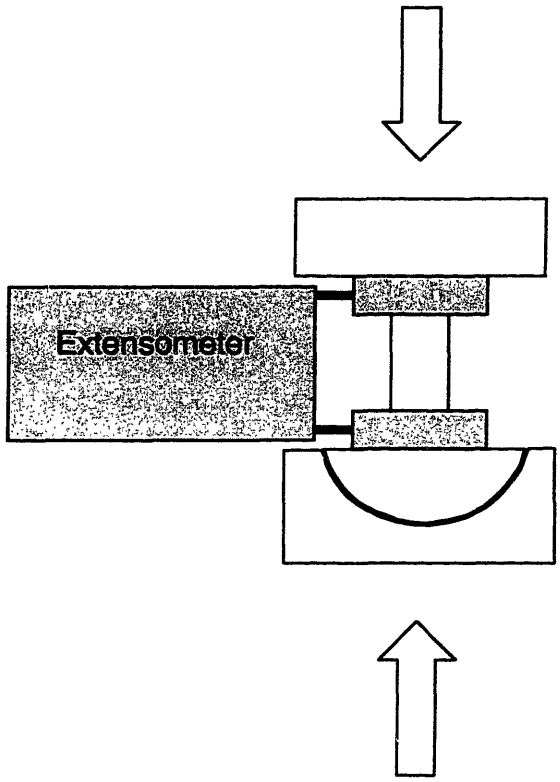

Figure 5.2: Experimental setup, including specimen geometry. An unwaisted cylinder is glued into brass end caps to minimize end effects. The specimen is loaded in compression between two platens (one fixed, one self-aligning) in a servohydraulic testing machine. An extensometer is attached to the specimen endcaps.

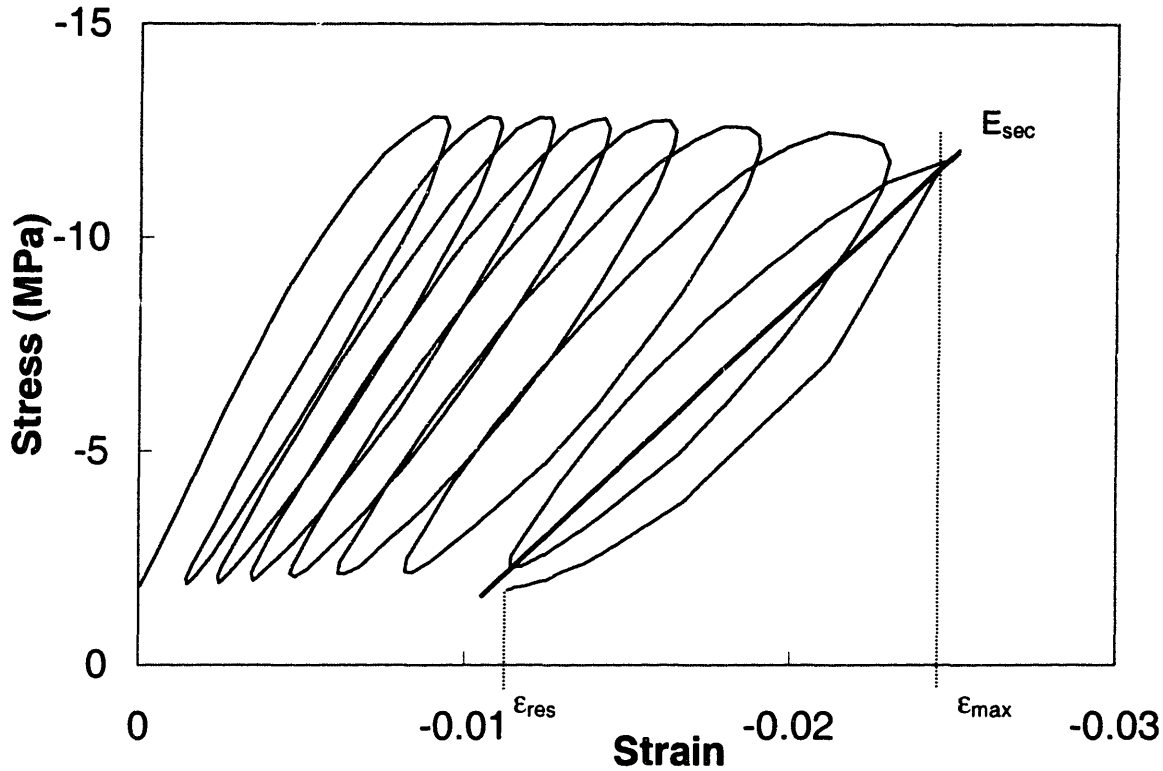

Figure 5.3: Typical fatigue test. Specimen was loaded at $\Delta\sigma/E_0 = 0.007$ to $\varepsilon_{max} = -2.5\%$. The specimen shows both cycle-dependent fatigue damage (modulus reduction, E_{sec}/E_0, with increasing cycles) and time-dependent creep damage (increase in residual or plastic strain, ε_{res}, with increasing number of cycles, N).

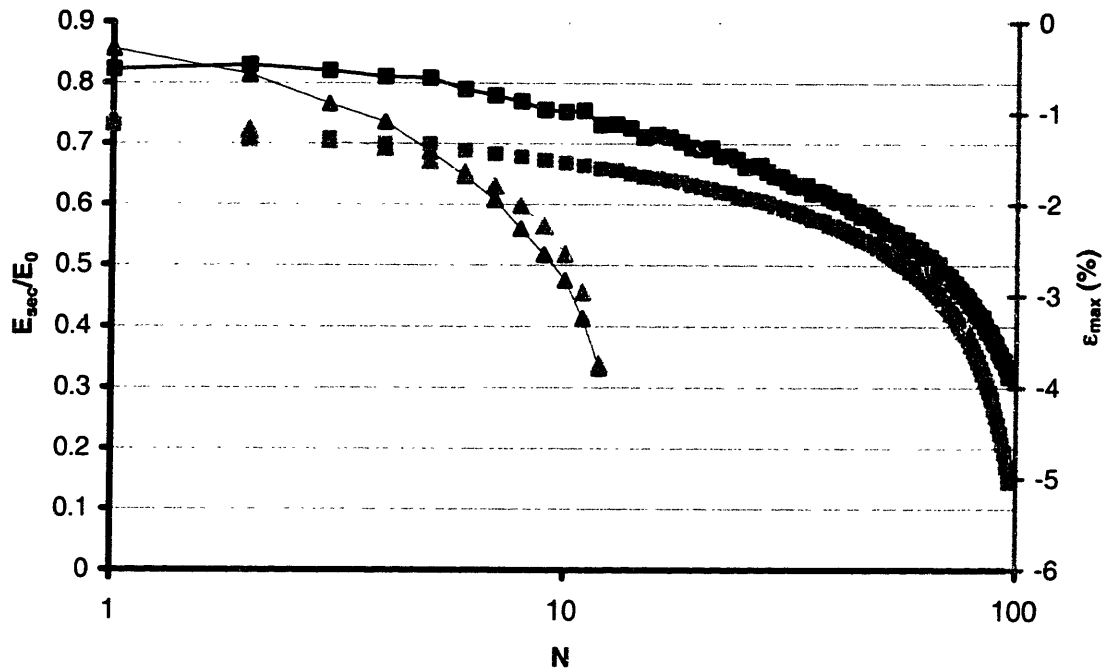

(a)

Figure 5.4: Modulus reduction, E_{sec}/E_0 (black), and maximum strain, ε_{max} (gray), are plotted as a function of number of cycles, N. Specimens stopped at a given maximum strain will have similar modulus reductions, but those stopped at a preset number of cycles may have different modulus reductions. Each symbol (square, triangle, diamond) represents a different specimen. (a) Two specimens from a previous study (Appendix B) tested at the same normalized stress ($\Delta\sigma/E_0 = 0.0085$). Data from the current fatigue tests shows that modulus reduction and maximum strain follow similar paths for (b) $\Delta\sigma/E_0 = 0.008$. (c) $\Delta\sigma/E_0 = 0.007$. (d) $\Delta\sigma/E_0 = 0.006$. (e) $\Delta\sigma/E_0 = 0.005$.

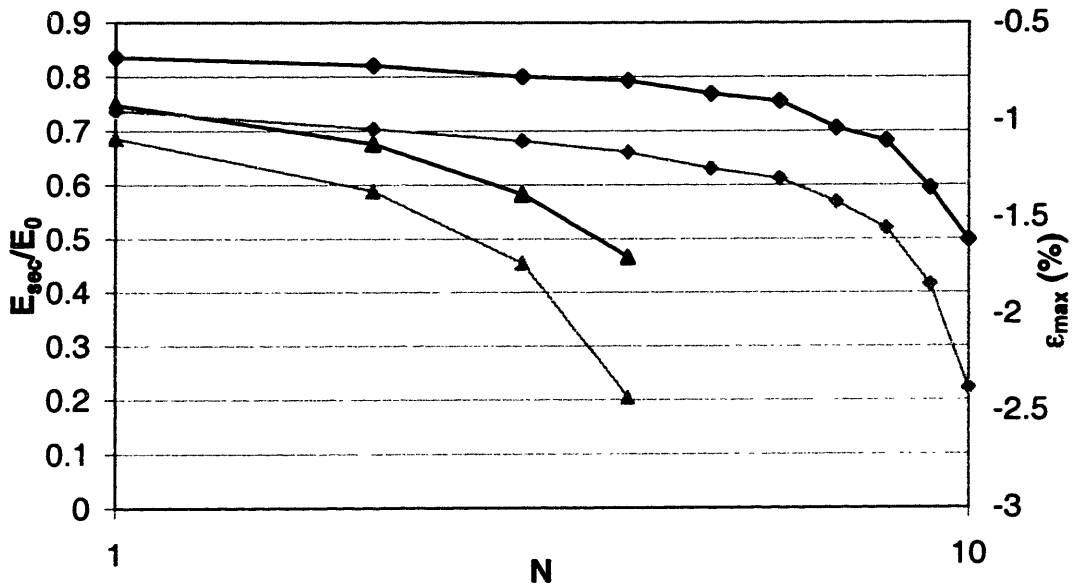

(b)

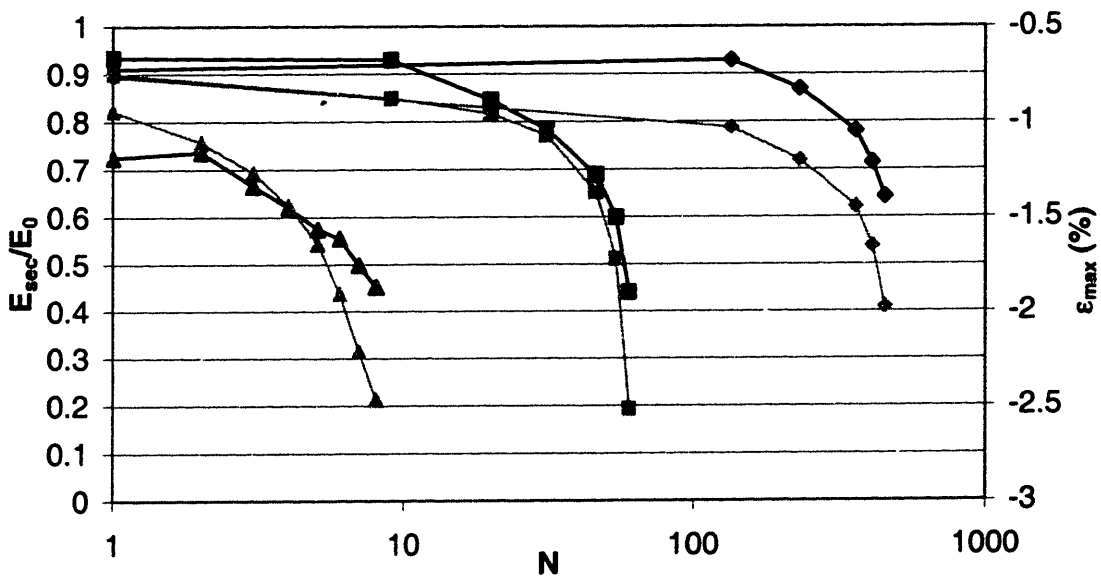

(c)

Figure 5.4: Modulus reduction, E_{sec}/E_0 (black), and maximum strain, ε_{max} (gray), are plotted as a function of number of cycles, N. Specimens stopped at a given maximum strain will have similar modulus reductions, but those stopped at a preset number of cycles may have different modulus reductions. Each symbol (square, triangle, diamond) represents a different specimen. (a) Two specimens from a previous study (Appendix B) tested at the same normalized stress ($\Delta\sigma/E_0 = 0.0085$). Data from the current fatigue tests shows that modulus reduction and maximum strain follow similar paths for (b) $\Delta\sigma/E_0 = 0.008$. (c) $\Delta\sigma/E_0 = 0.007$. (d) $\Delta\sigma/E_0 = 0.006$. (e) $\Delta\sigma/E_0 = 0.005$.

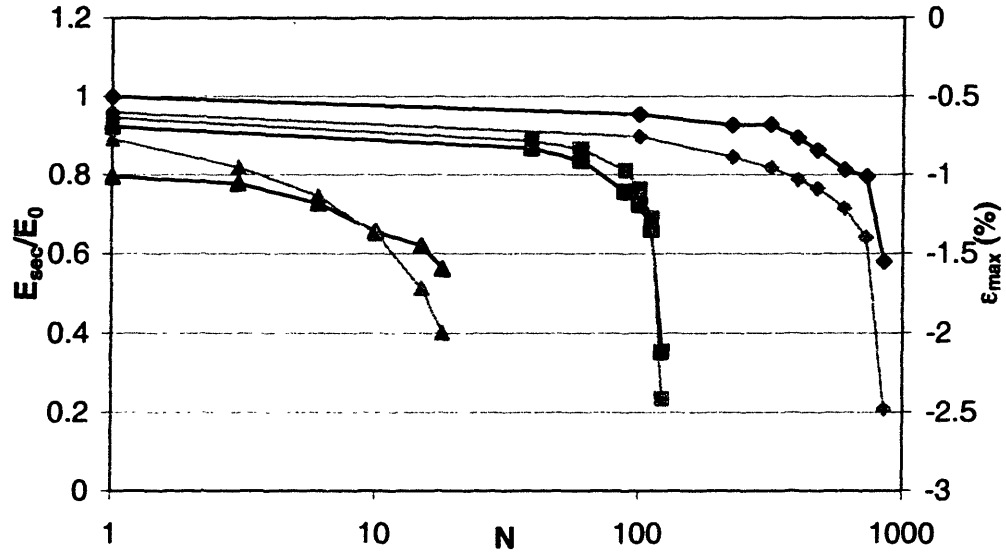

(d)

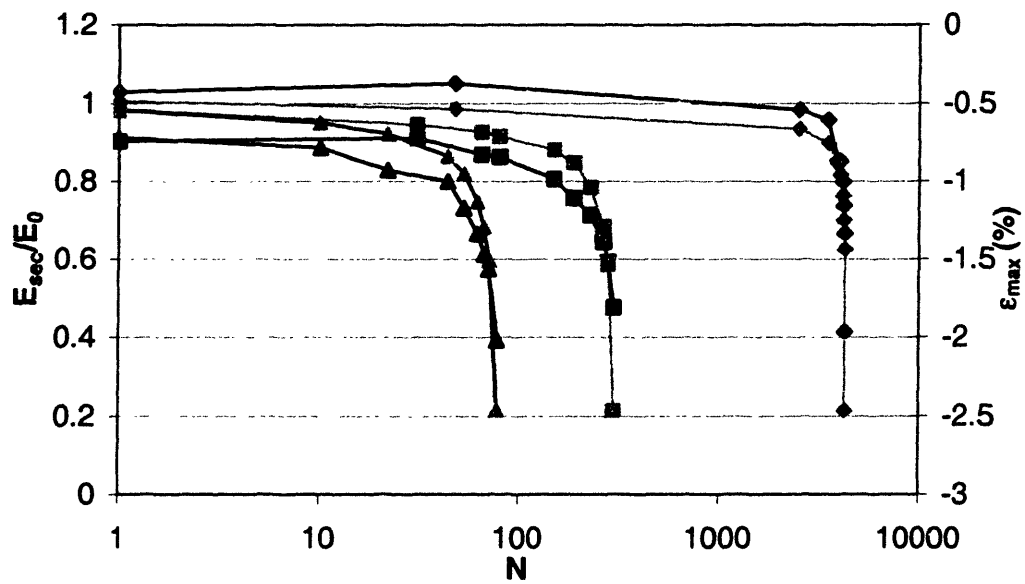

(e)

Figure 5.4: Modulus reduction, E_{sec}/E_0 (black), and maximum strain, ε_{max} (gray), are plotted as a function of number of cycles, N. Specimens stopped at a given maximum strain will have similar modulus reductions, but those stopped at a preset number of cycles may have different modulus reductions. Each symbol (square, triangle, diamond) represents a different specimen. (a) Two specimens from a previous study (Appendix B) tested at the same normalized stress ($\Delta\sigma/E_0 = 0.0085$). Data from the current fatigue tests shows that modulus reduction and maximum strain follow similar paths for (b) $\Delta\sigma/E_0 = 0.008$. (c) $\Delta\sigma/E_0 = 0.007$. (d) $\Delta\sigma/E_0 = 0.006$. (e) $\Delta\sigma/E_0 = 0.005$.

5.3 Results

110 fatigue tests were performed (typical test, **Figure 5.3**), with number of cycles, N, in individual tests ranging from 1 to 17,000 (**Table 5.2**). A typical S-N curve is shown in **Figure 5.5**. for a maximum strain of -1.3%. The number of cycles plotted corresponds to the point in the test when the specimen reached -1.3% strain. S-N curves for specimens tested to higher compressive strain levels, ε_{max}, were similar to Figure 5.5. For a given strain level, the number of cycles decreased with increasing normalized stress, according to a power law ($N = 7.47 \times 10^{-22}(\Delta\sigma/E_0)^{-10.4}$, $p < 0.05$, $R^2 = 0.62$). S-N curves corresponding to other maximum strains were similar; for instance, the power law relationships for specimens tested to -2.5% strain. ($N = 1.0 \times 10^{-20}(\Delta\sigma/E_0)^{-9.88}$, $p < 0.05$, $R^2 = 0.57$) was similar to that for specimens tested to $\varepsilon_{max} = -1.3\%$. Specimens tested to low numbers of cycles ($N < 100$) followed the Coffin-Manson Law ($\Delta\varepsilon_{pl}N^b = C_1$: $b = 1.10$, $C_1 = 0.691$, $R^2 = 0.82$), where $\Delta\varepsilon_{pl}$ is the plastic strain range over a given cycle and N is the number of cycles (**Figure 5.6**).

$\Delta\sigma/E_0$	Strain	E_0 (MPa)	N	E_r/E_0	E_{sec}/E_0	ε_{res} (%)
Control		N/A	0	N/A	N/A	N/A
Modulus		2252 (585)	0	N/A	N/A	-0.02 (0.01)
0.008	-1.3%	2021 (978)	9 (9)	0.794 (0.084)	0.765 (0.156)	-0.49 (0.15)
0.008	-1.65%	2489 (1068)	23 (15)	0.759 (0.087)	0.722 (0.197)	-0.64 (0.24)
0.008	-2.0%	2562 (540)	14 (6)	0.668 (0.074)	0.726 (0.200)	-0.85 (0.26)
0.008	-2.5%	1741 (322)	6 (3)	0.555 (0.135)	0.610 (0.171)	-1.30 (0.23)
0.007	-1.3%	1915 (975)	12 (11)	0.731 (0.048)	0.746 (0.071)	-0.40 (0.02)
0.007	-1.65%	1931 (980)	56 (62)	0.708 (0.042)	0.764 (0.116)	-0.77 (0.10)
0.007	-2.0%	2335(790)	437(451)	0.696 (0.153)	0.825 (0.304)	-1.04 (0.30)
0.007	-2.5%	1790 (727)	245 (503)	0.413(0.161)	0.533 (0.202)	-1.49 (0.57)
0.006	-0.8%	1673 (573)	280 (521)	0.975 (0.139)	1.046 (0.167)	-0.22 (0.09)
0.006	-1.1%	1745 (622)	320 (399)	0.874 (0.218)	0.927 (0.288)	-0.40 (0.14)
0.006	-1.3%	2421 (835)	145 (209)	0.660 (0.081)	0.715 (0.050)	-0.49 (0.06)
0.006	-1.65%	1841 (238)	78 (45)	0.582 (0.019)	0.667 (0.045)	-0.72 (0.06)
0.006	-2.0%	1466 (501)	121 (90)	0.626 (0.126)	0.659 (0.163)	-1.05 (0.17)
0.006	-2.5%	2090 (663)	339 (359)	0.505 (0.159)	0.586 (0.188)	-1.53 (0.32)
0.005	-0.8%	1713 (561)	1909 (2621)	0.992 (0.133)	1.018 (0.187)	-0.28 (0.08)
0.005	-1.1%	2323 (1111)	5324 (6747)	0.826 (0.316)	0.954 (0.313)	-0.48 (0.19)
0.005	-1.3%	2255 (802)	1693 (1450)	0.683 (0.159)	0.802 (0.208)	-0.62 (0.16)
0.005	-1.65%	2732 (1601)	1509 (1344)	0.518 (0.102)	0.707 (0.101)	-0.83 (0.14)
0.005	-2.0%	2120 (781)	751 (639)	0.492 (0.189)	0.565 (0.189)	-1.15 (0.22)
0.005	-2.5%	2053 (417)	1257 (1742)	0.364 (0.026)	0.455 (0.075)	-1.31 (0.22)

Table 5.2: Average mechanical property (± standard deviation) of all fatigue tests.

Both the reloading modulus, E_r/E_0, and the secant modulus, E_{sec}/E_0, decreased with increasing compressive strain, ε_{max} (**Figure 5.7, Figure 5.8**). There were no significant differences ($p < 0.05$) in the modulus reductions in specimens tested to the same ε_{max} at different normalized stress levels, $\Delta\sigma/E_0$, in almost all cases, for both E_r/E_0 and E_{sec}/E_0. Statistically significant differences were seen in only six of 26 paired comparisons of E_r/E_0: 4 of the 6 possible combinations of normalized stress at $\varepsilon_{max} = -1.65\%$ and between one pair of normalized stresses at $\varepsilon_{max} = -1.3\%$ and at $\varepsilon_{max} = -2.5\%$. There were no statistically significant differences in E_{sec}/E_0 between specimens tested to the same maximum strain at different normalized stresses. There was a linear relationship between the secant and reloading modulus reductions

($E_{sec}/E_0 = 0.92E_r/E_0 + 0.12$, $p < 0.05$, $R^2 = 0.77$). In five specimens, all loaded to either -0.8% or -1.1% strain, the initial modulus, E_0, was underestimated, and the measured modulus increased during the fatigue test, resulting in modulus reductions greater than 1 (**Figure 5.7, 5.8**). These data have not been excluded from the analysis.

The reduced reloading modulus, E_r/E_0, grouped for all normalized stresses, $\Delta\sigma/E_0$, at each level of ε_{max}, decreased linearly with ε_{max} according to the relationship: $E_r/E_0 = 0.27\varepsilon_{max} + 1.12$, $p < 0.05$, $R^2 = 0.48$) (**Figure 5.7b**). The intersection of the regression with $E_r/E_0 = 1$ (corresponding to no measured modulus loss) occurs at $\varepsilon_{max} = -0.44\%$. The reduced secant modulus, E_{sec}/E_0, grouped for all normalized stresses, $\Delta\sigma/E_0$, at each level of ε_{max}, decreased linearly with ε_{max} according to the relationship: $E_{sec}/E_0 = 0.25\varepsilon_{max} + 1.16$, $p < 0.05$, $R^2 = 0.35$ (**Figure 5.8b**). The intersection of the regression with $E_{sec}/E_0 = 1$ occurs at $\varepsilon_{max} = -0.64\%$. Multiple linear regressions (Eqn 5.3, 5.4) of the mechanical properties revealed that while maximum strain, ε_{max}, was the major determinant of both reloading and secant modulus loss, the relative density, ρ^*/ρ_s (measured as the bone area divided by the section area), normalized stress, $\Delta\sigma/E_0$, initial modulus, E_0, and number of cycles, N, were small but significant predictors as well (E_r/E_0: $R^2 = 0.73$; E_{sec}/E_0: $R^2 = 0.62$).

$$E_r/E_0 = 0.40 + 0.751\rho^*/\rho_s + 88.8\Delta\sigma/E_0 - 0.14E_0 + 0.66\log_{10}(N) + 0.27\varepsilon_{max},$$
$$p < 0.005, R^2 = 0.73 \qquad (5.3)$$

$$E_{sec}/E_0 = 0.206 + 1.035\rho^*/\rho_s + 89.8\Delta\sigma/E_0 - 0.15E_0 + 0.113\log_{10}(N) + 0.245\varepsilon_{max}$$
$$p < 0.005 \text{ for all slopes, intercept } p = 0.21, R^2 = 0.62 \qquad (5.4)$$

The maximum strain, ε_{max}, predicted the overall modulus reduction, E_r/E_0, better than number of cycles (**Figure 5.4**). The maximum strain tracked the modulus reduction over the course of the test at all normalized stress levels (**Figure 5.4b-e**). After a specimen reached a strain of approximately -1.3%, failure occurred within a few cycles. Specimens tested to the same maximum strain had similar modulus reductions, but

specimens tested to the same number of cycles did not necessarily have similar changes in modulus.

The compressive residual strain, ε_{res}, increased with increasing maximum compressive strain (**Table 5.2, Figure 5.9**). There was a linear relationship between the pooled residual strain for all normalized stresses and the maximum strain ($\varepsilon_{res} = 0.71\varepsilon_{max} + 0.39$, $p < 0.001$, $R^2 = 0.76$). Adding the normalized stress and initial modulus to the regression improved predictions by less than ten percent ($\varepsilon_{res} = 0.747\varepsilon_{max} + 65.2(\Delta\sigma/E_0) + 0.121E_0 - 0.213$, $R^2 = 0.84$). Only two statistically significant differences were found in the residual strain, ε_{res}, between specimens tested to the same maximum strain at different normalized stresses, both at $\varepsilon_{max} = -1.3\%$; otherwise the data was not statistically significant for different normalized stresses, $\Delta\sigma/E_0$, at a given maximum strain, ε_{max}. Based on the linear relationship between residual strain, ε_{res}, and maximum strain, ε_{max}, we calculated that $\varepsilon_{res} = 0$ at $\varepsilon_{max} = -0.55\%$, suggesting that there was little or no damage at strains up to that value.

Three to six slide sections were obtained for each specimen, with a mean section area of 118 ± 40 mm^2 and a bone area fraction of 0.46 ± 0.08 (**Table 5.3**). Both the untested controls and specimens with only initial modulus measurement showed little damage (**Table 5.4**), primarily at the outer edges of the sections, and was presumably caused by machining damage during specimen preparation. Microdamage was observed in the fatigue-tested specimens and was present as diffusely stained areas, single crack, parallel cracks, cross-hatching, or complete fracture (**Figures 5.10, 5.11**, Appendix D).

The number of damaged trabeculae per unit area and the damaged area fraction increased with increasing specimen compressive strain for each normalized stress level (**Table 5.4, Figure 5.12**). There was a linear relationship between the damaged area fraction (Y) and the number of damaged trabeculae (X) ($Y = 0.026X - 0.107$, $R^2 = 0.81$). Almost no damage was seen in the control specimens, and no significant differences were observed between controls specimens that were untested and those with modulus measurement only. The number of damaged trabeculae per unit area and the damaged area fraction both increased with increasing strain from strain levels of about -0.8% to -2.0%, and then were approximately constant between -2.0% and -2.5%. The total number of damaged trabeculae per unit area and damaged area fractions were similar in

specimens tested to the same maximum strain level at different normalized stresses (**Table 5.4; Figure 5.12**). There was an increase in microdamage parameters with decreasing E_r/E_0, but the reloading modulus was not as good a predictor of microdamage parameters as maximum strain ($p < 0.001$, $R^2 = 0.4$, typically) (example, **Figure 5.13**). Multiple linear regressions showed that all microdamage parameters were best predicted by the maximum strain, residual strain, secant modulus reduction, and the number of cycles (Eqn 5.5, 5.6, 5.7).

$$\text{Damaged Band Fraction} = 0.33 + 0.107\log_{10}(N) - 0.406\varepsilon_{max} + 0.462\varepsilon_{res} - 0.629E_{sec}/E_0$$

$$p < 0.05 \text{ for all slopes, intercept } p = 0.06,\ R^2 = 0.59 \qquad (5.5)$$

$$\text{Damaged Trabeculae/Area} = 0.23 + 0.117\log_{10}(N) - 0.469\varepsilon_{max} + 0.451\varepsilon_{res} - 0.614E_{sec}/E_0$$

$$p < 0.05 \text{ for all slopes, intercept } p = 0.06,\ R^2 = 0.51 \qquad (5.6)$$

$$\text{Damaged Area Frac.} = 0.053 + 0.0045\log_{10}(N) - 0.0173\varepsilon_{max} + 0.0156\varepsilon_{res} - 0.0129E_{sec}/E_0$$

$$p < 0.05 \text{ for all slopes, intercept } p = 0.06,\ R^2 = 0.58 \qquad (5.7)$$

$\Delta\sigma/E_0$	Strain	Section Area (mm^2)[a]	Bone Area (mm^2)[b]	Bone Area Fraction (mm^2/mm^2)[c]
Control		237 (46)	118 (30)	0.495 (0.060)
Modulus		245 (54)	111 (13)	0.470 (0.097)
0.008	-1.3%	153 (17)	72 (17)	0.471 (0.100)
0.008	-1.65%	160(20)	69 (5)	0.437 (0.085)
0.008	-2.0%	163 (11)	79 (10)	0.484 (0.036)
0.008	-2.5%	153 (18)	62 (9)	0.408 (0.053)
0.007	-1.3%	205 (40)	93 (21)	0.461 (0.094)
0.007	-1.65%	213 (44)	99 (29)	0.463 (0.095)
0.007	-2.0%	217 (37)	120 (31)	0.552 (0.072)
0.007	-2.5%	185 (19)	81 (32)	0.426 (0.134)
0.006	-0.8%	205 (45)	96 (33)	0.461 (0.093)
0.006	-1.1%	221 (42)	101 (20)	0.454 (0.026)
0.006	-1.3%	215 (28)	103 (20)	0.479 (0.057)
0.006	-1.65%	186 (14)	80 (8)	0.433 (0.058)
0.006	-2.0%	212 (9)	90 (19)	0.426 (0.080)
0.006	-2.5%	184 (24)	88 (12)	0.484 (0.069)
0.005	-0.8%	158 (25)	76 (15)	0.479 (0.072)
0.005	-1.1%	156 (11)	78 (7)	0.500 (0.057)
0.005	-1.3%	157 (19)	77 (6)	0.493 (0.041)
0.005	-1.65%	177 (19)	84 (11)	0.479 (0.096)
0.005	-2.0%	158 (28)	65 (18)	0.404 (0.057)
0.005	-2.5%	180 (31)	73 (12)	0.407 (0.036)

[a]total specimen area
[b]total amount of bone in the section area
[c]bone area divided by section area

Table 5.3: Average area measurements for 110 fatigue tests.

$\Delta\sigma/E_0$	Strain	Damaged Band Fraction[a]	Number of Damaged Trabeculae /Area (mm^{-2})[b]	Damaged Area Fraction (mm^2/mm^2)[c]	Percent Fractured Trabeculae[d]
Control		0	0.003 (0.005)	6E-05 (11E-05)	0
Modulus		0	0.002 (0.003)	2E-05 (5E-05)	0
0.008	-1.3%	0.141 (0.101)	0.152 (0.075)	0.0034 (0.0020)	0
0.008	-1.65%	0.264 (0.278)	0.292 (0.282)	0.0043 (0.0044)	0.10 (0.22)
0.008	-2.0%	0.474 (0.377)	0.419 (0.303)	0.0101 (0.0100)	0.11 (0.25)
0.008	-2.5%	0.331 (0.349)	0.369 (0.368)	0.0067 (0.0065)	1.35 (2.75)
0.007	-1.3%	0.366 (0.157)	0.345 (0.118)	0.0057 (0.0026)	0
0.007	-1.65%	0.248 (0.221)	0.296 (0.219)	0.0065 (0.0060)	0.28 (0.44)
0.007	-2.0%	0.482 (0.299)	0.619 (0.425)	0.0209 (0.0165)	0.64 (1.28)
0.007	-2.5%	0.509 (0.383)	0.588 (0.391)	0.0171 (0.0128)	1.88 (1.70)
0.006	-0.8%	0.085 (0.117)	0.096 (0.119)	0.0014 (0.0024)	0
0.006	-1.1%	0.284 (0.240)	0.300 (0.204)	0.0063 (0.0052)	0
0.006	-1.3%	0.186 (0.117)	0.161 (0.097)	0.0040 (0.0033)	0
0.006	-1.65%	0.635 (0.130)	0.714 (0.343)	0.0142 (0.0054)	0.39 (0.86)
0.006	-2.0%	0.618 (0.191)	0.815 (0.182)	0.0173 (0.0056)	0.53 (0.76)
0.006	-2.5%	0.425 (0.328)	0.600 (0.454)	0.0186 (0.0150)	2.34 (2.55)
0.005	-0.8%	0.169 (0.186)	0.164 (0.146)	0.0028 (0.0032)	0.52 (0.74)
0.005	-1.1%	0.323 (0.242)	0.324 (0.228)	0.0088 (0.0067)	4.60 (5.52)
0.005	-1.3%	0.313 (0.345)	0.300 (0.311)	0.0071 (0.0076)	1.88 (2.53)
0.005	-1.65%	0.494 (0.182)	0.538 (0.258)	0.0158 (0.0117)	1.11 (1.28)
0.005	-2.0%	0.499 (0.281)	0.517 (0.208)	0.0112 (0.0056)	5.20 (4.63)
0.005	-2.5%	0.643 (0.239)	0.707 (0.343)	0.0209 (0.0054)	5.78 (2.91)

[a]total area of the localized regions of damage, normalized by specimen section area
[b]total number of trabeculae containing damage in the section, normalized by specimen section area
[c]total section area containing damage, normalized by specimen section area
[d]percentage of total number of damaged trabeculae containing fractures

Table 5.4: Average microdamage parameters of 110 fatigue tests.

A weak but significant relationship was seen between damage parameters and the normalized stress and number of cycles using the power law relationship

$$D = k\left(\frac{\Delta\sigma}{E_0}\right)^q N \tag{5.2}$$

proposed by Martin (1992), where D is a damage parameter and k is the damage rate coefficient. Using the number of damaged trabeculae per unit area as the damage parameter, D, the damage rate coefficient, k, was 5.26×10^{16} (95% confidence interval, 7.88×10^{11} - 3.52×10^{21}) and the exponent of the normalized stress term, q, was 8.70 (95% CI: 6.52 - 10.89) (**Figure 5.14a**). Using damaged area fraction as the damage parameter gave a damage rate coefficient, k, of 1.06×10^{11} (95% CI: 1.76×10^{5} – 6.37×10^{16}) and an exponent, q, of 6.84 (95% CI: 4.22 – 9.45) (**Figure 5.14b**). This relationship explained more of the variance for the number of damaged trabeculae ($R^2 = 0.39$) than it did for the damaged area fraction ($R^2 = 0.22$).

Of 110 fatigue specimens, there were four modulus reduction levels that had sufficient numbers of specimens to compare the effect of number of cycles on other properties (**Table 5.5**). There was no correlation between the numbers of cycles and mechanical properties, including maximum strain, and residual strain for specimens tested in fatigue to the same modulus reduction.

Specimen	E_0	$\Delta\sigma/E_0$	ε_{max} (%)	N	E_r/E_0
81F1	760	0.006	-2	130	0.83
117B1	1547	0.005	-1.3	129	0.83
113D1	1533	0.008	-1.65	33	0.83
107B1	1621	0.008	-1.65	1	0.82
119B3	2114	0.008	-1.65	41	0.81
111B1	1855	0.006	-1.1	23	0.81
99C1	1874	0.007	-1.3	6	0.81
98B1	2992	0.008	-1.3	10	0.77
113A1	1646	0.005	-2	1568	0.77
111C2	1923	0.008	-1.3	1	0.77
95C2	1703	0.006	-1.1	34	0.77
103C1	1292	0.008	-2.5	7	0.77
121B2	1870	0.006	-1.3	5	0.77
106B2	1838	0.008	-2	9	0.76
105D1	1836	0.007	-1.65	100	0.75
102C2	3004	0.006	-1.3	90	0.62
115A4	2782	0.008	-2	17	0.62
89A1	1518	0.005	-1.65	3572	0.60
109A1	2504	0.007	-2.5	1144	0.60
100B1	2944	0.008	-2	9	0.60
84A1	1180	0.006	-2	18	0.60
115A2	1984	0.006	-1.65	74	0.59
78C1	1506	0.006	-1.65	37	0.59
79C1	1061	0.005	-2	43	0.59
94A1	2125	0.006	-1.65	154	0.59
88A1	1730	0.006	-1.65	62	0.58
107D2	3762	0.005	-1.1	322	0.58
103B1	3067	0.005	-1.3	2511	0.58
111D1	5457	0.005	-1.65	380	0.42
120C1	2354	0.007	-2.5	60	0.42
91F1	2355	0.005	-2	229	0.41
121C2	1807	0.007	-2.5	13	0.41
112C1	2011	0.005	-1.65	687	0.41
88A2	1591	0.005	-2.5	300	0.41
86A2	2716	0.006	-2.5	127	0.40
114B2	1975	0.008	-2.5	10	0.39

Table 5.5: Specimens tested to the same modulus reductions, with different maximum strains, ε_{max}, and numbers of cycles, N.

Sixteen groups of specimens (25 total pairs) were tested to the same maximum strain and modulus reduction at the same normalized stress level (**Table 5.6**, microdamage parameters are listed in Appendix D). An increase in microdamage parameters with increasing numbers of cycles was observed in approximately half of the pairs, but there was too much scatter to draw definitive conclusions.

$\Delta\sigma/E_0$	ε_{max} (%)	E_r/E_0	N (for each specimen)			
			1	2	3	4
0.005	-0.8	0.87	16	6250		
0.008	-1.65	0.82	1	33	41	
0.006	-1.1	0.81	23	465		
0.008	-1.3	0.77	1	10		
0.008	-2	0.76	9	22		
0.007	-1.65	0.73	13	19		
0.007	-1.3	0.70	22	26		
0.007	-1.65	0.67	3	143		
0.007	-2	0.64	48	453		
0.008	-2	0.60	9	17		
0.006	-1.65	0.59	37	62	74	154
0.005	-1.3	0.56	2581	3121		
0.008	-2.5	0.53	4	4		
0.006	-2.5	0.53	14	847		
0.007	-2.5	0.41	13	60		
0.005	-2.5	0.35	78	1125	4294	

Table 5.6: Groups of specimens tested to the same normalized stress, $\Delta\sigma/E_0$, and maximum compressive strain, ε_{max}, with different numbers of cycles, N.

For all normalized stress levels, the dominant pattern of damage was cross-hatching (**Figure 5.15**). The proportions of parallel cracks and complete fractures measured in specimens were higher in specimens tested at lower normalized stress levels (and therefore higher numbers of cycles) than in specimens tested to high normalized stresses (**Figure 5.15**). The proportion of single cracks declined with increasing maximum strain, while the proportions of diffuse damage and cross-hatching did not change with strain. Diffuse damage was rarely seen without accompanying microcracks.

When diffuse damage was associated with microcracks, the pattern of damage was classified according to the pattern of damage of the microcracks. Complete trabecular fractures (where a distinct separation of the crack edges was seen) were observed in specimens tested to low strains (< -1.1%) at low normalized stresses ($\Delta\sigma/E_0$ = 0.005), while complete fractures were not seen until at least -2.0% strain in specimens tested at higher normalized stresses ($\Delta\sigma/E_0$ = 0.005) (**Figure 5.15a,b**). Further analyses showed that a threshold number of cycles existed for fractures to form at each maximum strain, regardless of normalized stress, below which no trabecular fractures were present (**Figure 5.16**). This threshold for fractures increased with decreasing maximum strain on the specimen. At high strains (e.g. -2.5%), fractures were observed in specimens fatigued for fewer than ten cycles. In contrast, fractures are not observed in specimens loaded to -1.1% until the specimen has been loaded to about one thousand cycles.

Approximately half of all damaged trabeculae contained cracks that extended 100% of the way across the trabeculae (**Figure 5.17**). These would include, but were not limited to, trabecular fractures. The breakdown of number of damaged trabeculae per area by extent of damage across the thickness did not change significantly with changes in normalized stress; specimens loaded to other normalized stresses had breakdowns similar to those observed in Figure 5.17.

Localized regions of damage were observed at strain levels of -1.1% and higher, and a distinct band extending across the specimen was apparent by about -1.3% strain. The fraction of the specimen containing damage increased rapidly with increasing specimen strain until the strain was approximately -1.65%, then leveled off (**Table 5.3, Figure 5.18**). At strains higher than -1.65%, the damage increased by increases in the damage density within the band, not by increases in the size of the band.

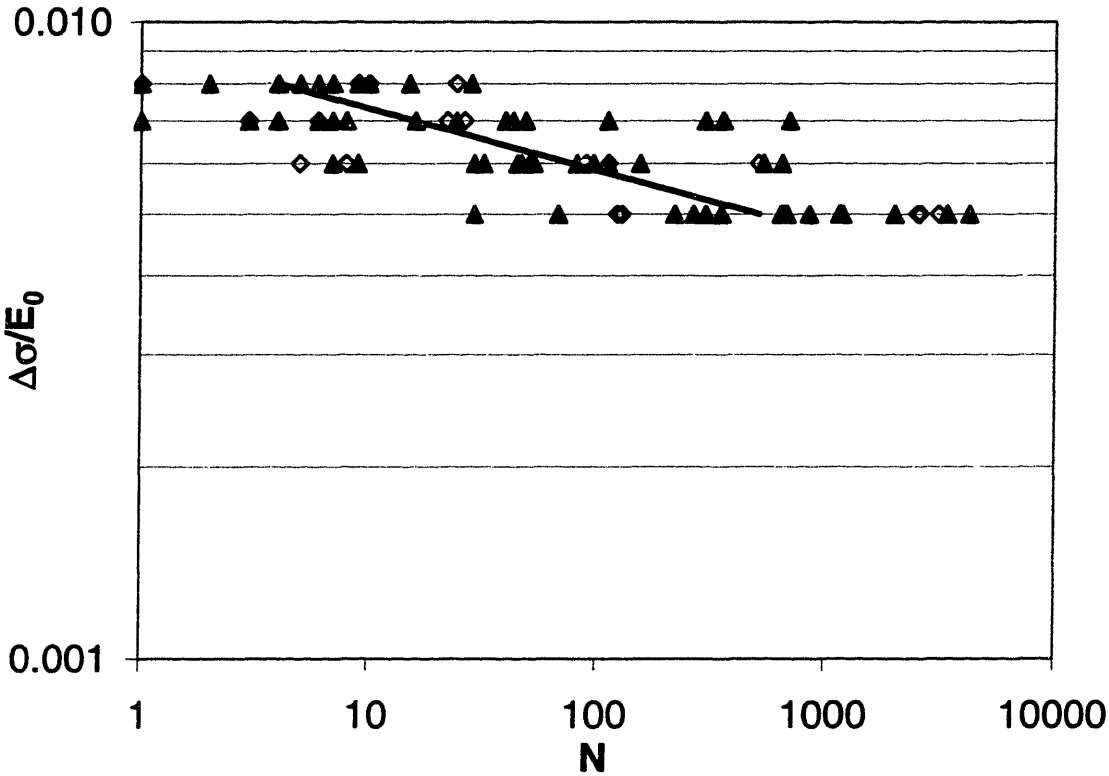

Figure 5.5: S-N curve for specimens at -1.3% strain. Open diamonds represent tests stopped at -1.3% strain; filled triangles represent specimens tested to strains greater than -1.3%. The data points plotted indicate the cycle number where -1.3% strain was exceeded. There is a power law relationship between normalized stress and number of cycles ($N = 7.47 \times 10^{-22} (\Delta\sigma/E_0)^{-10.4}$, $R^2 = 0.62$).

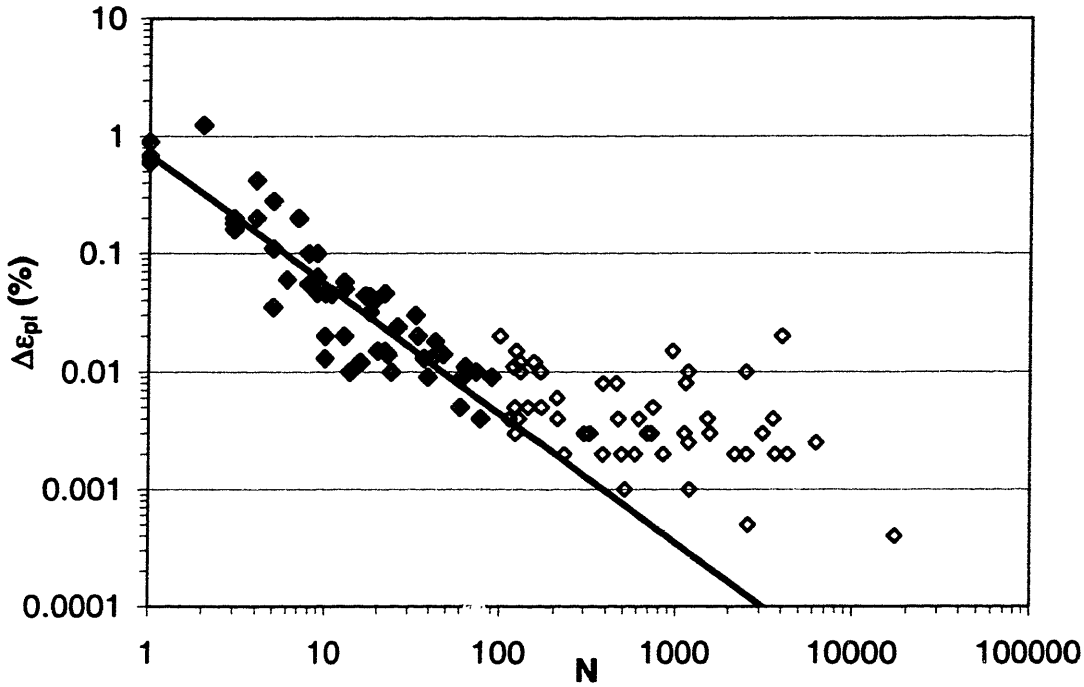

Figure 5.6: Bovine trabecular bone follows the Coffin-Manson law at low cycle numbers. There is a power law relationship between the change in the change in plastic strain in a single cycle, $\Delta\varepsilon_{pl}$, and number of cycles for specimens tested to less than 100 cycles (filled diamonds) ($\Delta\varepsilon_{pl} = 0.691\ N^{-1.10}$, $R^2 = 0.82$).

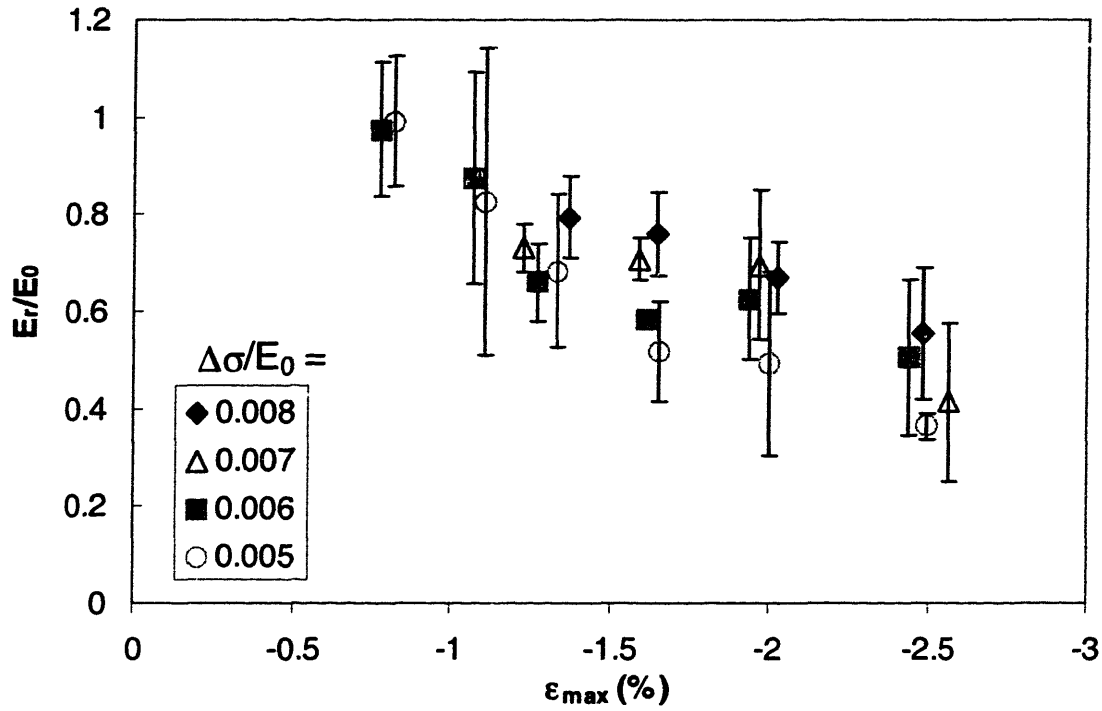

(a)

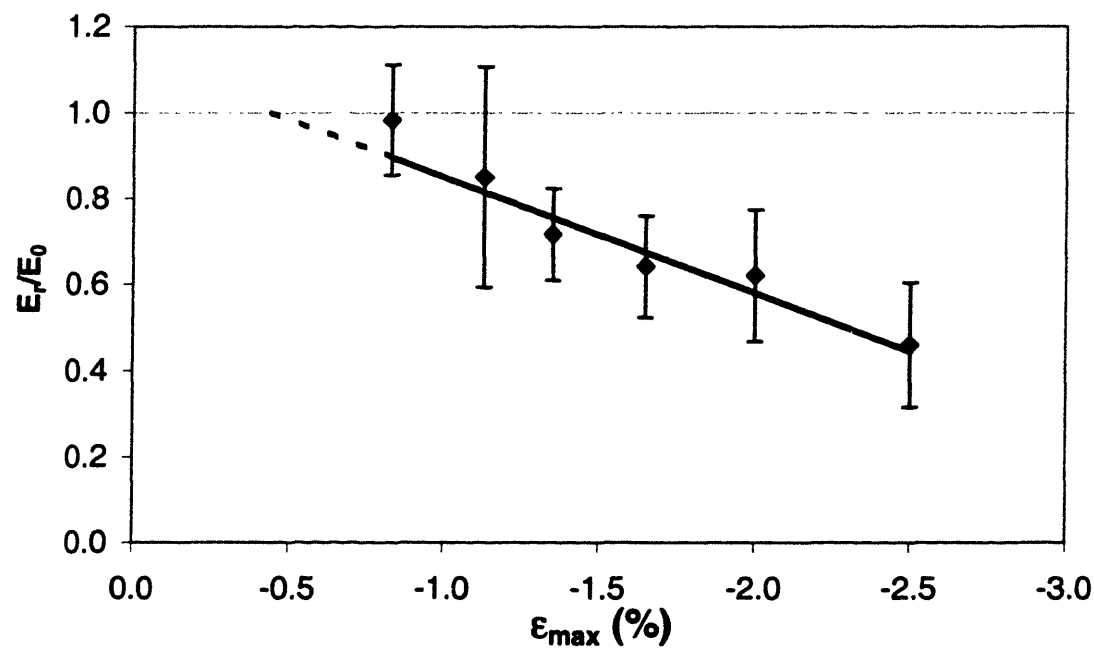

(b)

Figure 5.7: Plot of modulus reduction, E_r/E_0, as a function of maximum compressive strain, ε_{max}. (a) Data plotted by normalized stress. Data at each strain level spread for clarity. (b) Pooled fatigue data. The data are linearly related ($Y = 0.27X + 1.12$, $p < 0.05$, $R^2 = 0.48$). The regression intersects the line $E_r/E_0 = 1$ at $\varepsilon_{max} = -0.44\%$.

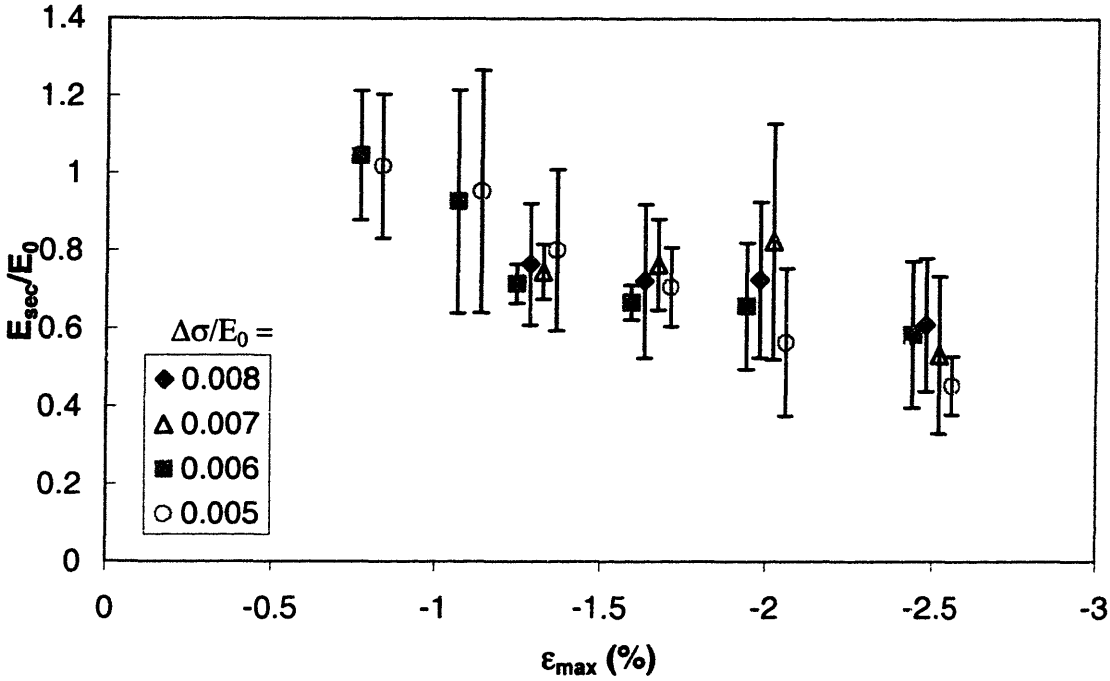

(a)

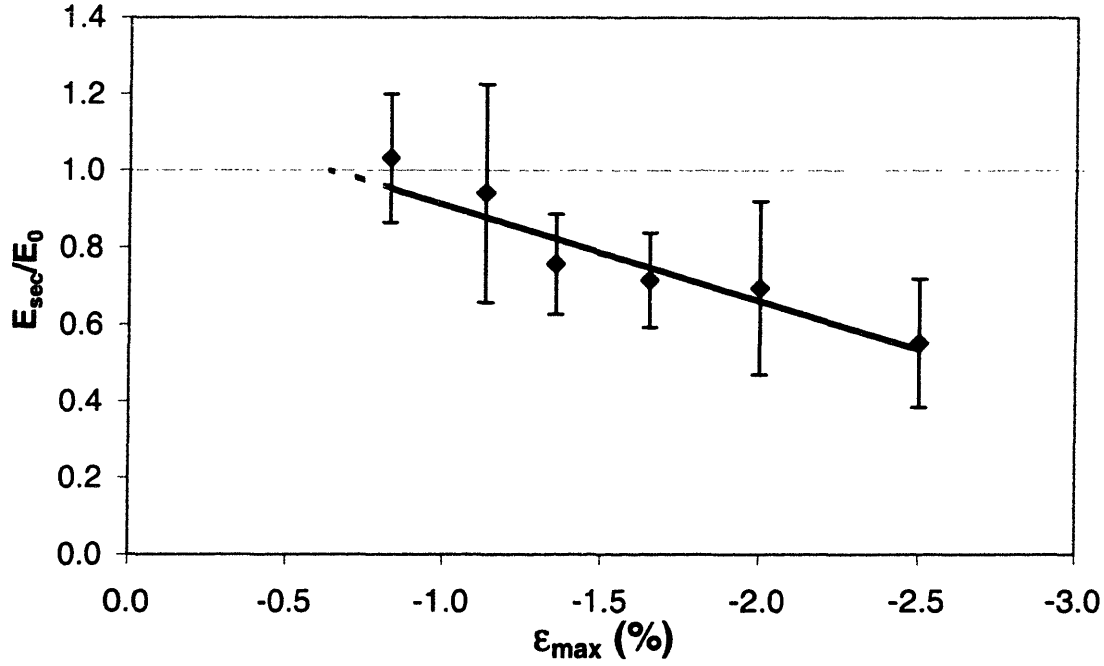

(b)

Figure 5.8: Plot of modulus reduction, E_{sec}/E_0, as a function of maximum compressive strain, ε_{max}. (a) Data plotted by normalized stress. Data at each strain level spread slightly for clarity. (b) Pooled fatigue data. The regression intersects the line $E_{sec}/E_0 = 1$ at $\varepsilon_{max} = -0.64\%$.

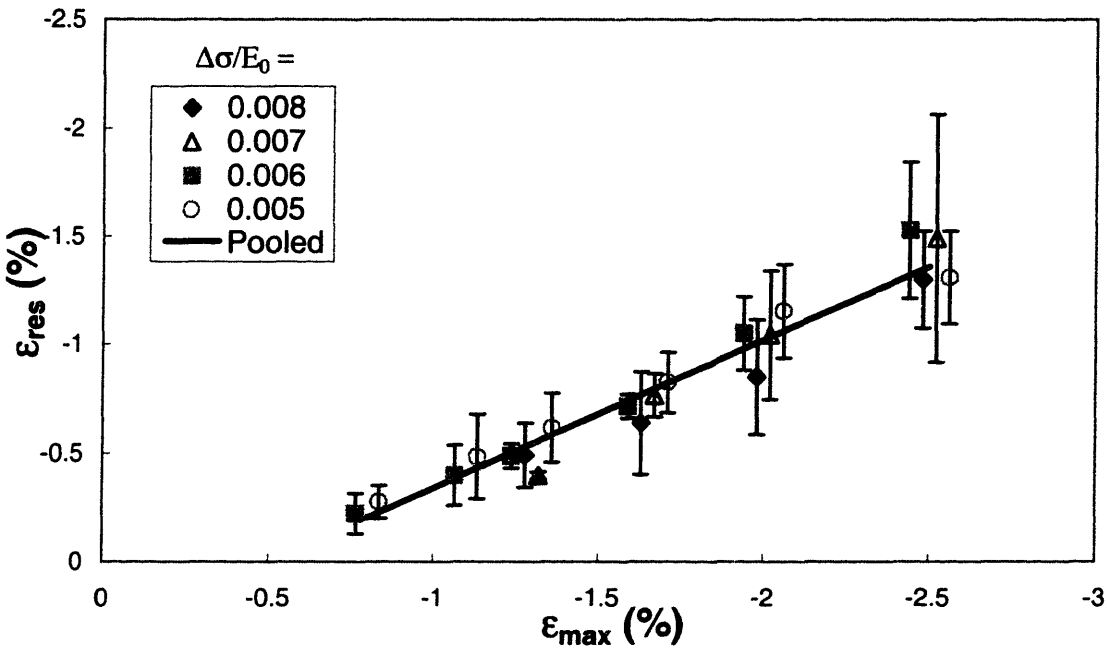

(a)

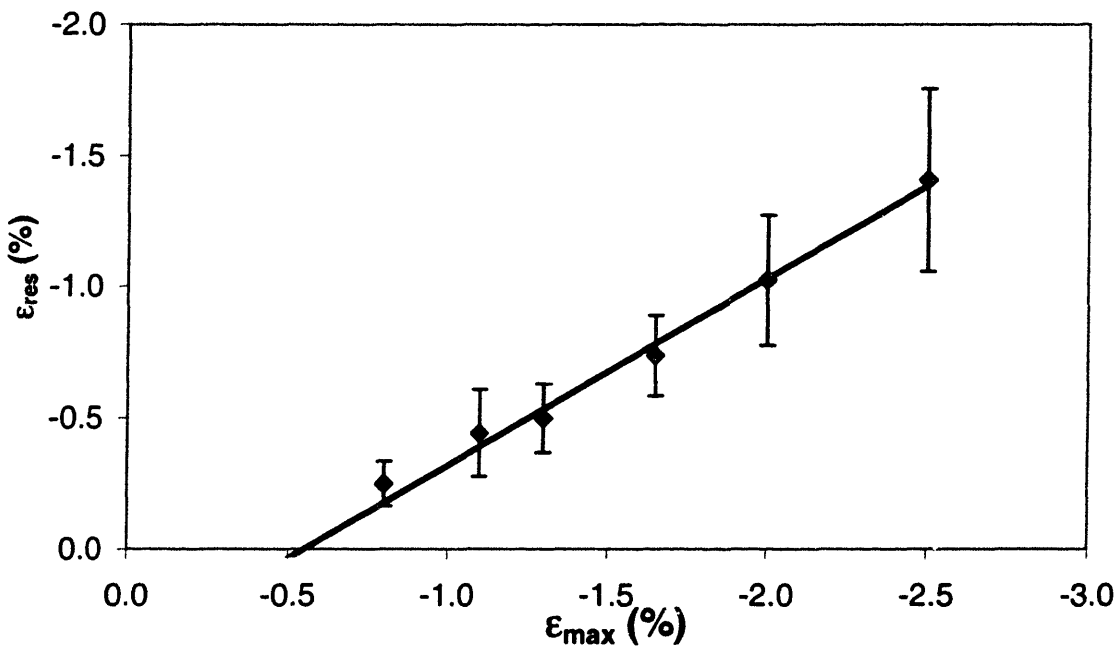

(b)

Figure 5.9: Plot of residual strain, ε_{res}, as a function of maximum compressive strain, ε_{max}. (a) Data plotted by normalized stress. Data at each strain level spread slightly for clarity. (b) Pooled fatigue data. There is a linear relationship between residual strain and maximimum strain ($\varepsilon_{res} = 0.71\varepsilon_{max} + 0.39$, $p < 0.001$, $p < 0.05$, $R^2 = 0.76$). The regression intersects the axis $\varepsilon_{res} = 0$ at $\varepsilon_{max} = -0.55\%$.

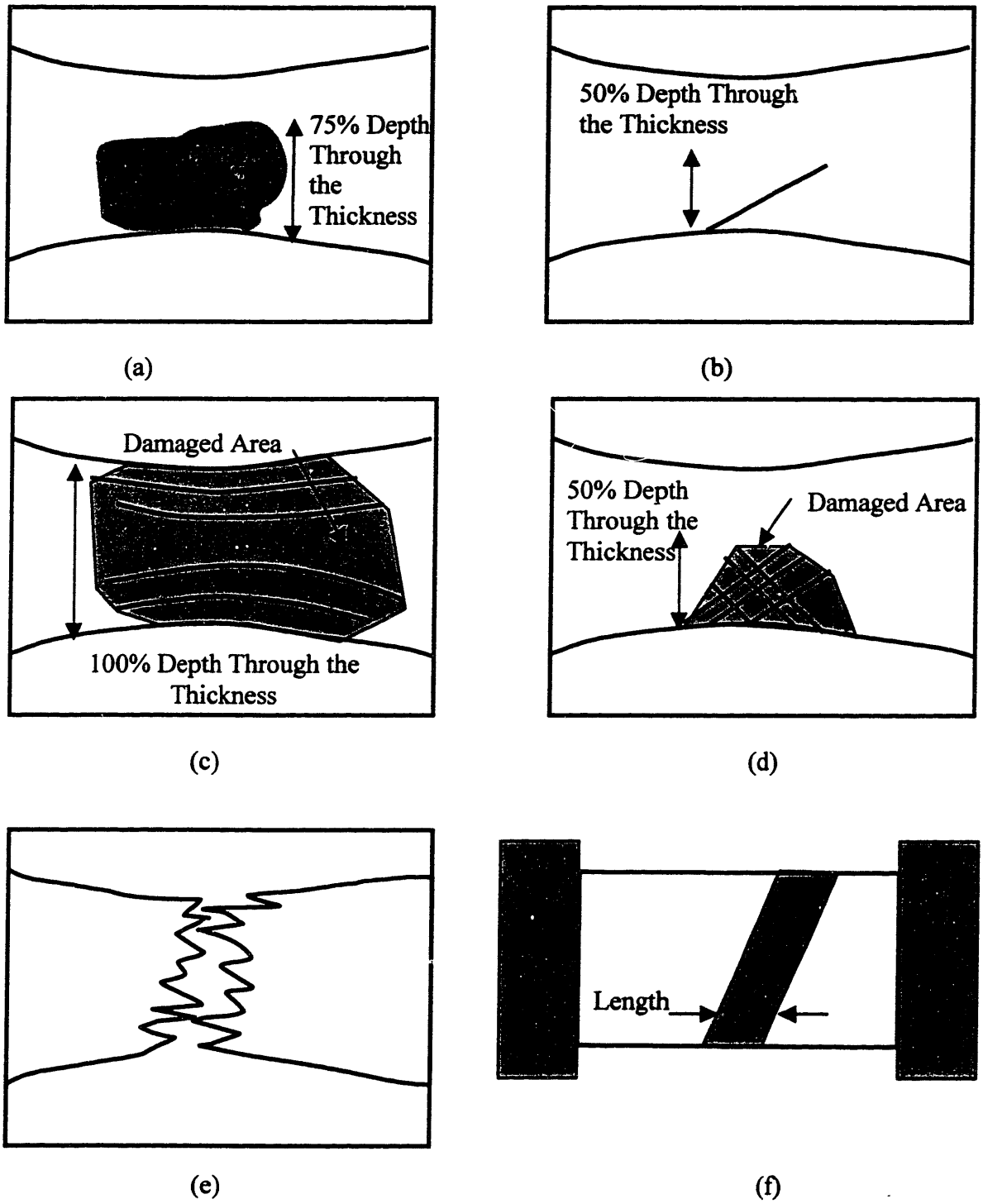

Figure 5.10: Examples of damage patterns observed, including (a) diffusely stained area, without visible cracks, (b) single crack, (c) parallel cracks, (d) cross-hatching, (e) complete trabecular fracture, and (f) local region of damage in the specimen.

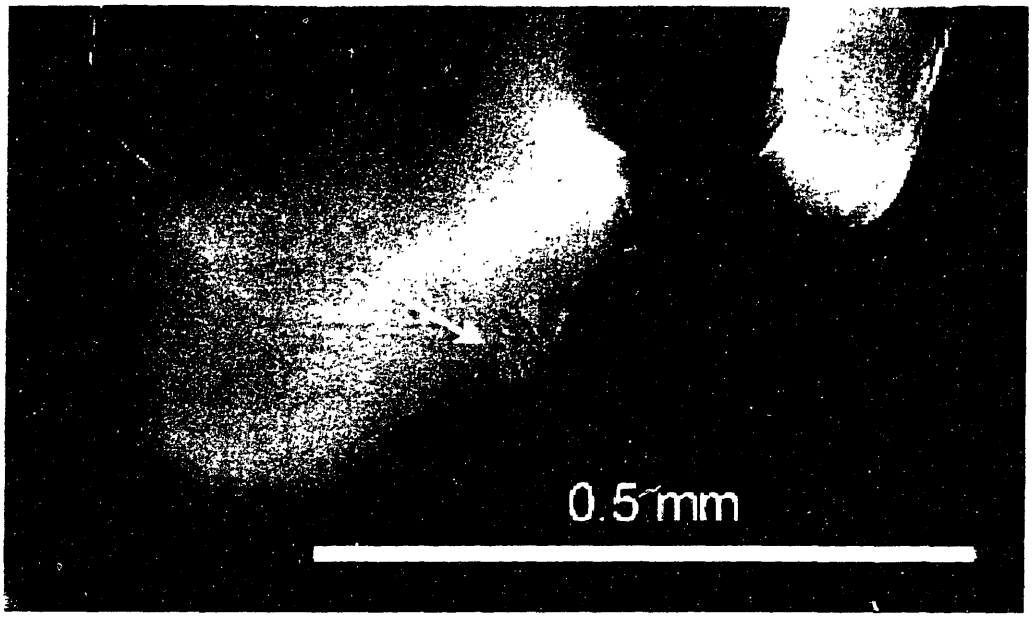

(a)

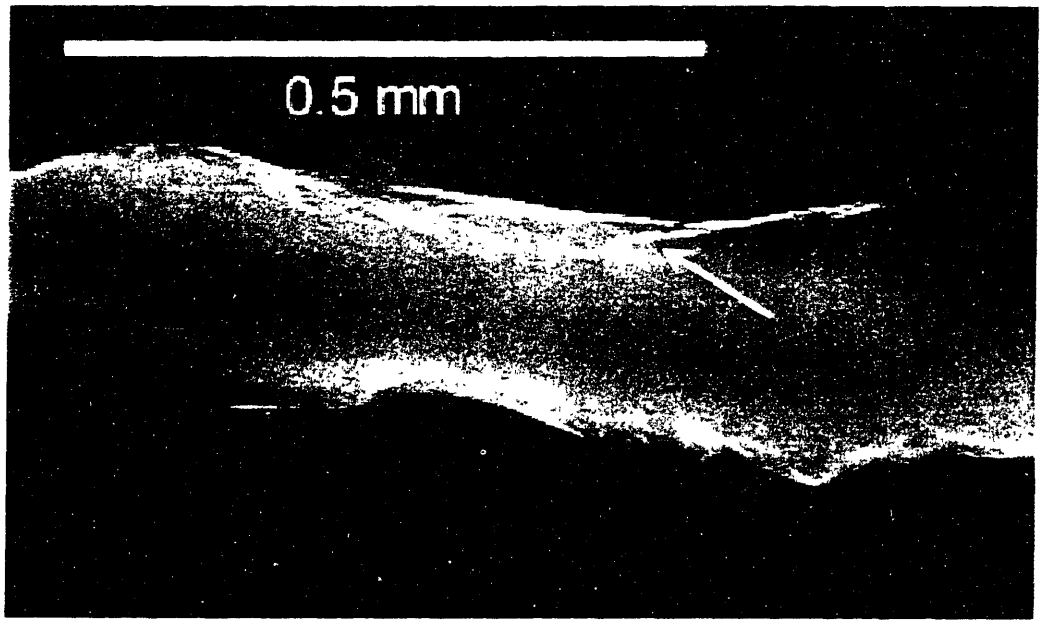

(b)

Figure 5.11: Examples of damage patterns observed. All images are taken from a single specimen tested to -2.0% strain at $1\sigma E_0 = 0.007$. (a) diffusely stained area, without visible cracks, (b) single crack, (c) parallel cracks, (d) cross-hatching, and (e) complete trabecular fracture

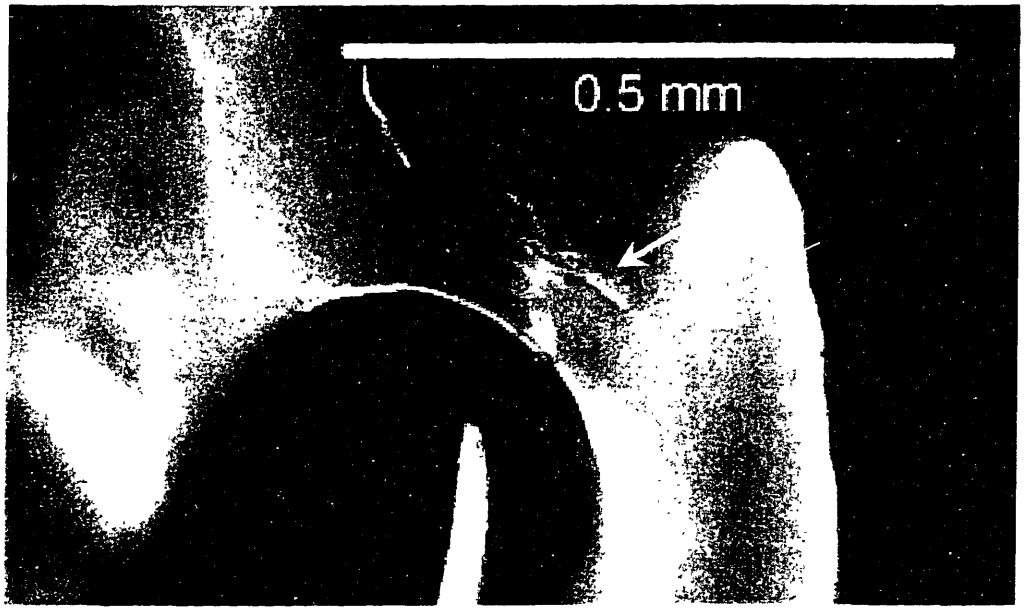

(c)

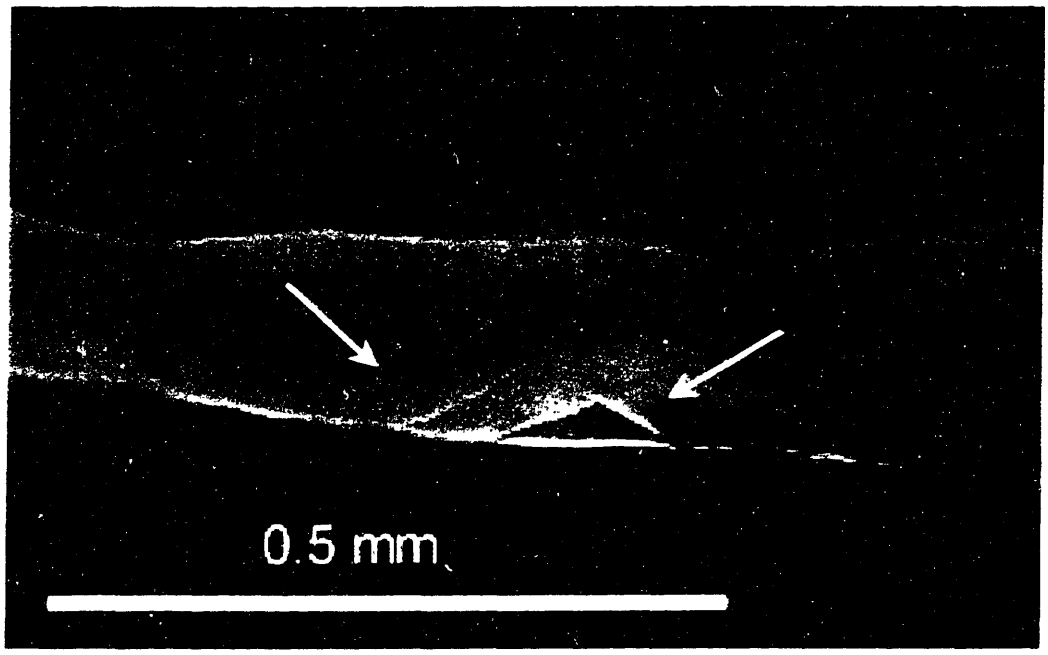

(d)

Figure 5.11: Examples of damage patterns observed. All images are taken from a single specimen tested to -2.0% strain at $\Delta\sigma/E_t = 0.007$. (a) diffusely stained area, without visible cracks, (b) single crack, (c) parallel cracks, (d) cross-hatching, and (e) complete trabecular fracture.

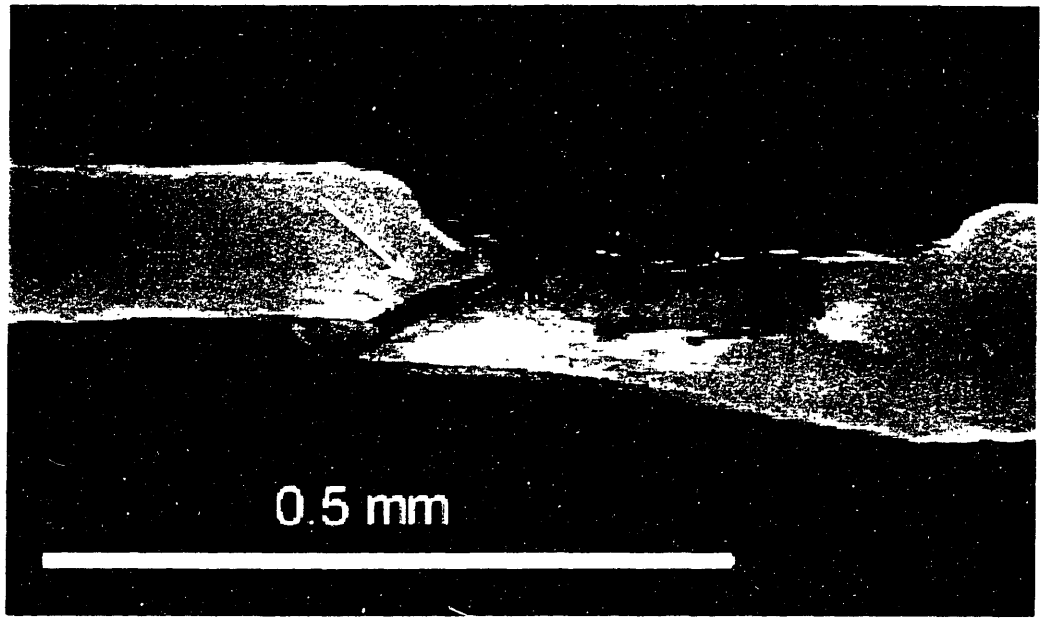

(e)

Figure 5.11: Examples of damage patterns observed. All images are taken from a single specimen tested to -2.0% strain at $.1\sigma/E$ = 0.007. (a) diffusely stained area, without visible cracks, (b) single crack, (c) parallel cracks, (d) cross-hatching, and (e) complete trabecular fracture.

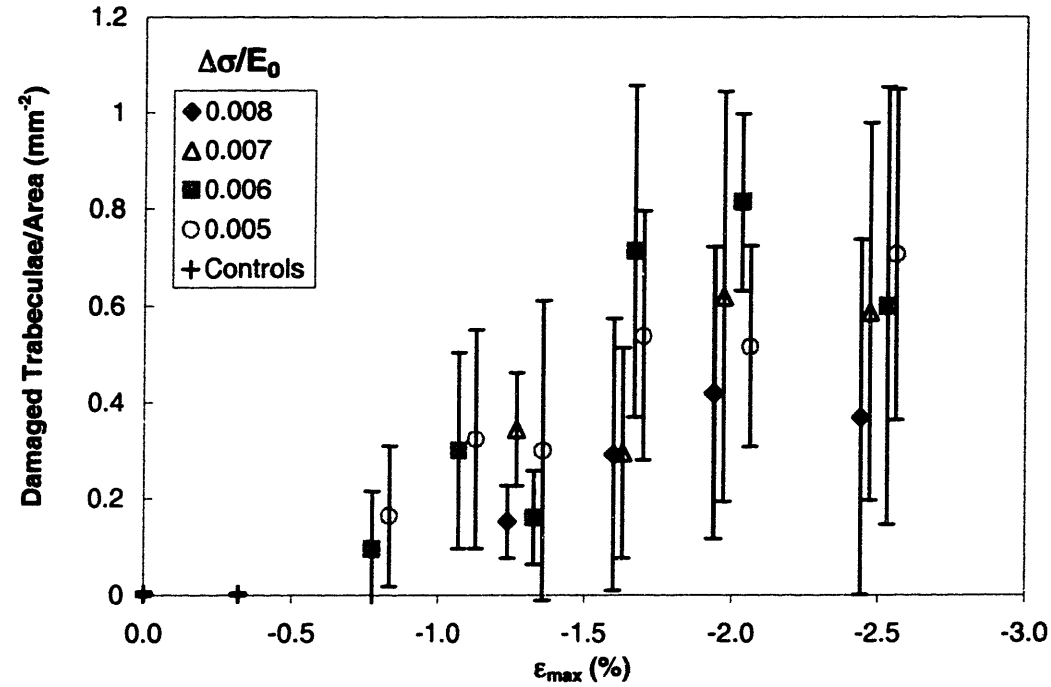

(a)

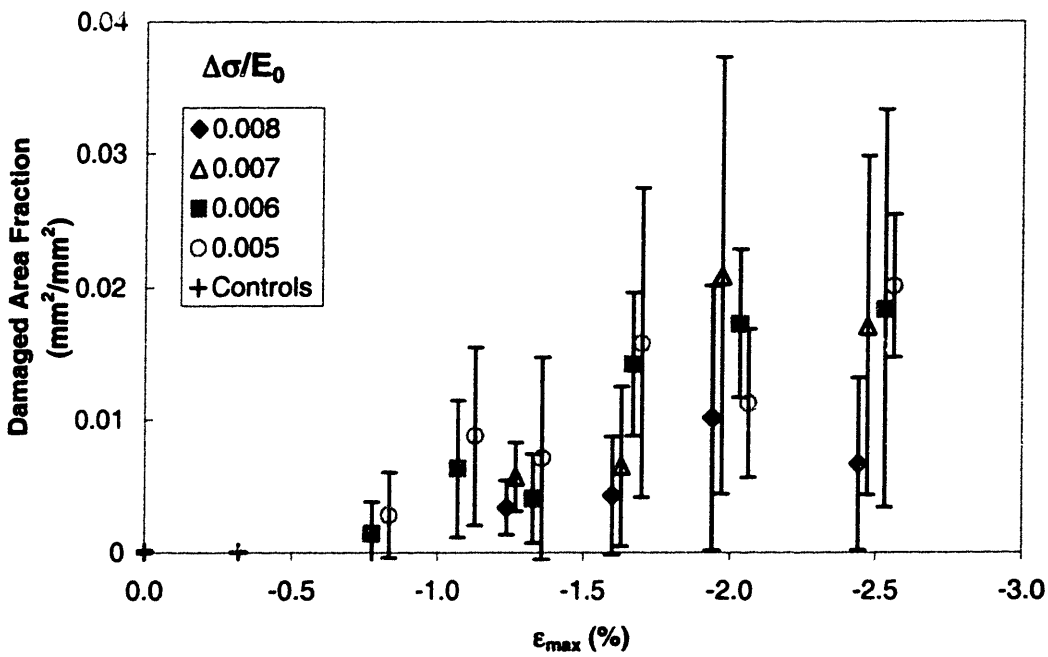

(b)

Figure 5.12: Plot of total number of (a) damaged trabeculae and (b) damaged area fraction vs. maximum compressive strain, ε_{max}. The numbers in the legend represent the normalized stress level. Data at each strain level spread slightly for clarity. Microdamage increases with increasing maximum strain, ε_{max}, after yield.

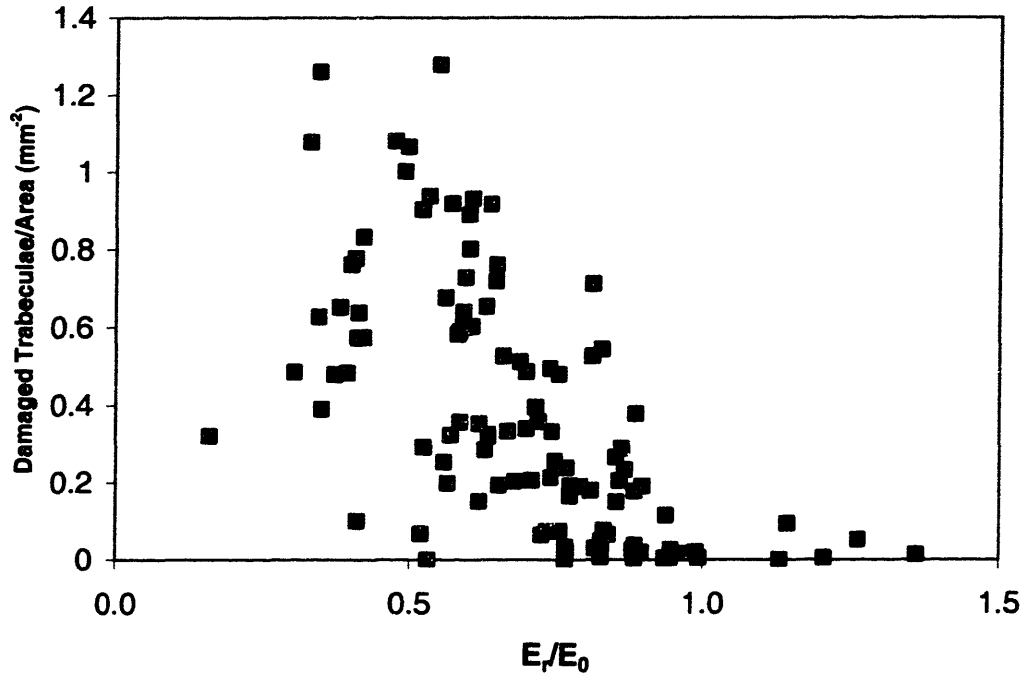

Figure 5.13: Microdamage parameters increased with increasing modulus reduction (decreasing E_r/E_0). The data plotted shows number of damaged trabeculae per unit area, but results are similar for other microdamage parameters.

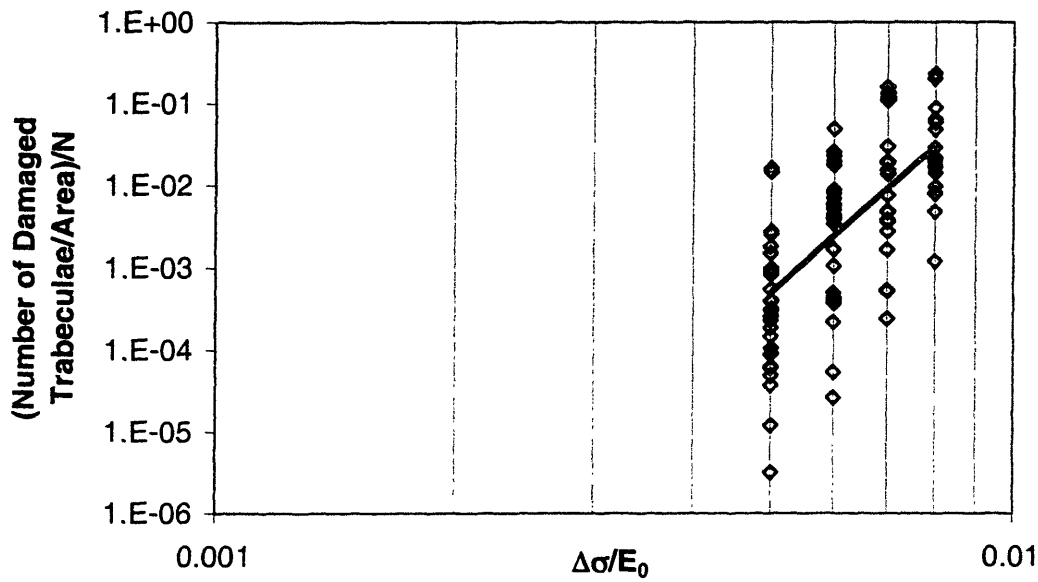

(a)

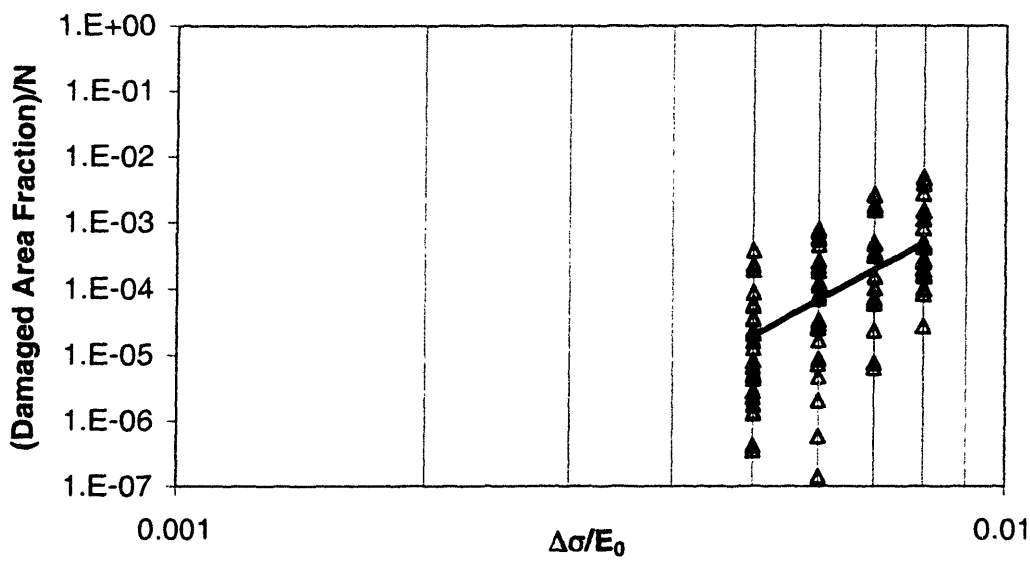

(b)

Figure 5.14: Plots of damage parameters showing the relationship between damage parameters, normalized stress, $\Delta\sigma/E_0$, and number of cycles, N. The damage parameter, D, is: (a) number of damaged trabecular per unit area. ($D/N = 5.26\times10^{16}(\Delta\sigma/E_0)^{8.7}$, $R^2 = 0.39$). (b) damaged area fraction. ($D/N = 1.06\times10^{11}(\Delta\sigma/E_0)^{6.84}$, $R^2 = 0.22$) A weak but significant relationship is seen in both cases.

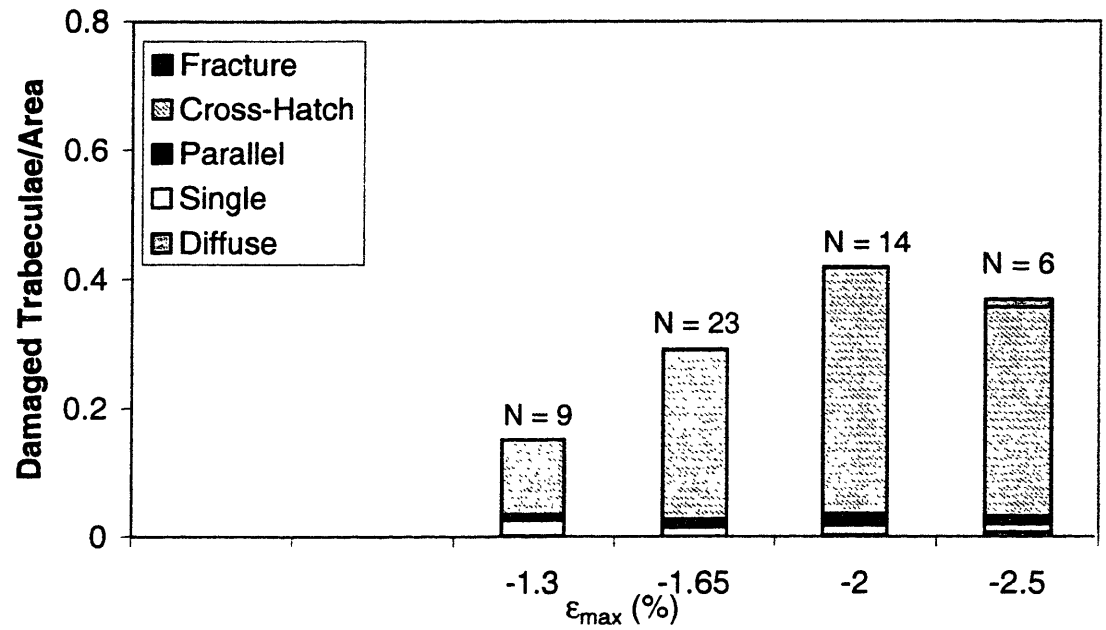

(a)

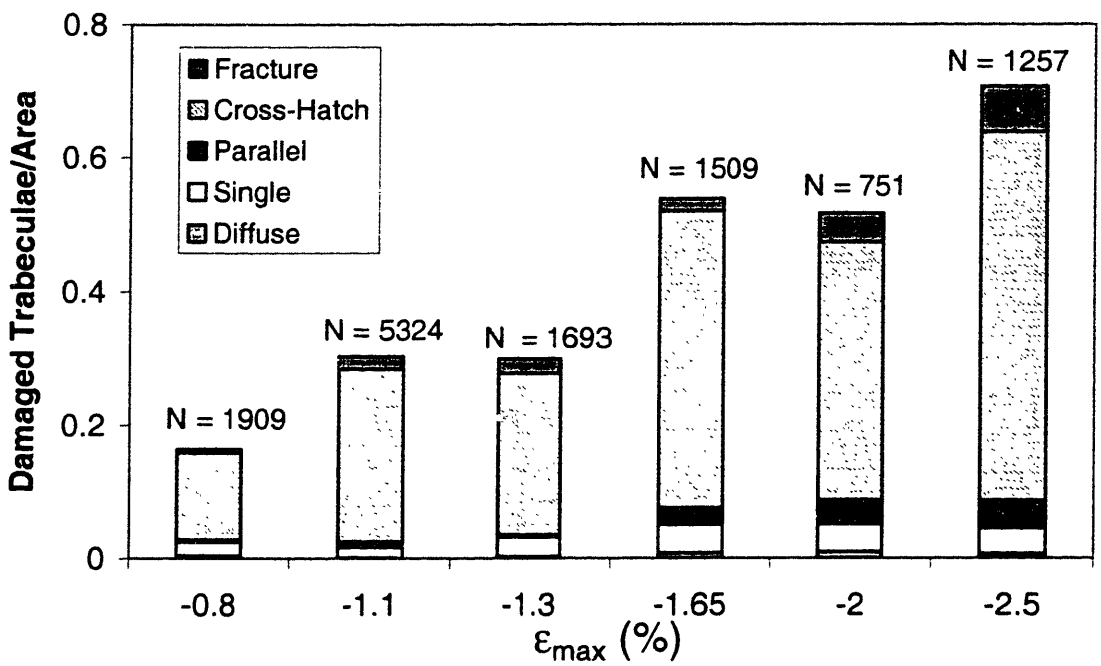

(b)

Figure 5.15: Patterns of microdamage observed in bone specimens, tested to two normalized stress levels. Number of specimens = 5 for each column. The numbers above each column represent the average number of cycles, N, needed to reach the maximum strain. (a) $\Delta\sigma/E_0 = 0.008$. No specimens were tested to strain levels less than $\varepsilon_{max} = -1.3\%$ at this normalized stress. (b) $\Delta\sigma/E_0 = 0.005$.

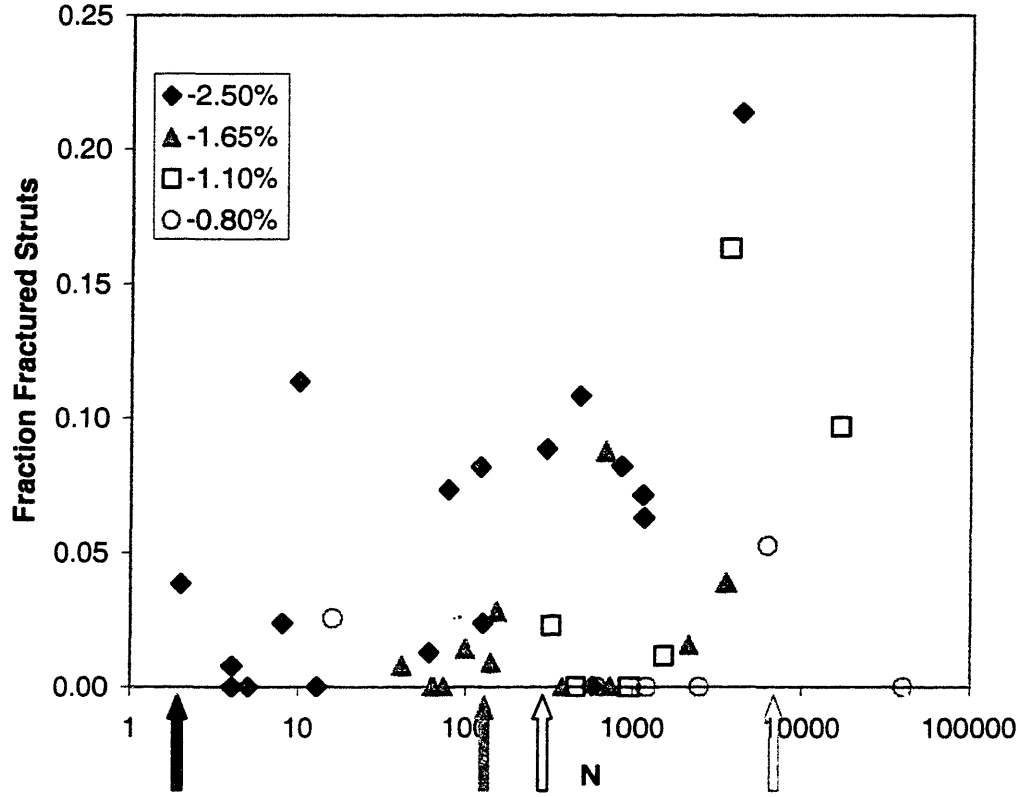

Figure 5.16: Plot of fraction of total trabeculae containing complete fractures. There is a threshold number of cycles needed for fractures to form. This threshold increases with decreasing maximum specimen strain, ε_{max} (arrows).

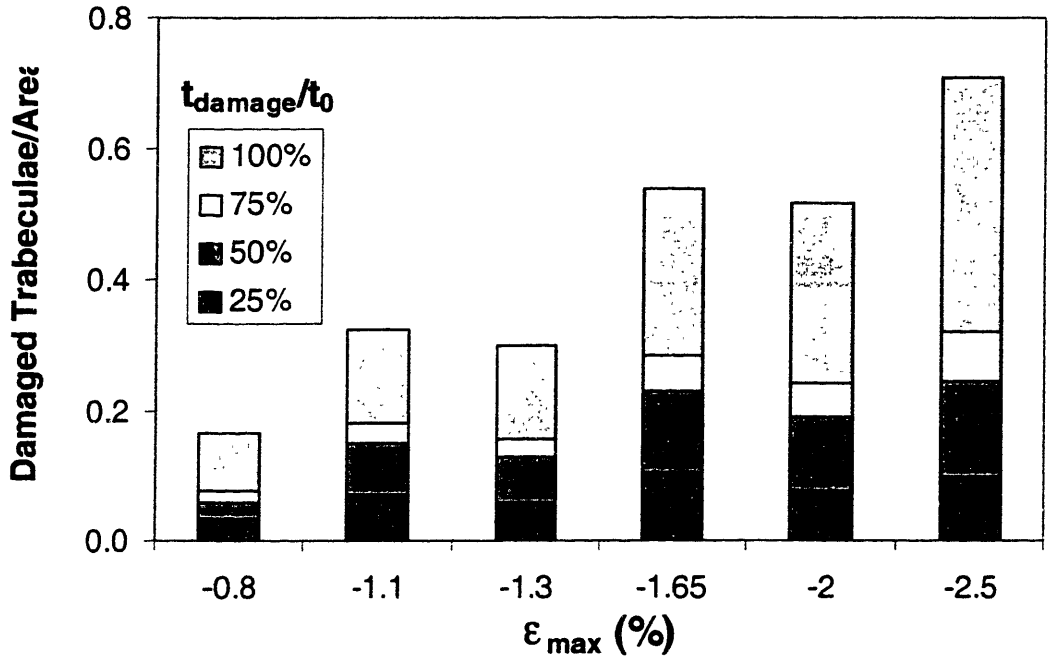

Figure 5.17: Extent of damage across the trabecular strut, rounded to the nearest one-quarter for specimens tested at a normalized stress of $\Delta\sigma/E_0 = 0.005$. Values were estimated to the nearest quarter. The trabecular damage extends all the way across the specimen approximately half the time. Relatively few cracks extend 75% of the distance across the trabecula. Results are typical for other normalized stress levels.

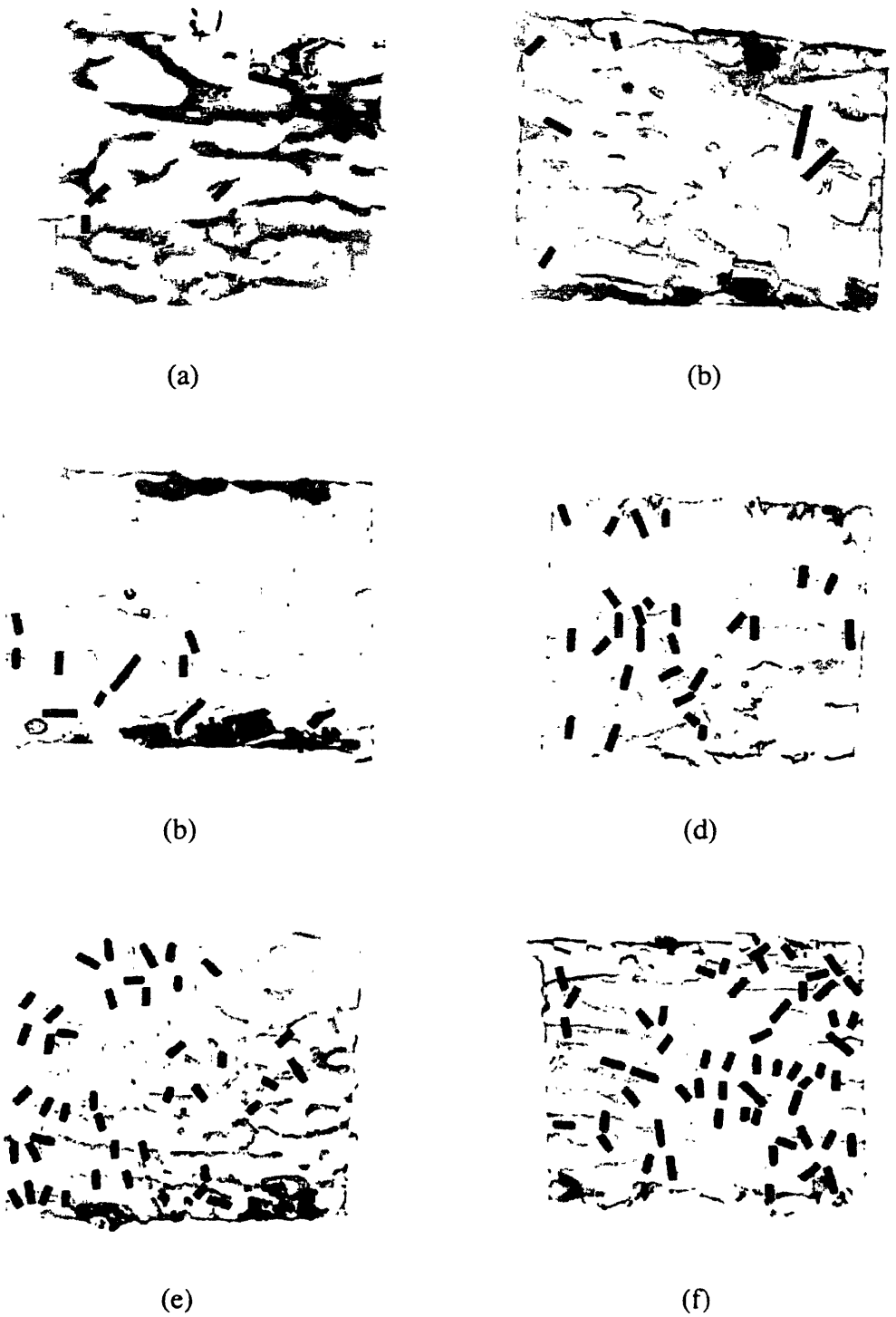

Figure 5.18: Progression of damage in typical sections. Each mark represents a damaged trabecula. All specimens shown here were tested (when applicable) at the same normalized stress level of $\Delta\sigma/E_0 = 0.006$. (a) untested control, (b) $\varepsilon_{max} = -0.8\%$, (c) $\varepsilon_{max} = -1.1\%$, (d) $\varepsilon_{max} = -1.3\%$, (e) $\varepsilon_{max} = -1.65\%$, (f) $\varepsilon_{max} = -2.0\%$, (g) $\varepsilon_{max} = -2.5\%$.

5.4 Model Predictions

The model developed for bovine trabecular bone tested in compression (Chapter 4) was applied directly to the data from 110 fatigue-tested specimens (**Figure 5.19**). This initial fit showed that the current model did not predict fatigue modulus losses as well as it did modulus losses in monotonic compression-tested specimens for either the rod or plate models, with the model only explaining approximately 40% of the variation in E_f/E_0 (**Table 5.7**).

To improve the fit, the model was adapted at the specimen level to better describe the general case of localized damage. In the initial model, all damage was assumed to occur in a distinct band across the specimen, as was observed in the experimental compression-tested specimens. Some specimens tested in fatigue showed this distinct band, but many others showed a local region of damage that did not extend across the specimen (**Figure 5.20**). In the initial estimate (**Figure 5.19**), all localized damage was assumed to be a band across the specimen with the same damaged area as the measured area. The equation for the final modulus, E', was extended from

$$\frac{E'}{E_0} = \frac{1}{1 + \frac{L_2}{L_0}\left(\frac{E_0}{E_2} - 1\right)} \tag{5.3}$$

in Chapter 4, to

$$\frac{E'}{E_0} = \frac{L_0 E_2 \left(E_2 d_1 + E_0 d_2\right)}{E_2^2 d_1 L_1 + \left(E_0\right)^2 d_2 L_2 + E_2 E_0 \left(d_2 L_1 + d_1 L_2 + \left(d_1 + d_2\right) L_3\right)} \tag{5.4}$$

where E' is the specimen damaged modulus, E_0 is the initial modulus, E_2 is the modulus in the localized damaged region, L_0 is the total specimen length, and L_1, L_2, L_3, d_1, and d_2 describe the size of the localized damaged area (**Figure 5.20**). The use of the general case appeared to improve the predicted results at moderate modulus reductions (E_f/E_0 from 0.5 – 0.8) (**Figure 5.21**), but overall fit parameters were unchanged (**Table 5.7**). The model did not appear to predict modulus reductions better when specimens loaded to different normalized stress levels were examined separately (**Figure 5.22**).

	Closed-Cell (Plate)				Open-Cell (Rod)			
	Slope	Int.	R^2	R_c^2	Slope	Int.	R^2	R_c^2
Monotonic (all specimens)	1.00* (0.08)	0.01 (0.05)	0.82	0.81	1.13* (0.09)	-0.16* (0.06)	0.83	0.75
Monotonic (n = 31)	1.02* (0.08)	-0.02 (0.05)	0.85	0.84	1.14* (0.09)	-0.18* (0.06)	0.85	0.75
Fatigue (Forced Band)	0.74* (0.09)	0.17* (0.07)	0.39	0.38	1.03* (0.12)	-0.20* (0.09)	0.41	0.23
Fatigue (general)	0.74* (0.09)	0.21* (0.06)	0.39	0.38	1.02* (0.12)	-0.11 (0.09)	0.42	0.31
Fatigue (no $E_r/E_0 > 1$)	0.83* (0.10)	0.16* (0.07)	0.38	0.34	1.15* (0.14)	-0.19 (0.10)	0.40	0.27

* significantly different from zero ($p < 0.05$)

Table 5.7: Summary of model fit parameters for a variety of different cases discussed in the text. Numbers in parentheses represent standard deviations. Data from monotonic compression tests are included for comparison.

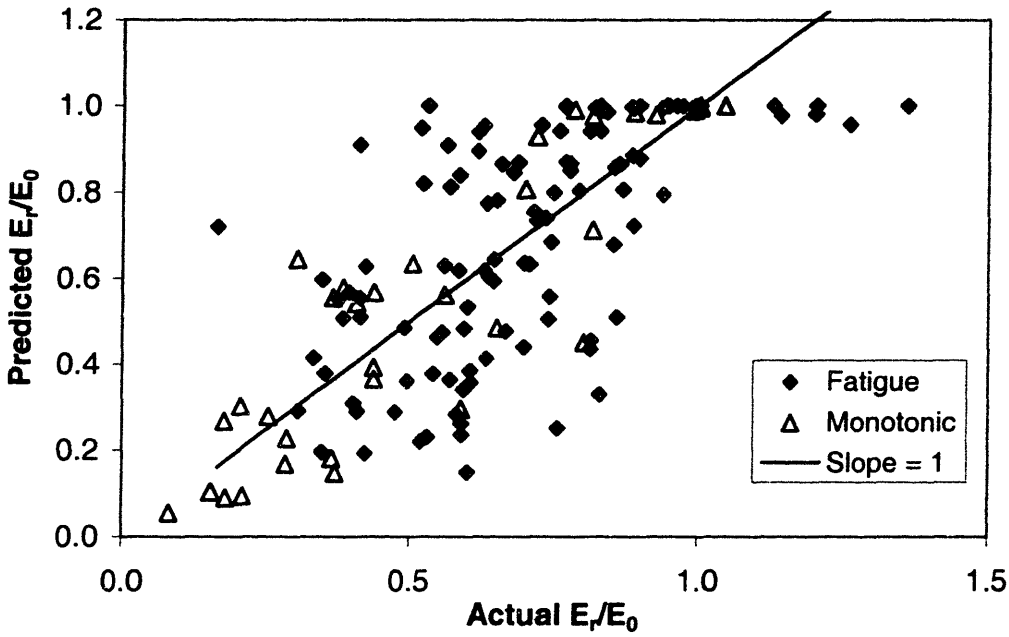

(a)

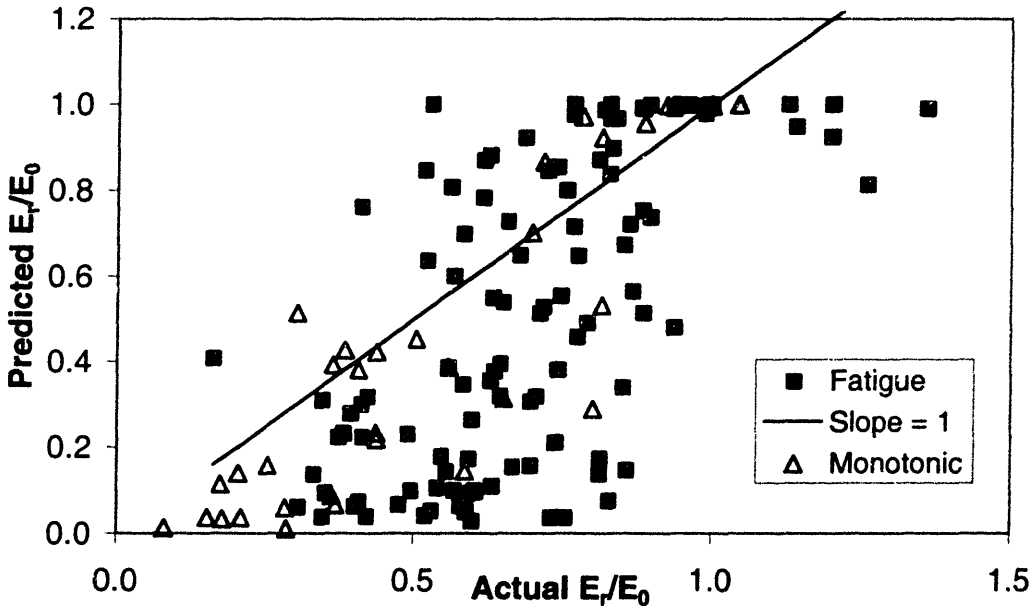

(b)

Figure 5.19: Comparison of model parameters with experimental results. Values for the monotonic tests (open triangles) are included for comparison. The solid line represents perfect agreement between the predicted and experimentally measured values. The correlation coefficient, R^2, and the concordance correlation, R_c^2, of the line Y = X were determined. (a) Closed-cell, plate model. ($Y = 0.74X + 0.17$, $R^2 = 0.39$, $R_c^2 = 0.38$) (b) Open-cell rod model. ($Y = 1.03X - 0.20$, $R^2 = 0.41$, $R_c^2 = 0.23$).

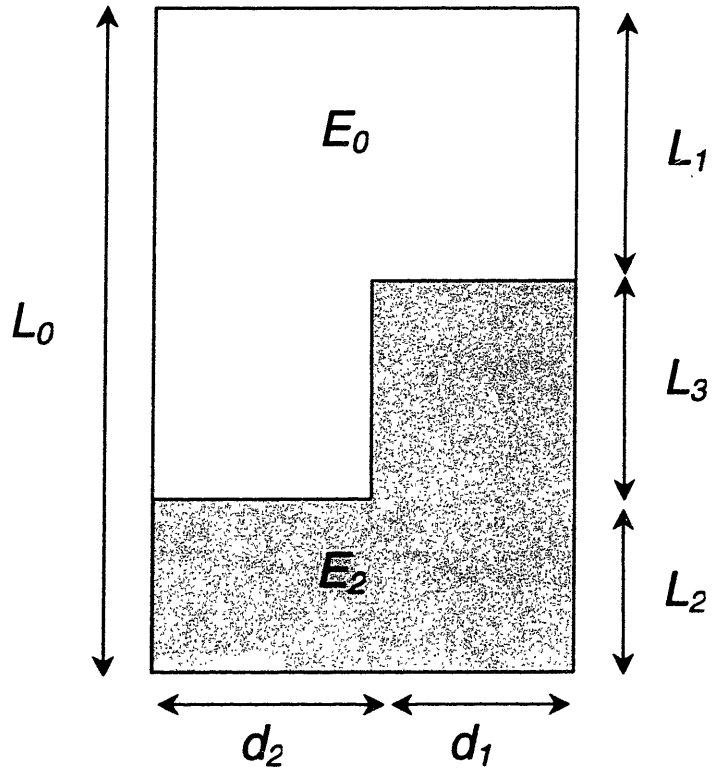

(a)

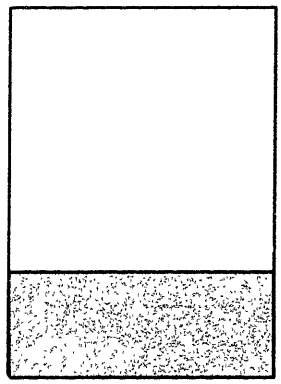

(b)

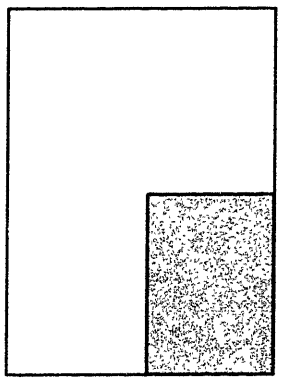

(c)

Figure 5.20: (a) General case of localized damage from an unwaisted fatigue specimen. Usually, damage forms (b) a band ($L_3 = 0$) or (c) a patch of damage ($L_2 = 0$). Compressive loading occurs in the vertical direction.

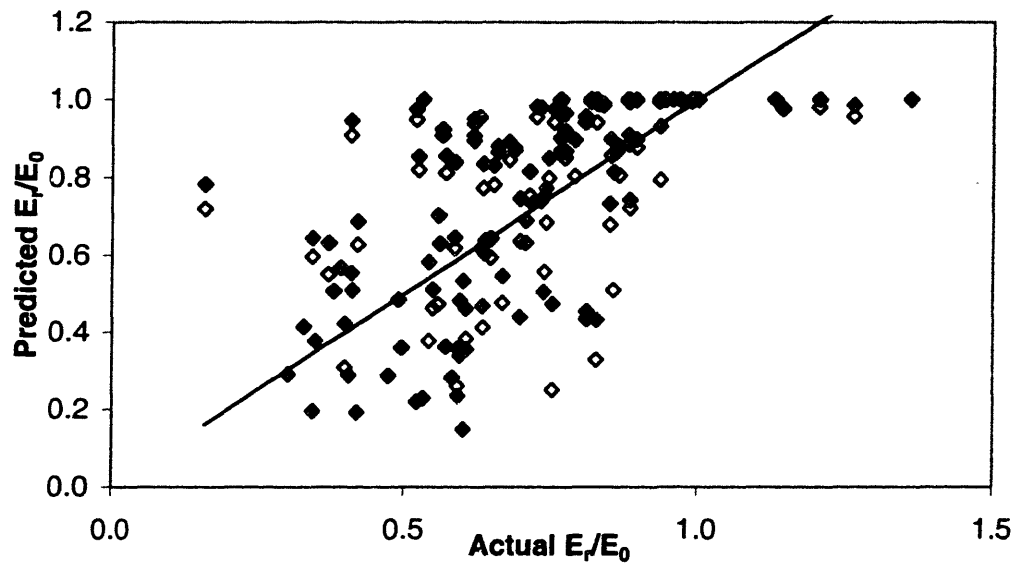

(a)

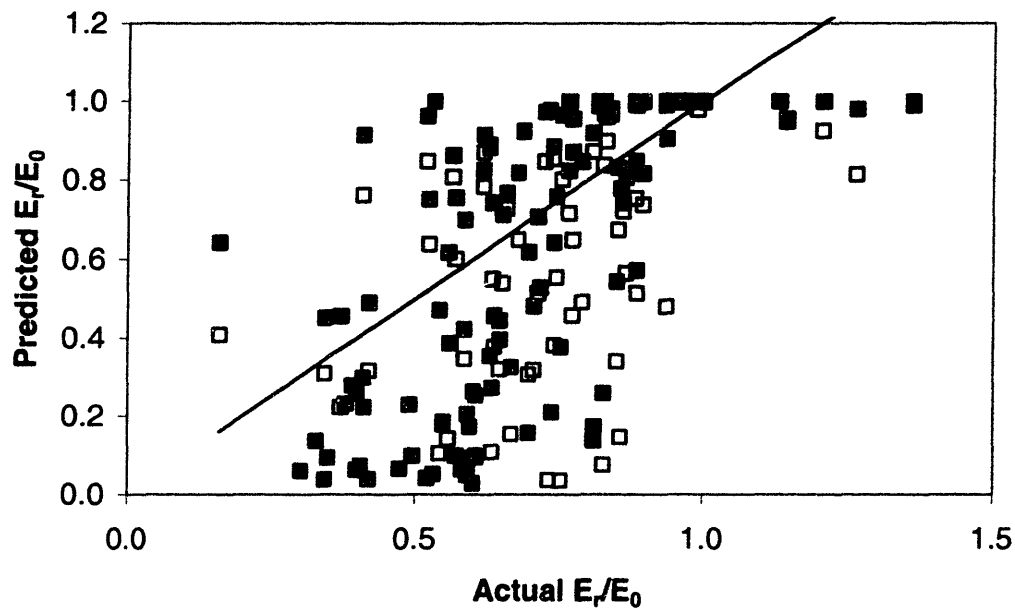

(b)

Figure 5.21: An improvement in model predictions was seen when the general equation was used to determine modulus reduction due to localized damage (closed symbols). The initial calculation (open symbols) assumed that damage always formed a distinct band. The solid line represents perfect agreement between the predicted and experimentally measured values. (a) Closed-cell, plate model ($Y = 0.74X + 0.21$, $R^2 = 0.39$, $R_c^2 = 0.38$). (b) Open-cell rod model ($Y = 1.02X - 0.11$, $R^2 = 0.42$, $R_c^2 = 0.31$).

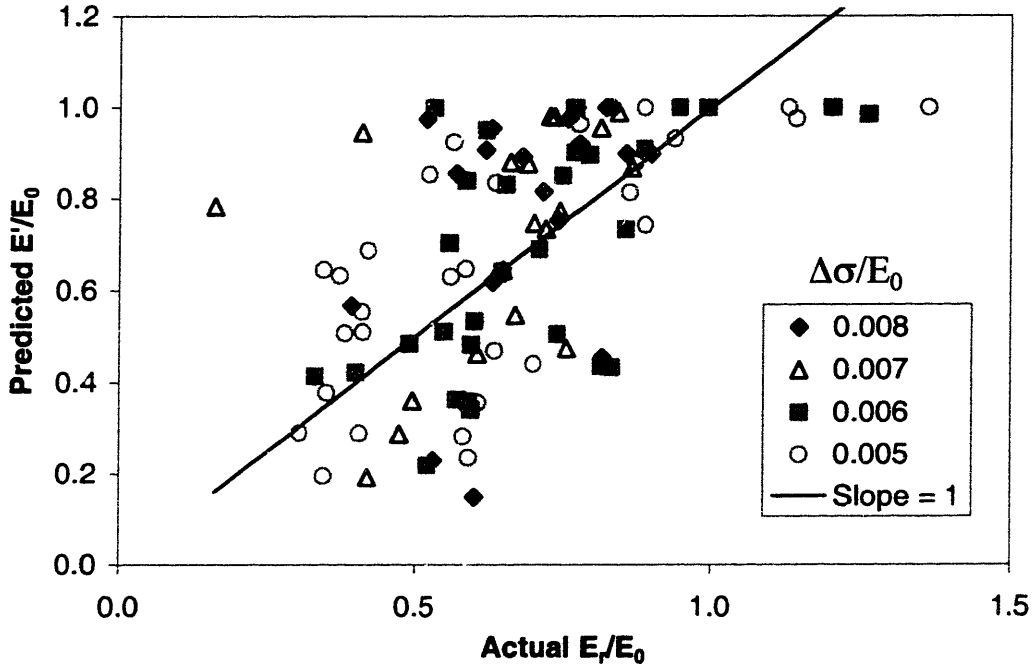

(a)

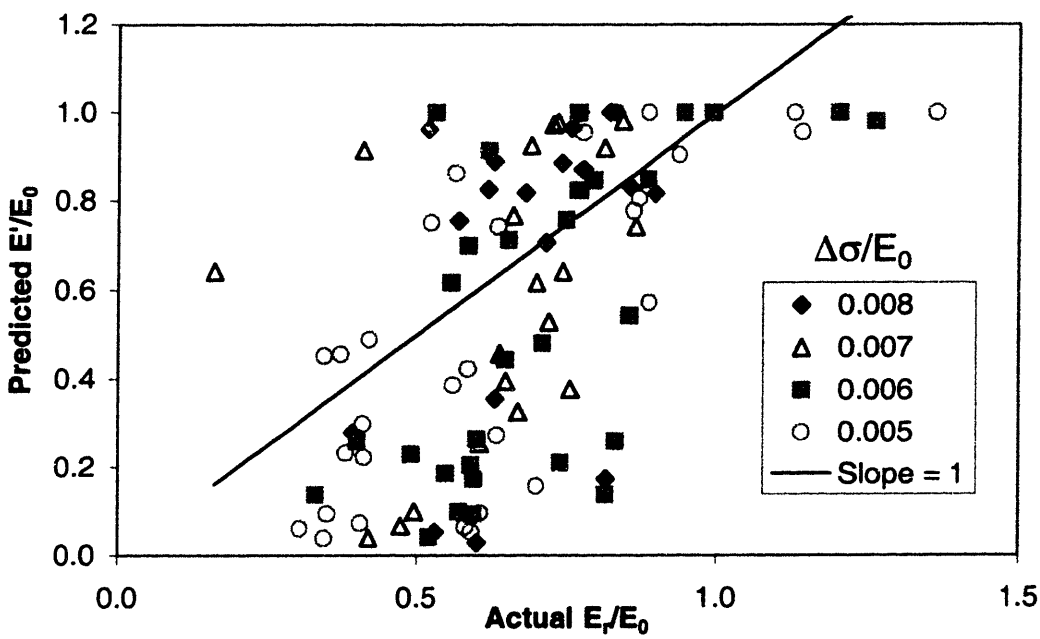

(b)

Figure 5.22: Breakdown of model predictions by normalized stress level for the (a) closed-cell and (b) open-cell model. The model predictions do not improve when each normalized stress is examined separately.

5.5 Discussion

This study examined mechanical property changes during compressive fatigue of bovine trabecular bone and observed that the reloading modulus reduction, E_r/E_0 (**Figure 5.7**), the secant modulus reduction, E_{sec}/E_0 (**Figure 5.8**), and the residual strain, ε_{res} (**Figure 5.9**), were linearly related to the maximum strain, ε_{max}. The fatigue behavior of trabecular bone could be explained using the Basquin Law ($(\Delta\sigma/E_0)N^a = C_1$), for all specimens, or the Coffin-Manson Law ($\Delta\varepsilon_{pl}N^b = C_1$), for specimens tested to less than 100 cycles. These relationships were independent of normalized stress, $\Delta\sigma/E_0$, and number of cycles, N, supporting a strain-based failure criterion for bone. The concept of a strain-based failure criteria will be investigated further in the following chapter, which studies the relationships between mechanical property changes and microdamage accumulation in trabecular bone specimens tested in different loading modes, including monotonic compression, compressive fatigue, and compressive creep (Pierce, 1999).

Regressions from this study predicted that minimum strain levels ($\varepsilon_{max} \approx$ -0.5%)were necessary before changes were observed in the reloading modulus (E_r/E_0 = 1 at ε_{max} = -0.44%, **Figure 5.7b**), the secant modulus ($E_{sec}/E_0 = 1$ at ε_{max} = -0.64%, **Figure 5.8b**), and the residual strain, ($\varepsilon_{res} = 0$ at ε_{max} = -0.55%, **Figure 5.9b**). As well, microdamage is not observed at maximum strains below approximately -0.5% (**Figure 5.12**). These results indicate that a threshold strain, or endurance limit, exists, near -0.5%, below which no microdamage accumulates, and no mechanical property changes are observed. Such a damage strain threshold was found at 4000 $\mu\varepsilon$ in compressive fatigue tests of human cortical bone (Pattin *et al.*, 1996). As well, characterizations of the fatigue behavior of bovine trabecular bone (Guo, 1993; Guo *et al.*, 1994; Cheng, 1995; Appendix B; **Figure 5.1**) has shown evidence of a fatigue endurance limit for bovine trabecular bone at a normalized stress level of about $\Delta\sigma/E_0$ = -0.035 for compression.

At strains above the threshold strain, loading bovine trabecular bone in fatigue produces changes in mechanical properties throughout the test, including increasing modulus reduction, E_{sec}/E_0 and increasing plastic strain accumulation, ε_{res} throughout the

test (**Figure 5.3**). As the specimen neared failure, modulus reductions per cycle and strain accumulation per cycle increased dramatically and failure occurred rapidly after a modulus loss of approximately 10 – 15%, and maximum strains of approximately -0.8% (**Figure 5.4**). The slope of the S-N curves for specimens loaded to different maximum strains were similary, because all the maximum strains chosen occurred beyond the "knee" of the modulus reduction versus number of cycles curve (**Figure 5.4**), when failure was imminent.

Differences in the slope of the S-N curves for different strains may also not have observed due to the amount of scatter in the data. There were typically two, and up to three orders of magnitude of scatter in the S-N curve (**Figure 5.5**). Considerable scatter, however, is also present in fatigue tests of traditional engineering materials, with a considerably less complex architecture than trabecular bone. For example, Figure 12.10 in (Hertzberg, 1989), shows scatter of approximately two orders of magnitude for a solid aluminum alloy. Low cycle fatigue (N < 100 cycles) followed the Coffin-Manson law, with a power law relationship between the change in plastic strain in one cycle, $\Delta\varepsilon_{pl}$, and the number of cycles, N (**Figure 5.6**). A transition exists between low cycle fatigue (dominated by plastic strain) and high cycle fatigue (dominated by stress, see **Figure 5.5**). Results from the plastic strain-based Coffin-Manson law suggest that this transition occurs at approximately 100 cycles (**Figure 5.6**), but there is too much scatter in the data to determine where the transition occurs in the stress-based plot (**Figure 5.5**). Additional tests at low normalized stresses and high numbers of cycles are necessary to identify the cutoff between stress- and strain-controlled fatigue. We observed less scatter in the data when the strain amplitude, $\Delta\varepsilon_{pl}$, was used to plot fatigue results (R^2 = 0.82) and more scatter when the stress amplitude was used (R^2 = 0.62). However, we did not observe any relationships between strain amplitude and microdamage parameters.

In five fatigue-tested specimens, the value of reloading modulus, E_r, increased during the test (**Figure 5.7, 5.8, Table 5.2**). This occurred in specimens tested at the two lowest normalized stresses, $\Delta\sigma/E_0$ = 0.006 and $\Delta\sigma/E_0$ = 0.005, to low strains, ε_{max} = -0.8% and ε_{max} = -1.1%. We believe this occurred because the initial specimen modulus, E_0, was underestimated in the original measurement. In these specimens, the loading modulus of the first fatigue cycle, E_1, was larger than the initial modulus, E_0, and the

modulus increased over subsequent cycles until a plateau value near the reloading modulus, E_r, was reached after usually 5-10 cycles. Microdamage accumulation in all five specimens was negligible, so we assume that little, if any, changes in mechanical properties took place. Underestimation of initial modulus may have also occurred in other specimens; however, preliminary analysis has not indicated this.

Microdamage observations in fatigue-tested specimens showed similar patterns of cracking for as those observed in specimens tested in uniaxial compression (**Figure 5.11**). As in those tests, little damage is present *in vivo,* as observed in the control specimens. Damage observations in control specimens were seen on the outer surface of the specimen and most likely occurred during specimen preparation. The unwaisted fatigue specimens had less damage present before testing than the waisted cylindrical specimens used for monotonic compression testing, probably because waisting the specimens on a lathe created additional damage.

All microdamage parameters increased with increasing maximum specimen strain after yield (**Figure 5.12**) and also increased with increasing modulus reduction, E_r/E_0 (**Figure 5.13**). Microdamage parameters were best explained by the maximum strain, ε_{max}, residual strain, ε_{res}, secant modulus reduction, E_{sec}/E_0, and the number of cycles, N. No significant differences in total amounts of microdamage were observed in specimens tested to the same maximum strain at different normalized stresses. However, as hypothesized by Martin (1992), a weak but significant relationship was found when microdamage was taken to be a function of normalized stress and number of cycles (**Figure 5.14**). This relationship has implications for physiologic loading, as human bone is loaded *in vivo* for a relatively large number of cycles at very low strains (or normalized stresses). According to this relationship, normal physiologic damage accumulation per cycle will be considerably less than that observed in this study.

While we observed no relationship between total microdamage accumulation and normalized stress level, some differences were noted when the damage was broken down by damage patterns. With decreasing normalized stress, $\Delta\sigma/E_0$, the average number of cycles increases (**Figure 5.4**), allowing opportunities for crack initiation and growth in later cycles. Increased opportunities for crack initiation were expected to decrease the proportion of single cracks seen in specimens tested to a large number of cycles, which

was observed (**Figure 5.15**). Crack growth in later cycles was expected to increase the proportion of trabecular fractures in specimens tested to high numbers of cycles, which was also observed (**Figure 5.15**) and to increase the proportion of damaged trabeculae containing cracks across the thickness in those specimens (100% of the way across the thickness), which was not observed (**Figure 5.17**). The presence of trabecular fractures was associated with a threshold number of cycles, below which no fractures were observed. This threshold increased with decreasing maximum strain (**Figure 5.16**). For example, trabecular fractures were observed in specimens tested to -1.1% strain, but only in those specimens loaded for more than 1000 cycles.

Overall, the progression of microdamage accumulation with increasing strain (**Figure 5.18**) was similar to observations made in specimens tested in uniaxial compression (Chapter 3, **Figure 3.11**). On loading to low strain levels, little change in modulus with increasing cycles was measured, and correspondingly little damage was observed. However, small cracks did form at low strains (**Figure 5.18**). Microdamage began to accumulate by strain levels of -0.8%. These cracks grew in subsequent cycles, leading to a slow accumulation of damage and even trabecular fracture in a local area. Eventually, the specimen reached a critical point, where microdamage accumulation (and specimen strain) began to increase rapidly (**Figure 5.4**). At that point, the damage band began to form. then elongated and the damage within the band densified. During this time, complete trabecular fractures were observed. Once the complete fractures extended across the specimen cross-section, specimen fracture had occurred.

The specimen geometry used for fatigue tests was an unwaisted cylindrical specimen, while previous tests used waisted cylindrical specimens. Damage and failure were confined to the gauge length in the waisted specimens; in contrast, damage may occur anywhere along the cylinder in unwaisted specimens, including near the specimen ends. The unwaisted cylinder was glued into brass end caps to minimize end effects, then the end caps were removed after testing by cutting the bone flush with the end caps. Some damage may have been present outside of the region cut out for microdamage analysis, but less than 3 mm of bone was removed from either end of the specimen, and the cut ends were glued in place and are expected to be stiffer than the rest of the specimen.

Considerably more scatter was seen in fatigue-tested specimens than in the monotonic compression samples analyzed previously (Chapter 3). Because only five specimens were tested at each combination of normalized stress and maximum strain, it was difficult to draw statistically significant conclusions from these data. Power analysis from the monotonic compression study indicated that more than twenty-five specimens would need to be tested for each category to achieve statistical significance; we expect that similar numbers of specimens would be needed for a comparable fatigue analysis. Microdamage analysis for so many specimens would be prohibitive. We feel that the initial study performed here shows the progression of microdamage and identifies areas to be studied in more detail in later work.

We previously developed a model to predict changes in modulus based on observed microdamage parameters in monotonic compression-tested specimens (Chapter 4). This model was applied to specimens tested in compressive fatigue. The correlations between model predictions and experimental results were significant, but weaker than that obtained for monotonic compression-tested specimens ($R_c^2 = 0.38$ versus $R_c^2 = 0.81$ for the closed-cell model) (**Figure 5.19**). Modifications to the model did not improve the predictions (**Figure 5.21**). Specimens loaded in fatigue showed considerably more scatter in the experimental data, so it is not unexpected that the model predictions also show more scatter. However, the model consistently underpredicted actual results at low modulus reductions and overpredicted actual modulus reductions in specimens with large amounts of damage. These trends were also observed when the model predictions were compared to specimens tested in monotonic compression (Chapter 4).

The model underpredicted modulus reductions at modulus reductions near $E_r/E_0 = 1$. The model assumptions required that microdamage be present for a modulus reduction to occur; no observed microdamage resulted in no predicted change in modulus. Other studies have not observed microdamage until 15 - 30% of the original modulus has been lost (Burr *et al.*, 1998). Presumably, this initial modulus reduction occurs as a result of another mechanism not observable by light microscopy. This inability to predict small modulus reductions is a serious limitation of the model. In specimens tested to higher modulus reductions, where significant microdamage was

present, some damage may have been present outside the region used for microdamage analysis, which could also explain some of the underprediction.

The model also overpredicted modulus reduction at high modulus reductions. We assumed that the observed damage extended through the depth of the trabeculae, based on our two-dimensional observations of damage. Therefore, any crack that was observed to extend across the entire trabecula was assumed to completely eliminate the load-carrying capacity of that strut. However, it is likely that some of these cracks do not extend all the through the depth of the trabeculae (in three dimensions) and the strut retains some load-carrying capacity, particularly in compressive loading. Thus, the actual modulus reduction, E'/E_0, will be larger than that predicted by this model. As well, even completely fractured trabeculae may retain some load-carrying capacity in compression, when the crack surfaces are in contact.

Observations of fatigue-damaged specimens showed a relationship between number of cycles and microdamage parameters for fatigue-tested specimens (**Figure 5.14**). The relationship between modulus reduction and number of cycles was less strong, and we found no evidence to support a relationship between modulus reduction and normalized stress level for a given strain (**Figure 5.7**). As well, modulus reduction showed a small but significant dependence on density-related parameters (relative density, ρ^*/ρ_s, and initial modulus, E_0), while microdamage parameters were not dependent on density. This suggests that different damage formation mechanisms are present in different loading modes, and no generalized model can predict modulus reduction based solely on microdamage observations. As well, both modulus reduction and microdamage parameters depend on maximum strain and number of cycles, neither of which are accounted for in this model.

Chapter 6: Comparison of Microdamage Accumulation in Specimens Tested in Different Loading Modes

Abstract

Specimens were tested in a variety of loading modes (uniaxial compression, fatigue, and creep (Pierce, 1999)) and mechanical properties and microdamage parameters were measured. The original analysis, described in the previous chapters, attempted to classify microdamage based on maximum compressive strain and modulus reduction. Changes in mechanical properties and microdamage accumulation were compared in specimens tested in different loading modes, including monotonic compression, compressive fatigue at different normalized stress levels, and compressive creep (Pierce, 1999). In general, relationships between mechanical properties and microdamage accumulation were similar for specimens tested to the same maximum strain in different loading modes. No changes in mechanical properties and no microdamage accumulation was observed at low strains. Residual strain after testing was significantly higher in fatigue-tested specimens than in either monotonic or creep specimens. Microdamage was significantly higher in fatigue specimens at strains near yield.

6.1 Introduction

During the activities of daily living, bone is loaded in a variety of ways, including static loading, repetitive activities at high and low physiologic loads, and isolated instances of overloads. The load levels, loading rates, and frequency of occurrences varies. However, all loading types have been shown to cause damage in the form of reduced mechanical properties and microdamage accumulation in cortical and trabecular bone. We are not aware of any studies comparing microdamage accumulation parameters in trabecular bone specimens tested in different loading modes.

There is some evidence that a relationship exists between mechanical properties and loading parameters. A weak power law relationship (exponent of 0.05 - 0.07) has

been observed between stiffness and strain rate, and between strength and strain rate (Carter and Hayes, 1977c; Linde *et al.*, 1991) in bovine trabecular bone. However, fatigue studies of cortical bone have suggested that there is increased damage formation at high strain rates (Schaffler *et al.*, 1989). McCubbrey *et al.* (1990) found that the failure of whole human vertebrae tested in static and fatigue loading configurations were best predicted by density measurements from different localized regions of the vertebrae, suggesting that local failure in monotonic compression and fatigue depends on different components of bone architecture. These studies described mechanical property changes with loading mode but did not examine microdamage accumulation.

Our study of fatigue microdamage (Chapter 5) showed an increase in damage with increasing normalized stress and number of cycles (**Figure 5.12**). However, we did not observe a relationship between microdamage and number of cycles in specimens tested to the same modulus reduction, although we expected that microdamage would continue to increase in later cycles. Based on our fatigue results and strain rate observations, we expect that specimens tested at high normalized stress and high strain rates (monotonic compression, low cycle fatigue) will have more microdamage accumulation than specimens tested at lower normalized stresses and strain rates (creep, high cycle fatigue).

The original analyses, described in Chapters 3 and 5, classified microdamage based on maximum compressive strain and modulus reduction for specimens tested in uniaxial compression and compressive fatigue. As well, mechanical property and microdamage data were available from a preliminary study of microdamage accumulation in bovine bone specimens tested in compressive creep (Pierce, 1999). This chapter compares microdamage parameters and mechanical properties for specimens tested in different loading modes, including uniaxial compression, high and low cycle compressive fatigue, and compressive creep.

We asked the following questions: (1) Does loading mode affect the mechanical properties of specimens tested to the same maximum strain or modulus reduction?, and (2) Does loading mode affect microdamage accumulation in specimens tested to the same maximum compressive strain or modulus reduction in different loading modes?.

6.2 Materials and Methods

Specimens were tested in three different loading modes: uniaxial compression, compressive fatigue, and compressive creep (**Table 6.1**). All compression (n = 38) and creep (n = 13) tests were performed using waisted cylindrical specimens of bovine trabecular bone taken from the proximal tibia (Keaveny *et al.*, 1994a). Fatigue tests (n = 110) were performed on unwaisted cylindrical specimens of bovine trabecular bone taken from the proximal tibia, using a modified version of the specimen geometry developed by Keaveny *et al.* (1997). All bone specimens were glued into brass end caps to minimize end effects. Because of the differences in specimen geometry, specimens may contain differences in microdamage that are a result of changes in experimental techniques and specimen geometries instead of resulting from changes in loading mode (Linde *et al.*, 1992). All specimens have similar diameters of approximately 6.0 mm (actual values varied within 5%), so size effects are not anticipated to be large.

Loading Type	ε_{max} (%)	Number	Loading Type	ε_{max} (%)	$\Delta\sigma/E_0$	Number
Monotonic	0.0	4	Fatigue	Control		5
Monotonic	-0.4	2	Fatigue	Modulus		5
Monotonic	-0.8	2	Fatigue	-1.3	0.008	5
Monotonic	-1.1	5	Fatigue	-1.65	0.008	5
Monotonic	-1.3	5	Fatigue	-2.0	0.008	5
Monotonic	-2.0	5	Fatigue	-2.5	0.008	5
Monotonic	-2.5	5	Fatigue	-1.3	0.007	5
Monotonic	-3.0	5	Fatigue	-1.65	0.007	5
Monotonic	-4.0	5	Fatigue	-2.0	0.007	5
Creep	-0.45	1	Fatigue	-2.5	0.007	5
Creep	-1.1	4	Fatigue	-0.8	0.006	5
Creep	-1.3	2	Fatigue	-1.1	0.006	5
Creep	-2.0	3	Fatigue	-1.3	0.006	5
Creep	-2.5	2	Fatigue	-1.65	0.006	5
Creep	-3.6	1	Fatigue	-2.0	0.006	5
			Fatigue	-2.5	0.006	5
			Fatigue	-0.8	0.005	5
			Fatigue	-1.1	0.005	5
			Fatigue	-1.3	0.005	5
			Fatigue	-1.65	0.005	5
			Fatigue	-2.0	0.005	5
			Fatigue	-2.5	0.005	5

Table 6.1: Overview of all tested specimens, including monotonic compression, compressive creep, and compressive fatigue tests.

All specimens were radiographed, and test specimens were selected such that the specimen axis corresponded with the trabecular orientation. Specimens were kept moist throughout the specimen preparation process, and kept frozen at -18°C between processing steps. Before testing, the diameter of each specimen was measured six (6) times with a digital calipers and the cross-sectional area was calculated.

Prior to testing, all specimens were stained with a chelating fluorochrome, which labeled all damage present *in vivo* as well as that created during specimen preparation. Specimens were stained overnight at room temperature and pressure with either oxytetracycline (n = 7, all monotonic compression tests) or alizarin complexone (remainder of tests).

All compression and fatigue tests were performed in a servohydraulic testing machine (Instron Corp., Canton MA). Details of monotonic compression and fatigue testing can be found in Chapters 3 and 5 respectively. Specimens undergoing monotonic compression tests were loaded in strain control at 0.5%/sec to one of nine (9) predetermined strains (**Table 6.1**) and unloaded to zero strain at the same strain rate. Mechanical properties measured included the initial modulus, E_0 (measured as the slope of the loading curve from -0.1% to -0.4%), the secant modulus, E_{sec}, the maximum strain, ε_{max}, and the residual strain at zero load, ε_{res}.

Fatigue tests were performed in a servohydraulic testing machine (Instron Corp., Canton MA) with the specimen placed between two platens (one fixed, one self-aligning). The specimens were pre-conditioned for ten (10) cycles in strain control from 0.0% strain to -0.3% strain, and the initial modulus, E_0, was measured. The specimen was then fatigued in load control at 2.0 Hz to one of four normalized stresses and stopped when a predetermined maximum compressive strain, ε_{max}, was reached. After testing, the reloading modulus, E_r, was measured as the slope of the loading curve during a single compression cycle from 0.0% to -0.3% strain. Mechanical properties measured included the initial modulus, E_0, the maximum strain, ε_{max}, the residual strain after testing, ε_{res}, and the reloading modulus, E_r.

Thirteen compressive creep tests were performed in a separate study (Pierce, 1999). The initial modulus, E_0, of creep specimens was measured non-destructively in a servohydraulic testing machine under displacement control prior to creep loading. The initial modulus, E_0, was defined as the slope of the loading curve from -0.1% to -0.4%. All creep tests were performed in a custom designed jig that placed a static load on the specimen. A miniature extensometer measured strain throughout the test. When the specimen reached a predetermined strain, or was about to fracture, the load was removed (**Figure 6.1**). Mechanical properties measured included the initial modulus, E_0, the time to stop, t_{stop}, the maximum strain, ε_{max}, and the residual strain after unloading, ε_{res}.

After all tests, the loaded portion of the specimen was removed (either the nominal waisted region, in the case of waisted specimens, or the entire bone specimen between the end caps, in unwaisted specimens) from the end caps with a diamond saw (Isomet Low Speed Saw, Buehler, Lake Bluff IL), and the marrow was removed from the

cut ends. The specimen was stained overnight in a second fluorochrome (calcein (green) in most cases; xylenol orange was used in 4 of the 7 monotonic compression tests stained originally with oxytetracycline; the other 3 tests stained with oxytetracycline did not have a second stain, but the oxytetracycline diffused into all cracks, allowing microdamage observations). The specimens were then dehydrated in ethanol, embedded in poly(methyl methacrylate), and cut into thin sections on a diamond saw. Section areas were measured from projections of the entire section (ImageTool 1.25, UTHSCSA, San Antonio TX), and the bone area fraction was measured by thresholding techniques, as described in previous chapters.

Several microdamage parameters were measured in each specimen, including damaged area fraction, number of damaged trabeculae (including patterns of damage and extent of damage across the thickness), and size of the localized damage band. As well, number and length of individual cracks were counted in the uniaxial compression and creep specimens. Individual cracks were not counted in fatigue specimens. Values for the size of the damaged band were not compared between fatigue-tested specimens and other loading modes due to differences in specimen geometry. To avoid interuser bias, all microdamage parameters were measured by the same investigator, which included re-measurement of microdamage parameters in all creep specimens.

Specimens tested to the same maximum strain or the same modulus reduction in different loading modes (uniaxial compression, creep, and fatigue) were compared to determine if there was a difference in mechanical properties or microdamage accumulation based on loading mode. Fatigue specimens tested at different normalized stresses were compared to each other in Chapter 5; in the cases where no significant differences were found, the data were pooled. Microdamage parameters, including number of damaged trabeculae, damaged area fraction, crack number, and crack length) for fatigue, creep, and monotonic compression specimens tested to the same strain were compared using t-tests when sufficient specimens were available for analysis. Multiple linear regressions were performed on monotonic and creep data, and the results were compared to multiple linear regressions performed previously on fatigue-tested specimens (Chapter 5).

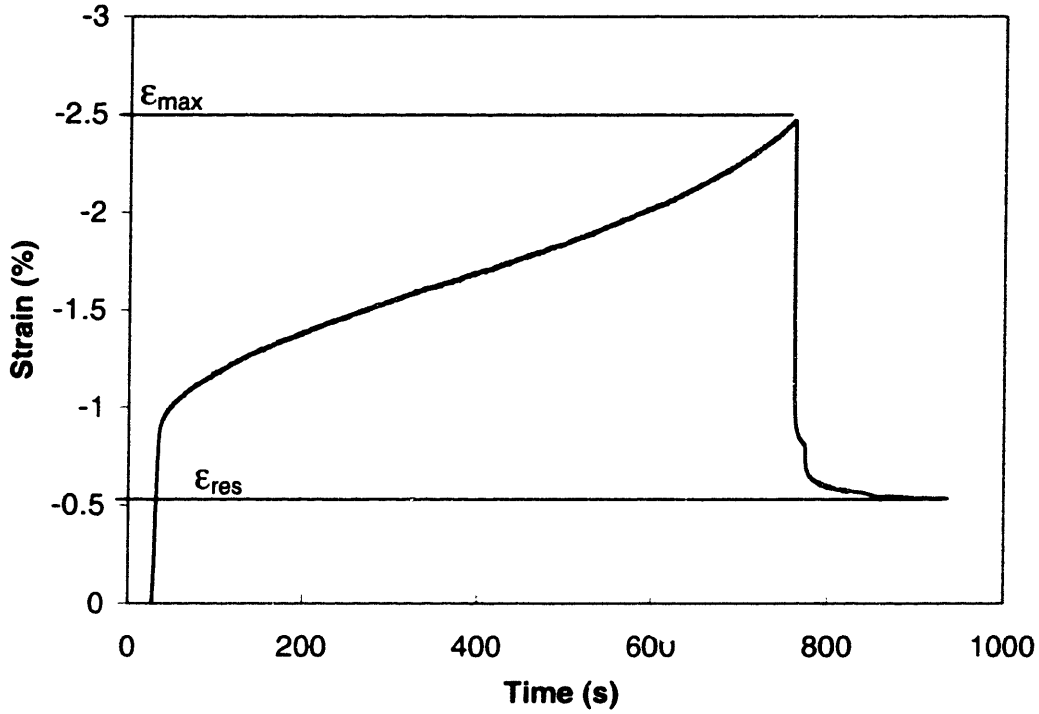

Figure 6.1: Typical creep test, specimen 65E, loaded at $\Delta\sigma/E_0 = 0.0082$ to $\varepsilon_{max} = -2.5\%$ strain. The specimen shows typical creep behavior, with a primary, secondary, and tertiary regime. A residual strain, ε_{res}, was present on unloading.

6.3 Results

The stress-strain curves for monotonic compression and cyclic loading in fatigue were shown in **Figure 3.1** and **Figure 5.3** respectively. A typical creep curve, taken from Pierce (1999), is shown in **Figure 6.1**. Mechanical properties and microdamage parameters were measured for monotonic compression (Appendix C), fatigue (Appendix D), and creep (**Table 6.2, 6.3, 6.4**). Creep microdamage parameters were re-measured by the author to avoid bias from different operators. There were no significant differences in the mean initial moduli, E_0, between monotonic compression specimens (2.60 ± 1.21 GPa), fatigue specimens (2.07 ± 0.79 GPa), and creep specimens (2.89 ± 0.93 GPa) ($p > 0.05$). The specimen geometry used for creep and monotonic compression specimens had a greater section area (312 ± 70 mm^2 for monotonic compression, 367 ± 70 mm^2 for creep, $p > 0.05$) than that used for fatigue specimens (188 ± 40 mm^2). However, the bone area fractions were not significantly different between loading types (compression, 0.43 ± 0.09; fatigue, 0.46 ± 0.08; creep, 0.47 ± 0.04, $p > 0.05$).

Specimen	E_0 (GPa)	$\Delta\sigma/E_0$	ε_{max} (%)	ε_{res} (%)	Section Area (mm^2)[a]
57B	3.140	0.0081	-0.45	0	271.91
67B	1.909	0.0090	-1	-0.37	508.73
82B	1.810	0.0065	-1.08	-0.23	303.50
78A	3.250	0.0065	-1.08	-0.29	365.25
79F	4.660	0.0040	-1.09	-0.36	310.74
81B	2.450	0.0055	-1.29	-0.27	407.11
84B	2.670	0.0060	-1.4	-0.29	362.70
83C	3.380	0.0070	-1.92	-0.52	472.75
85B	2.920	0.0055	-2.11	-0.97	387.23
72A	4.400	0.0082	-2.19	-0.37	314.78
65E	2.590	0.0082	-2.46	-0.46	329.28
80B	1.440	0.0065	-2.56	*	311.46
82G	3.000	0.0065	-3.6	-0.91	419.26

*data acquisition error; no measurement taken
[a]total specimen area

Table 6.2: Mechanical property data for all creep tests (Pierce, 1999).

Specimen	Damage Band Length (mm)	Damaged Trabeculae /Area (mm^{-2})	Damaged Area Fraction (mm^2/mm^2)	Cr.Num. /Area (mm^{-2})	Cr.Len. /Area ($\mu m/mm^2$)	Mean Cr.Len. (μm)
57B	0.000	0.023	0.0002	0.06	4.95	89.80
67B	0.000	0.008	0.0003	0.03	2.78	88.52
82B	4.356	0.145	0.0033	0.70	59.64	84.98
78A	0.194	0.022	0.0010	0.14	13.74	100.41
79F	0.669	0.064	0.0020	0.31	30.62	99.11
81B	2.406	0.162	0.0052	0.95	79.90	84.49
84B	0.880	0.077	0.0013	0.35	30.22	87.00
83C	6.047	0.503	0.0174	4.58	351.75	76.84
85B	2.512	0.168	0.0057	1.31	134.97	102.68
72A	3.489	0.705	0.0224	6.52	478.24	73.33
65E	7.077	0.371	0.0234	7.44	555.50	74.69
80B	3.423	0.363	0.0046	2.20	136.42	61.94
82G	3.929	0.172	0.0065	2.02	138.47	68.38

[a]length of the section of the specimen containing damage

[b]total number of trabeculae containing damage in the section, normalized by specimen section area

[c]total area of the localized regions of damage, normalized by specimen section area

[d]total number of cracks in the specimen, normalized by specimen section area

[e]total length of cracks in the specimen, normalized by specimen section area

[f]Cr.Len./Cr.Num.

Table 6.3: Microdamage data for all creep tests.

Specimen	Single	Parallel	Cross-Hatch	Fracture	25%	50%	75%	100%	Total
57B	2	3	3	0	4	2	0	2	8
67B	1	1	1	1	2	1	0	1	4
82B	9	6	29	0	18	8	2	16	44
78A	3	0	5	0	3	1	1	3	8
79F	3	0	17	0	5	4	3	8	20
81B	10	5	51	0	23	16	8	19	66
84B	9	6	13	0	12	9	1	6	28
83C	9	8	218	3	55	52	40	91	238
85B	7	1	58	0	11	21	7	26	65
72A	11	12	199	0	65	45	18	94	222
65E	9	13	100	0	32	19	10	61	122
80B	14	10	89	0	30	30	13	40	113
82G	7	5	60	0	21	24	10	17	72

Table 6.4: Breakdown of number of damaged trabecula for all creep tests, by patterns of damage and by the extent of the damage across the trabeculae thickness, rounded to the nearest quarter.

Modulus reductions increased with increasing strain magnitude, ε_{max}, and the modulus reductions were similar for specimens tested to the same maximum strain, ε_{max}, in uniaxial compression and fatigue (**Figure 6.2**). The reloading modulus, E_r/E_0, was not measured for creep specimens. Few significant differences were observed in the modulus reductions of fatigue-tested specimens loaded to the same strain at different normalized stresses (Chapter 5), so the data was pooled for each value of maximum strain, ε_{max}. Monotonic regressions were plotted for all data and over the same range of data available for fatigue specimens (excluding $\varepsilon_{max} > -2.5\%$). Modulus reduction was linearly related to maximum compressive strain for specimens tested in compression and fatigue (monotonic compression: $Y = 0.23X + 1.02$, $p < 0.05$, $R^2 = 0.77$; monotonic compression excluding specimens tested to strains greater than -2.5%: $Y = 0.34X + 1.18$, $p < 0.05$, $R^2 = 0.78$; fatigue: $Y = 0.27X + 1.12$, $p < 0.05$, $R^2 = 0.48$). Multiple linear regressions showed that monotonic secant modulus reduction had a small but significant dependence on initial modulus, E_0, and relative density, ρ^*/ρ_s, but the fit parameters improved only slightly ($E_{sec}/E_0 = 0.817 - 0.086E_0 + 0.23\varepsilon_{max} + 1.101\ \rho^*/\rho_s$, $R^2 = 0.86$). Multiple linear

regressions for fatigue tested specimens did not show a significant relationship between reloading modulus reduction and initial modulus but did find relationships between modulus reduction and normalized stress and between modulus reduction and number of cycles (Eqn. 5.3, $R^2 = 0.73$). Three significant differences were found in modulus reductions between the unpooled fatigue specimens and monotonic compression specimens tested to the same maximum strain, all for specimens tested to -2.0% strain. The modulus reductions, E_r/E_0, for the pooled fatigue data were not significantly different from the monotonic compression modulus reductions, E_{sec}/E_0, except at -2.0% strain. As discussed in Chapter 5, minimum strain thresholds existed at approximately $\varepsilon_{max} = -0.5\%$, below which we do not expect to see damage. The threshold for monotonic compression-tested specimens was lower than that for fatigue-tested specimens ($E_r/E_0 = 1$ at $\varepsilon_{max} = -0.44\%$ for fatigue, at $\varepsilon_{max} = -0.09\%$ for compression, $\varepsilon_{max} = -0.52\%$ for monotonic compression excluding strains greater than -2.5%).

The residual strain, ε_{res}, was similar for specimens tested in monotonic compression and creep to the same maximum strain, ε_{max}. Considerable hysteresis was observed in fatigue-tested specimens, and the residual strain was significantly higher in magnitude for both pooled and unpooled fatigue specimens compared with the monotonic and creep specimens tested to the same maximum strain (**Figure 6.3a**). Slope and intercept results for residual strains of fatigue tests tested to different numbers of cycles or for specimens tested at different normalized stresses were not significantly different, so results were pooled (**Figure 6.3b**). The residual strain, ε_{res}, was linearly related to the maximum strain, ε_{max}, for specimens tested in fatigue ($Y = 0.71X + 0.39$, $p < 0.05$, $R^2 = 0.76$), monotonic compression ($Y = 0.43X + 0.33$, $p < 0.05$, $R^2 = 0.83$, excluding strains greater than -2.5%, $Y = 0.31X + 0.17$, $p < 0.05$, $R^2 = 0.74$) and creep ($Y = 0.26X + 0.003$, $R^2 = 0.65$) (**Figure 6.3b**). Additional input parameters did not improve the regressions significantly in monotonic compression- or creep-tested specimens, but fatigue-tested specimens showed a small dependence on initial modulus and relative density ($\varepsilon_{res} = 0.747\varepsilon_{max} + 65.2(\Delta\sigma/E_0) + 0.121E_0 - 0.213$, $R^2 = 0.84$). Residual strains also increased with increasing modulus reductions for specimens tested in monotonic compression and fatigue. The threshold residual strain level was comparable in fatigue-tested specimens ($\varepsilon_{max} = -0.55\%$) and in monotonic compression-tested specimens

(ε_{max} = -0.77%, ε_{max} = -0.55% when strains greater than -2.5% are excluded). Regressions were not plotted for creep-tested specimens, as only 13 specimens were tested. Weak linear relationships existed between residual strain, ε_{res}, and modulus loss, E/E_0 (**Figure 6.4**). Specimens tested in compression ($Y = 1.43X - 1.36$, $p < 0.05$, $R^2 = 0.64$) were associated with smaller residual strains at a given modulus loss than pooled fatigue-tested specimens ($Y = 1.04X - 1.50$, $p < 0.05$, $R^2 = 0.25$) (**Figure 6.4**).

Microdamage increased with increasing maximum strain, ε_{max}, and increasing modulus reduction, E/E_0 (**Figures 6.5, 6.6, 6.7**). Damage was observed in specimens tested in all loading modes when the specimens exceeded yield (**Figures 6.5, 6.6**). The same patterns of damage (diffuse regions of staining without distinct microcracks, single cracks, parallel cracks, cross-hatching, and complete fractures) were observed in all loading modes, including creep (see **Figure 3.4, 5.9**). Progression of damage with increasing maximum strain, ε_{max}, followed the same sequence in specimens tested in all loading modes: damage began at random locations, then tended to localize around previously damaged trabeculae, and coalesced to form a localized band of damage that grew and densified until specimen fracture (**Figure 3.10, 5.16**). Both the number of damaged trabeculae and the damaged area fraction increased with decreasing modulus loss (**Figure 6.7**). It was difficult to draw conclusions from the data, including regressions, due to the large amount of scatter in the data. The average mean crack length was not significantly different ($p < 0.05$) for specimens tested in monotonic compression (78.4 ± 16.1 μm; n = 38) and creep (84.0 ± 12.6 μm; n = 13), and the crack length frequency distribution of specimens tested in compressive creep were similar to that of specimens tested to the same maximum strain in monotonic compression (**Figure 3.9a, Figure 6.8**). Crack numbers and lengths were not measured in fatigue specimens.

All microdamage parameters increased with increasing strain for fatigue, creep and monotonic compression specimens at strains greater than the yield strain of approximately -0.7% (**Figure 6.5, 6.6**). There were few statistically significant differences in the number of damaged trabeculae per unit area in specimens tested in fatigue, monotonic compression, and creep; most differences were among the fatigue specimens (**Figure 6.5a**). Specifically, we observed significant differences in seven of sixteen comparisons between unpooled fatigue specimens (three of which were at the two

lowest strains and the two lowest normalized stresses) and one of fourteen comparisons between fatigue specimens and creep specimens ($\Delta\sigma/E_0$ = 0.008 at ε_{max} = -1.3%). Statistically significant differences were observed in the number of damaged trabeculae per unit area at all but one strain level (-1.3%) between the pooled fatigue specimens and monotonic compression specimens and at two of the four strains (-1.1%, -2.5%) compared between the pooled fatigue data and the creep data (**Figure 6.5b**).

Regressions of microdamage parameters found that microdamage parameters in fatigue-tested specimens were best explained by the maximum strain, residual strain, secant modulus reduction, and the number of cycles (see Chapter 5: Damaged Band Fraction: R^2 = 0.59, Number of Damaged Trabeculae/Area: R^2 = 0.53, Damaged Area Fraction: R^2 = 0.58, Eqn. 5.5, 5.6, 5.7). Some microdamage parameters (damaged area fraction, crack number, and crack length) in monotonic compression-tested specimens were best explained by the residual strain, ε_{res}, and the initial modulus, E_0, while others (damage band length, number of damaged trabeculae per unit area) were better explained by the modulus reduction, E_{sec}/E_0, and the relative density, ρ^*/ρ_s. The maximum strain was a significant predictor of microdamage accumulation for all microdamage parameters, but multiple regressions using maximum strain explained ten to fifteen percent less of the variation than the regressions shown below (Eqn. 6.1-6.5). There were too few creep-tested specimens available (n = 13) to make significant predictions.

$$\text{Damaged Area Fraction} = -0.0108 + 0.0045E_0 - 0.016\varepsilon_{res}$$
$$p < 0.05, R^2 = 0.74 \quad (6.1)$$

$$Cr.Num./\text{Area} = -5.55 + 1.58E_0 - 9.59\varepsilon_{res}$$
$$p < 0.05, R^2 = 0.71 \quad (6.2)$$

$$Cr.Len./\text{Area} = -393 + 124E_0 - 612\varepsilon_{res}$$
$$p < 0.05, R^2 = 0.74 \quad (6.3)$$

$$\text{Damage Band Length} = 3.37 + 4.67\rho^*/\rho_s - 5.29E_{sec}/E_0$$
$$p < 0.05, R^2 = 0.72 \quad (6.4)$$

$$\text{Number of Damaged Trabeculae/Area} = 0.202 + 0.706\rho^*/\rho_s - 0.517\, E_{sec}/E_0$$
$$p < 0.05 \text{ for all slopes, intercept } p = 0.07, R^2 = 0.69 \quad (6.5)$$

There were no statistically significant differences between damaged area fractions in unpooled fatigue specimens tested to the same strains and monotonic compression and creep specimens. (**Figure 6.6a**). However, we found statistically significant differences between the pooled fatigue damaged area fraction and the damaged area fractions for both monotonic compression and creep specimens at strains of ε_{max} = -0.8% and ε_{max} = -1.1% (**Figure 6.6b**). There was consistently more scatter in the fatigue specimens than in specimens tested in monotonic compression and compressive creep at strains near yield (**Figure 6.6b**).

Crack number and length measurements were similar in specimens tested in monotonic compression and creep to the same maximum strain (**Figure 6.8**). The crack length histogram showed a peak frequency near 50 μm, similar to that seen in monotonic compression-tested specimens (**Figure 3.7**). As mentioned previously, there were no significant differences in the mean crack length.

Values of damage band length, crack numerical density (*Cr.Num.*/Area), and crack length density (*Cr.Len.*/Area) increased with increasing maximum strain, ε_{max}, for specimens tested in creep and monotonic compression (**Figure 6.9, 6.10**). No statistically

significant differences were found between these two loading modes for any microdamage parameters. Crack number and length were not measured for fatigue-tested specimens, and the differing specimen geometry prevented a comparison of damage band length between fatigue and the other specimens.

The same patterns of microdamage (diffuse staining, single cracks, parallel cracks, cross-hatching, and fracture) were observed in specimens tested in monotonic compression, fatigue and creep. When the number of damaged trabeculae was broken down by pattern (**Figure 6.11**), no differences were seen in the proportions of different patterns with either increases in maximum strain or changes in loading mode, except with trabecular fractures. The proportion of trabecular fractures increased with increasing maximum strain for specimens tested in monotonic compression and at all normalized stress levels of compressive fatigue (**Figure 6.12**). More trabecular fractures were observed in specimens tested in fatigue at low normalized stresses (high number of cycles) than in specimens tested in fatigue at high normalized stresses or in monotonic compression-tested specimens. Fractured trabeculae were seen at lower maximum strain, ε_{max}, in fatigue specimens, especially those tested at low normalized strains (high number of cycles), than in monotonic compression specimens (**Figure 6.12**). Only one creep specimen contained any fractures (**Table 6.4**). The breakdown of damaged trabeculae by extent of damage across the thickness (25%, 50%, 75%, or 100%) was unaffected by changes in loading mode or by changes in normalized stress in fatigue-tested specimens (**Figure 6.13**).

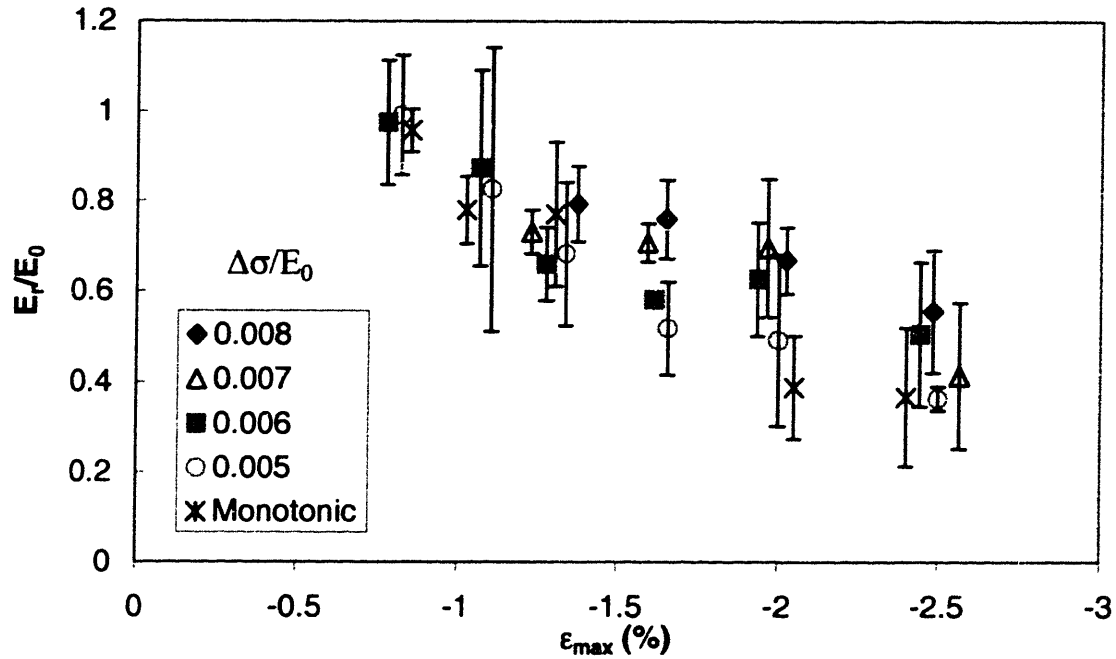

(a)

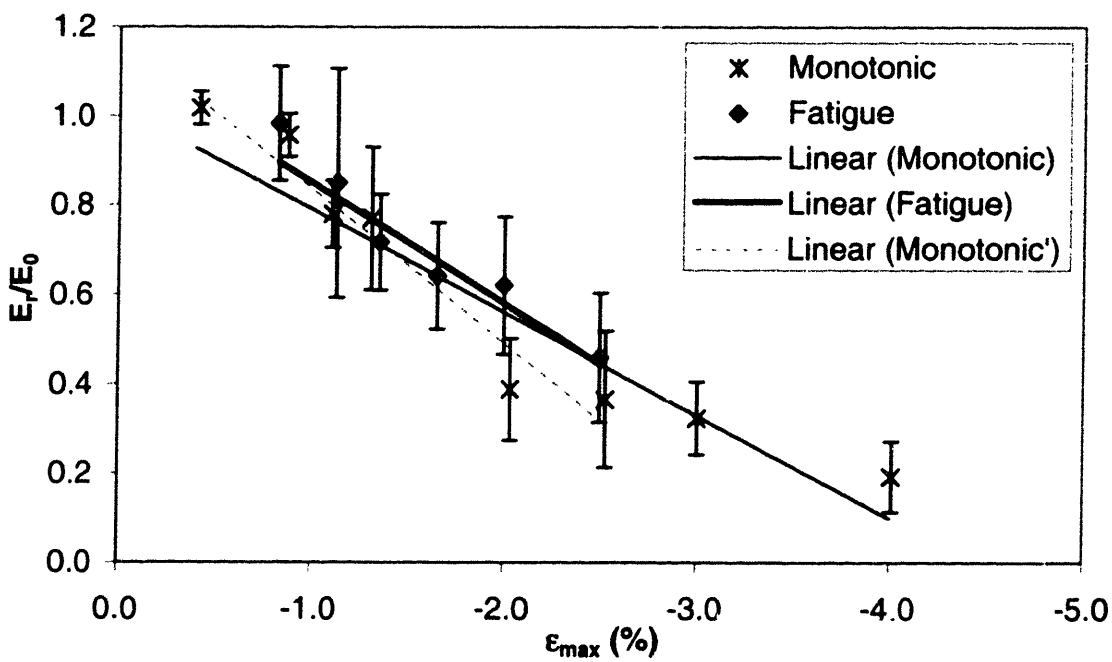

(b)

Figure 6.2: (a) Plot of modulus reduction, E_r/E_0, as a function of maximum strain. Data points have been separated for clarity. The same figure, without the monotonic data, is seen as Figure 5.4. (a) Fatigue data separated by normalized stress. (b) Pooled fatigue data. The equations of the regression lines are: fatigue, $Y = 0.27X + 1.12$, $p < 0.05$, $R^2 = 0.48$; monotonic, $Y = 0.23X + 1.02$, $p < 0.05$, $R^2 = 0.77$, monotonic without $\varepsilon_{max} = -3.0\%, -4.0\%$: $Y = 0.34X + 1.18$, $p < 0.05$, $R^2 = 0.74$.

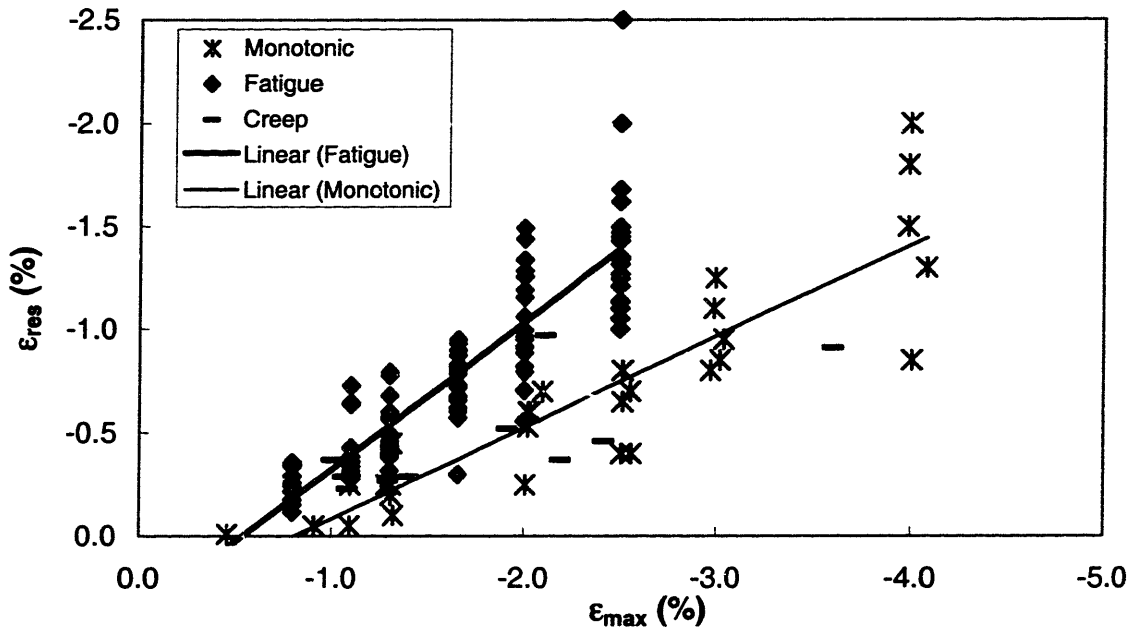

(a)

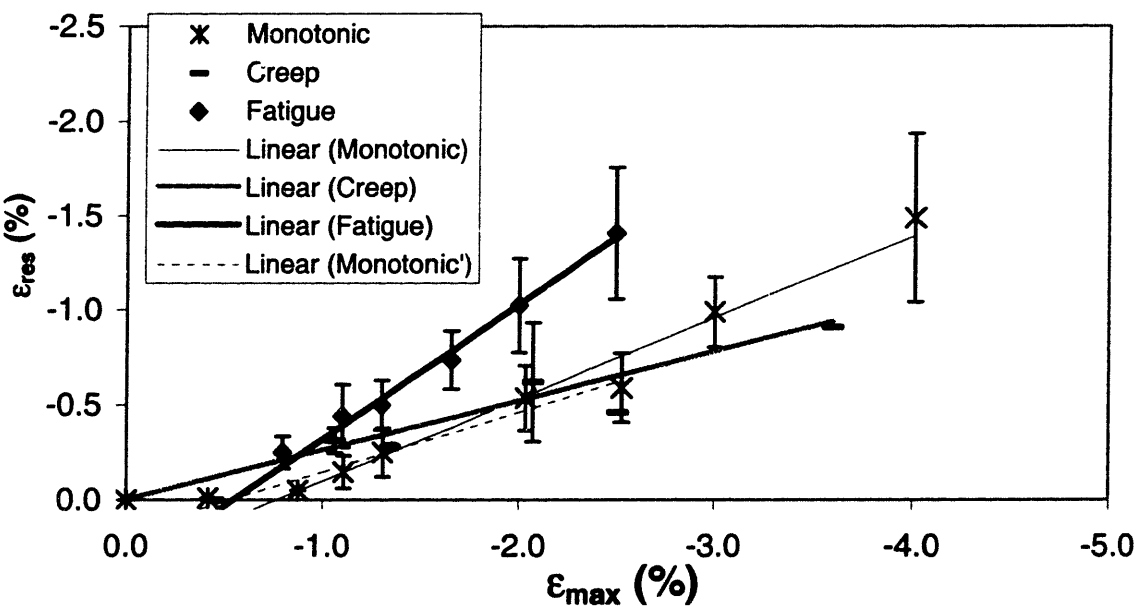

(b)

Figure 6.3: Residual strain after loading, ε_{res}, as a function of maximum strain, ε_{max}, for various loading modes. (a) Specimens plotted individually. The slope of the regression for the fatigue data ($Y = 0.71X + 0.39$, $p < 0.05$, $R^2 = 0.76$) was significantly different from the slope of the monotonic data ($Y = 0.43X + 0.33$, $p < 0.05$, $R^2 = 0.83$), the creep data ($Y = 0.26X - 0.003$, $R^2 = 0.65$, not plotted in (a)), and the monotonic data excluding data points at strains greater than $\varepsilon_{max} = -2.5\%$ ($Y = 0.31X + 0.17$, $p < 0.05$, $R^2 = 0.74$). (b) Pooled strain data. Data points have been separated for clarity.

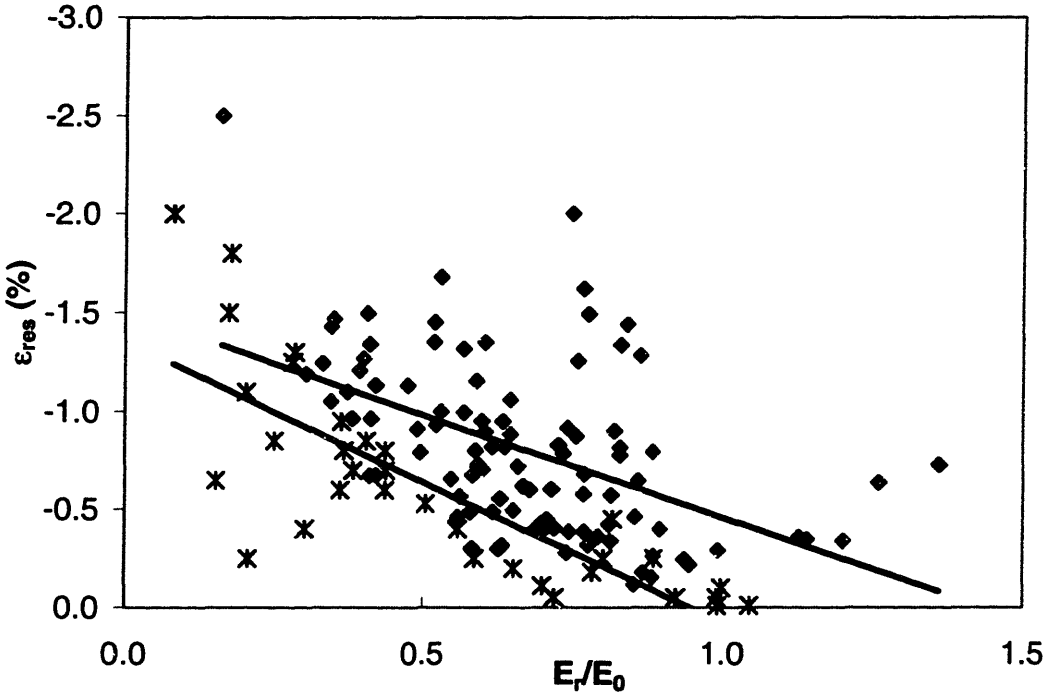

Figure 6.4: Plot of residual strain vs. modulus reduction for specimens tested in monotonic compression (stars) and compressive fatigue (diamonds). The fatigue specimens tested at different strain levels were not significantly different, so the data were pooled. The slopes and intercepts of the two regression lines were: monotonic compression, $Y = 1.43X - 1.36$, $p < 0.05$, $R^2 = 0.64$; fatigue, $Y = 1.04X - 1.50$, $p < 0.05$, $R^2 = 0.25$).

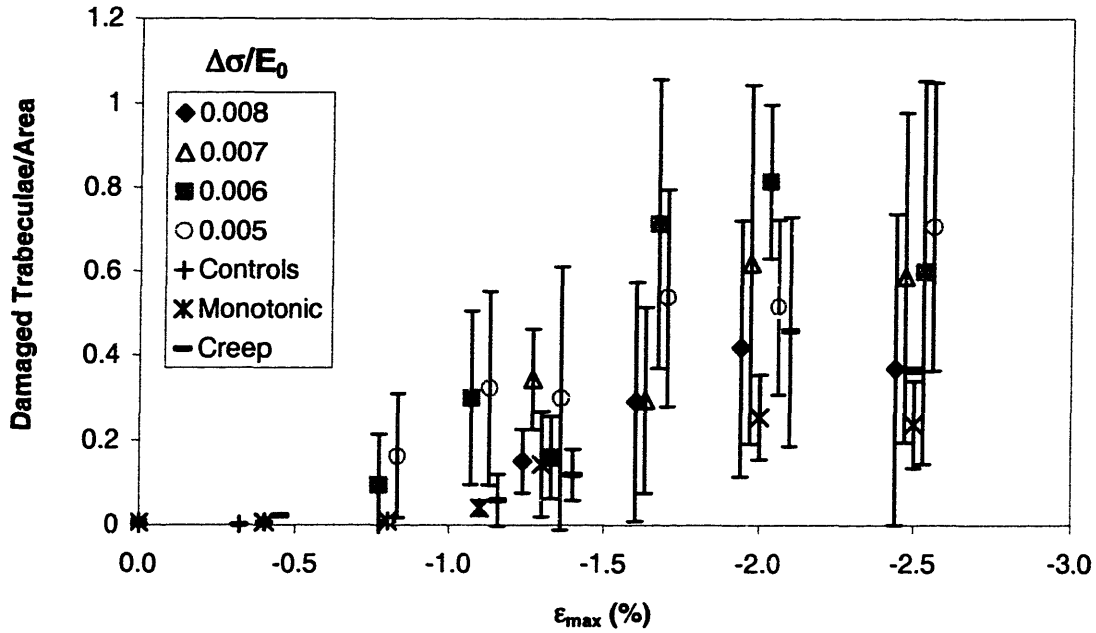

(a)

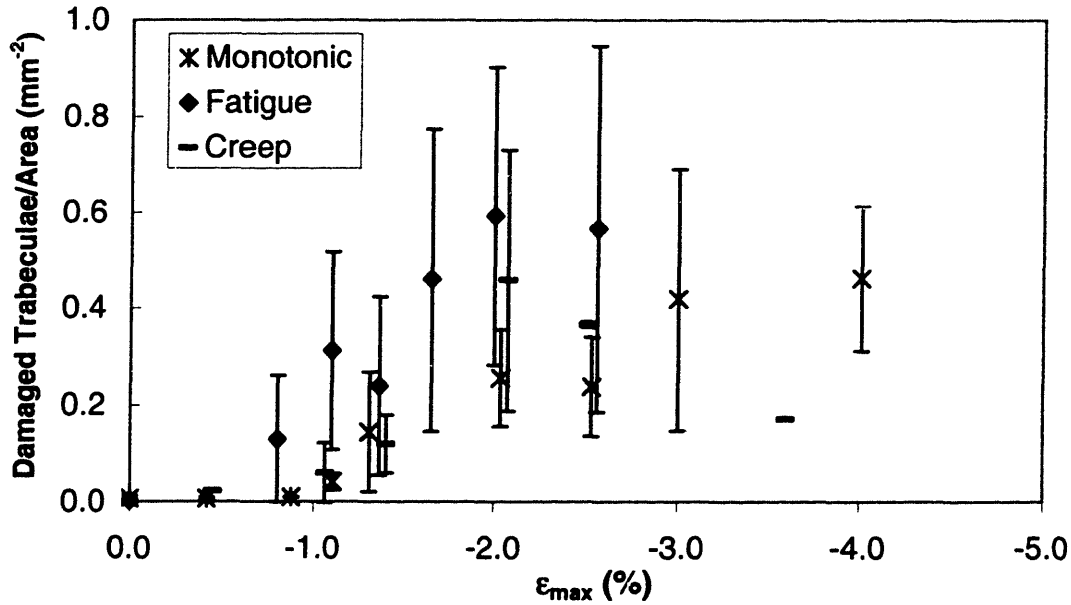

(b)

Figure 6.5: Plot of total number of damaged trabeculae vs. maximum compressive strain, ε_{max}. The numbers in the legend represent the normalized stress level. The damage increases with increasing strain. Microdamage parameters from monotonic compression tests and creep tests are lower than microdamage from fatigue-tested specimens loaded to the same strain, particularly near yield. Data points have been separated for clarity. The same plot, without monotonic and creep data, is seen as Figure 5.10(a). (a) Fatigue specimens separated by normalized stress. (b) Pooled fatigue data.

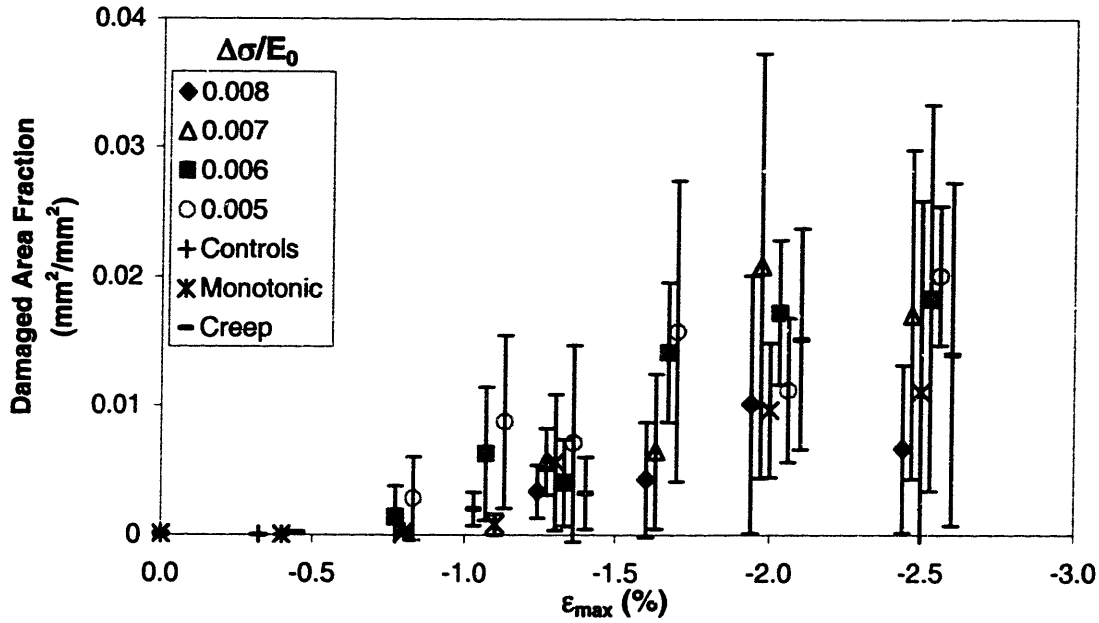

(a)

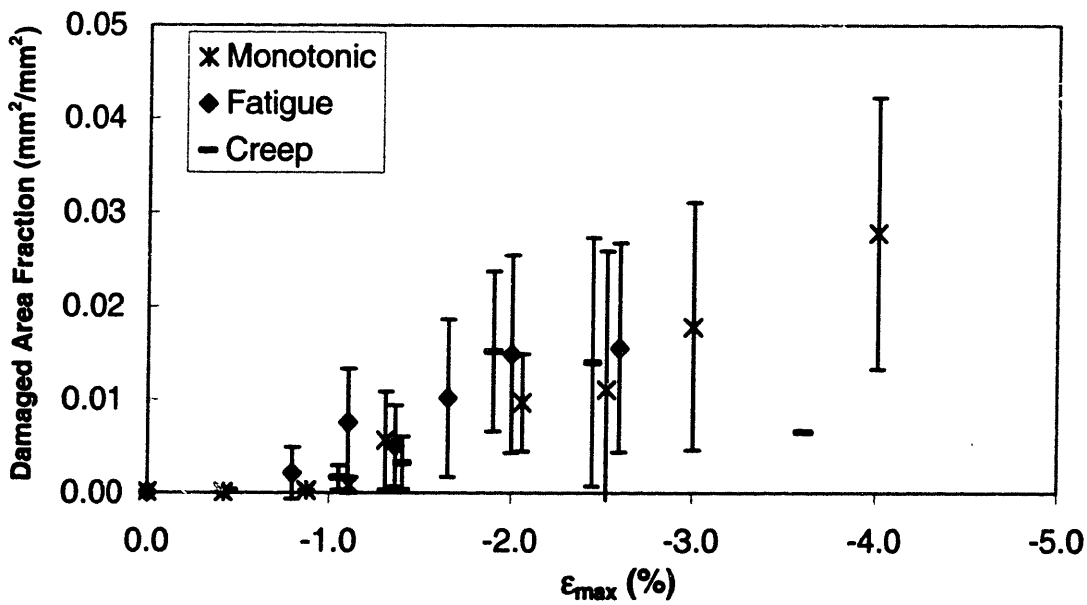

(b)

Figure 6.6: Plot of total damaged area fraction vs. maximum compressive strain, ε_{max}. The numbers in the legend represent the normalized stress level. Microdamage parameters from monotonic compression tests and creep tests are smaller than microdamage from fatigue-tested specimens loaded to the same strain, particularly near yield. Data points have been separated for clarity. The same plot, without monotonic and creep data, is seen as Figure 5.10(b). (a) Fatigue specimens separated by normalized stress. (b) Pooled fatigue data.

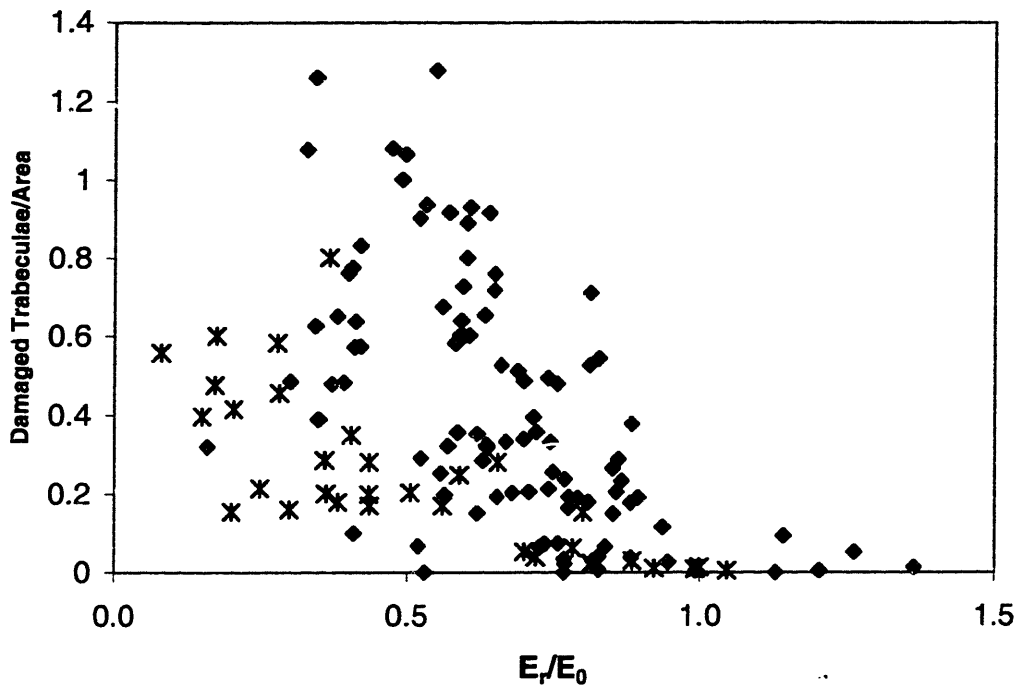

(a)

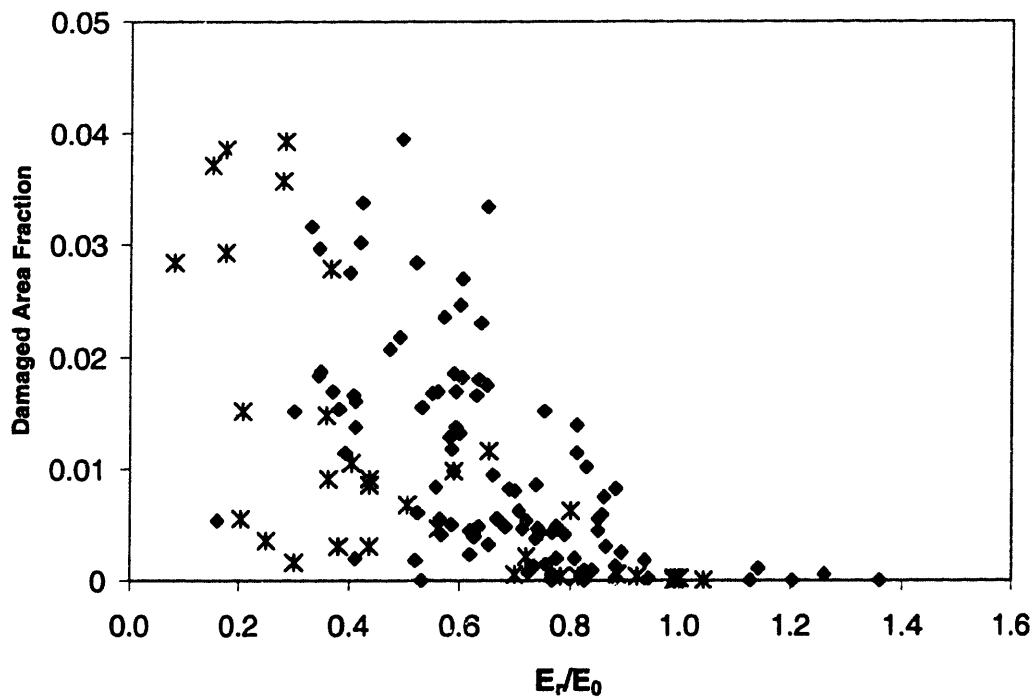

(b)

Figure 6.7: Damage parameters as a function of modulus reduction. Damage parameters increased with increasing modulus loss (decreasing E_r/E_0). (a) Number of damaged trabeculae per unit area. (b) Damaged area fraction.

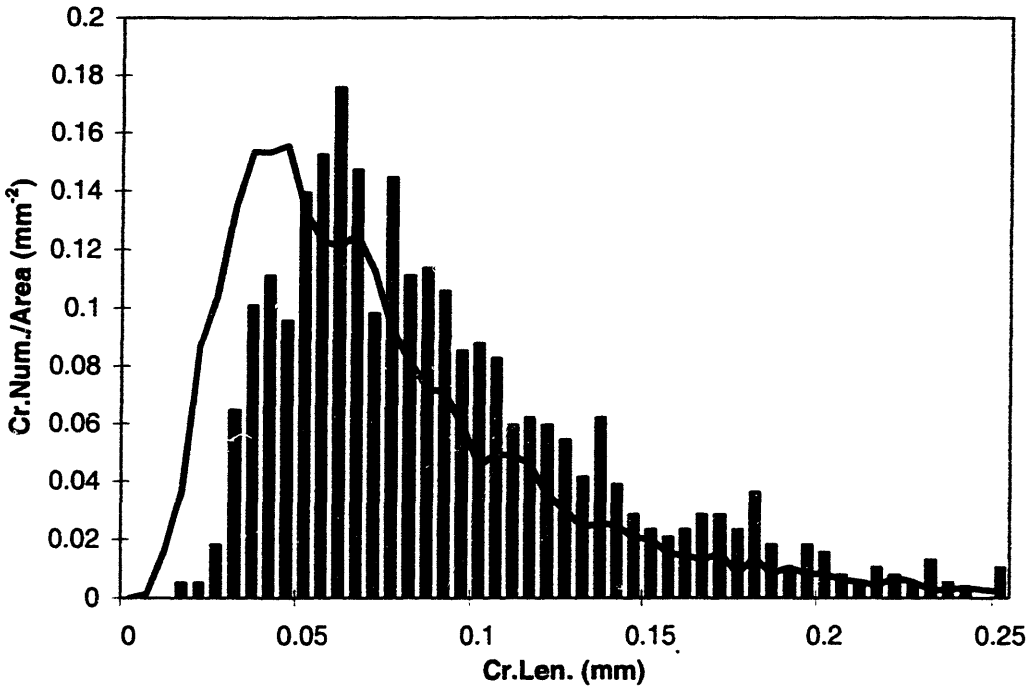

Figure 6.8: Crack length histogram for a typical creep specimen, 85B, tested to ε_{max} = -2.0% at a normalized stress level of $\Delta\sigma/E_0$ = 0.0055. The solid line represents the average value of five specimens tested to ε_{max} = -2.0% in monotonic compression.

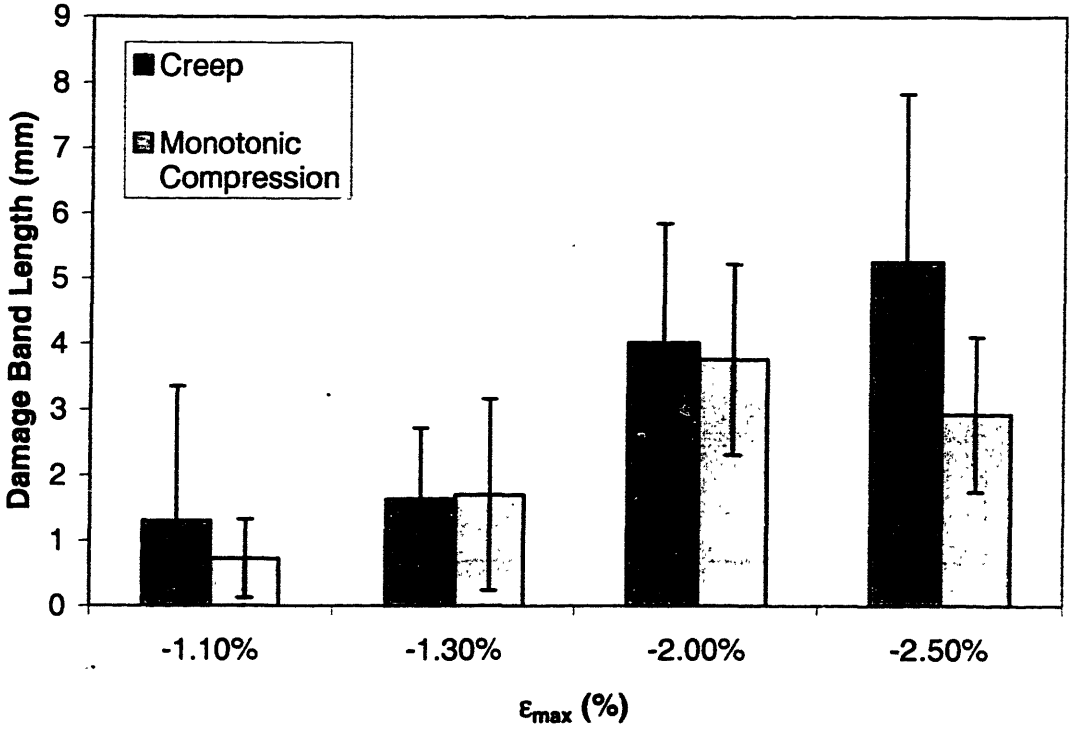

Figure 6.9: Damage band comparisons for specimens tested in compression and creep. Damage band length increased with increasing maximum strain, ε_{max}. No significant differences were seen between groups tested to the same strains.

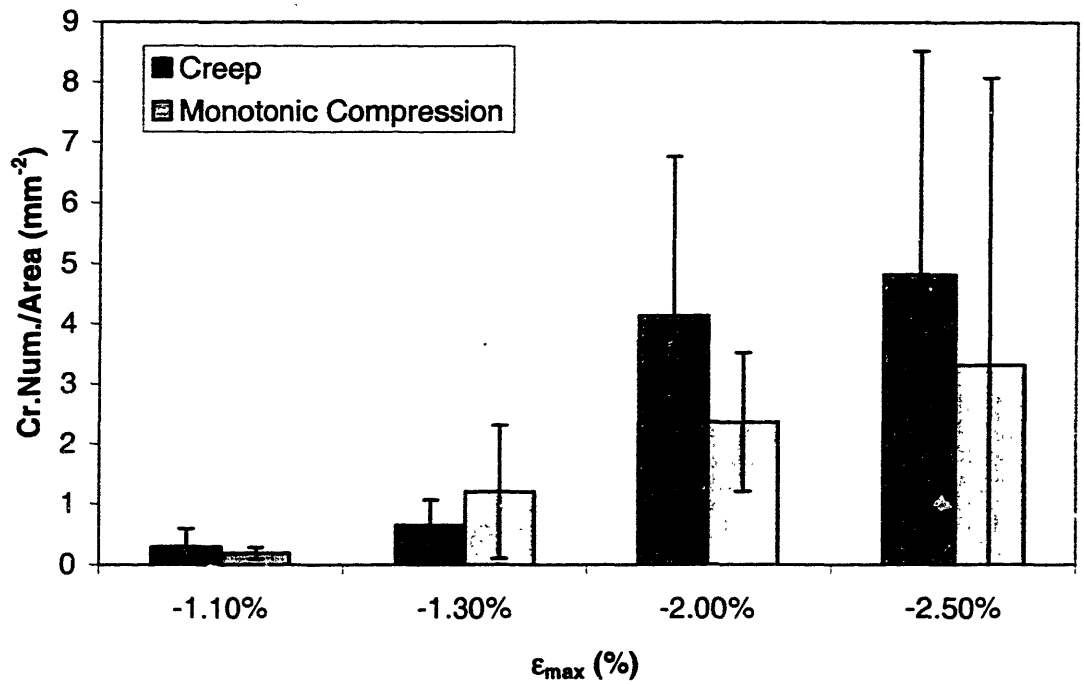

(a)

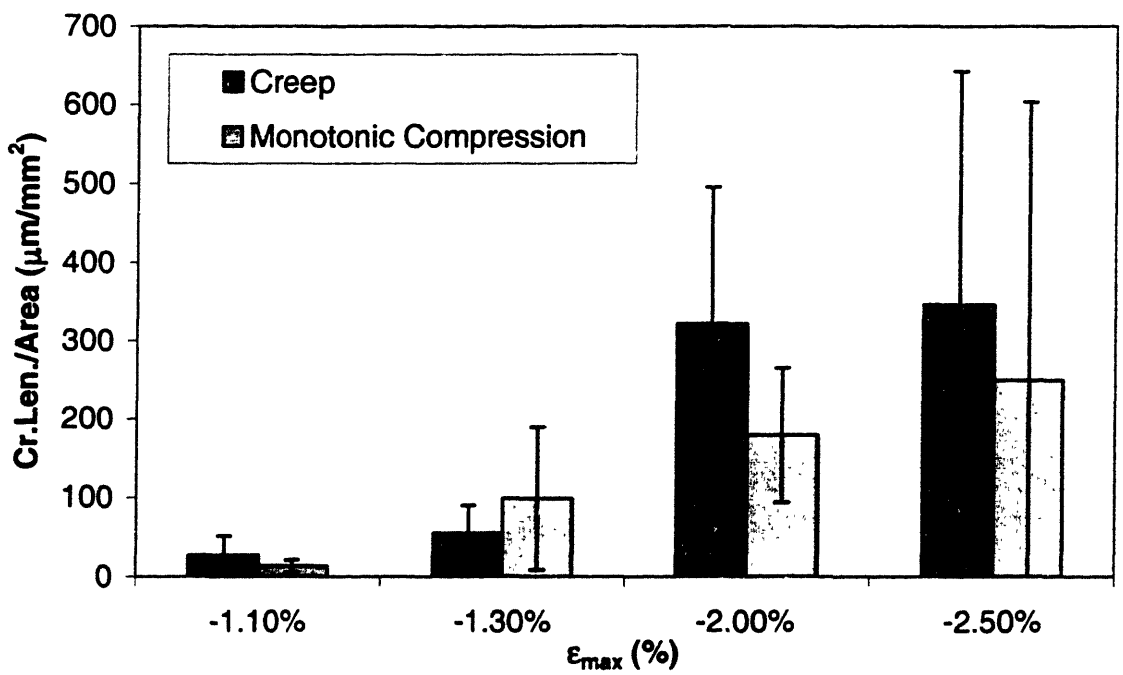

(b)

Figure 6.10: Comparison of crack number and length for specimens tested in monotonic compression and compressive creep. Both crack numerical density and crack length density increased with increasing maximum strain, ε_{max}. No significant differences were seen between groups tested to the same maximum strain.

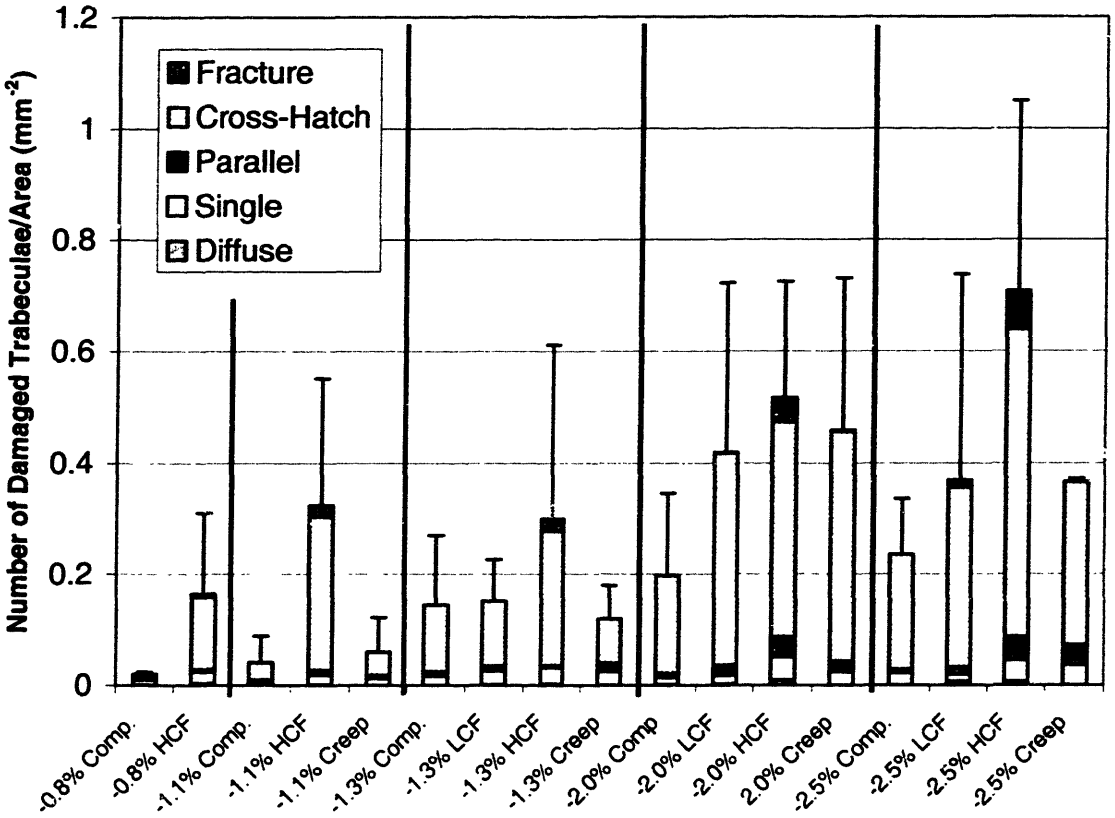

Figure 6.11: Breakdown of number of damaged trabeculae by damage pattern, normalized by section area, for the various loading modes. Low cycle fatigue (LCF) is represented by specimens tested at $\Delta\sigma/E_0 = 0.008$; high cycle fatigue (HCF) is represented by specimens tested at $\Delta\sigma/E_0 = 0.005$.

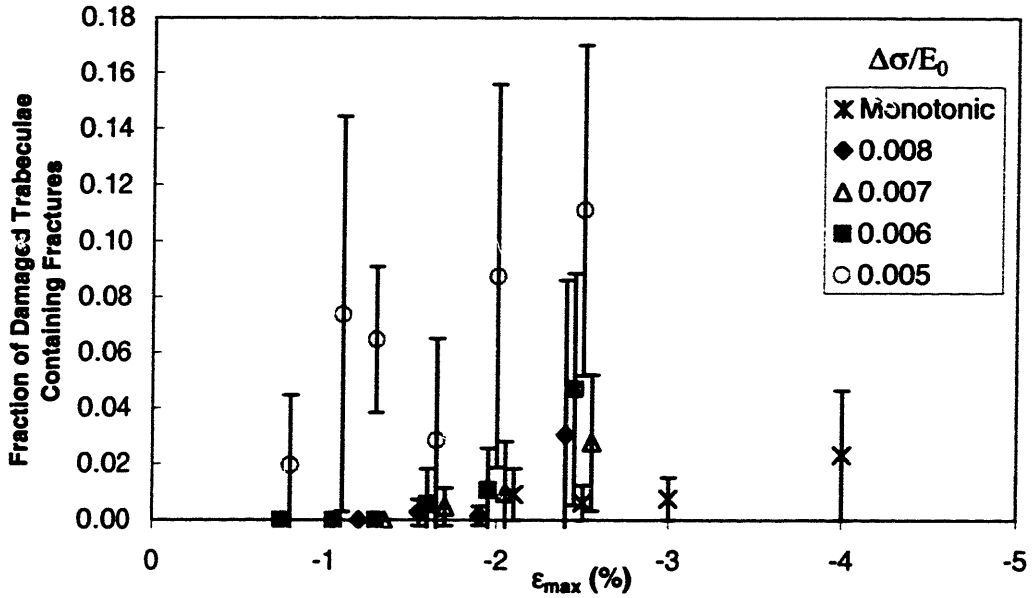

Figure 6.12: Fraction of damaged trabeculae containing complete fractures, with separated ends. Creep specimens contained almost no fractures and, for clarity, are not plotted. No fractures were observed in specimens tested in monotonic compression at strains below -2.0%. Specimens fatigued at low normalized stresses (high number of cycles) had an increased proportion of fractures compared to specimens tested at higher normalized stresses (lower number of cycles) and specimens tested in monotonic compression and creep. Data points have been spread out for clarity.

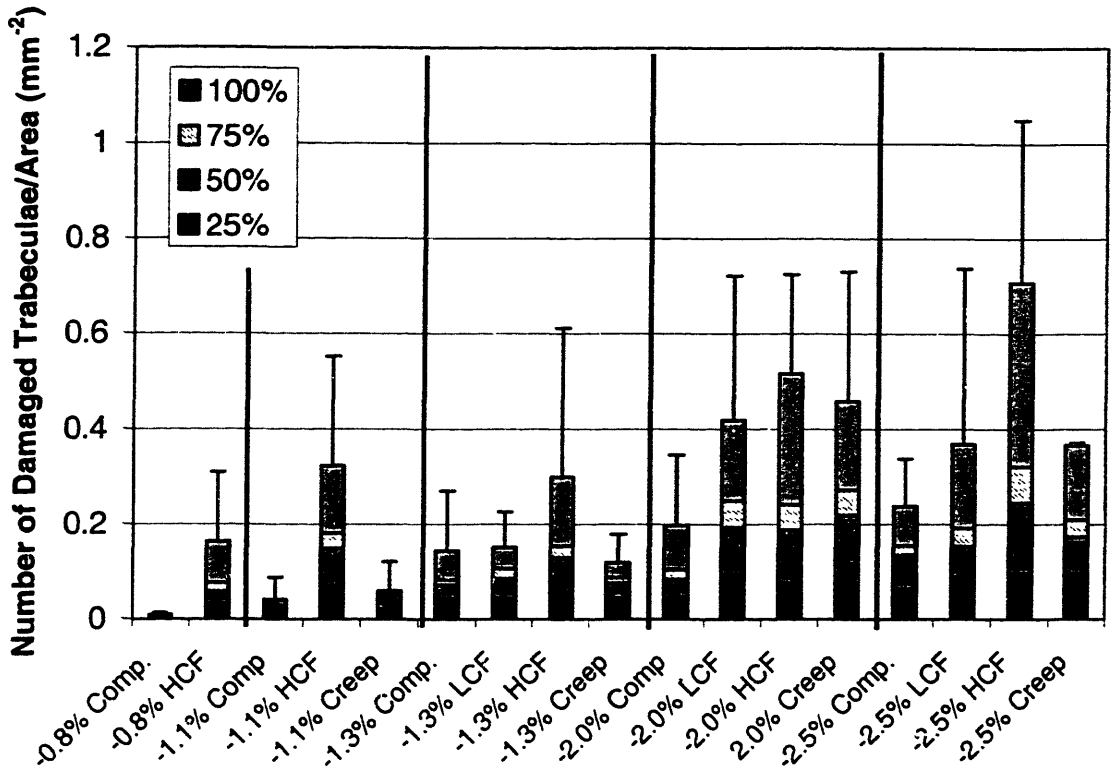

Figure 6.13: Breakdown of number of damaged trabeculae by damage pattern for the various loading modes. Low cycle fatigue (LCF) is represented by specimens tested at $\Delta\sigma/E_0 = 0.008$; high cycle fatigue (HCF) is represented by specimens tested at $\Delta\sigma/E_0 = 0.005$.

6.4 Discussion

In many respects, microdamage accumulation with increasing load was similar in specimens tested in different loading modes. Microdamage was not observed in specimens loaded below yield (**Figure 6.5**). The progressions of damage accumulation with increasing strain and the breakdowns of microdamage by pattern and by extent of the cracking across the trabeculae were similar in specimens tested in all loading modes. After yielding, we found few significant differences between modulus reduction, E_r/E_0 or E_{sec}/E_0, for specimens tested in monotonic compression and fatigue to the same maximum strain, ε_{max} (**Figure 6.2**). The mean crack length was not significantly different for specimens loaded in monotonic compression and creep, adding weight to the hypothesis that mean crack length is determined by the bone structure, possibly the spacing between osteocyte lacunae (Chapter 3; Reilly, 2000).

In compression-tested specimens and fatigue-tested specimens, the maximum strain, ε_{max}, explained more of the residual strain accumulation (monotonic compression: $R^2 = 0.83$, fatigue: $R^2 = 0.76$) than the modulus reduction, E/E_0 (monotonic compression: $R^2 = 0.64$, fatigue: $R^2 = 0.25$) (**Figure 6.5, 6.6, 6.7**). The residual strain was weakly but significantly dependent on density-dependent parameters, (relative density and initial modulus), but 90% of the variation in residual strain was explained by maximum strain alone. The residual strain also increased in fatigue-tested specimens loaded to the same modulus reduction, E/E_0 (**Figure 6.4**), compared to monotonic compression-tested specimens, although the differences were not as distinct as when the residual strain was plotted as a function of maximum strain (**Figure 6.2**). However, we did not observe a significant change in residual strain with increasing number of cycles in specimens tested to the same modulus reduction (Chapter 5).

However, some differences in damage accumulation were found between specimens tested in different loading modes. The residual strain, ε_{res}, is significantly greater in fatigue-tested specimens (**Figure 6.3b**), and the slope of the linear regression of residual strain and maximum strain was significantly larger than that for either monotonic or creep data (**Figure 6.3a**). Residual strains were observed at lower maximum strains in fatigue-tested specimens, and the residual strain threshold was

smaller in fatigue-tested specimens (-0.55%) than in monotonic compression-tested specimens (-0.82%). We expect that residual strains were higher in fatigue-tested specimens due to cumulative plastic deformation during multiple cycles, and the residual strain depended on the normalized stress level. We also expected to see a similar trend in modulus reduction, with the "no modulus reduction" point (E_r/E_0 = 1) occurring at a higher strain in monotonic compression than in fatigue. Instead, we found that the "no modulus reduction" strain in monotonic compression (-0.09%) was smaller than that in fatigue (-0.44%) and was not significantly different from zero (**Figure 6.2b**). When we re-calculated the regression using data from the same maximum strain range as that seen in fatigue (0.0% to -2.5%) we found that the intersection occurred at a strain of ε_{max} = -0.52%, which is essentially the same as the value determined for fatigue-tested specimens. Further monotonic compression tests to maximum strains in the range of -1.3% to -2.0% may help to "fill in the gaps"

We also noticed significant differences in the proportion of damaged trabeculae containing complete fractures, although the proportions of other patterns of damage were independent of loading mode. The proportion of fractures increased with increasing maximum strain, ε_{max}, for all loading types and for specimens tested to different normalized stress levels in fatigue. The fraction of fractures was the only parameter that was dependent on normalized stress in the fatigue tests, with increased fractures seen at low normalized stresses (**Figure 6.12**). Low normalized stresses correspond to high number of cycles, suggesting that small cracks initiated early in a test can grow to become fractures if given sufficient cycles. At low normalized stresses, more cycles are needed for a given crack to propagate to the critical length for fracture than at higher stresses. This is supported by the "threshold" number of cycles needed for fractures to be present, which increases with decreasing maximum strain (**Figure 5.14**).

Significantly more microdamage was observed in the fatigue-tested specimens at strains near the yield strain of approximately -1.0%, compared to monotonic compression-tested specimens and creep specimens (**Figure 6.5, 6.6**), suggesting that there may be differences in damage accumulation near yield. There was also a significant increase in the fraction of trabecular fractures at these low strain levels (**Figure 6.12**). If damage occurs in fatigue at load levels below those that cause damage

in uniaxial compression, as suggested by the appearance of residual strains at lower maximum strains in fatigue, then damage accumulation at these strains will differ from that in compression-tested specimens.

We observed significantly more microdamage in fatigue-tested specimens near the yield strain than in monotonic compression- or creep-tested specimens (**Figure 6.5, 6.6**). The fatigue specimens were subjected to higher average strain rates (2 - 3%/sec) than either the monotonic (0.5%/sec) or creep tests. Fatigue tests of bovine cortical bone found that damage is dependent on strain rate (Schaffler *et al.*, 1989); this relationship may explain some of the differences in damage accumulation. However, the experiments performed here were performed to different normalized stress levels at a constant frequency, so although strain rates changed, we could not separate the effects of stress level from strain rate, which also affects microdamage accumulation according to a power law relationship (**Figure 5.13**). Further tests are needed to fully understand the influence of strain rate on trabecular bone.

Differences in loading mode were not apparent after yield (**Figure 6.5, 6.6**). With load increases, the damage increases rapidly and expands across the specimen. Once a significant fraction of the specimen contains damage, differences in damage initiation will not be apparent. Additional observations of microdamage creation during yield may increase our understanding of the phenomenon.

Trabecular bone may have different failure mechanisms depending on the stress and strain levels during loading. Trabecular bone failure occurs locally, as a result of tissue strain. Tissue level strains for trabecular bone are not known specifically, but do correlate with the bulk strain (Hollister *et al.*, 1991, 1994). High bulk strains lead to higher local strains, and may result in failure of multiple trabeculae at the same time. Since damage progresses by failure of the trabeculae surrounding the initial failed strut, the number and location of failure initiation sites will determine the amount and appearance of damage at the specimen level until the initiation sites coalesce into a single damage band, i.e. at low strains. More failure initiation sites are expected at higher normalized stress.

Two different specimen geometries were used over the course of testing: a waisted specimen geometry for the monotonic compression and creep tests and an

unwaisted specimens for the fatigue tests. Damage was concentrated in the gauge region of monotonic and creep specimens, and spread out along the entire length of fatigue specimens. A small amount of damage may have been removed when the bone was cut out of the end caps, but that amount was a small fraction of the total (less than 3 mm at each end of the specimen, all of which was glued securely into the end caps). Fatigue specimens also had a smaller section area than monotonic or creep specimens. While we normalized the damage parameters by section area, the differences in areas might affect our results, particularly because of changes in cross-sectional area at the ends of the waisted specimens. Additional work, including mechanical tests of bone specimens with the same specimen geometry, must be performed before definitive conclusions can be drawn.

A large amount of scatter is seen in the mechanical properties and microdamage parameters in all loading modes. There were no more than five specimens tested at any given set of loading parameters, and much larger numbers of specimens (> 25) would be needed to show more significance (Chapter 3). Creep data is especially lacking, with only 13 specimens tested. For more conclusive results, more tests would have to be performed, particularly creep tests and tests to strain levels near yield in all loading modes.

Some studies in the literature have hypothesized that trabecular bone failure is best explained by a strain-based criteria. Bovine trabecular bone failure strains were found to be independent of relative density, at least over the range of densities present in bovine trabecular bone (Keaveny *et al.*, 1994c; Kopperdahl and Keaveny, 1998), and trabecular bone yield strains can be considered constant for a given anatomical site (Morgan and Keaveny, 2001). As well, trabecular bone yield strains are isotropic (Chang *et al.*, 1999), while trabecular bone architecture is usually anisotropic.

We observed several results that suggest that strain may be an important contributor to trabecular bone failure. The maximum strain was a strong predictor of changes in mechanical properties and microdamage accumulation in trabecular bone (**Figure 6.2, 6.3, 6.5**), suggesting that a strain-based failure criterion exists for bovine trabecular bone. In most cases, either maximum strain or residual strain (which is itself best predicted by the maximum strain), or in some cases, both, accounted for much of the

explained variation in modulus reduction and microdamage accumulation. We also observed that low cycle fatigue of bovine trabecular bone ($N < 100$ cycles) was better explained by the strain-based Coffin-Manson Law (**Figure 5.6**) then by the stress-based Basquin Law (**Figure 5.5**). We also noted that the cellular solid model, which is stress-based, did not predict modulus reductions well for fatigue-tested specimens (Chapter 5.4, **Figure 5.19**). This suggests that a stress-based failure criterion may not accurately reflect the behavior of bovine trabecular bone.

However, we observed significant differences in residual strain accumulation between single-cycle tests and multiple-cycle tests. There are also indications that damage accumulation near yield differs in specimens tested in different loading modes. This suggests that different damage formation mechanisms may occur during different loading conditions. Further study of damage accumulation, particularly near yield, might provide further insights.

Chapter 7: Conclusions

7.1 Summary of Results

Microdamage is present in normal human bones and can be created by overloads or by fatigue loading. If microdamage is not repaired, it can accumulate and lead to a stress fracture. This work characterizes microdamage accumulation in bovine trabecular bone tested in monotonic compression and compressive fatigue, and investigates relationships between changes in mechanical properties and microdamage accumulation parameters.

The staining process developed by Lee *et al.* (Lee, 1997; Lee *et al.*, 2000) was modified to determine optimal stain concentrations and two-stain sequences. Tests were performed on cracked cortical bone beam specimens. The stain sequencing results were extrapolated to three-, four-, and five- stain sequences for future use. The optimal concentrations, based on the relative ratios developed by Rahn (1977), were as follows: alizarin complexone (red), 0.03%; calcein blue, 0.03%, calcein (green), 0.01%; oxytetracycline (yellow), 0.03%; and xylenol orange, 0.09%. The optimal stain sequence was alizarin complexone, followed by calcein green. This sequence was used in all subsequent experiments.

Waisted cylindrical specimens of bovine trabecular bone were loaded in monotonic compression under strain control to strain levels ranging from pre-yield (-0.4%) to beyond the ultimate strain (-4.0%). Mechanical properties measured included initial modulus, E_0, secant modulus, E_{sec}, maximum strain, ε_{max}, and residual strain, ε_{res}. Microdamage parameters measured included crack number, crack length, damaged area fraction, number of damaged trabeculae, pattern of damage, extent of damage across the trabecular thickness, and size of the localized damage band. All microdamage parameters began to accumulate once the specimen has been loaded beyond yield, and microdamage parameters increased with increasing maximum compressive strain and increasing damage, as assessed by the damage parameter, $1 - E_{sec}/E_0$.

A cellular solid model was developed to predict modulus reduction based on observations of microdamage accumulation. Modulus reductions were considered on

three different levels within the specimen. First, regions of microdamage in individual trabeculae were considered, and the stiffness reduction of the trabeculae was determined. Then the individual trabeculae were incorporated into a cellular solid network, consisting of intact trabeculae, damaged trabeculae with reduced load bearing capacity, and fractured trabeculae with no load bearing capacity. The reduced modulus of the damaged cellular solid was calculated. Finally, the damaged region was considered as a portion of the specimen, with a region of localized damage and a region of intact bone, and an overall modulus reduction for the specimen was calculated.

Two models were developed: an open-cell model where individual trabeculae consist of rods that deform in bending, and a closed-cell model where individual trabeculae consist of plates that deform axially. The bovine trabecular bone used in this work is approximately a closed-cell foam, but trabecular bone structure varies between species and anatomic sites, so an open-cell model may be more appropriate if trabecular bone specimens from other sites are used. The model predictions were compared with the monotonic compression experimental results described in the previous paragraph (Chapter 3), and agreement between the closed-cell model and experimental predictions was good ($R^2 = 0.81$).

Cylindrical specimens of bovine trabecular bone were loaded in fatigue in load control at 2.0 Hz to one of four normalized stresses, $\Delta\sigma/E_0$, and stopped at one of six maximum strains, ranging from -0.8% to -2.5%. Mechanical properties measured included initial modulus, E_0, secant modulus of the final cycle, E_{sec}, maximum strain, ε_{max}, residual strain, ε_{res}, reloading modulus, E_r, and number of cycles, N. Trabecular bone had an S-N curve typical for an engineering material ($R^2 = 0.62$). Specimens tested in low cycle fatigue ($N < 100$ cycles) followed the strain amplitude-based Coffin-Manson Law ($R^2 = 0.82$) better than the stress-based Basquin Law ($R^2 = 0.62$).

Microdamage parameters measured included damaged area fraction, number of damaged trabeculae, pattern of damage, extent of damage across the trabecular thickness, and size of the localized damage band. Microdamage increased with increasing specimen strain and increasing modulus reduction. We observed no relationship between normalized stress level and amount of microdamage for a given maximum strain, ε_{max}. The cellular solid model developed for monotonic compression was used to predict

modulus reductions for the fatigue-tested specimens. Agreement between experimental and predicted results was not as good for fatigue as for monotonic compression samples ($R^2 = 0.38$).

Finally, specimens tested in both loading modes, as well as specimens tested in creep (Pierce, 1999), were compared to determine the effect of loading mode on changes in mechanical properties and microdamage accumulation. Specimens compressed to the same maximum strain at any normalized stress had similar modulus reductions, which were comparable to modulus reductions seen in specimens tested in monotonic compression to the same strains. The maximum strain, ε_{max}, was the largest single predictor of modulus reduction, but relative density, initial modulus, and, in the case of fatigue-tested specimens, normalized stress and number of cycles had small but significant effects.

Residual strains were comparable in monotonic compression- and creep-tested specimens loaded to the same maximum strain, but fatigue-tested specimens had significantly higher residual strains than specimens tested in either creep or monotonic compression to the same strain. Maximum strain was the only significant predictor of residual strain in specimens tested in monotonic compression or creep, but normalized stress and initial modulus had small but significant effects on residual strain accumulation in fatigue-tested specimens.

Changes in microdamage parameters were best explained by changes in maximum strain, if only one parameter was used, but number of cycles, residual strain, and secant modulus reduction were all significant predictors of changes in microdamage parameters in fatigue-tested specimens. Predictors of changes in microdamage parameters in monotonic compression-tested specimens varied: initial modulus and residual strain predicted the changes in damaged area fraction, crack number, and crack length best, while the relative density and the secant modulus reduction predicted changes best in the number of damaged trabeculae and the damage band length.

We measured a strain threshold of approximately -0.5%, below which no changes in mechanical properties and no microdamage accumulation was observed. This level corresponds well with the endurance limit of approximately -0.35% measured for bovine

trabecular bone. The results compare well with a published measure of a fatigue endurance limit in human cortical bone (Pattin *et al.*, 1996).

There were few significant differences in modulus reduction or microdamage accumulation parameters between specimens tested to the same maximum strain, ε_{max}, in different loading modes. Even in cases where differences exist, maximum strain is the best predictor for each loading mode. The maximum strains corresponding to no modulus reduction, residual strain accumulation, and microdamage accumulation are similar in monotonic compression- and fatigue-tested specimens. As well, trabecular bone fatigue at low cycles ($N < 100$) was better explained by strain amplitude than stress amplitude. Finally, the stress-based cellular solid model did not explain the fatigue results well. These results support the hypothesis of a strain-based failure criteria for trabecular bone.

However, some differences were observed between specimens tested to the same strain in different loading modes. The residual strain was significantly higher in fatigue-tested specimens than in specimens tested in either monotonic compression or creep. At strains below yield, there was an increase in microdamage in specimens tested in higher cycle fatigue ($N > 100$ cycles), compared to low cycle fatigue, monotonic compression, and creep. Complete trabecular fractures were not observed in specimens tested to low strains (< 2.0%) in monotonic compression; however, fractures were seen in specimens tested to -1.1% strain in high cycle fatigue. A threshold number of cycles existed for each strain, below which fractures were not seen. This threshold number of cycles decreased with increasing maximum strain.

7.2 Strengths and Limitations

7.2.1 Strengths

Strengths of this study include a well-defined specimen geometry for the monotonic compression tests that has been used in a number of other studies. Our results compare well with previous results using the same specimen geometry (Bowman *et al.*, 1994; Guo *et al.*, 1994; Keaveny *et al.*, 1994a, 1994b, 1994c, 1994d; Cheng, 1995; Ford

and Keaveny, 1996; Wachtel and Keaveny, 1997). We have used a wide range of maximum strains in both loading modes, ranging from zero strain to strains near fracture. Similarly, the fatigue tests were performed at normalized stresses, $\Delta\sigma/E_0$, ranging from levels high enough to cause failure within a few ($N < 10$) cycles to levels where more than 1000 cycles are necessary to cause failiure. The use of chelating fluorochromes allowed the differentiation of damage created before testing from damage created during testing.

The progression of microdamage accumulation from no load to fracture was similar in bovine trabecular bone specimens testing in monotonic compression, high and low cycle fatigue, and compressive creep. Although bovine bone has a higher density than human bone, trabecular bone from different anatomic sites with different structures can be expected to follow a similar progression to failure. Similarly, the cellular solid model can be easily applied to other types of trabecular bone.

7.2.2 Limitations

A major limitation of this study was the scatter in the data, particularly in the fatigue tests, making it difficult to draw statistically significant conclusions from the data. Increasing the number of specimens from n = 5 in each category would improve the scatter somewhat, but the non-uniform structure and composition of trabecular bone means that there will always be more scatter than a non-cellular material of uniform composition. The destructive nature of microdamage evaluation means that a different specimen has to be tested for each strain level, and there can be large differences in the initial modulus, relative density, and bone architecture between specimens.

Microdamage is quantified by histological evaluation of three to six sections cut through the central region of the bone cylinder. The majority of the bone material is lost during the cutting process, and the resulting sections offer two-dimensional planes of a three-dimensional structure. The current method for evaluating microdamage is time-consuming and would be difficult to automate. An initial study of sampling (Appendix A) has shown that the three to six sections obtained per specimen provide a reasonable estimate of the data; however, further work would need to be done to develop and

validate a protocol to estimate microdamage parameters using a portion of the data obtained by sectioning.

The destructive nature of the microdamage quantification process makes it impossible to use in a clinical situation. New, non-destructive methods for imaging microdamage *in vivo* need to be developed before this work can be applied to microdamage accumulation in humans.

All experiments were conducted on bovine bone, which is considerably denser than human trabecular bone. As well, the specimens used in the study were all taken from young animals, while the major implications for microdamage accumulation are in elderly, osteoporotic subjects with reduced remodeling ability. Microdamage increases exponentially with increasing age, so young specimens have very little microdamage present prior to mechanical testing.

There are several limitations associated with the cellular solid model. The model assumes an isotropic structure, which is not true for trabecular bone. Microdamage is classified by damaged area fraction, and there is no accounting for different patterns of damage. Any crack that extends across a trabecular strut is assumed to extend through the depth of the strut, when some portion of the trabeculae may be intact and retain some load carrying capacity. The model does not account for crack growth during later fatigue cycles, which may account for the lack of agreement between model predictions and fatigue experimental results.

7.3 Future Work

This study evaluated the effect of two different types of loading, overload and repetitive fatigue loading, on mechanical properties and microdamage accumulation in bovine trabecular bone. While our work examined these effects separately, both will occur concurrently during physiologic conditions. For example, after sustaining a fall (overload condition), a subject will continue with daily activities (fatigue loading). Examining how fatigue life is changed after a moderate overload may provide insights on changes in fracture risk in patients after an overload. Recent work has shown that the damage behavior of cortical bone is path-dependent (Zioupos and Casinos, 1998), where

specimens tested in fatigue at low stress, followed by additional cycling at high stress (low/high), show different damage accumulation behaviors than specimens tested in the high/low configuration. Additional studies of complex loading situations are necessary to understand the mechanical behavior of trabecular bone under physiologic loading conditions.

The experiments described here were all conducted on bovine bone, which is considerably denser than human bone. Most human trabecular bone has a mostly open celled structure, while the bovine bone used here has a predominantly closed cell structure. Experiments on human bone would determine the progression of microdamage in human trabecular bone and validate the open-cell model. As well, human bone specimens are available from a variety of ages, so the effects of bone loss and increasing *in vivo* microdamage can be studied.

While this work looked at *in vitro* microdamage accumulation under known loading, bone is not a static organ. In the body, bone is constantly being modified to optimally support the loads placed on it and repairing damage. Microdamage is known to be a stimulus for bone remodeling, and microdamage accumulation over the long term cannot be understood without accounting for remodeling. Additional experiments using animal models could be conducted. However, it should be noted that mechanical property measurements will be less accurate when measured *in vivo*.

There are several ways to improve the microdamage analysis process. The sampling methods discussed briefly in Appendix A could be expanded to create and validate a sampling procedure for trabecular bone to speed the analysis process. Confocal microscopy could be used to examine microdamage within the specimen, as well as microdamage on the surface; this technique would allow the examination of several planes of damage in a single specimen.

A new approach for visualizing microdamage radiologically has been suggested (Lee, private communication). If a chelating stain that was more radio-opaque than bone was developed, damage could be observed in a micro-computed tomography scan, without sectioning the specimen. This would give a view of all the damage present in a tested specimen, in three dimensions. Because microdamage analysis would be non-destructive, this method would also allow the evaluation of microdamage at different

time points in the same specimen. Finally, micro-computed tomography can also be used to simultaneously determine bone architecture parameters. No study integrating mechanical properties, microdamage accumulation, and bone architecture has been performed to date.

The model developed in Chapters 4 and 5 could be extended to better represent the structure of trabecular bone. The current model is isotropic, while trabecular bone is usually orthotropic. The two models developed here for a rod-like open-celled structure and a plate-like closed-celled structure could be combined to better represent trabecular bone, which is often composed of both rods and plates. The modulus reduction due to strut loss in the model is based on the assumption that trabecular struts are removed randomly, while actual strut loss occurs initially in thin or otherwise compromised trabeculae, then locally around the initial microdamage. The distribution of damaged area could be altered to better represent the distribution of damage (for example, by assigning more damaged area to cross-hatched cracks and less to single cracks).

New modeling methods could be developed and applied to the experimental data. Micro-finite element models using a large number of elements to simulate details in bone architecture are currently used to model realistic trabecular structures. Finite element models can be developed from micro-computed tomography scans of actual bones, which would then be mechanically tested and compared to the model results. The micro-finite element models can also be used in conjunction with the cellular solid model approach developed in this work. Individual elements in a trabecular strut can be removed to simulate the load redistributions in the local region surrounding a crack. These models could also be used to predict the local loading conditions on individual trabeculae, which could be compared to microdamage observations.

Bisphosphonates have been used to treat osteoporosis. Bisphosphonates increase bone mass by suppressing bone resorption without a corresponding decrease in bone deposition. The suppression of resorption also causes microdamage to accumulate (Forwood *et al.*, 2000b; Hirano *et al.*, 2000; Mashiba *et al.*, 2000). Increasing bone mass increases bone stiffness and strength, while microdamage accumulation decreases bone stiffness and strength. A trade-off exists between the increase in bone mass and the decrease in bone quality as a result of microdamage accumulation. At some point,

microdamage levels may increase to the point where any benefits from increased bone mass are cancelled out. The model developed here can be used to predict modulus loss assuming physiologic levels of microdamage accumulation, which can then be compared to the modulus gain due to bone mass increases from bisphosphonate therapy, to determine if and at what point bisphosphonate therapy becomes clinically detrimental.

7.4 Overall Conclusions

Microdamage accumulates in bovine trabecular bone with increasing compressive strain. At low strains prior to yield ($\varepsilon_{max} < -0.5\%$), no changes in modulus reduction and no residual strain accumulation were observed. Negligible amounts of microdamage were observed in specimens tested to these strains.

Microdamage begins to accumulate when the bone reaches yield, when reductions in modulus and residual strains are first observed. Microdamage forms in isolated areas, in trabeculae that are relatively weaker than surrounding trabeculae and are subjected to higher local strains. At this point, the locations of damage formation depend largely on bone architecture. Damage forms as small regions of cracking, often as single cracks.

Once a trabecula contains damage, its load-carrying capacity is reduced. The local load is redistributed to surrounding trabeculae, increasing their local strains, and thus increasing the likelihood that they will crack. Microdamage within the already-damaged trabecula may also increase, leading to the formation of regions of cross-hatching. In fatigue-tested specimens, the initial cracks can also grow in later cycles, which decrease the load-carrying capacity of the initially damaged strut and increase the load redistributed to surrounding trabeculae. With increasing load, additional damage is more likely to occur near previously damaged trabeculae than in a region distant from damaged trabeculae.

With increasing strain, more trabeculae are damaged, the load continues to be redistributed among the local area of damage, and the region of damage expands. At this point, two situations are observed. First, the localized damaged region expands and multiple regions of damage may coalesce to form a band across the specimen. Secondly, individual trabeculae may fracture completely, and lose all load-bearing capabilities.

While this is occurring, the specimen modulus decreases and residual strain increases. Damage band formation occurs at strains near -2.0% in specimens tested in monotonic compression and creep, and at lower strains (as low as -1.1%) in fatigue-tested specimens.

After band formation, damage continues to increase by expanding the size of the band. The damage band will grow with increasing strain to include the entire specimen. After this point, microdamage increases by densifying within the band. As well, the number of complete trabecular fractures also increases with increasing specimen strain. When the trabecular fractures extend across the entire specimen, specimen fracture has occurred.

Observations of the progression of microdamage with increasing strain were similar in all loading modes. However, the microdamage accumulation and mechanical property changes began to occur at lower maximum strains in specimens tested in fatigue than in specimens tested in monotonic compression or creep. We found that fractures were more likely to occur at lower strains in fatigue-tested specimens, especially in specimens tested to high numbers of cycles. A threshold number of cycles existed at each maximum strain level, below which fractures were not seen. This threshold increased with decreasing maximum strain, so fractures were observed in monotonic compression-tested specimens only at high strains (> -2.0%), but were observed at strains as low as -0.8% in fatigue-tested specimens.

We have developed a model to predict changes in modulus based on microdamage accumulation in bone (Chapter 4). The model predicts modulus reductions by distributing observed microdamage, in the form of completely broken trabeculae and partially damaged trabeculae, randomly throughout the localized damaged region of an idealized cellular solid. The non-linear model accounts for the complexity of trabecular bone structure and depends on a number of input parameters, including the damaged area fraction, the distribution of damage extent across the thickness, and the length of the damaged band. Models were developed for open- and closed-cell cellular solids, since trabecular bone structure varies from open-celled in osteoporotic human vertebrae to nearly closed-cell in bovine tibial trabecular bone. The closed-cell model predicted modulus reductions well in specimens tested in monotonic compression ($R_c^2 = 0.81$), and

less well in specimens tested in compressive fatigue ($R_c^2 = 0.38$). The results suggest that microdamage accumulation is responsible for changes in mechanical properties in trabecular bone, although other mechanisms also affect modulus loss in fatigue-tested specimens.

Both microdamage accumulation observations and changes in mechanical properties can be used to characterize trabecular bone behavior. After yield, damage in trabecular bone appears to be mainly a function of strain and is mostly independent of loading mode. Strain amplitude can be used to describe the fatigue behavior of bovine trabecular bone in low cycle fatigue tests to less than 100 cycles. The stress-based cellular solid model, while predicting modulus reduction well in monotonic compression-tested specimens, does not predict modulus reduction well for fatigue-tested specimens. Specimens loaded to the same maximum strain, ε_{max}, in monotonic compression, compressive fatigue, and compressive creep had similar measured modulus reductions, E/E_0, and microdamage accumulation. As well, there were few differences in modulus reduction, residual strain, ε_{res}, and microdamage parameters between specimens tested in fatigue to the same maximum strains at different normalized stress levels. The breakdown of the number of damaged trabeculae by pattern of damage and extent of damage across the trabecular thickness was similar in all specimens, with a small increase in the proportion of complete trabecular fractures in specimens tested to high numbers of cycles. These results support a strain-based failure criterion for bone at high strain levels.

Near yield, at maximum strains between -0.8% and -1.1%, there appear to be some differences between loading modes. Residual strains are higher in fatigue-tested specimens than in monotonic compression-tested specimens or creep specimens loaded to the same strains, as is microdamage accumulation. Microdamage accumulation and mechanical property changes initiate at lower strains in fatigue-tested specimens. Crack growth, inferred by the number of complete trabecular fractures, is observed in fatigue specimens loaded to large numbers of cycles at these strain levels, and not in specimens loaded to lower numbers of cycles.

At very low strains, less than -0.5% in fatigue-tested specimens and less than -0.8% in monotonic compression-tested specimens, we do not observe any microdamage accumulation or changes in mechanical properties. Characterization of the fatigue

behavior of bovine trabecular bone predicted an endurance limit near $\Delta\sigma/E_0 = 0.0035$, corresponding to a strain of -0.35% (Appendix B). Pattin *et al.* (1996) also found a damage threshold of 4000 $\mu\varepsilon$ for human cortical bone fatigued in compression, corresponding to a loading strain of -0.4%. Based on linear regression data, we do not expect to observe any modulus loss at strains below about -0.5% for fatigue and montonic compression. As well, residual strains are not expected at strains less than -0.55% for fatigue-tested specimens, and -0.77% for monotonic compression-tested specimens. Also, no microdamage accumulation is observed at strains below these limits. These results support our observations of an endurance limit for bovine trabecular bone in compression, which occurs at a strain level of less than about -0.4%. The majority of physiologic loading occurs at strains below the endurance limit, suggesting that microdamage is created only during extremes of loading or in diseased bone with reduced load-carrying capacity (e.g. osteoporotic bone). When microdamage does occur, the bone remodeling process will replace the damaged bone within a few months, and return the bone to its original state.

Microdamage accumulation occurs in bovine trabecular bone when it is loaded beyond yield. Microdamage can occur during a single overload or as a result of fatigue damage. However, microdamage is not created at strains well below yield (< 0.5%), where most physiologic loading occurs. Microdamage is created during extreme physiologic loading, and damaged bone is replaced by the bone remodeling process. Microdamage creation may serve as an energy dissipation method in bone, a process that can sustain occasional overloads without increasing the bone strength, and thus mass, to prohibitively high levels.

References

Aaron, J. E., Makins, N., B., Francis, R. M. and Peacock, M. (1984). "Stainir.g of the calcification front in human bone using contrasting fluorochromes *in vitro*." *Journal of Histochemistry and Cytochemistry*, **32**(12): 1251-61.

Alexeera, L., Burkhardt, P., Christiansen, C. *et al.* (1994). *Assessment of fracture risk and application to screening for post-menopausal osteoporosis*. World Health Organinzation Technical Report Series 843. World Health Organization, Geneva.

Amling, M., Herden, S., Posl, M., Hahn, M., Ritzel, H. and Delling, G. (1996). "Heterogeneity of the skeleton: comparison of the trabecular microarchitecture of the spine, the iliac crest, the femur, and the calcaneus." *Journal of Bone and Mineral Research*, **11**(1): 36-45.

Andrews, E. W., Gioux, G., Onck, P. and Gibson, L. J. (2001). "Size effects in ductile cellular solids. Part II: experimental results." *International Journal of Mechanical Sciences*, **43**: 701-13.

Archdeacon, M. T., Davy, D. T. and Jepsen, K. J. (1997). "Time dependent damage accumulation in bovine bone loaded in torsion." *Transactions of the Orthopaedic Research Society*, **22**: 40.

Ashman, R. B. and Rho, J. Y. (1988). "Elastic modulus of trabecular bone material." *Journal of Biomechanics*, **21**(3): 177-81.

Bart-Smith, H., A.-F., B., Mumm, D. R., Evans, A. G., Sypeck, D. J. and Wadley, H. N. G. (1998). "Compressive deformation and yielding mechanisms in cellular Al alloys determined using x-ray tomography and surface strain mapping." *Acta Materiala*, **46**(10): 3583-92.

Bastawros, A.-F., Bart-Smith, H. and Evans, A. G. (2000). "Experimental analysis of deformation mechanisms in a closed-cell Al alloy foam." *Journal of the Mechanics and Physics of Solids*, **48**: 301-22.

Bay, B. K., Yerby, S. A. and McLain, R. F. (1997). "Spatial distribution of strain within vertebral trabecular bone." *Transactions of the Orthopaedic Research Society*, **22**: 797.

Beaupré, G. S. and Hayes, W. C. (1985). "Finite element analysis of a three-dimensional open-celled model for trabecular bone." *Journal of Biomechanical Engineering*, **107**(3): 249-56.

Bentolila, V., Boyce, T. M., Fyhrie, D. P., Drumb, R., Skerry, T. M. and Schaffler, M. B. (1998). "Intracortical remodeling in adult rat long bones after fatigue loading." *Bone*, **23**(3): 275-81.

Bergot, C., Laval-Jeantet, A.-M., Preteux, F. and Meunier, A. (1988). "Measurement of anisotropic vertebral trabecular bone loss during aging by quantitative image analysis." *Calcified Tissue International*, **43**(3): 143-9.

Bowman, S. M. (1997). *Creep of Trabecular Bone*. Ph.D. Thesis. Harvard University, Cambridge, Massachusetts.

Bowman, S. M., Gibson, L. J., Hayes, W. C. and McMahon, T. A. (1999). "Results from demineralized bone creep tests suggest that collagen is responsible for the creep behavior of bone." *Journal of Biomechanics*, **121**(2): 253-8.

Bowman, S. M., Guo, X. E., Cheng, D. W., Keaveny, T. M., Gibson, L. J., Hayes, W. C. and McMahon, T. A. (1998). "Creep contributes to the fatigue behavior of bovine trabecular bone." *Journal of Biomechanical Engineering*, **120**(5): 647-54.

Bowman, S. M., Keaveny, T. M., Gibson, L. J., Hayes, W. C. and McMahon, T. A. (1994). "Compressive creep behavior of bovine trabecular bone." *Journal of Biomechanics*, **27**(3): 301-10.

Boyce, T. M., Fyhrie, D. P., Glotkowski, M. C., Radin, E. L. and Schaffler, M. B. (1998). "Damage type and strain mode associations in human compact bone bending fatigue." *Journal of Orthopaedic Research*, **16**(3): 322-9.

Budiansky, B. and O'Connell, R. J. (1976). "Elastic moduli of a cracked solid." *International Journal of Solids and Structures*, **12**: 81-97.

Burr, D. B. (2000). "Damage detection and behavior in bone." 12th conference of the European Society of Biomechanics, Dublin, Ireland, p. 38-9.

Burr, D. B., Forwood, M. R., Fyhrie, D. P., Martin, R. B., Schaffler, M. B. and Turner, C. H. (1997). "Bone microdamage and skeletal fragility in osteoporotic and stress fractures." *Journal of Bone and Mineral Research*, **12**(1): 6-15.

Burr, D. B. and Hooser, M. (1995). "Alterations to the *en bloc* basic fuchsin staining protocol for the demonstration of microdamage produced *in vivo*." *Bone*, **17**(4): 431-3.

Burr, D. B., Martin, R. B., Schaffler, M. B. and Radin, E. L. (1985). "Bone remodeling in response to *in vivo* fatigue microdamage." *Journal of Biomechanics*, **18**(3): 189-200.

Burr, D. B. and Stafford, T. (1990). "Validity of the bulk-staining technique to separate artifactual from *in vivo* bone microdamage." *Clinical Orthopaedics and Related Research*, **260**(260): 305-8.

Burr, D. B., Turner, C. H., Naick, P., Forwood, M. R., Ambrosius, W., Hasan, M. S. and Pidaparti, R. (1998). "Does microdamage accumulation affect the mechanical properties of bone?" *Journal of Biomechanics*, **31**: 337-45.

Caler, W. E. and Carter, D. R. (1989). "Bone creep-fatigue damage accumulation." *Journal of Biomechanics*, **22**(6-7): 625-35.

Carter, D. R. and Caler, W. E. (1983). "Cycle-dependent and time-dependent bone fracture with repeated loading." *Journal of Biomechanical Engineering*, **105**(2): 166-70.

Carter, D. R. and Caler, W. E. (1985). "A cumulative damage model for bone fracture." *Journal of Orthopaedic Research*, **3**(1): 84-90.

Carter, D. R. and Hayes, W. C. (1976). "Fatigue life of compact bone-I. Effects of stress amplitude, temperature and density." *Journal of Biomechanics*, **9**: 27-34.

Carter, D. R. and Hayes, W. C. (1977a). "Compact bone fatigue damage - I. residual strength and stiffness." *Journal of Biomechanics*, **10**: 325-37.

Carter, D. R. and Hayes, W. C. (1977b). "Compact bone fatigue damage: a microscopic examination." *Clinical Orthopaedics and Related Research*, **127**: 265-74.

Carter, D. R. and Hayes, W. C. (1977c). "The compressive behavior of bone as a two-phase porous structure." *Journal of Bone and Joint Surgery [Am]*, **59**(7): 954-62.

Chang, W. C. W, Christensen, T. M., Pinilla, T. P., and Keaveny, T. M. (1999). "Isotropy of uniaxial yield strains for bovine trabecular bone." *Journal of Orthopaedic Research*, **17**: 582-5.

Cheng, D. W. (1995). *Compressive High Cycle at Low Strain Fatigue Behavior of Bovine Trabecular Bone*. S.M. Thesis. Massachusetts Institute of Technology, Cambridge, Massachusetts.

Ciarelli, M. J., Goldstein, S. A., Kuhn, J. L., Cody, D. D. and Brown, M. B. (1991). "Evaluation of orthogonal mechanical properties and density of human trabecular bone from the major metaphyseal regions with materials testing and computed tomography." *Journal of Orthopaedic Research*, **9**(5): 674-82.

Cowin, S. C. (1986). "Wolff's law of trabecular architecture at remodeling equilibrium." *Journal of Biomechanical Engineering*, **108**(1): 83-8.

Daffner, R. H. and Pavlov, H. (1992). "Stress fractures: current concepts." *American Journal of Roentgenology*, **159**(8): 245-52.

Dargent-Molina, P. (1998). "Risk factors and prevention of fractures in the elderly." *Current Opinion in Orthopedics*, **9**: 43-7.

DeHoff, R. T. and Rhines, F. N. (1968). *Quantitative Microscopy*. McGraw-Hill, New York.

Deligianni, D. D., Maris, A. and Missirlis, Y. F. (1994). "Stress relaxation behaviour of trabecular bone specimens." *Journal of Biomechanics*, **27**(12): 1469-76.

Ding, M., Dalstra, M., Danielsen, C. C., Kabel, J., Hvid, I. and Linde, F. (1997). "Age variations in the properties of human tibial trabecular bone." *Journal of Bone and Joint Surgery [Br]*, **79**(6): 995-1002.

Donahue, S. W., Sharkey, N. A., Modanlou, K. A., Swqueira, L. N. and Martin, R. B. (2000). "Bone strain and microcracks at stress fracture sites in human metatarsals." *Bone*, **27**(6): 827-33.

Ducheyne, P., Heymans, L., Martens, M., Aernoudt, E., de Meester, P. and Mulier, J. C. (1977). "The mechanical behaviour of intracondylar cancellous bone of the femur at different loading rates." *Journal of Biomechanics*, **10**(11/12): 747-62.

Dunn, M. G., McBride, D. J. and Shapiro, J. R. (1995). "Absence of the collagen alpha2(I) chain dimishes the mechanical properties of bone." *Transactions of the Orthopaedic Research Society*, **20**: 153.

Fazzalari, N. L., Forwood, M. R., Manthey, B. A., Smith, K. and Kolesik, P. (1998a). "Three-dimensional confocal images of microdamage in cancellous bone." *Bone*, **23**(4): 373-8.

Fazzalari, N. L., Forwood, M. R., Smith, K., Manthey, B. A. and Herreen, P. (1998b). "Assessment of cancellous bone quality in severe osteoarthrosis: bone mineral density, mechanics, and microdamage." *Bone*, **22**(4): 381-8.

Fazzalari, N. L., Vernon-Roberts, B. and Darracott, J. (1987). "Osteoarthritis of the hip. Possible protective and causative roles of trabecular microfractures in the head of the femur." *Clinical Orthopaedics and Related Research*, **216**: 224-33.

Fondrk, M., Bahniuk, E., Davy, D. T. and Michaels, C. (1988). "Some viscoplastic characteristics of bovine and human cortical bone." *Journal of Biomechanics*, **21**(8): 623-30.

Ford, C. M. and Keaveny, T. M. (1996). "The dependence of shear failure properties of trabecular bone on apparent density and trabecular orientation." *Journal of Biomechanics*, **29**(10): 1309-17.

Forwood, M. R., Burr, D. B., Takano, Y., Eastman, D. F., Smith, P. N. and Schwardt, J. D. (1995). "Risedronate treatment does not increase microdamage in the canine femoral neck." *Bone*, **16**(6): 643-50.

Forwood, M. R., Mashiba, T., Hirano, T., Turner, C. H., Johnston, C. C. and Burr, D. B. (2000a). "Bisphosphonates are associated with microdamage accumualation at clinically relevant skeletal sites in beagles." *Bone*, **27**(4 Suppl): 27S.

Forwood, M. R., Mashiba, T., Turner, C. H., Hirano, T., Jacob, D. S., Johnston, C. C. and Burr, D. B. (2000b). "Effects of etidronate on microdamage and mechanical properties of bone prior to the occurrence of spontaneous fractures in beagles." *Bone*, **27**(4 Suppl): 38S.

Forwood, M. R. and Parker, A. W. (1989). "Microdamage in response to repetitive torsional loading in the rat tibia." *Calcified Tissue International*, **45**(1): 47-53.

Fox Ray, N., Chan, J. K., Thamer, M. and Melton, L. J. I. (1997). "Medical expenditures for the treatment of osteoporotic fractures in the United States in 1995: report from the National Osteoporosis Foundation." *Journal of Bone and Mineral Research*, **12**(1): 24-35.

Freeman, M. A. R., Todd, R. C. and Ririe, C. J. (1974). "The role of fatigue in the pathogenesis of senile femoral neck fractures." *Journal of Bone and Joint Surgery*, **56B**(4): 698-702.

Frost, H. M. (1958). "Preparation of thin undecalcified bone sections by rapid manual method." *Stain Technology*, **33**: 273-7.

Frost, H. M. (1960). "Presence of microscopic cracks *in vivo* in bone." *Bulletin of the Henry Ford Hospital*, **8**: 23-35.

Frost, H. M. (1963). "Measurement of human bone formation by means of tetracycline labelling." *Canadian Journal of Biochemistry and Physiology*, **41**: 31-42.

Frost, H. M. (1969). "Tetracycline-based histological analysis of bone remodeling." *Calcified Tissue Research*, **3**: 211-37.

Frost, H. M. (1989). "Transient-steady state phenomena in microdamage physiology: a proposed algorithm for lamellar bone." *Calcified Tissue International*, **44**: 367-81.

Frost, H. M., Villanueva, A. R., Roth, H. and Stanisavljevic, S. (1961). "Tetracycline bone labeling." *Journal of New Drugs*, **1**: 206-16.

Fyhrie, D. P. and Schaffler, M. B. (1994). "Failure mechanisms in human vertebral cancellous bone." *Bone*, **15**(1): 105-9.

Fyhrie, D. P. and Vashishth, D. (2000). "Bone stiffness predicts strength similarly for human vertebral cancellous bone in compression and for cortical bone in tension." *Bone*, **26**(2): 169-73.

Gibson, L. J. (1985). "The mechanical behaviour of cancellous bone." *Journal of Biomechanics*, **18**(5): 317-28.

Gibson, L. J. and Ashby, M. F. (1997). *Cellular Solids*. Cambridge University Press, Cambridge.

Goldstein, S. A., Goulet, R. and McCubbrey, D. (1993). "Measurement and significance of three-dimensional architecture to the mechanical integrity of trabecular bone." *Calcified Tissue International*, **53**(Suppl 1): S127-S33.

Goulet, R. W., Goldstein, S. A., Ciarelli, M. J., Kuhn, J. L., Brown, M. B. and Feldkamp, L. A. (1994). "The relationship between the structural and orthogonal compressive properties of trabecular bone." *Journal of Biomechanics*, **27**(4): 375-89.

Grenestedt, J. L. and Bassinet, F. (2000). "Influence of cell wall thickness variations on elastic stiffness of closed cell cellular solids." *International Journal of Mechanical Science*, **42**: 1327-38.

Grynpas, M. (1993). "Age and disease-related changes in the mineral of bone." *Calcified Tissue International*, **53**(Suppl 1): S57-S64.

Guo, X. E. (1993). *Fatigue of Trabecular Bone*. Ph.D. Thesis. Harvard University, Cambridge, Massachusetts.

Guo, X. E., Gibson, L. J., McMahon, T. A., Keaveny, T. M. and Hayes, W. C. (1992). "Finite element modeling of fatigue damage accumulation in trabecular bone." *Transactions of the Orthopaedic Research Society*, **17**: 164.

Guo, X. E., McMahon, T. A., Keaveny, T. M., Hayes, W. C. and Gibson, L. J. (1994). "Finite element modeling of damage accumulation in trabecular bone under cyclic loading." *Journal of Biomechanics*, **27**(2): 145-55.

Guo, X. E., Weissmean, D. E., Goulet, R. W., Hollister, S. J., Derwin, K. A. and Golstein, S. A. (1995). "Characterization of local failure in vertebral trabecular bone." *Transactions of the Orthopaedic Research Society*, **20**: 532.

Haddock, S. M., Yeh, O. C., Mummaneni, P. V., Rosenberg, W. S. and Keaveny, T. M. (2000). "Fatigue behavior of human vertebral trabecular bone." *Transactions of the Orthopaedic Research Society*, **25**: 733.

Heaney, R. P. (1993). "Is there a role for bone quality in fragility fractures?" *Calcified Tissue International*, **53**(Suppl 1): S3-5.

Hertzberg, R. W. (1989). *Deformation and fracture mechanics of engineering materials.* Wiley, New York.

Hirano, T., Turner, C. H., Forwood, M. R., Johnston, C. C. and Burr, D. B. (2000). "Does suppression of bone turnover impair mechanical properties by allowing microdamage accumulation?" *Bone*, **27**(1): 13-20.

Hollister, S. J., Brennan, J. M. and Kikuchi, N. (1994). "A homogenization sampling procedure for calculating trabecular bone effective stiffness and tissue level stress." *Journal of Biomechanics*, **27**(4): 433-44.

Hollister, S. J., Fyhrie, D. P., Jepsen, K. J. and Goldstein, S. A. (1991). "Application of homogenization theory to the study of trabecular bone mechanics." *Journal of Biomechanics*, **24**(9): 825-39.

Hoshaw, S. J., Cody, D. D., Saad, A. M. and Fyhrie, D. P. (1997). "Decrease in canine proximal femoral ultimate strength and stiffness due to fatigue damage." *Journal of Biomechanics*, **30**(4): 323-9.

Huja, S. S., Hasan, M. S., Pidaparti, R., Turner, C. H., Garetto, L. P. and Burr, D. B. (1999). "Development of a fluorescent light technique for evaluating microdamage in bone subjected to fatigue loading." *Journal of Biomechanics*, **32**(11): 1243-9.

Hvid, I., Bentzen, S. M., Linde, F., Mosekilde, L. and Pongsoipetch, B. (1989). "X-ray quantitative computed tomography: the relations to physical properties of proximal tibial trabecular bone specimens." *Journal of Biomechanics*, **22**(8-9): 837-44.

Hvid, I., Jensen, N. C., Bunger, C., Solund, K. and Djurhuus, J. C. (1985). "Bone mineral assay: its relation to the mechanical strength of cancellous bone." *Engineering Medicine*, **14**(2): 79-83.

Jepson, K. J., Davy, D. T. and Krzypow, D. J. (1999). "The role of the lamellar interface during torsional yielding of human cortical bone." *Journal of Biomechanics*, **32**: 303-10.

Kasra, M. and Grynpas, M. D. (1998). "Static and dynamic finite element analyses of an idealized structural model of vertebral trabecular bone." *Journal of Biomechanical Engineering*, **120**(2): 267-72.

Keaveny, T. M., Borchers, R. E., Gibson, L. J. and Hayes, W. C. (1993a). "Theoretical analysis of the experimental artifact in trabecular bone compressive modulus." *Journal of Biomechanics*, **26**(4-5): 599-607.

Keaveny, T. M., Borchers, R. E., Gibson, L. J. and Hayes, W. C. (1993b). "Trabecular bone modulus and strength can depend on specimen geometry." *Journal of Biomechanics*, **26**(8): 991-1000.

Keaveny, T. M., Guo, X. E. and Wachtel, E. F. (1993c). "Trabecular bone is linearly elastic up to yielding and yields by cracking." *Transactions of the Orthopaedic Research Society*, **18**: 586.

Keaveny, T. M., Guo, X. E., Wachtel, E. F., McMahon, T. A. and Hayes, W. C. (1994a). "Trabecular bone exhibits fully linear elastic behavior and yields at low strains." *Journal of Biomechanics*, **27**(9): 1127-36.

Keaveny, T. M. and Hayes, W. C. (1993b). "A 20-year perspective on the mechanical properties of trabecular bone." *Journal of Biomechanical Engineering*, **115**(4B): 534-42.

Keaveny, T. M., Pinilla, T. P., Crawford, R. P., Kopperdahl, D. L. and Lou, A. (1997). "Systematic and random errors in compression testing of trabecular bone." *Journal of Orthopaedic Research*, **15**(1): 101-10.

Keaveny, T. M., Wachtel, E. F., Cutler, M. J. and Pinilla, T. P. (1994b). "Yield strains for bovine trabecular bone are isotropic but asymmetric." *Transactions of the Orthopaedic Research Society*, **19**: 428.

Keaveny, T. M., Wachtel, E. F., Ford, C. M. and Hayes, W. C. (1994c). "Differences between the tensile and compressive strengths of bovine tibial trabecular bone depend on modulus." *Journal of Biomechanics*, **27**(9): 1137-46.

Keaveny, T. M., Wachtel, E. F., Guo, X. E. and Hayes, W. C. (1994d). "Mechanical behavior of damaged trabecular bone." *Journal of Biomechanics*, **27**(11): 1309-18.

Keaveny, T. M., Wachtel, E. F. and Kopperdahl, D. L. (1999). "Mechanical behavior of human trabecular bone after overloading." *Journal of Biomechanics*, **17**: 346-53.

Kinney, J. H. and Ladd, A. J. C. (1998). "The relationship betwen three-dimensional connectivity and the elastic properties of trabecular bone." *Journal of Bone and Mineral Research*, **13**(5): 839-45.

Kopperdahl, D. L. and Keaveny, T. M. (1998). "Yield strain behavior of trabecular bone." *Journal of Biomechanics*, **31**: 601-8.

Ladd, A. J. C., Kinney, J. H., Haupt, D. L. and Goldstein, S. A. (1998). "Finite-element modeling of trabecular bone: comparison with mechanical testing and determination of tissue modulus." *Journal of Orthopaedic Research*, **16**: 622-8.

Landis, W. J. (1995). "The strength of a calcified tissue depends in part on the molecular structure and organization of its constituent mineral crystals in theri organic matrix." *Bone*, **16**(5): 533-44.

Lane, J. M. and Myers, E. R. (1996). "Biomechanical aspects of osteoporosis and fractures." *Osteoporosis: Diagnosis and Treatment*. Sartoris, D. J. Marcel Dekker, New York.

Lee, T. C. (1995). *Functional adaptation in compact bone*. Ph.D. Thesis. University of Dublin, Dublin, Ireland.

Lee, T. C. (1997). *Detection and Accumulation of Microdamage in Bone*. M.D. Thesis. University of Dublin, Dublin, Ireland.

Lee, T. C., Arthur, T. L., Gibson, L. J. and Hayes, W. C. (2000). "Sequential labelling of microdamage in bone using chelating agents." *Journal of Orthopaedic Research*, **18**: 322-5.

Lee, T. C., Arthur, T. L., Hayes, W. C. and Gibson, L. J. (1997a). "Detection of fatigue crack growth in bone." ASME Summer Bioengineering Conference, Sun River, Oregon.

Lee, T. C., Myers, E. R. and Hayes, W. C. (1997b). "Microdamage detection in compact bone." *Transactions of the Orthopaedic Research Society*, **22**: 333.

Lee, T. C., Myers, E. R. and Hayes, W. C. (1998). "Fluorescence-aided detection of microdamage in compact bone." *Journal of Anatomy*, **193**(Pt 2): 179-84.

Li, J., Mashiba, T. and Burr, D. B. (2001). "Bisphosphonate treatment suppresses targeted repair of microdamage." *Transactions of the Orthopaedic Research Society*, **26**: 320.

Linde, F. and Hvid, I. (1989). "The effect of constraint on the mechanical behavior of trabecular bone specimens." *Journal of Biomechanics*, **22**(5): 485-90.

Linde, F., Hvid, I. and Madsen, F. (1992). "The effect of specimen geometry on the mechanical behaviour of trabecular bone specimens." *Journal of Biomechanics*, **25**(4): 359-68.

Linde, F., Norgaard, P., Hvid, I., Odgaard, A. and Soballe, K. (1991). "Mechanical properties of trabecular bone. Dependency on strain rate." *Journal of Biomechanics*, **24**(9): 803-9.

Mammone, J. F. and Hudson, S. M. (1993). "Micromechanics of bone strength and fracture." *Journal of Biomechanics*, **26**(4-5): 439-46.

Martin, R. B. (1991). "Determinants of the mechanical properties of bones." *Journal of Biomechanics*, **24**(Suppl 1): 79-88.

Martin, R. B. (1992). "A theory of fatigue damage accumulation and repair in cortical bone." *Journal of Orthopaedic Reseach*, **10**(6): 818-25.

Martin, R .B. (1995). "Mathematical model for repair of fatigue damage and stress fracture in osteonal bone." *Journal of Orthopaedic Research*, **13**(3): 309-16.

Martin, R. B. (2000). "Toward a unifying theory of bone remodeling." *Bone*, **26**(1): 1-6.

Martin, R. B. and Boardman, D. L. (1993). "The effects of collagen fiber orientation, porosity, density, and mineralization on bovine cortical bone bending properties." *Journal of Biomechanics*, **26**(9): 1047-54.

Martin, R. B., Lau, S. T., Mathews, P. V., Gibson, V. A. and Stover, S. M. (1996a). "Collagen fiber organization is related to mechanical properties and remodeling in equine bone. A comparison of two methods." *Journal of Biomechanics*, **29**(12): 1515-21.

Martin, R. B., Mashiba, T., Hirano, T. and Burr, D. B. (2000). "Computer simulation of the effects of bone remodeling suppression on microdamage." *Transactions of the Orthopaedic Research Society*, **25**: 35.

Martin, R. B., Stover, S. M., Gibson, V. A., Gibeling, J. C. and Griffin, L. V. (1996b). "*In vitro* fatigue behavior of the equine third metacarpus: remodeling and microcrack damage analysis." *Journal of Orthopaedic Research*, **14**: 794-801.

Mashiba, T., Hirano, T., Turner, C. H., Forwood, M. R., Johnston, C. C. and Burr, D. B. (2000). "Suppressed bone turnover by bisphosphonates increases microdamage accumulation and reduces some biomechanical properties in dog rib." *Journal of Bone and Mineral Research*, **15**(4): 613-20.

McClung, M. R. (1996). "Current bone mineral density data on bisphosphonates in postmenopausal osteoporosis." *Bone*, **19**(5): 195S-8S.

McCubbrey, D. A., Cody, D. D., Kuhn, J. L., Goldstein, S. A. and Flynn, M. J. (1990). "Static and fatigue failure properties of the thoracic and lumbar vertebral bodies and their relation to regional density." *Transactions of the Orthopaedic Research Society*, **15**: 178.

McCullough, K. Y. G., Fleck, N. A. and Ashby, M. F. (1999a). "The stress-life fatigue behavior of aluminum alloy foams." *Fatigue and Fracture of Engineering Materials and Structures*, **23**(3): 2323-30.

McCullough, K. Y. G., Fleck, N. A. and Ashby, M. F. (1999b). "Uniaxial stress-strain behaviour of aluminium alloy foams." *Acta Materiala*, **47**(8): 2323-30.

Michel, M. C., Guo, X. D., Gibson, L. J., McMahon, T. A. and Hayes, W. C. (1993). "Compressive fatigue behavior of bovine trabecular bone." *Journal of Biomechanics*, **26**(4-5): 453-63.

Morgan, E. F., Yeh, O. C., Chang, W. C. and Keaveny, T. M. (2000). "Non-linear behavior of trabecular bone at small strains." *Transactions of the Orthopaedic Research Society*, **25**: 31.

Morgan, E. F. and Keaveny, T. M. (2001). "Dependence of yield strain of human trabecular bone on anatomic site." *Journal of Biomechanics*, **34**: 569-77.

Mori, S. and Burr, D. B. (1993). "Increased intracortical remodeling following fatigue damage." *Bone*, **14**(2): 103-9.

Mori, S., Harruff, R., Ambrosius, W. and Burr, D. B. (1997). "Trabecular bone volume and microdamage accumulation in the femoral heads of women with and without femoral neck fractures." *Bone*, **21**(6): 521-6.

Mosekilde, L. (1993). "Vertebral structure and strength *in vivo* and *in vitro*." *Calcified Tissue International*, **53**(Suppl 1): S121-S6.

Mosekilde, L., Mosekilde, L. and Danielsen, C. C. (1987). "Biomechanical competence of vertebral trabecular bone in relation to ash density and age in normal individuals." *Bone*, **8**(2): 79-85.

Muir, P., Johnson, K. A. and Ruaux-Mason, C. P. (1999). "*In vivo* matrix microdamage in a naturally occurring canine fatigue fracture." *Bone*, **25**(5): 571-6.

Mueller, R., Gerber, S. C. and Hayes, W. C. (1998). "Micro-compression: a novel technique for the nondestructive assessment of local bone failure." *Technology and Health Care*, **6**(5-6): 433-44.

Mueller, R. and Ruegsegger, P. (1995). "Three-dimensional finite element modelling of non-invasively assessed trabecular bone structures." *Medical Engineering and Physics*, **17**(2): 126-33.

Mueller, R. and Ruegsegger, P. (1996). "Analysis of mechanical properties of cancellous bone under conditions of simulated bone atrophy." *Journal of Biomechanics*, **29**(8): 1053-60.

Nieber, G. L., Yuen, J. C. and Keaveny, T. M. (2000). "Role of hard tissue quality in trabecular bone failure mechanisms." *Transactions of the Orthopaedic Research Society*, **25**: 11.

Nordin, M. and Frankel, V. H. (1989). *Biomechanics of Bone*. Lea and Febiger, Philidelphia.

Nunamaker, D. M., Butterweck, D. M. and Provost, M. T. (1990). "Fatigue fractures in thoroughbred racehorses: relationships with age, peak bone strain, and training." *Journal of Orthopaedic Research*, **8**(4): 604-11.

O'Brien, F. J. (2001). *Microcracks and the fatigue behaviour of compact bone*. Ph.D. Thesis. Trinity College and Royal College of Surgeons in Ireland, Dublin, Ireland.

O'Brien, F. J., Grady, T., Diamond, D., Taylor, D. and Lee, T. C. (1999a). "The use of fluorescent chelating agents in the detection of microdamage in compact bone." *Journal of Bone and Joint Surgery [BR]*, **81-B**(S3): 321.

O'Brien, F. J., Taylor, D., Dickson, G. R. and Lee, T. C. (2000). "Visualisation of three-dimensional microcracks in compact bone." *Journal of Anatomy*, **197 Pt 3**(2): 413-20.

O'Brien, F. J., Taylor, D. and Lee, T. C. (1999b). "Visualisation of microdamage in compact bone." *Irish Journal of Medical Sciences*, **168**(3): 216.

Oden, Z. M., Sevitelli, D. M., Hayes, W. C. and Myers, E. R. (1998). "The effect of trabecular structure on DXA-based predictions of bovine bone failure." *Calcified Tissue International*, **63**(1): 67-73.

Odgaard, A., Hvid, I. and Linde, F. (1989). "Compressive axial strain distributions in cancellous bone specimens." *Journal of Biomechanics*, **22**(8-9): 829-35.

Odgaard, A. and Linde, F. (1991). "The underestimation of Young's modulus in compressive testing of cancellous bone specimens." *Journal of Biomechanics*, **24**(8): 691-8.

Olerud, S. and Lorenzi, G. L. (1970). "Triple fluorochrome labeling in bone formation and bone resorption." *Journal of Bone and Joint Surgery*, **52-A**(2): 274-8.

Olurin, O. B., Fleck, N. A. and Ashby, M. F. (1999). "Deformation and fracture of aluminum foams." *Materials Science and Engineering A*, **291**(1-2): 136-46.

Onck, P. R., Andrews, E. W. and Gibson, L. J. (2001). "Size effects in ductile cellular solids. Part I: modeling." *International Journal of Mechanical Sciences*, **43**: 681-99.

Parfitt, A. M., Numdy, G. R., Roodman, G. D., Hughes, D. E. and Boyce, B. F. (1996). "A new model for the regulation of bone resorption, with particular reference to the effects of bisphosphonates." *Journal of Bone and Mineral Research*, **11**(2): 150-8.

Pattin, C. A., Caler, W. E. and Carter, D. R. (1996). "Cyclic mechanical property degradation during fatigue loading of cortical bone." *Journal of Biomechanics*, **29**(1): 69-79.

Pierce, R. K. (1999). *Creep microdamage in trabecular bone*. Bachelor of Science Thesis. Massachusetts Institute of Technology, Cambridge, Massachusetts.

Pugh, J. W., Rose, R. M. and Radin, E. L. (1973). "Elastic and viscoelastic properties of trabecular bone: dependence on structure." *Journal of Biomechanics*, **6**(5): 475-85.

Rahn, B. A. (1977). "Polychrome fluorescence labelling of bone formation - Instrumental aspects and experimental use." *Zeiss Information*, **22**(85): 36-9.

Rahn, B. A. and Perren, S. M. (1970). "Calcein blue as a fluorescent label in bone." *Experientia*, **26**(5): 519-20.

Rahn, B. A. and Perren, S. M. (1971). "Xylenol orange, a fluorochrome useful in polychrome sequential labeling of calcifying tissues." *Stain Technology*, **46**(3): 125-9.

Rahn, B. A. and Perren, S. M. (1972). "Alizarinkomplexon - fluorchrom zur makierung von knochen- und dentinonbau." *Experientia*, **28**: 180.

Recker, R. R. (1993). "Architecture and vertebral fracture." *Calcified Tissue International*, **53**(Suppl 1): S139-42.

Reilly, G. C. (2000). "Observations of microdamage around osteocyte lacunae in bone." *Journal of Biomechanics*, **33**: 1131-4.

Reilly, G. C. and Currey, J. D. (1999). "The development of microcracking and failure in bone depends on the loading mode to which it is adapted." *Journal of Experimental Biology*, **202**(5): 543-52.

Rho, J. Y., Tsui, T. Y. and Pharr, G. M. (1997). "Elastic properties of human cortical and trabecular lamellar bone measured by nanoindentation." *Biomaterials*, **18**(20): 1325-30.

Rice, J. C., Cowin, S. C. and Bowman, J. A. (1988). "On the dependence of the elasticity and strength of cancellous bone on apparent density." *Journal of Biomechanics*, **21**(2): 155-68.

Rimnac, C. M., Petco, A. A., Santer, T. J. and Wright, T. M. (1993a). "Creep of compact human bone." *Transactions of the Orthopaedic Research Society*, **18**: 172.

Rimnac, C. M., Petko, A. A., Santner, T. J. and Wright, T. M. (1993b). "The effect of temperature, stress and microstructure on the creep of compact bovine bone." *Journal of Biomechanics*, **26**(3): 219-28.

Schaffler, M. B., Boyce, T. M. and Fyhrie, D. P. (1996). "Tissue and matrix failure modes in human compact bone during tensile fatigue." *Transactions of the Orthopaedic Research Society*, **21**: 57.

Schaffler, M. B., Boyce, T. M., Lundin-Cannon, K. D., Milgrom, C. and Fyhrie, D. P. (1995a). "Age-related architectural changes and microdamage accumulation in the human femoral neck cortex." *Transactions of the Orthopaedic Research Society*, **20**: 549.

Schaffler, M. B., Choi, K. and Milgrom, C. (1995b). "Aging and matrix microdamage accumulation in human compact bone." *Bone*, **17**(6): 521-25.

Schaffler, M. B. and Jepsen, K. J. (2000). "Fatigue and repair in bone." *International Journal of Fatigue*, **22**: 839-46.

Schaffler, M. B., Pitchford, W. C., Choi, K. and Riddle, J. M. (1994). "Examination of compact bone microdamage using back-scattered electron microscopy." *Bone*, **15**(5): 483-8.

Schaffler, M. B., Radin, E. L. and Burr, D. B. (1989). "Mechanical and morphological effects of strain rate on fatigue of compact bone." *Bone*, **10**(3): 207-14.

Schaffler, M. B., Radin, E. L. and Burr, D. B. (1990). "Long-term fatigue behavior of compact bone at low strain magnitude and rate." *Bone*, **11**(5): 321-6.

Schaffner, G., Guo, X. E., Silva, M. J. and Gibson, L. J. (2000). "Modelling fatigue damage accumulation in two-dimensional Voronoi honeycombs." *International Journal of Mechanical Sciences*, **42**(4): 645-56.

Schneider, P. F., Fischer, M., Allolio, B., Felsenberg, D., Schroder, U., Semler, J. and Ittner, J. R. (1999). "Alendronate increases bone density and bone strength at the distal radius in postmenopausal women." *Journal of Bone and Mineral Research*, **14**(8): 1387-93.

Schnitzler, C. M. (1993). "Bone quality: a determinant for certain risk factors for bone fragility." *Calcified Tissue International*, **53**(Suppl 1): S27-31.

Seireg, A. and Kempke, W. (1969). "Behavior of *in vivo* bone under cyclic loading." *Journal of Biomechanics*, **2**: 455-61.

Silva, M. J. and Gibson, L. J. (1997a). "The effects of non-periodic microstructure and defects on the compressive strength of two-dimensional cellular solids." *International Journal of Mechanics Science*, **39**(5): 549-63.

Silva, M. J. and Gibson, L. J. (1997b). "Modeling the mechanical behavior of vertebral trabecular bone: effects of age-related changes in microstructure." *Bone*, **21**(2): 191-9.

Snyder, B. D., Piazza, S., Edwards, W. T. and Hayes, W. C. (1993). "Role of trabecular morphology in the etiology of age-related vertebral fractures." *Calcified Tissue International*, **53**(Suppl 1): S14-22.

Stauffer, D. and Aharony, A. (1992). *Introduction to Percolation Theory*. Taylor and Francis, London.

Stover, S. M., Martin, R. B., Pool, R. R., Taylor, K. T. and Harrington, T. M. (1993). "*In vivo* labeling of microdamage in cortical bone tissues." *Transactions of the Orthopaedic Research Society*, **18**: 541.

Sugimura, Y., Rabiei, A., Evans, A. G., Harte, A. M. and Fleck, N. A. (1998). "Compression fatigue of a cellular Al alloy." *Materials Science and Engineering A*, **269**(1-2): 38-48.

Suzuki, H. K. and Mathews, A. (1966). "Two-color fluorescent labeling of mineralizing tissues with tetracycline and 2,4-bis[n, n'-di-(carbomethyl)aminomethyl] fluorescein." *Stain Technology*, **41**(1): 57-60.

Tantillo, M. (1999). *Image-guided assessment of local bone failure*. Bachelor of Science Thesis. Boston University, Boston, Massachusetts.

Taylor, D. (1998a). "Fatigue of bone and bones: an analysis based on stressed volume." *Journal of Orthopaedic Research*, **16**: 163-9.

Taylor, D. (1998b). "Microcrack growth parameters for compact bone deduced from stiffness variations." *Journal of Biomechanics*, **31**: 587-92.

Taylor, D. and Lee, T. C. (1998). "Measuring the shape and size of microcracks in bone." *Journal of Biomechanics*, **31**: 1177-80.

Turner, C. H. (1989). "Yield behavior of bovine cancellous bone." *Journal of Biomechanical Engineering*, **111**(8): 256-60.

Turner, C. H. (1998). "Three rules for bone adaptation to mechanical stimuli." *Bone*, **23**(5): 399-407.

Turner, C. H. (1999). "Toward a mathematical description of bone biology: the principle of cellular accomodation." *Calcified Tissue International*, **65**: 466-71.

Turner, C. H., Cowin, S. C., Rho, J. Y., Ashman, R. B. and Rice, J. C. (1990). "The fabric dependence of the orthotropic elastic constants of cancellous bone." *Journal of Biomechanics*, **23**(6): 549-61.

Vajjhala, S., Kraynik, A. M. and Gibson, L. J. (2000). "A cellular solid model for modulus reduction due to resorption of trabeculae in bone." *Journal of Biomechanical Engineering*, **22**: 511-5.

Vajjhalla, S. (1999). *Finite element analysis of Voronoi cellular solids*. S.M. Thesis. Massachusetts Institute of Technology, Cambridge, Massachusetts.

van Rietbergen, B., Manumdar, S., Pistoia, W., Newitt, D. C. and Kothari, M. (1998a). "Assessment of cancellous bone mechanical properties from micro-FE models based on micro-CT, pQCT and MR images." *Technology and Health Care*, **6**: 413-20.

van Rietbergen, B., Odgaard, A., Kabel, J. and Huiskes, R. (1996). "Direct mechanics assessment of elastic symmetries and properties of trabecular bone architecture." *Journal of Biomechanics*, **29**(12): 1653-7.

van Rietbergen, B., Odgaard, A., Kabel, J. and Huiskes, R. (1998b). "Relationships between bone morphology and bone elastic properties can be accurately quantified using high-resolution computer reconstructions." *Journal of Orthopaedic Research*, **16**(1): 23-8.

van Rietbergen, B., Weinans, H., Huiskes, R. and Odgaard, A. (1995). "A new method to determine trabecular bone elastic properties and loading using micromechanical finite-element models." *Journal of Biomechanics*, **28**(1): 69-81.

Vashishth, D., Johnson, C., Clovis, N., Tanner, K. E. and Bonfield, W. (1994). "Double staining technique for histological evaluation of microcracks in cortical bone." Proceedings of the Second World Congress of Biomechanics, Netherlands.

Vashishth, D., Koontz, J., Qiu, S. J., Lundin-Cannon, D., Yeni, Y. N. and Schaffler, M. B. (2000a). "*In vivo* diffuse damage in human vertebral trabecular bone." *Bone*, **26**(2): 147-52.

Vashishth, D., Verborgt, O., Divine, G., Scharrler, M. B. and Fyhrie, D. P. (2000b). "Decline in osteocyte lacunar density in human cortical bone is associated with accumulation of microcracks with age." *Bone*, **26**(4): 275-380.

Verborgt, O., Gibson, G. J. and Schaffler, M. B. (2000). "Loss of osteocyte integrity in association with microdamage and bone remodeling after fatigue *in vivo*." *Journal of Bone and Mineral Research*, **15**(1): 60-7.

Wachtel, E. F. and Keaveny, T. M. (1995). "The dependence of trabecular damage on applied strain level for bovine trabecular bone." *Transactions of the Orthopaedic Research Society*, **20**: 132.

Wachtel, E. F. and Keaveny, T. M. (1997). "Dependence of trabecular damage on mechanical strain." *Journal of Orthopedic Research*, **15**(5): 781-7.

Wenzel, T. E., Schaffler, M. B. and Fyhrie, D. P. (1996). "*In vivo* trabecular microcracks in human vertebral bone." *Bone*, **19**(2): 89-95.

Wilson, J. F., Jepsen, K. J., Bensusan, J. S. and Davy, D. T. (2000). "Simple mechanical measures as predictors of tensile failure in human cortical bone." *Transactions of the Orthopaedic Research Society*, **25**: 963.

Woo, S. L.-Y., Kuei, S. C., Amiel, D., Gomez, M. A., Hayes, W. C., White, F. C. and Akeson, W. H. (1981). "The effect of prolonged physical training on the properties of long bone: a study of Wolff's Law." *Journal of Bone and Joint Surgery [American]*, **63**(5): 780-7.

Yeh, O. C. and Keaveny, T. M. (1999). "Biomechanical effects of intraspecimen variations in trabecular architecture: a three-dimensional finite element study." *Bone*, **25**(2): 223-8.

Yeh, O. C. and Keaveny, T. M. (2000). "Roles of microdamage and microfracture in the mechanical behaviour of trabecular bone." *Transactions of the Orthopaedic Research Society*, **25**: 34.

Zhu, M., Keller, T. S. and Spengler, D. M. (1994). "Effects of specimen load-bearing and free surface layers on the compressive mechanical properties of cellular materials." *Journal of Biomechanics*, **27**(1): 57-66.

Zioupos, P. (2001). "Ageing human bone: factors affects its biomechanical properties and the role of collagen." *Journal of Biomaterials Applications*, **15**(1): 187-229.

Zioupos, P. and Casinos, A. (1998). "Cumulative damage and the response of human bone in two-step loading fatigue." *Journal of Biomechanics*, **31**: 825-33.

Zioupos, P. and Currey, J. D. (1994). "The extent of microcracks and the morphology of microcracks in damaged bone." *Journal of Materials Science*, **29**: 978-86.

Zioupos, P. and Currey, J. D. (1998). "Changes in the stiffness, strength, and toughness of human cortical bone with age." *Bone*, **22**(1): 57-66.

Zioupos, P., Currey, J. D., Mirza, M. S. and Barton, D. C. (1995). "Experimentally determined microcracking around a circular hole in a flat plate of bone: comparison with predicted stresses." *Philisophical Transactions of the Royal Society of London B*, **347**(1322): 383-96.

Zioupos, P., Currey, J. D. and Sedman, A. J. (1994). "An examination of the micromechanics of failure of bone and antler by acoustic emission tests and laser scanning confocal microscopy." *Medical Engineering and Physics*, **16**(5): 203-12.

Zioupos, P., Wang, X. T. and Currey, J. D. (1996a). "The accumulation of fatigue microdamage in human cortical bone of two different ages *in vitro*." *Clinical Biomechanics*, **11**(7): 365-75.

Zioupos, P., Wang, X. T. and Currey, J. D. (1996b). "Experimental and theoretical quantification of the development of damage in fatigue tests of bone and antler." *Journal of Biomechanics*, **29**(8): 989-1002.

Zysset, P. K., Guo, X. E., Hoffler, C. E., Moore, K. E. and Goldstein, S. A. (1998). "Mechanical properties of human trabecular bone lamellae quantified by nanoindentation." *Technology and Health Care*, **6**: 429-32.

Appendix A: Sampling Issues in Quantifying Microdamage Accumulation

A.1 Introduction

Small amounts of microdamage are present in normal bone. Current methods of quantifying microdamage involve bulk staining the bone to make microcracks visible, then observing damage microscopically in thin sections of bone. This method has previously been used in cortical bone specimens (Frost, 1960; Burr and Stafford, 1990; Burr and Hooser, 1995) and has only been recently applied to trabecular bone (Lee *et al.*, 2000). Trabecular bone is a cellular solid consisting of interconnected rods and plates, and microdamage tends to occur as groupings of short cracks on multiple trabeculae. This structural arrangement can result in a large number of microcracks, especially when the specimens have been loaded to high strain levels and large modulus reductions.

Trabecular bone is a three-dimensional structure, and thin sections only show the portion of damage that intersects with the two-dimensional plane of the section. The average bone specimen yielded three to six sections, displaying only a small sample of the total microdamage in the specimen. Because this approach shows only a portion of the damage, the observed damage may not correctly estimate the total amount of damage.

To improve the efficiency of microdamage quantification, sampling techniques are needed to estimate the amount of microdamage present in a given specimen without measuring each crack. As well, the damage estimates can be compared to the total damage to determine if the analysis provides an accurate measure of total specimen damage. If the damage estimated from a portion of the available data is not significantly different from the value obtained from all the data, we can expect that both estimates accurately reflect the total damage in the specimen.

A.2 Methods

The sampling analysis was performed on trabecular bone specimens that were mechanically tested in either monotonic compression (n = 42 specimens, Chapter 3) or in compressive creep (n = 13 specimens, (Pierce, 1999)). All trabecular bone cores were

then prepared for histology using the same procedure. The specimens were first sequentially dehydrated in ethanol according to the following schedule (**Table A.1**):

Solution (% EtOH)	Time (h)
50%	12
70%	12
80%	12
95%	12
100%	12
100%	12
100%	12
100%	12

Table A.1: Dehydration schedule for trabecular bone cores.

After dehydration, specimens were embedded in poly(methyl methacrylate) (PMMA). Specimens were immersed in MMA I (methyl methacrylate) for 48 hours at 4° C, and then immersed in MMA II (methyl methacrylate plus 2 wt % benzyl peroxide) for 24 hours at 4° C. Specimens were transferred to a vial with a base of polymerized MMA III (methyl methacrylate plus 4 wt % benzyl peroxide). The specimens were partially submerged in MMA III and degassed for approximately 2 hours. After degassing, the vials were filled with MMA III, polymerized in a water bath at 40°C for 16 hours, and hardened for 24 hours at 80°C. Specimens were cut into 100-150 μm slices longitudinally using a diamond saw (Isomet, Buehler, Lake Bluff IL). Each section was washed with distilled water and mounted on a glass slide with a cover slip using Eukitt's mounting medium (Electron Microscopy Sciences, Fort Washington PA). Three to six slides were obtained for each embedded sample.

Specimens were examined under ultraviolet fluorescent light ($\lambda = 365$ nm). Digital images of all visible damage were acquired from all specimens. Each section was scanned in a raster pattern (back-and-forth) to ensure that no regions of damage are missed. Damage occurred in localized bands across the specimens, so it is expected that the damage will not be randomly distributed.

Microdamage parameters (crack number, crack length, damaged area; see Chapter 3) were determined for each image. Microdamage parameters (normalized by the

number of digital images used) were estimated from subsets of the total number of images. The estimates were then compared to the microdamage parameters calculated using all of the digital images, normalized by the total number of digital images.

To calculate the estimates, an image was selected at random and the number of cracks, length of cracks, and damaged area in that image were used as the initial estimate. A second image was then chosen randomly, and the average for each microdamage parameter was determined. A third image was chosen, and cumulative averages calculated for the microdamage parameters. This continued until all the digital images for the specimen were used. After each new image, the percentage error between the current estimate and the final estimate (using all images) was calculated. Specimens with fewer than twenty images were not included in the study.

After the estimates were calculated, the microdamage parameters (crack number, crack length, and damaged area were plotted against the fraction of images used in the estimate to determine how many images were necessary to obtain a reasonable estimate of damage. Specimens with relatively little damage were examined to determine how many digital images were needed to obtain a reasonable estimate without quantifying all the damage in the specimen.

A.3 Results

Thirty-one of the 55 specimens had significant damage (at least 20 images of damage per specimen) and were used to evaluate sampling. All microdamage parameter estimates approached the final estimate as increasing numbers of images were used to calculate the estimate (**Figures A.1 - A.6**). The fraction of images necessary to obtain an estimate within 10% of the final estimate was recorded (**Table A.2**).

Specimen	Number of Images	Cr.Num.	Cr.Len	Damaged Area
79F	20	0.15	0.65	0.65
84B	30	0.87	0.80	0.92
55D	40	0.78	0.80	0.75
82B	40	0.60	0.28	0.60
83A	41	0.76	0.76	0.61
77E	41	0.24	0.71	0.63
88B	48	0.27	0.52	0.63
81B	50	0.46	0.18	0.86
87A	60	0.23	0.51	0.73
80E	61	0.54	0.66	0.75
65H	67	0.58	0.60	0.46
85B	68	0.63	0.63	0.63
80B	77	0.43	0.53	0.33
65A	81	0.49	0.49	0.35
79D	85	0.27	0.67	0.52
82G	88	0.26	0.18	0.51
67D	95	0.97	0.54	0.74
76D	97	0.10	0.10	0.67
24B	98	0.44	0.24	0.30
68A	118	0.30	0.30	0.45
93E	121	0.50	0.31	0.48
65E	138	0.37	0.38	0.68
90G	138	0.52	0.55	0.13
87B	153	0.50	0.54	0.65
90C	163	0.29	0.33	0.27
52A	165	0.75	0.73	0.69
85D	178	0.51	0.50	0.20
89D	189	0.13	0.13	0.30
72A	196	0.31	0.31	0.42
49C	199	0.30	0.31	0.43
83C	215	0.40	0.42	0.10

Table A.2: Fraction of total available images of microdamage required for microdamage parameter estimates to approach within 10% of final estimates.

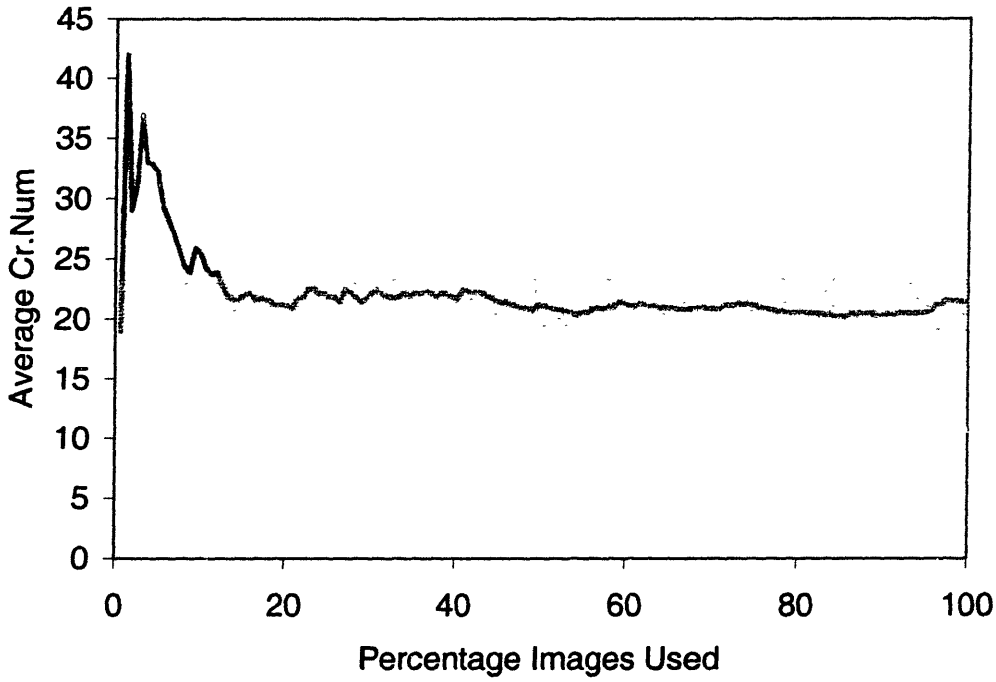

Figure A.1: Images showing running averages of crack number, *Cr.Num.*, as more images are used to compute the average in a specimen with a substantial amount of damage (89D, 159 images of damage). The shaded band indicates the range within ten percent of the final estimate.

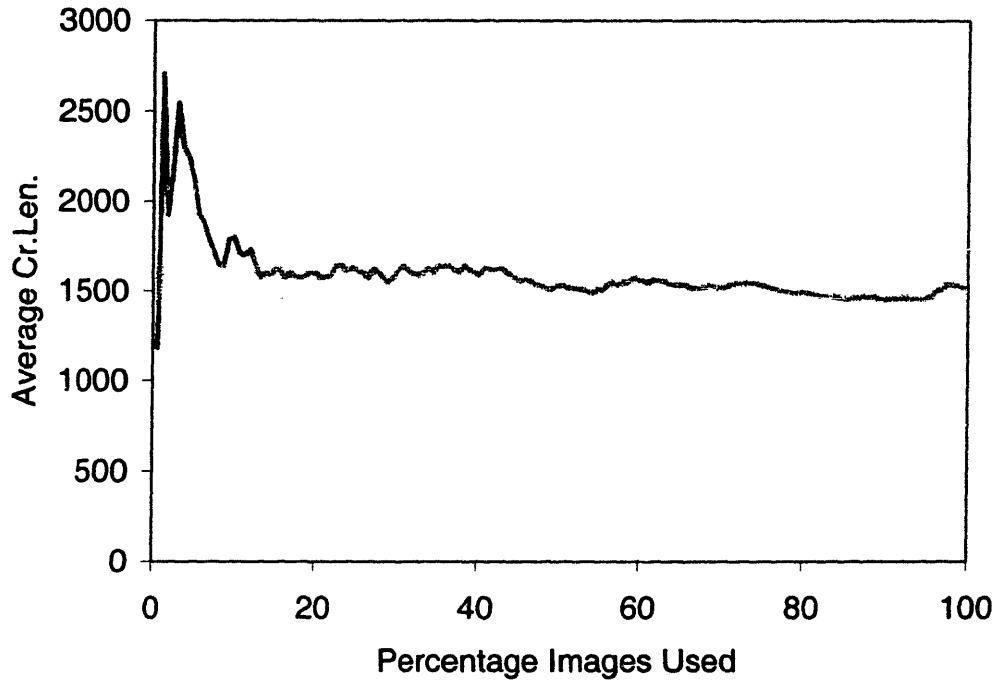

Figure A.2: Images showing running averages of crack length, *Cr.Len.*, as more images are used to compute the average in a specimen with a substantial amount of damage (89D, 159 images of damage). The shaded band indicates the range within ten percent of the final estimate.

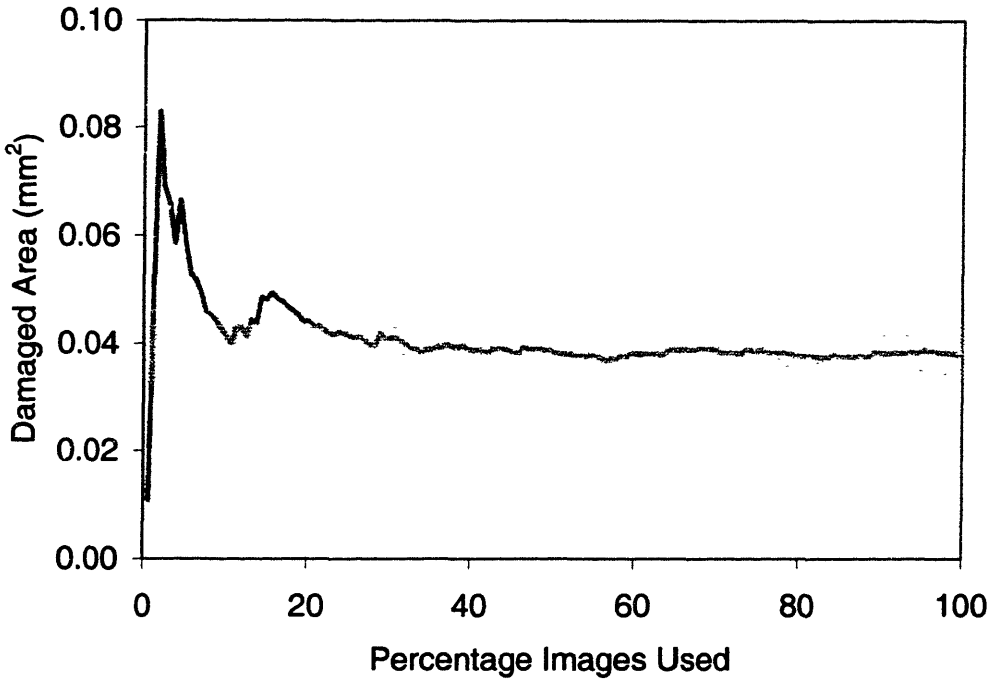

Figure A.3: Images showing running averages of damaged area as more images are used to compute the average in a specimen with a substantial amount of damage (89D, 159 images of damage). The shaded band indicates the range within ten percent of the final estimate.

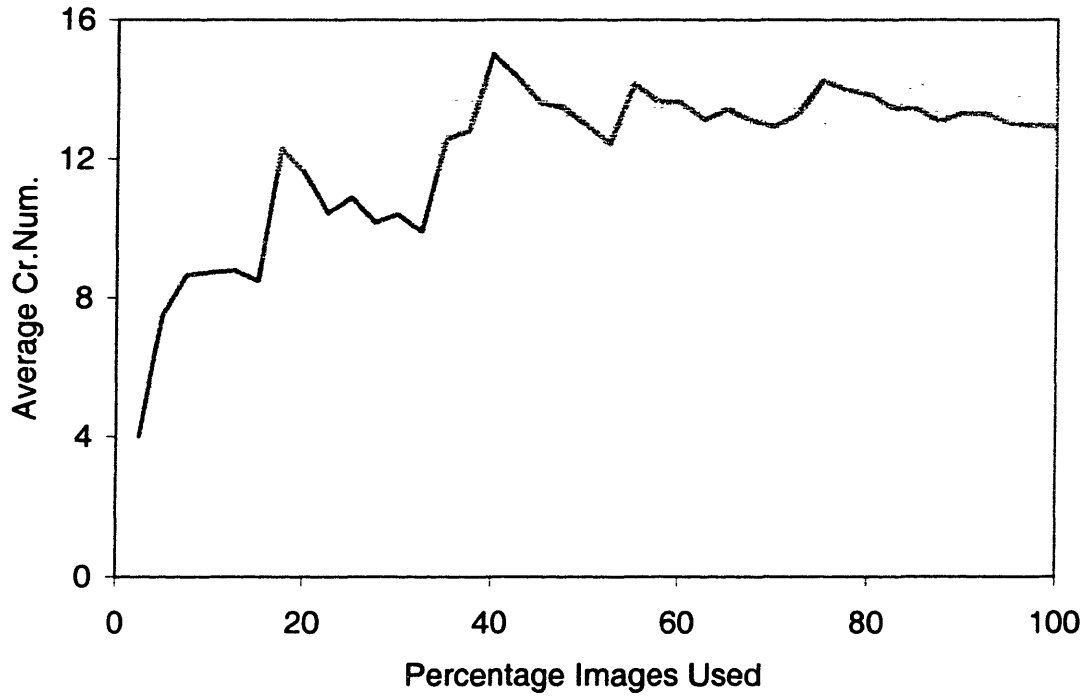

Figure A.4: Images showing running average of crack number, *Cr.Num.*, as more images are used to compute the average in a specimen with a small amount of damage (55D, 40 images of damage). The shaded band indicates the range within ten percent of the final estimate.

Figure A.5: Images showing running averages of crack length, *Cr.Len.*, as more images are used to compute the average in a specimen with a small amount of damage (55D, 40 images of damage). The shaded band indicates the range within ten percent of the final estimate.

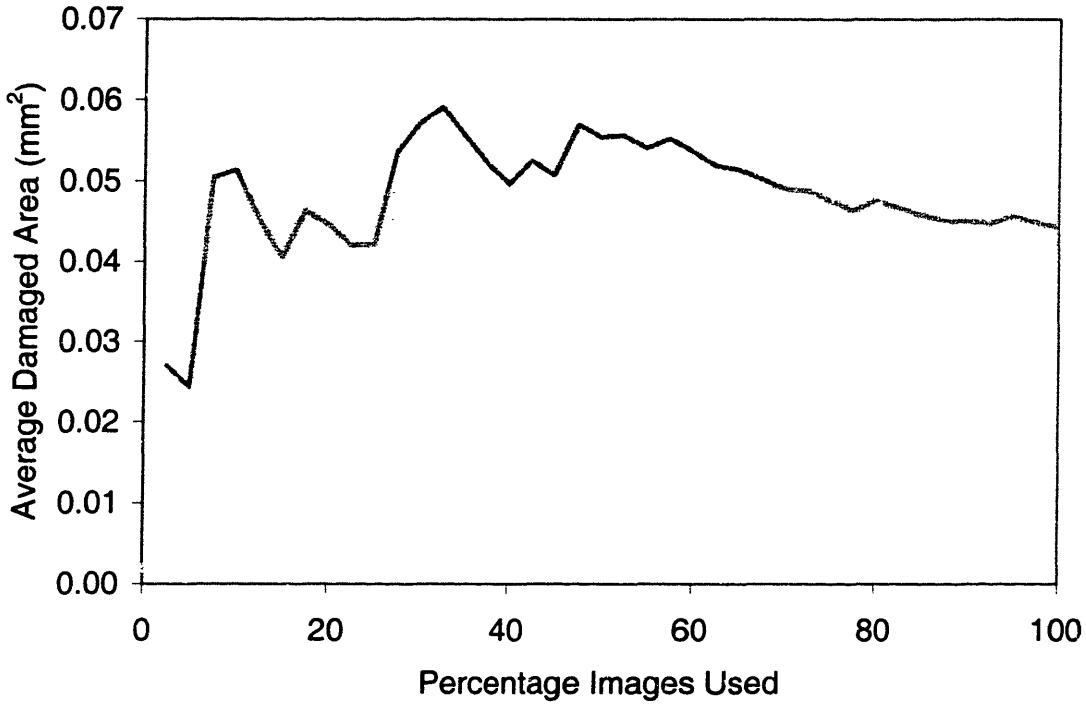

(c)

Figure A.6: Images showing running averages of damaged area as more images are used to compute the average in a specimen with a small amount of damage (55D, 40 images of damage). The shaded band indicates the range within ten percent of the final estimate.

A.4 Discussion

For specimens with a significant amount of damage (> 100 images), averaging the parameters for half of the specimens was sufficient to closely approach the final estimate (**Figure A.1, A.2, A.3**). We can be confident that the measurements of microdamage parameters accurately reflect the total amount of microdamage present. Microdamage estimates in specimens with fewer than 100 images of damage also agree reasonably well with final values (**Figure A.4, A.5, A.6**). It is difficult to determine how well the estimates agree with the final estimate in specimens with relatively little damage (< 20 images), as the scatter can be large.

The observations in this study were based on the total amount of observed microdamage. However, alterations can be made in future protocols that reduce the amount of observations without sacrificing accuracy of results. In the cases of specimens with substantial amounts of damage, not all images need to be analyzed to obtain a reasonable estimate of the data. In these cases (specimens with more than 100 images of damage), a randomly chosen subset of one-half of the images may be sufficient to obtain reasonable values for microdamage parameters.

Appendix B: Low Cycle Fatigue Testing of Trabecular Bone

B.1 Introduction

Fatigue damage is a stimulus for bone remodeling (Burr *et al.*, 1985; Martin, 1992; Mori and Burr, 1993; Martin, 1995). As well, fatigue damage in bone contributes to stress fractures and age-related fragility fractures in the elderly (Burr *et al.*, 1997), which occur preferentially in trabecular bone. Fatigue damage in the form of a stiffness loss has been shown to occur in compact bone (Carter and Hayes, 1976, 1977a, b) and trabecular bone (Guo, 1993; Guo *et al.*, 1994). Understanding the fatigue behavior of trabecular bone is a prerequisite to predicting the fatigue behavior of a whole bone, which consists of both trabecular and cortical bone in a complex geometry.

It has been hypothesized (Carter and Caler, 1985) that fatigue damage in low cycle fatigue is due mainly to creep, while fatigue damage in high cycle fatigue is due mainly to slow crack growth. More recent analysis of trabecular bone fatigue results suggest that creep is a major component of fatigue damage at all stress ranges (Bowman *et al.*, 1998). If high and low cycle fatigue behaviors are dominated by different damage mechanisms, then the slope of the S-N curve will change with changes in applied stress.

Earlier studies (Guo, 1993; Cheng, 1995) characterized the fatigue behavior of forty trabecular bone specimens. The slope of the resulting normalized stress versus number of cycles to failure curve were compared for low cycle fatigue and high cycle fatigue (with the cutoff between high and low cycle fatigue defined as 100 cycles (Guo, 1993)), and no significant difference between the slopes was found.

Microdamage has been implicated as a stimulus for bone remodeling (Mori and Burr, 1993; Lee, 1995). Fatigue loading creates microdamage in cortical bone (Burr *et al.*, 1985; Forwood and Parker, 1989; Boyce *et al.*, 1998; Muir *et al.*, 1999; Verborgt *et al.*, 2000); however, the relationship has not been well quantified in trabecular bone (Burr *et al.*, 1997). A staining method using chelating fluorochromes has been developed to identify microdamage created *in vitro* and to distinguish between microdamage that occurred before testing (*in vivo* and that created during specimen preparation) and damage created during testing (Lee *et al.*, 1997b, 2000). All tested specimens were

stained with chelating fluorochromes and histological specimens prepared from the failure specimens were examined for microdamage created during testing.

We asked two research questions: first, is there a difference between the low cycle and high cycle fatigue behavior of trabecular bone? To answer this question, an appropriate cutoff point between high and low cycle fatigue mustbe determined. A secondary aim was to determine if bovine trabecular bone, like some engineering materials, has a fatigue endurance limit, defined as a stress level below which fatigue failure does not occur. The second research question was whether chelating fluorochromes could be used to detect and quantify damage in trabecular bone samples tested in fatigue.

B.2 Materials and Methods

All samples were prepared from bovine trabecular bone taken from the proximal tibia. The waisted cylindrical specimens of aligned trabecular bone were prepared using the procedure developed by Keaveny *et al.* (1994a). Whole bovine tibias were obtained (Bertolino Beef Company, South Boston MA), and the proximal head was sliced sagittally into slices approximately 11 mm thick. Parallelepipeds of aligned trabeculae were selected using contact radiographs of the sagittal slices and cut out. Cores of trabecular bone, 8.3 mm in diameter, were obtained from the parallelepipeds. Specimens were kept wet during processing steps and kept frozen at -20°C between preparation steps. Before testing, the ends of the cores were defatted and press-fit into custom-machined brass end caps, and glued in place using cyanoacrylate glue. The specimens were then frozen in dry ice and immediately turned down on a lathe to create a wasted gauge length (diameter nominally 6 mm, gauge length nominally 5 mm).

Prior to testing, the specimens were thawed and a high-pressure water jet was used to remove the marrow from the gauge length. Removing marrow improved stain penetration into the interior of the specimen. The specimens were stained in either 0.3% oxytetracycline (yellow; 3 specimens) or 0.3% calcein blue (18 specimens) under vacuum for 16 hours. This staining step was performed to label all damage that existed in the

specimen before testing, including damage present *in vivo* and damage created during specimen preparation.

Before testing, the gauge diameter of each specimen was measured six (6) times along the gauge length with digital calipers, and the mean cross-sectional area was calculated. All testing was performed on an hydraulic testing machine (Instron 1331 with an Interlaken UTP-III controller, Canton MA). Specimens were loaded into two aligned three-jaw chucks, and a miniature extensometer (MTS 632.290-30, MTS, Eden Prairie MN), with a 5 mm gauge length, was attached directly to the bone using metal clips. The sample was kept moist with physiologic saline (0.9% NaCl) during testing.

After the specimen was mounted in the testing machine, 10 preconditioning cycles of -0.2% compressive strain were applied. The maximum strain of -0.2% was much less than the yield strain and was not expected to create damage. Load and strain were recorded on a 486 series computer (Dell 486D/25, Dell Computer Corporation, Austin TX) and data were acquired at 50 Hz (Acknowledge 2.0, Biopac Systems Inc., Santa Barbara CA. The initial specimen modulus, E_0, was determined from the slope of the stress-strain curves plotted during the preconditioning cycles.

Testing load levels were calculated so that the specimen was loaded to a predetermined normalized stress level, $\Delta\sigma/E_0$. Each specimen was fatigued from a small compressive preload (-10 N) to the predetermined maximum load at 2.0 Hz until either the specimen fractured or a strain of -5.0% was reached. Load and strain data were acquired throughout the test 25 Hz, and stress-strain curves were plotted. The modulus loss over the course of the test was calculated, and failure was defined as either a ten percent reduction in modulus or a specimen strain of -5.0%.

The data from all tests was pooled with data from two other studies (Guo, 1993; Cheng, 1995), and the results were plotted on a normalized stress vs. number of cycles to failure curve. Logarithmic regressions of both low cycle fatigue ($N_f < 100$) and high cycle fatigue ($N_f > 100$) were plotted, and slopes obtained for each curve. The slopes were then compared to see if there was a statistically significant difference between the two curves. One hundred cycles was chosen as the cutoff based on the results of an earlier study (Guo, 1993). The slope of the high cycle fatigue regression was also examined to see if it was significantly different from zero, indicating that an endurance

limit exists for bovine trabecular bone in compression. Initial observations suggested that 100 cycles may not be an appropriate cutoff point; other cutoff points were selected and tested once data from the new tests was available.

After testing, the gauge length of each specimen was removed. One half of each broken specimen was stained overnight in 0.3% xylenol orange. The other half of each specimen was left as a control and not stained so that damage prior to testing could be observed. Unfractured specimens were randomly selected to be either stained in xylenol orange or left unstained. Specimens were dehydrated in ethanol, embedded in poly (methyl methacylate), and cut into thin sections of approximately 100 μm, and mounted on glass slides (Appendix A).

Each slide was observed under fluorescence microscopy. Images of damaged areas, viewed under UV epifluorescence (λ = 365 nm), were captured using a color digital camera and an image capture program. Images were examined qualitatively for types of damage and amounts of microdamage.

B.3 Results

Twenty-one fatigue tests were performed successfully (**Table B.1**). **Table B.2** summarizes the results of fatigue tests performed in other studies (Guo, 1993; Cheng, 1995) using the same protocol. S-N curves for all tests (**Figure B.1**), low cycle fatigue only (**Figure B.2**), and high cycle fatigue only (**Figure B.3**) were plotted, using a cutoff of 100 cycles to distinguish between the high and low cycle regimes.

Specimen	E_0 (MPa)	$\Delta\sigma/E_0$	Load (N)	N_f	$N_{fracture}$
34B	3615	0.0095	-1019	1	96
19C	3083	0.0095	-837	1	2
21A	2742	0.0095	-761	3	336
33A	3534	0.0095	-971	1	26
39A	2401	0.0095	-664	1	13
32A	3811	0.0090	-989	1	16
37A	4060	0.0090	-1063	1	4
24C	3469	0.0090	-874	1	5
31B	1188	0.0090	-311	1	31
22A	1609	0.0085	-403	1	885
27B	2500	0.0085	-655	1	60
36D	1588	0.0085	-364	1	16
23B	4032	0.0085	-1012	1	94
27C	3344	0.0085	-864	2	25
38C	3455	0.0080	-770	3	77
28C	3587	0.0075	-737	79	168
33B	3540	0.0075	-768	1	169
38A	4489	0.0075	-1040	588	673
39C	2973	0.0070	-617	15	872
35A	4798	0.0070	-974	284	2281
32B	5537	0.0065	-1063	31	31

Table B.1: Low cycle fatigue test results. Failure occurred at ten percent modulus loss or at fracture, whichever occurred first.

Specimen	$\Delta\sigma/E_0$	N_f	Specimen	$\Delta\sigma/E_0$	N_f	Specimen	$\Delta\sigma/E_0$	N_f
XEG9A	0.0100	1	XEG25C	0.0080	78	27AL	0.0040	29994
XEG2A	0.0100	2	TLA33B	0.0075	1	XEG5A	0.0040	44432
XEG29C	0.0100	9	TLA28C	0.0075	79	130BL	0.0040	366277
TLA19C	0.0095	1	TLA38A	0.0075	588	123BL3	0.0038	49994
TLA34B	0.0095	1	TLA39C	0.0070	15	22DL	0.0037	3365
TLA33A	0.0095	1	TLA35A	0.0070	284	9BL	0.0037	5994
TLA39A	0.0095	1	TLA32B	0.0065	31	54AL	0.0037	10298
TLA21A	0.0095	3	XEG3A	0.0060	22	21AL	0.0036	9994
TLA32A	0.0090	1	XEG7A	0.0060	829	132EL	0.0036	17487
TLA37A	0.0090	1	XEG11A	0.0060	1880	11DL	0.0036	18145
TLA24C	0.0090	1	108BL	0.0054	794	51AL	0.0036	44617
TLA31B	0.0090	1	spec 15	0.0053	295	12BL2	0.0035	18635
TLA36D	0.0085	1	17CL	0.0052	194	XEG54C	0.0035	21043
TLA27B	0.0085	1	104BL	0.0045	1935	XEG30C	0.0035	73145
TLA23B	0.0085	1	126AL	0.0042	5994	XEG48A	0.0035	400520
TLA22A	0.0085	1	63AL	0.0041	2443	XEG51B	0.0035	601520
TLA27C	0.0085	2	133HL	0.0040	923	2EL	0.0034	17999
XEG1A	0.0080	1	XEG20A	0.0040	2263	23AL	0.0034	32686
TLA38C	0.0080	3	XEG61A	0.0040	2495	44AL	0.0032	29994
XEG27C	0.0080	7	XEG13A	0.0040	29342	48EL	0.0029	319751
XEG12A	0.0080	32						

Table B.2: Summary of all fatigue results to date. Tests were performed by three different operators, as indicated by the specimen prefix.

Microdamage was observed in all specimens. It was difficult to draw conclusions about the relationship between microdamage and loading in fractured specimens because the local strains on the specimens at the time of fracture cannot be accurately measured by the extensometer. In the unfractured specimens (loaded to -5.0% strain), considerable amounts of damage were seen. Damage patterns included diffuse damage (without visible distinct cracks), single cracks, cracks running parallel to the axis of the trabeculae, regions of cross-hatching at 45° to the axis of the trabeculae, and complete trabecular fracture.

Linear regressions of the transformed values (log values of all data points) were performed on the high and low cycle normalized stress versus number of cycles to failure

curves using the statistical analysis program RS/1 (BBN Technologies, GTE Corp., Irving TX). The results were as follows:

All Fatigue ($R^2 = 0.89$, $p < 0.001$, $n = 61$)

$$N_f = 2.71\times10^{-24}\left(\frac{\Delta\sigma}{E_0}\right)^{-11.6} \tag{B.1}$$

Low Cycle Fatigue ($R^2 = 0.36$, $p < 0.001$, $n = 27$)

$$N_f = 6.37\times10^{-41}\left(\frac{\Delta\sigma}{E_0}\right)^{-19.6} \tag{B.2}$$

High Cycle Fatigue ($R^2 = 0.56$, $p < 0.001$, $n = 34$)

$$N_f = 8.36\times10^{-27}\left(\frac{\Delta\sigma}{E_0}\right)^{-13.0} \tag{B.3}$$

No statistically significant difference was detected between the slopes of the high and low cycle fatigue S-N curves ($F = 1.623$, $p = 0.21$).

When the statistical analysis was repeated using a cutoff of 3000 cycles (**Figure B.4, B.5**), the following results were obtained:

Low Cycle Fatigue ($R^2 = 0.76$, $p < 0.001$, $n = 39$)

$$N_f = 2.34\times10^{-25}\left(\frac{\Delta\sigma}{E_0}\right)^{-12.1} \tag{B.4}$$

High Cycle Fatigue ($R^2 = 0.08$, $p = 0.191$, $n = 22$)

$$N_f = 1.31\times10^{-140}\left(\frac{\Delta\sigma}{E_0}\right)^{-59.2} \tag{B.5}$$

When the slopes for the low and high cycle fatigue curves were compared, they were found to be significantly different ($p < 0.01$). Additionally, the slope of the high cycle fatigue regression curve is not significantly different from zero ($F = 1.84$, $p = 0.19$).

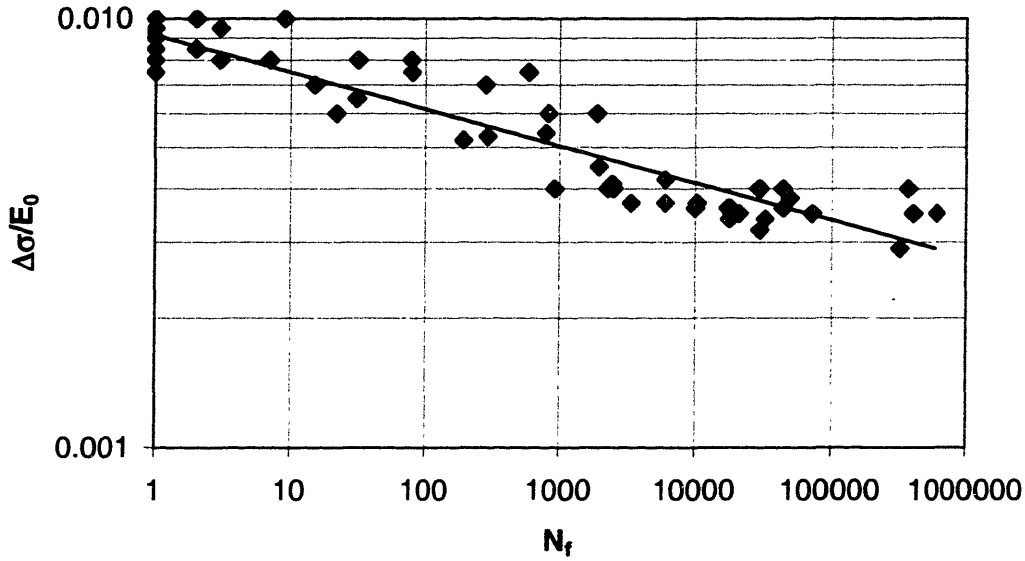

Figure B.1: Normalized stress, $\Delta\sigma/E_0$, versus number of cycles to failure, N_f, for 61 fatigue specimens.

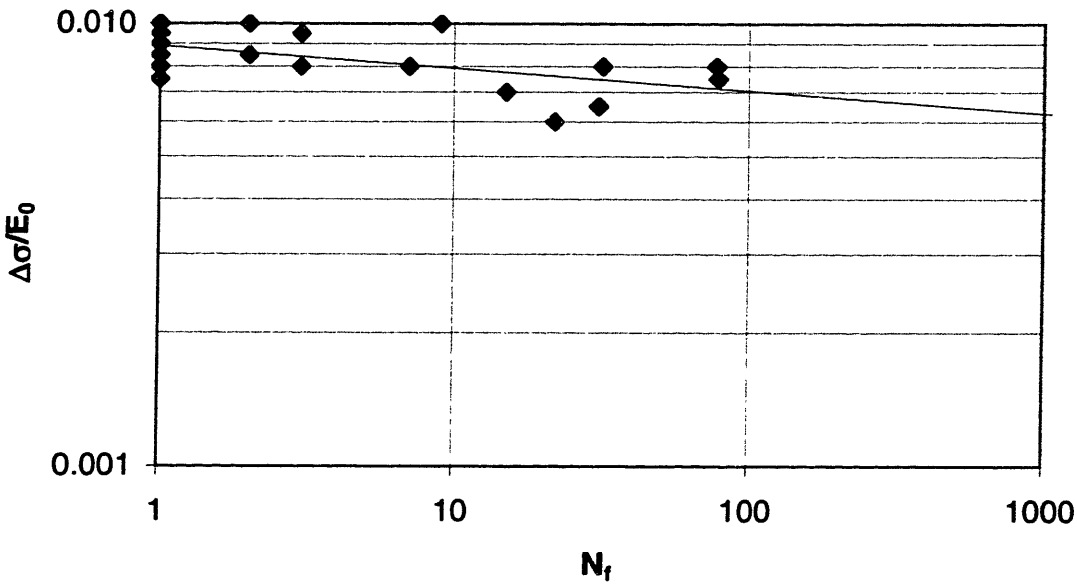

Figure B.2: Normalized stress, $\Delta\sigma/E_0$, versus number of cycles to failure, N_f, of 27 specimens tested in low cycle fatigue (cutoff, N = 100).

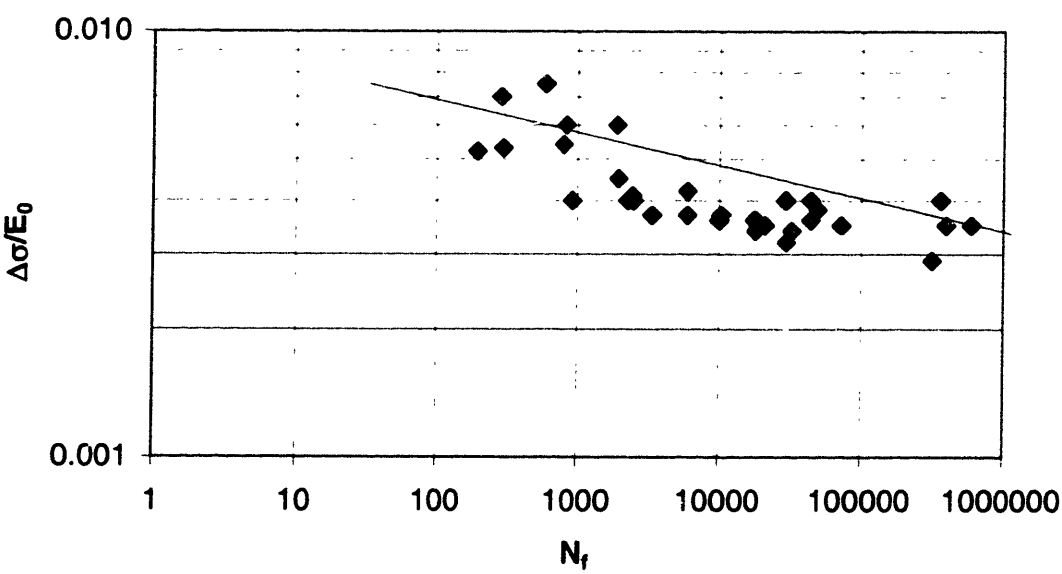

Figure B.3: Normalized stress, $\Delta\sigma/E_0$, versus number of cycles to failure, N_f, of 34 specimens tested in high cycle fatigue (cutoff, N = 100).

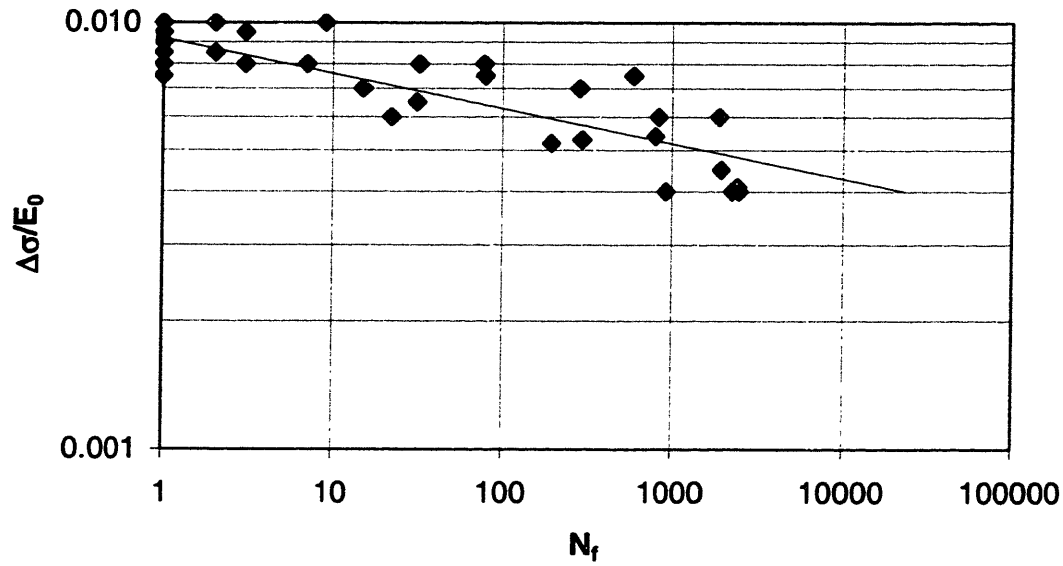

Figure B.4: Normalized stress, $\Delta\sigma/E_0$, versus number of cycles to failure, N_f, of 39 specimens tested in low cycle fatigue (cutoff, N = 3000).

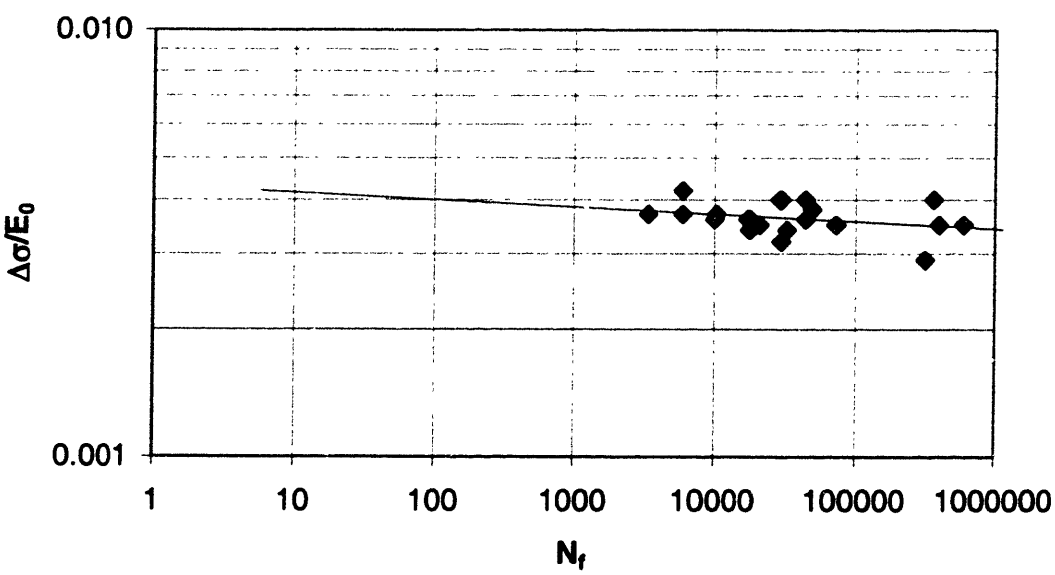

Figure B.5: Normalized stress, $\Delta\sigma/E_0$, versus number of cycles to failure, N_f, of 22 specimens tested in high cycle fatigue (cutoff, N = 3000).

B.4 Discussion

No statistically significant difference was observed between the slopes of the normalized stress versus number of cycles to failure curve for low cycle fatigue ($N_f < 100$) and high cycle fatigue ($N_f > 100$). However, after visually observing the curve, it was hypothesized that the cutoff of $N_f = 100$ cycles, chosen from observations of 20 fatigue tests, might be incorrect. The addition of more specimens to the normalized stress versus number of cycles to failure curve suggested that the demarcation between low and high cycle fatigue occurred at a higher number of cycles than was originally estimated. As well, the slope of the transformed high cycle fatigue values using a cutoff of 100 cycles was more negative than the low cycle fatigue values, while the slope of the stress-number of cycles to failure curve for engineering materials generally becomes less negative as the number of cycles to failure increases.

Regression analyses were repeated using a cutoff of $N_f = 3000$ cycles to failure, which did show a significant difference between the slopes of the high and low cycle fatigue curves. The slope of the transformed low cycle fatigue data was more negative than that of the high cycle fatigue data, as is expected for engineering materials. Additionally, the slope of the high cycle fatigue curve was not significantly different from zero. This suggests that there may be an endurance limit in trabecular bone (a stress level below which fatigue does not occur). These results confirm earlier results by Pattin *et al.* (1996) who found a fatigue threshold of approximately 4000 $\mu\varepsilon$ (microstrain) for cortical bone compression, below which modulus reduction does not occur.

Testing to failure is not an appropriate way to quantify damage because the two halves of the specimen crush each other during fracture, and there will be large variations in local strains as the fracture surfaces contact. A quantitative comparison between accumulated damage and loss of stiffness of the specimen can only be performed on unfractured specimens. As well, the contact of the fracture surfaces creates large amounts of microdamage which are difficult to separate from damage created prior to fracture. Specimens to be used in microdamage quantification should not be mechanically tested to fracture.

The 61 fatigue tests used for the statistical analysis were performed by three different operators. **Figure B.6** plots the transformed fatigue data by operator. No

differences between operators were apparent, although the data was not statistically analyzed.

Fatigue microdamage occurred in bovine trabecular bone loaded in compression. We observed significant differences in the slopes of the high and low cycle fatigue portions of the stress-number of cycles to failure curve, with a cutoff between high and low cycle fatigue occurring at $N_f = 3000$ cycles. Significant amounts of microdamage accumulation were observed in all fatigue-tested specimens.

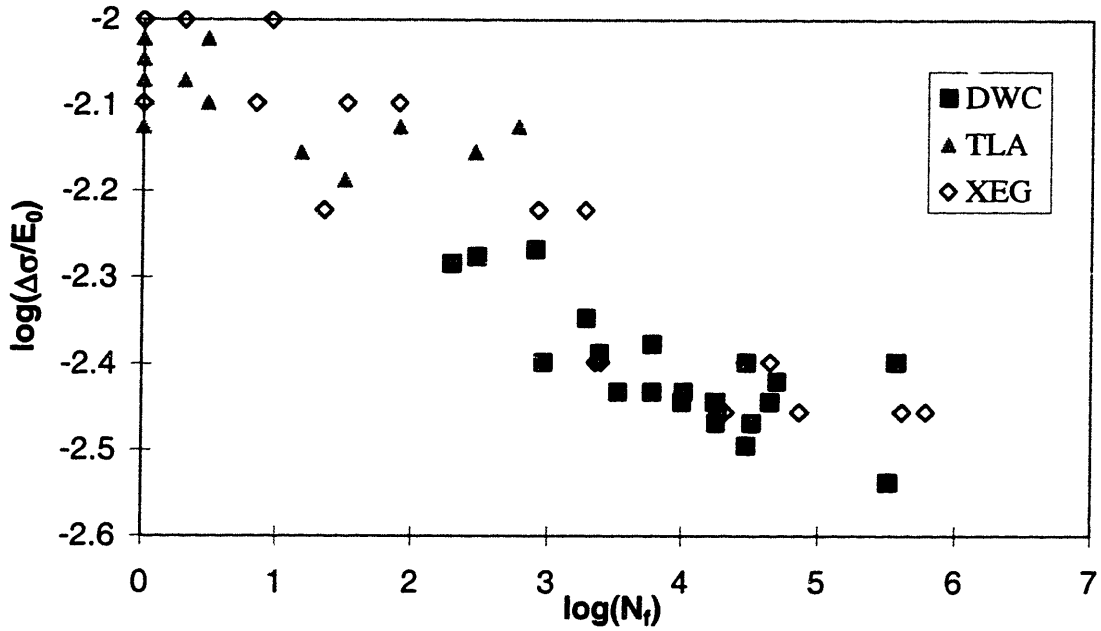

Figure B.6: Comparison of fatigue tests performed by three operators, as indicated in the legend. No differences were apparent.

Appendix C: Monotonic Testing

Legend for microdamage parameters:

[a]Section Area	- total specimen area
[b]Damage Band Length	- length of the section of the specimen containing damage
[c]Damaged Trabeculae/Area	- total number of trabeculae containing damage in the section, normalized by specimen section area
[d]Damaged Area	- total area of the localized regions of damage
[e]Damaged Area Fraction	- total area of the localized regions of damage, normalized by specimen section area
[f]Cr.Num.	- total number of cracks in the specimen
[g]Cr.Num./Area	- total number of cracks in the specimen, normalized by specimen section area
[h]Cr.Len.	- total length of cracks in the specimen
[i]Cr.Len./Area	- total length of cracks in the specimen, normalized by specimen section area
[j]Mean Cr.Len.	- Cr.Len./Cr.Num.

	E_0 (GPa)	E_{sec} (GPa)	E_{sec}/E_0	Damage ($1 - E_{sec}/E_0$)	ε_{max} (%)	ε_{res} (%)	Stress (MPa)	$\Delta\sigma/E_0$	Section Area (mm^2)[a]
65B	N/A	N/A	1.000	0.000	0.00	0.00	N/A	N/A	239.37
21B	N/A	N/A	1.000	0.000	0.00	0.00	N/A	N/A	314.94
45C	N/A	N/A	1.000	0.000	0.00	0.00	N/A	N/A	251.39
27A	N/A	N/A	1.000	0.000	0.00	0.00	N/A	N/A	426.26
50D	2.119	2.103	0.992	0.008	-0.38	-0.01	-8.33	-0.0039	232.99
48A	2.640	2.759	1.045	-0.045	-0.46	-0.01	-11.81	-0.0045	189.15
14A	2.034	2.016	0.991	0.009	-0.85	-0.05	-17.03	-0.0084	222.06
90D	2.786	2.571	0.923	0.077	-0.91	-0.05	-23.42	-0.0084	285.90
17C	1.787	1.250	0.699	0.301	-1.06	-0.11	-17.30	-0.0097	302.56
53B	4.065	3.177	0.782	0.218	-1.13	-0.18	-35.91	-0.0088	440.05
14B	2.065	1.682	0.815	0.185	-1.15	*	-19.38	-0.0094	264.21
93B	1.096	0.971	0.886	0.114	-1.10	-0.25	-10.63	-0.0097	371.44
84C	2.632	1.891	0.718	0.282	-1.09	-0.05	-20.70	-0.0079	206.66
55E	1.639	1.637	0.999	0.001	-1.32	-0.10	-21.60	-0.0132	357.60
91A	1.191	0.970	0.814	0.186	-1.31	-0.45	-11.48	-0.0096	293.88
88B	2.099	1.679	0.800	0.200	-1.28	-0.25	-21.55	-0.0103	344.54
87A	3.036	1.980	0.652	0.348	-1.31	-0.20	-25.83	-0.0085	273.89
79D	2.431	1.429	0.588	0.412	-1.31	-0.25	-18.81	-0.0077	377.62
65A	3.678	0.757	0.206	0.794	-2.01	-0.25	-17.29	-0.0047	230.56
43B	3.222	1.626	0.505	0.495	-2.02	-0.53	-33.19	-0.0103	327.68
42C	1.766	0.768	0.435	0.565	-2.02	-0.60	-15.98	-0.0090	259.79
67D	1.313	0.474	0.361	0.639	-2.03	-0.60	-11.01	-0.0084	348.50
77E	2.685	1.171	0.436	0.564	-2.10	-0.70	-28.56	-0.0106	287.23
10A	2.085	1.168	0.560	0.440	-2.51	-0.40	-29.49	-0.0141	359.16
11D	2.595	1.130	0.435	0.565	-2.52	-0.80	-29.23	-0.0113	361.46
68A	6.238	0.941	0.151	0.849	-2.52	-0.65	-36.38	-0.0058	326.54
12C	1.642	0.628	0.382	0.618	-2.55	-0.70	-16.29	-0.0099	266.69
16B	4.249	1.281	0.301	0.699	-2.56	-0.40	-32.82	-0.0077	448.05
49C	4.714	1.731	0.367	0.633	-2.97	-0.80	-51.87	-0.0110	342.87
55D	1.589	0.321	0.202	0.798	-2.99	-1.10	-11.48	-0.0072	315.57
76D	2.413	0.977	0.405	0.595	-3.02	-0.85	-29.61	-0.0123	288.40
43D	2.745	0.997	0.363	0.637	-3.04	-0.95	-30.53	-0.0111	228.18
90C	2.809	0.790	0.281	0.719	-3.00	-1.25	-26.14	-0.0093	315.87
24B	3.991	0.690	0.173	0.827	-3.98	-1.50	-32.27	-0.0081	194.62
52A	5.324	0.937	0.176	0.824	-3.99	-1.80	-48.95	-0.0092	290.54
65H	0.728	0.183	0.251	0.749	-4.00	-0.85	-7.92	-0.0109	340.43
45B	2.798	0.795	0.284	0.716	-4.08	-1.30	-36.28	-0.0130	271.11
93E	1.595	0.127	0.080	0.920	-4.00	-2.00	-12.12	-0.0076	261.27

*data acquisition error, no measurement taken

Table C.1: Mechanical properties measured for 38 monotonic tests unloaded to zero strain.

	Damage Band Length (mm)[b]	Damaged Trabeculae /Area[c]	Damaged Area (mm^2)[d]	Damaged Area Fraction (mm^2/mm^2)[e]	Cr. Num.[f]	Cr. Num. /Area (mm^{-2})[g]	Cr. Len. (μm)[h]	Cr.Len. /Area ($\mu m/mm^2$)[i]	Mean Cr.Len. (μm)[j]
65B	0	0.017	0.0649	0.00027	8	0.03	878	3.67	109.74
21B	0	0.003	0.0162	5.2E-05	6	0.02	337	1.07	56.22
45C	0	0.004	0.0108	4.3E-05	1	0.00	90	0.36	90.35
27A	0	0.005	0.0108	2.5E-05	2	0.00	205	0.48	102.72
50D	0	0.009	0.0108	4.6E-05	2	0.01	130	0.56	65.16
48A	0	0.005	0.0000	5.3E-10	3	0.02	234	1.24	78.01
14A	0	0.009	0.0432	0.00020	7	0.03	845	3.81	120.76
90D	0	0.010	0.0811	0.00028	10	0.03	971	3.40	97.11
17C	1.556	0.053	0.1622	0.00054	51	0.17	3199	10.57	62.73
53B	0.170	0.063	0.1676	0.00038	81	0.18	4802	10.91	59.28
14B	1.170	0.020	0.0811	0.00031	30	0.11	2257	8.54	75.22
93B	0.371	0.030	0.2108	0.00057	50	0.13	3681	9.91	73.62
84C	0.375	0.039	0.4595	0.0022	73	0.35	5636	27.27	77.21
55E	0	0.014	0.0541	0.00015	9	0.03	1053	2.94	116.99
91A	0.241	0.024	0.1081	0.00037	19	0.06	1802	6.13	94.83
88B	2.428	0.154	2.1678	0.00629	609	1.77	44590	129.4	73.22
87A	2.927	0.281	3.1679	0.0116	470	1.72	41475	151.4	88.24
79D	2.917	0.249	3.6815	0.00975	935	2.48	77239	204.5	82.61
65A	4.233	0.416	3.4977	0.0152	722	3.13	56379	244.5	78.09
43B	3.790	0.204	2.2327	0.00681	586	1.79	49740	151.8	84.88
42C	3.105	0.200	2.2165	0.00853	661	2.54	46976	180.8	71.07
67D	5.820	0.287	5.1519	0.0148	1277	3.66	93395	268.0	73.14
77E	1.876	0.171	0.8866	0.00309	206	0.72	14719	51.24	71.45
10A	1.562	0.170	1.6650	0.00464	542	1.51	37909	105.6	69.94
11D	3.257	0.282	3.2760	0.00906	814	2.25	63165	174.8	77.60
68A	4.734	0.398	12.1203	0.0371	3829	11.73	285745	875.1	74.63
12C	2.637	0.180	0.7947	0.00298	219	0.82	18359	68.84	83.83
16B	2.446	0.161	0.7190	0.00161	135	0.30	10337	23.07	76.57
49C	6.352	0.802	9.5740	0.0279	5794	16.90	402165	1173	69.41
55D	2.083	0.155	1.7678	0.00560	516	1.64	46325	146.8	89.78
76D	3.387	0.350	3.0598	0.0106	1285	4.46	71644	248.4	55.75
43D	2.777	0.202	2.0921	0.00917	631	2.77	48443	212.3	76.77
90C	5.196	0.584	11.2985	0.0358	5604	17.74	343571	1088	61.31
24B	4.033	0.478	5.7033	0.0293	1253	6.44	102917	528.8	82.14
52A	6.339	0.602	11.1850	0.0385	6907	23.77	459881	1582	66.58
65H	2.943	0.214	1.1947	0.00351	985	2.89	52852	155.3	53.66
45B	4.519	0.457	10.6282	0.0392	3271	12.07	265513	979.4	81.17
93E	3.941	0.559	7.4116	0.0287	6060	23.19	349821	1339	57.73

Table C.2: Microdamage parameters measured for 38 monotonic tests unloaded to zero strain.

	Diffuse	Single	Parallel	Cross- Hatch	Fracture	25%	50%	75%	100%	Total
65B	5	3	1	0	0	2	2	0	0	9
21B	24	1	0	0	0	1	0	0	0	25
45C	1	0	0	1	0	1	0	0	0	2
27A	8	2	0	0	0	0	2	0	0	10
50D	2	1	1	0	0	2	0	0	0	4
48A	0	0	1	0	0	1	0	0	0	1
14A	3	2	0	0	0	0	0	1	1	5
90D	2	1	0	2	0	2	0	0	1	5
14B	6	4	0	10	0	3	6	1	4	20
17C	21	4	0	15	0	7	3	3	6	40
53B	47	2	1	6	0	4	3	0	2	56
93B	1	0	2	9	0	6	3	1	1	12
84C	0	1	1	6	0	3	0	1	4	8
55E	8	3	1	1	0	5	0	0	0	13
91A	5	2	0	5	0	1	0	0	6	12
88B	1	3	2	48	0	18	10	3	22	54
87A	8	13	1	63	0	24	17	6	30	85
79D	7	5	9	80	0	22	22	8	42	101
65A	0	7	5	82	2	15	18	11	52	96
43B	2	4	0	62	1	24	13	4	26	69
42C	0	1	0	51	0	9	10	8	25	52
67D	3	8	3	88	1	18	21	14	47	103
77E	0	5	4	40	0	17	9	4	19	49
10A	21	9	2	50	0	18	19	7	17	82
11D	17	11	0	91	0	23	35	13	31	119
68A	2	7	7	112	4	43	27	3	57	132
12C	1	2	0	49	0	8	21	5	14	49
16B	4	13	0	59	0	20	21	6	25	76
49C	5	19	6	250	0	67	77	33	98	280
55D	6	10	6	32	1	11	14	5	19	55
76D	0	6	0	95	0	34	33	5	29	101
43D	1	2	1	43	0	14	11	3	18	47
90C	3	10	7	153	3	46	47	18	62	176
24B	8	8	5	79	1	7	26	18	42	101
52A	6	10	8	156	1	41	32	20	82	181
65H	2	12	6	54	1	9	14	9	41	75
45B	1	2	1	118	3	27	31	12	54	125
93E	1	8	15	114	9	19	39	14	74	147

Table C.3: Damaged trabeculae in each of 38 monotonic tests unloaded to zero strain, classified by pattern of damage and by extent of damage across the trabeculae, rounded to the nearest quarter.

	E_0 (GPa)	E_{sec} (GPa)	E_{sec}/E_0	Damage ($1 - E_{sec}/E_0$)	ε_{max} (%)	ε_{res} (%)	Stress (MPa)	$\Delta\sigma/E_0$	Section Area (mm^2)[a]
85D	4.248	2.456	0.578	0.422	-2.02	-0.50	-50.31	-0.0118	307.14
83A	4.129	2.057	0.498	0.502	-2.01	-0.37	-42.55	-0.0103	224.95
80E	2.056	0.733	0.356	0.644	-2.01	-0.51	-16.66	-0.0081	279.5
87B	1.682	0.424	0.252	0.748	-4.00	-1.10	-21.42	-0.0127	309.57
89D	1.347	0.351	0.261	0.739	-3.98	-1.25	-16.38	-0.0122	417.98
90G	3.448	0.774	0.224	0.776	-4.01	-1.50	-35.06	-0.0102	240.13

Table C.4: Mechanical properties measured for 6 monotonic tests unloaded to zero load.

	Damage Band Length (mm)[b]	Damaged Trabeculae /Area[c]	Damaged Area (mm^2)[d]	Damaged Area Fraction (mm^2/mm^2)[e]	Cr. Num.[f]	Cr. Num. /Area (mm^{-2})[g]	Cr. Len. (μm)[h]	Cr.Len. /Area ($\mu m/mm^2$)[i]	Mean Cr.Len. (μm)[j]
85D	4.959	0.632	8.920	0.0290	4222	13.75	359834	1172	85.23
83A	2.505	0.222	2.433	0.0108	926	4.116	64527	286.9	69.68
80E	2.838	0.233	2.314	0.00828	938	3.356	64347	230.2	68.60
87B	4.869	0.630	7.395	0.0239	2980	9.626	206780	668.0	69.39
89D	5.148	0.421	6.136	0.0147	3384	8.096	240444	575.3	71.05
90G	4.632	0.629	12.482	0.0520	5295	22.05	396317	1650	74.85

Table C.5: Microdamage parameters measured for 6 monotonic tests unloaded to zero load.

	Diffuse	Single	Parallel	Cross-Hatch	Fracture	25%	50%	75%	100%	Total
85D	1	6	5	183	0	56	54	21	63	195
83A	0	0	3	47	0	19	12	6	13	50
80E	0	8	6	51	0	23	11	7	24	65
87B	0	10	12	172	1	55	51	17	72	195
89D	1	18	23	134	1	29	33	21	93	177
90G	2	7	7	136	1	28	25	14	84	153

Table C.6: Damaged trabeculae in each of for 6 monotonic tests unloaded to zero load, classified by pattern of damage and by extent of damage across the trabeculae, rounded to the nearest quarter.

Appendix D: Fatigue Testing

Legend for microdamage parameters:

[a]Section Area	- total specimen area
[b]Bone Area	- total bone area
[c]Bone Area Fraction	- Section Area divided by Bone Area
[d]Specimen Length	- length of the specimen loaded during mechanical testing
[e]Damaged Band Fraction	- total section area containing damage, normalized by specimen section area
[f]Damaged Trabeculae/Area	- total number of trabeculae containing damage in the section, normalized by specimen section area
[g]Damaged Area Fraction	- total area of the localized regions of damage, normalized by specimen section area

	E_0 (MPa)	ε (%)	Stress Ratio	N	E_r (MPa)	E_r/E_0	E_{sec} (MPa)	E_{sec}/E_0	ε_{max} (%)	ε_{res} (%)
95A1	N/A	0.00	N/A	0	N/A	N/A	N/A	N/A	N/A	N/A
96D2	N/A	0.00	N/A	0	N/A	N/A	N/A	N/A	N/A	N/A
97A1	N/A	0.00	N/A	0	N/A	N/A	N/A	N/A	N/A	N/A
102C1	N/A	0.00	N/A	0	N/A	N/A	N/A	N/A	N/A	N/A
107A2	N/A	0.00	N/A	0	N/A	N/A	N/A	N/A	N/A	N/A
92F2	2866	0.30	N/A	0	N/A	N/A	N/A	N/A	-0.35	-0.03
95B2	2739	0.30	N/A	0	N/A	N/A	N/A	N/A	-0.31	-0.02
103A1	2024	0.30	N/A	0	N/A	N/A	N/A	N/A	-0.32	-0.01
100A2	1415	0.30	N/A	0	N/A	N/A	N/A	N/A	-0.33	-0.01
107F1	2220	0.30	N/A	0	N/A	N/A	N/A	N/A	-0.31	-0.01
98B1	2992	-1.30	14.48	10	2317	0.774	2414	0.807	-1.32	-0.32
95C1	1232	-1.30	6.36	9	1050	0.852	1115	0.905	-1.30	-0.46
109C1	3040	-1.30	14.98	24	2723	0.896	2768	0.911	-1.29	-0.40
111C2	1923	-1.30	9.80	1	1476	0.768	1214	0.631	-1.48	-0.68
105A1	921	-1.30	5.16	1	625	0.679	527	0.572	-1.47	-0.60
99B1	3180	-1.65	15.44	18	2270	0.714	2455	0.772	-1.65	-0.60
107B1	1621	-1.65	8.40	1	1325	0.817	760	0.469	-1.72	-0.90
113D1	1533	-1.65	8.26	33	1268	0.827	1535	1.001	-1.63	-0.82
116D1	3998	-1.65	20.12	20	2506	0.627	2477	0.620	-1.65	-0.30
119B3	2114	-1.65	10.86	41	1717	0.812	1587	0.751	-1.61	-0.57
106B2	1838	-2.00	9.46	9	1390	0.756	1948	1.060	-2.01	-1.26
100B1	2944	-2.00	14.24	9	1765	0.600	1649	0.560	-2.05	-0.70
115A4	2782	-2.00	13.76	17	1716	0.617	1922	0.691	-1.99	-0.82
117B2	3091	-2.00	15.06	11	1945	0.629	1802	0.583	-1.94	-0.56
121B1	2153	-2.00	10.90	22	1593	0.740	1583	0.735	-2.01	-0.92
103C1	1292	-2.50	6.94	7	990	0.766	1145	0.886	-2.52	-1.62
101B1	1549	-2.50	8.04	5	881	0.569	843	0.544	-2.59	-1.32
118B2	2083	-2.50	10.54	4	1080	0.518	1372	0.659	-2.49	-1.35
112B2	1808	-2.50	9.54	4	960	0.531	839	0.464	-2.43	-1.00
114B2	1975	-2.50	10.24	10	775	0.392	984	0.498	-2.38	-1.21

Table D.1: Mechanical properties measured for 20 fatigue tests tested to a normalized stress of $\Delta\sigma/E_0 = 0.008$, plus 10 control specimens.

	E_0 (MPa)	ε (%)	Stress Ratio	N	E_r (MPa)	E_r/E_0	E_{sec} (MPa)	E_{sec}/E_0	ε_{max} (%)	ε_{res} (%)
92F1	2342	N/A	10.28	1	2272	0.970	2141	0.914	-0.77	-0.09
98B2	2382	N/A	10.52	1	2245	0.942	2567	1.078	-0.65	-0.07
94B1	2372	N/A	10.28	1	2239	0.944	2208	0.931	-0.76	-0.07
97A2	1472	N/A	6.82	1	1455	0.988	1403	0.953	-0.76	-0.06
83B1	1571	N/A	7.50	1	1300	0.827	1156	0.736	-0.95	-0.14
107C1	3008	-1.30	13.18	22	2100	0.698	2341	0.778	-1.29	-0.38
99C1	1874	-1.30	8.48	6	1516	0.809	1469	0.784	-1.30	-0.42
100E1	1390	-1.30	6.46	3	1032	0.742	951	0.684	-1.26	-0.39
115A1	2331	-1.30	10.30	26	1603	0.688	1921	0.824	-1.28	-0.40
113C1	974	-1.30	4.98	3	700	0.719	642	0.659	-1.26	-0.40
103C2	1553	-1.65	7.22	13	1126	0.725	1207	0.777	-1.67	-0.83
105D1	1836	-1.65	8.34	100	1385	0.754	1626	0.886	-1.66	-0.87
114B1	1199	-1.65	5.98	19	879	0.733	982	0.819	-1.63	-0.79
117D1	1433	-1.65	6.84	3	956	0.667	822	0.574	-1.60	-0.62
86C1	3636	-1.65	15.52	143	2394	0.658	2785	0.766	-1.65	-0.72
111C1	1661	-2.00	7.68	119	1393	0.839	2119	1.276	-1.99	-1.44
92C2	3378	-2.00	14.92	453	2184	0.647	2168	0.642	-1.98	-0.89
118C1	1653	-2.00	7.62	48	1052	0.636	1015	0.614	-1.99	-0.82
88D1	2024	-2.00	9.00	1183	1743	0.861	2037	1.006	-1.99	-1.28
112C2	2961	-2.00	13.44	380	1467	0.495	1744	0.589	-2.01	-0.79
95D1	668	-2.50	6.36	2	107	0.160	268	0.401	-2.60	-2.50
109A1	2504	-2.50	11.06	1144	1512	0.604	2232	0.891	-2.50	-1.35
102B2	1619	-2.50	7.44	8	767	0.474	732	0.452	-2.47	-1.13
120C1	2354	-2.50	10.66	60	988	0.420	1036	0.440	-2.52	-1.13
121C2	1807	-2.50	8.40	13	740	0.410	867	0.480	-2.49	-1.34

Table D.2: Mechanical properties measured for 20 fatigue tests tested to a normalized stress of $\Delta\sigma/E_0 = 0.007$.

	E_0 (MPa)	ε (%)	Stress Ratio	N	E_r (MPa)	E_r/E_0	E_{sec} (MPa)	E_{sec}/E_0	ε_{max} (%)	ε_{res} (%)
109C2	2396	-0.80	9.22	169	2881	1.202	3101	1.294	-0.80	-0.34
96D1	945	-0.80	4.20	13	939	0.994	1063	1.125	-0.80	-0.29
83B2	1911	-0.80	7.76	10	1687	0.883	1713	0.896	-0.84	-0.15
103A2	1260	-0.80	5.34	5	1191	0.945	1275	1.012	-0.79	-0.22
112C3	1851	-0.80	7.62	1203	1575	0.851	1672	0.903	-0.78	-0.12
95C2	1703	-1.10	5.66	34	1307	0.767	1422	0.835	-1.10	-0.39
111B1	1855	-1.10	7.30	23	1505	0.811	1450	0.782	-1.10	-0.34
120B1	2565	-1.10	10.18	465	2028	0.791	2093	0.816	-1.11	-0.36
93A1	818	-1.10	3.78	956	1031	1.260	1178	1.440	-1.08	-0.64
76B2	1783	-1.10	7.28	121	1317	0.739	1363	0.764	-1.08	-0.28
102C2	3004	-1.30	11.30	90	1854	0.617	2211	0.736	-1.29	-0.49
121B2	1870	-1.30	7.40	5	1433	0.766	1455	0.778	-1.28	-0.58
92D1	1249	-1.30	5.10	8	883	0.707	799	0.640	-1.32	-0.45
67E1	3239	-1.30	12.64	509	1803	0.557	2295	0.709	-1.27	-0.44
69A1	2745	-1.30	10.66	113	1787	0.651	1958	0.713	-1.32	-0.50
94A1	2125	-1.65	8.14	154	1252	0.589	1580	0.744	-1.65	-0.80
115A2	1984	-1.65	7.80	74	1178	0.594	1323	0.667	-1.65	-0.73
78C1	1506	-1.65	5.90	37	893	0.593	954	0.633	-1.64	-0.72
118C2	1861	-1.65	7.32	64	1020	0.548	1186	0.637	-1.61	-0.66
88A1	1730	-1.65	7.02	62	1011	0.584	1135	0.656	-1.63	-0.68
99A1	1677	-2.00	6.72	39	822	0.490	826	0.493	-1.99	-0.91
107B2	2046	-2.00	8.08	209	1321	0.646	1499	0.733	-1.87	-1.06
119B2	1669	-2.00	6.80	207	951	0.570	1004	0.602	-1.99	-0.99
81F1	760	-2.00	3.52	130	629	0.828	687	0.904	-1.96	-1.34
84A1	1180	-2.00	5.00	18	707	0.599	663	0.562	-2.00	-0.95
100C1	1723	-2.50	6.86	583	1287	0.747	1492	0.866	-2.50	-2.00
116C1	1423	-2.50	5.86	847	740	0.520	826	0.580	-2.48	-1.45
113D2	2886	-2.50	11.22	122	953	0.330	1016	0.352	-2.42	-1.25
117C1	1701	-2.50	7.04	14	902	0.530	1063	0.625	-2.49	-1.68
86A2	2716	-2.50	10.42	127	1085	0.399	1372	0.505	-2.45	-1.27

Table D.3: Mechanical properties measured for 20 fatigue tests tested to a normalized stress of $\Delta\sigma/E_0 = 0.006$.

	E_0 (MPa)	ε (%)	Stress Ratio	N	E_r (MPa)	E_r/E_0	E_{sec} (MPa)	E_{sec}/E_0	ε_{max} (%)	ε_{res} (%)
97B1	1564	-0.80	5.44	612	1465	0.937	1439	0.920	-0.79	-0.24
95D2	1218	-0.80	4.46	2500	1390	1.141	1453	1.193	-0.81	-0.35
94A2	1637	-0.80	5.66	167	1847	1.128	2027	1.238	-0.79	-0.36
98A1	2676	-0.80	8.64	6250	2368	0.885	2484	0.928	-0.81	-0.26
82E1	1469	-0.80	5.12	16	1273	0.867	1193	0.812	-0.78	-0.18
100A1	1326	-1.10	4.76	4011	1803	1.360	1876	1.415	-1.09	-0.73
107D2	3762	-1.10	11.72	322	2197	0.584	2482	0.660	-1.09	-0.30
102B1	1387	-1.10	5.00	1523	968	0.698	1152	0.831	-1.09	-0.43
109B2	1908	-1.10	6.44	17080	1636	0.857	2154	1.129	-1.10	-0.65
92C1	3233	-1.10	10.68	3685	2045	0.633	2380	0.736	-1.03	-0.32
103B1	3067	-1.30	9.58	2511	1781	0.581	2057	0.671	-1.28	-0.49
105C2	2254	-1.30	7.44	3121	1270	0.563	1521	0.675	-1.32	-0.57
117B1	1547	-1.30	5.38	129	1279	0.827	1556	1.006	-1.30	-0.78
118B1	1366	-1.30	4.90	123	1207	0.884	1433	1.049	-1.27	-0.79
116B1	3043	-1.30	-8.10	2581	1703	0.560	1859	0.611	-1.30	-0.46
111D1	5457	-1.65	16.38	380	2295	0.421	4137	0.758	-1.65	-0.68
121C1	2845	-1.65	9.40	741	1487	0.523	2117	0.744	-1.64	-0.93
120C2	1828	-1.65	6.42	2166	1158	0.633	1458	0.798	-1.62	-0.95
89A1	1518	-1.65	5.06	3572	918	0.605	1057	0.696	-1.63	-0.90
112C1	2011	-1.65	6.96	687	825	0.410	1080	0.537	-1.62	-0.67
79C1	1061	-2.00	3.90	43	626	0.590	602	0.567	-2.00	-1.16
91F1	2355	-2.00	7.84	229	970	0.412	995	0.423	-2.01	-0.96
86A1	3080	-2.00	9.90	725	1173	0.381	1495	0.485	-1.97	-0.96
113A1	1646	-2.00	5.70	1568	1274	0.774	1466	0.891	-1.97	-1.49
114C2	2457	-2.00	8.24	1190	745	0.303	1132	0.461	-1.93	-1.19
119B1	1983	-2.50	6.72	1125	684	0.345	1095	0.552	-2.50	-1.05
93A2	2095	-2.50	7.10	78	723	0.345	824	0.393	-2.46	-1.43
87D2	2720	-2.50	8.58	486	1013	0.372	*	*	-2.50	-1.10
88A2	1591	-2.50	5.52	300	646	0.406	757	0.476	-2.45	-1.50
76B1	1876	-2.50	6.36	4294	657	0.350	746	0.398	-2.47	-1.47

*data acquisition error, no measurement taken

Table D.4: Mechanical properties measured for 30 fatigue tests tested to a normalized stress of $\Delta\sigma/E_0 = 0.005$.

	Section Area (mm^2)[a]	Bone Area (mm^2)[b]	Bone Area Fraction (mm^2/mm^2)[c]	Specimen Length (mm)[d]	Damaged Band Fraction (mm^2/mm^2)[e]	Damaged Trabeculae /Area (mm^{-2})[f]	Damaged Area Fraction (mm^2/mm^2)[g]
95A1	178.13	98.9	0.555	7.336	0.000	0.000	0
96D2	223.35	92.02	0.412	9.448	0.000	0.009	0.00024
97A1	239.85	109.93	0.458	8.578	0.000	0.000	0
102C1	238.42	120.31	0.505	8.516	0.000	0.008	0.00007
107A2	306.64	167.27	0.545	10.89	0.000	0.000	0
92F2	172.81	95.18	0.551	5.962	0.000	0.000	0
95B2	206.59	118.2	0.572	7.05	0.000	0.000	0
103A1	262.74	125.76	0.479	7.735	0.000	0.000	0
100A2	288.46	116.54	0.404	8.065	0.000	0.003	0
107F1	296.88	101.66	0.342	8.455	0.000	0.007	0.00011
98B1	166.26	93.89	0.565	7.103	0.087	0.192	0.00491
95C1	133.81	48.39	0.362	7.028	0.202	0.149	0.00448
109C1	156.91	77.71	0.495	7.12	0.258	0.191	0.00241
111C2	136.18	76.65	0.563	8.15	0.000	0.022	0.00020
105A1	172.06	63.75	0.371	7.128	0.158	0.203	0.00474
99B1	151.78	73.63	0.485	6.625	0.316	0.395	0.00463
107B1	171.85	68.02	0.396	7.585	0.000	0.029	0.00044
113D1	173.95	63.2	0.363	7.693	0.000	0.040	0.00090
116D1	129.63	73.22	0.565	7.677	0.340	0.285	0.00388
119B3	174.31	65.96	0.378	7.383	0.665	0.711	0.01150
106B2	148.75	73.74	0.496	6.505	0.042	0.074	0.00142
100B1	165.95	76.57	0.461	7.06	1.000	0.801	0.0246
115A4	178.33	95.94	0.538	7.54	0.332	0.353	0.00449
117B2	163.64	72.82	0.445	7.028	0.702	0.654	0.0165
121B1	159.48	76.64	0.481	6.88	0.293	0.213	0.00369
103C1	147.49	66.31	0.450	6.465	0.000	0.034	0.00059
101B1	151.55	57.83	0.382	6.45	0.255	0.323	0.00414
118B2	148.49	71.13	0.479	6.718	0.025	0.067	0.00171
112B2	134.41	48.01	0.357	7.128	0.802	0.937	0.0156
114B2	181.85	67.69	0.372	7.498	0.570	0.484	0.0116

Table D.5: Microdamage parameters measured for 30 fatigue tests tested to a normalized stress of $\Delta\sigma/E_0 = 0.008$, plus 10 control specimens.

	Section Area (mm^2)[a]	Bone Area (mm^2)[b]	Bone Area Fraction (mm^2/mm^2)[c]	Specimen Length (mm)[d]	Damaged Band Fraction (mm^2/mm^2)[e]	Damaged Trabeculae /Area (mm^{-2})[f]	Damaged Area Fraction (mm^2/mm^2)[g]
107C1	158.68	80.74	0.509	6.78	0.341	0.340	0.00811
99C1	172.43	98.78	0.573	7.15	0.143	0.180	0.00204
100E1	225.61	91.69	0.406	7.538	0.339	0.332	0.00467
115A1	257.52	125.45	0.487	7.157	0.438	0.513	0.00821
113C1	209.56	69.22	0.330	6.808	0.572	0.358	0.00529
103C2	264.84	133.07	0.502	8.86	0.031	0.064	0.00078
105D1	145.82	69.45	0.476	6.155	0.311	0.480	0.0152
114B1	231.62	103.31	0.446	7.526	0.014	0.073	0.00133
117D1	218.94	69.26	0.316	7.212	0.358	0.333	0.00558
86C1	204.96	117.77	0.575	6.852	0.527	0.527	0.00955
111C1	154.2	84.38	0.547	6.578	0.043	0.065	0.00091
92C2	247.2	166.5	0.674	8.002	0.708	0.761	0.0333
118C1	242.16	131.61	0.543	6.917	0.605	0.917	0.0230
88D1	218.3	109.15	0.500	7.296	0.310	0.289	0.00753
112C2	221.52	109.93	0.496	7.16	0.745	1.065	0.0395
95D1	161.95	34.86	0.215	7.208	0.248	0.321	0.00531
109A1	210.64	123.08	0.584	7.154	0.434	0.603	0.0271
102B2	194.35	85.25	0.439	7.05	0.793	1.081	0.0208
120C1	186.08	88.74	0.477	7.74	1.000	0.833	0.0302
121C2	169.96	70.67	0.416	8.273	0.072	0.100	0.00204

Table D.6: Microdamage parameters measured for 20 fatigue tests tested to a normalized stress of $\Delta\sigma/E_0 = 0.007$.

	Section Area (mm^2)[a]	Bone Area (mm^2)[b]	Bone Area Fraction (mm^2/mm^2)[c]	Specimen Length (mm)[d]	Damaged Band Fraction (mm^2/mm^2)[e]	Damaged Trabeculae /Area (mm^{-2})[f]	Damaged Area Fraction (mm^2/mm^2)[g]
109C2	225.15	139.01	0.617	6.357	0.000	0.004	0.00002
96D1	204.55	93.36	0.456	6.87	0.000	0.005	0.00003
83B2	140.82	54.29	0.386	5.848	0.187	0.178	0.00123
103A2	192.9	76.47	0.396	6.946	0.000	0.026	0.00014
112C3	263.58	118.54	0.450	8.652	0.237	0.266	0.00558
95C2	159.18	66.76	0.419	6.715	0.209	0.239	0.00425
111B1	216.33	100.72	0.466	7.346	0.541	0.527	0.014
120B1	242.1	113.97	0.471	7.972	0.115	0.190	0.00406
93A1	212.84	102.26	0.480	7.024	0.023	0.052	0.00056
76B2	273	118.88	0.435	7.653	0.533	0.495	0.00859
102C2	218.05	122.04	0.560	7.188	0.152	0.151	0.00228
121B2	177.87	77.26	0.434	7.6	0.000	0.000	0
92D1	232.96	96.93	0.416	7.568	0.300	0.206	0.00629
67E1	248.12	123.6	0.498	8.08	0.253	0.254	0.00845
69A1	196.64	95.28	0.485	7.895	0.226	0.193	0.00319
94A1	175.49	71.39	0.407	5.97	0.498	0.604	0.0186
115A2	196.43	81.43	0.415	6.49	0.499	0.601	0.0137
78C1	204.64	80.23	0.392	6.97	0.703	0.728	0.0169
118C2	181.41	75.56	0.417	5.906	0.785	1.279	0.0167
88A1	173.62	92.96	0.535	7.13	0.691	0.357	0.00498
99A1	215.69	89.221	0.414	7.508	0.816	1.001	0.0218
107B2	222.67	119.57	0.537	7.36	0.435	0.719	0.0176
119B2	214.61	75.82	0.353	7.43	0.730	0.918	0.0235
81F1	205.83	72.43	0.352	8.375	0.392	0.544	0.0102
84A1	198.78	94.74	0.477	6.626	0.716	0.890	0.0133
100C1	171.78	99.92	0.582	7.128	0.181	0.256	0.00425
116C1	216.05	85.6	0.396	7.36	0.716	0.903	0.0285
113D2	204.04	101.35	0.497	6.842	0.745	1.078	0.0316
117C1	163.74	81.59	0.498	6.9	0.000	0.000	0
86A2	165.33	73.64	0.445	6.858	0.482	0.762	0.0275

Table D.7: Microdamage parameters measured for 30 fatigue tests tested to a normalized stress of $\Delta\sigma/E_0 = 0.006$.

	Section Area (mm^2)[a]	Bone Area (mm^2)[b]	Bone Area Fraction (mm^2/mm^2)[c]	Specimen Length (mm)[d]	Damaged Band Fraction (mm^2/mm^2)[e]	Damaged Trabeculae /Area (mm^{-2})[f]	Damaged Area Fraction (mm^2/mm^2)[g]
97B1	182.27	74.72	0.410	7.855	0.121	0.115	0.00172
95D2	170.99	87.98	0.515	7.638	0.064	0.094	0.00104
94A2	118.18	51.65	0.437	6.68	0.000	0.000	0
98A1	150.61	88.54	0.588	6.944	0.480	0.378	0.00818
82E1	166.78	74.72	0.448	7.16	0.179	0.234	0.00311
100A1	155.98	65.9	0.422	6.998	0.000	0.013	0
107D2	147.7	80.55	0.545	6.523	0.496	0.589	0.0118
102B1	174.57	80.39	0.461	8.393	0.593	0.487	0.00799
109B2	151.05	78.61	0.520	6.58	0.162	0.205	0.00598
92C1	150.74	83.28	0.552	6.45	0.366	0.325	0.0181
103B1	150.98	72.27	0.479	6.743	0.590	0.583	0.0129
105C2	131.2	74.32	0.566	7.007	0.223	0.198	0.00548
117B1	157.08	73.79	0.470	6.738	0.000	0.006	0
118B1	160.69	77.56	0.483	6.89	0.000	0.037	0.00017
116B1	183.37	85.98	0.469	7.16	0.754	0.676	0.0170
111D1	153.07	97.83	0.639	6.615	0.438	0.575	0.0338
121C1	160.92	77.17	0.480	6.815	0.373	0.292	0.00601
120C2	197.24	90.82	0.460	6.956	0.296	0.319	0.00491
89A1	193.37	83.6	0.432	8.4	0.621	0.931	0.0182
112C1	179.54	69.03	0.384	7.123	0.739	0.574	0.0160
79C1	117.16	40.65	0.347	6.79	0.710	0.640	0.00983
91F1	155.08	63.67	0.411	6.728	0.661	0.638	0.0138
86A1	161.07	75.62	0.469	6.77	0.673	0.652	0.0154
113A1	163.24	56.12	0.344	6.693	0.045	0.165	0.00202
114C2	195.15	87.2	0.447	8.11	0.407	0.487	0.0152
119B1	178.53	67.96	0.381	7.79	0.616	0.627	0.0185
93A2	151.48	60.69	0.401	6.368	1.000	1.261	0.0296
87D2	154.18	71.98	0.467	6.928	0.421	0.480	0.0170
88A2	189.16	71.85	0.380	7.705	0.738	0.777	0.0167
76B1	227.94	93.33	0.409	7.604	0.440	0.390	0.0187

Table D.8: Microdamage parameters measured for 30 fatigue tests tested to a normalized stress of $\Delta\sigma/E_0 = 0.005$.

	Diffuse	Single	Parallel	Cross-Hatch	Fracture	25%	50%	75%	100%	Total
95A1	0	0	0	0	0	0	0	0	0	0
96D2	0	2	0	0	0	2	0	0	0	2
97A1	0	0	0	0	0	0	0	0	0	0
102C1	0	1	0	1	0	1	1	0	0	2
107A2	0	0	0	0	0	0	0	0	0	0
92F2	0	0	0	0	0	0	0	0	0	0
95B2	0	0	0	0	0	0	0	0	0	0
103A1	0	0	0	0	0	0	0	0	0	0
100A2	0	1	0	0	0	1	0	0	0	1
107F1	0	1	0	1	0	2	0	0	0	2
98B1	0	6	1	25	0	8	8	4	12	
95C1	0	3	2	15	0	6	6	4	4	20
109C1	0	3	1	26	0	11	6	5	8	30
111C2	1	2	0	0	0	2	1	0	0	3
105A1	0	5	3	27	0	7	12	4	12	35
99B1	0	3	3	54	0	20	12	7	21	60
107B1	0	0	1	4	0	3	1	0	1	5
113D1	0	0	1	6	0	1	1	0	5	7
116D1	0	2	0	35	0	20	9	2	6	37
119B3	0	7	5	111	1	28	35	10	51	124
106B2	0	0	0	11	0	1	3	2	5	11
100B1	2	3	9	118	1	21	28	16	68	133
115A4	0	6	3	54	0	21	16	10	16	63
117B2	0	2	2	103	0	25	25	16	41	107
121B1	0	2	1	31	0	11	10	3	10	34
103C1	0	1	0	4	0	3	1	0	1	5
101B1	1	2	1	45	0	16	9	5	19	49
118B2	1	0	0	9	0	4	2	0	4	10
112B2	3	2	4	116	1	26	18	9	73	126
114B2	0	5	5	68	10	17	21	17	33	88

Table D.9: Damaged trabeculae in each of 20 fatigue tests tested to a normalized stress of $\Delta\sigma/E_0 = 0.008$, plus 10 control specimens, classified by pattern of damage and by extent of damage across the trabeculae, rounded to the nearest quarter.

	Diffuse	Single	Parallel	Cross-Hatch	Fracture	25%	50%	75%	100%	Total
107C1	0	1	0	53	0	16	12	7	19	54
99C1	0	1	0	30	0	12	6	3	10	31
100E1	1	14	2	58	0	15	14	15	31	75
115A1	5	12	3	112	0	33	39	17	43	132
113C1	0	4	3	68	0	15	16	13	31	75
103C2	1	2	0	14	0	6	4	2	5	17
105D1	1	3	4	61	1	6	12	9	43	70
114B1	0	2	1	14	0	1	3	1	12	17
117D1	2	2	2	67	0	14	16	6	37	73
86C1	3	17	2	85	1	46	32	9	21	108
111C1	1	0	1	8	0	1	3	1	5	10
92C2	9	14	10	154	1	65	43	28	52	188
118C1	3	11	6	202	0	42	37	32	111	222
88D1	2	5	2	54	0	24	17	9	13	63
112C2	2	14	6	204	10	60	49	37	90	236
95D1	3	2	11	34	2	13	19	7	13	52
109A1	1	2	4	112	8	31	22	15	59	127
102B2	5	13	13	174	5	24	44	21	121	210
120C1	0	7	5	141	2	23	37	15	80	155
121C2	0	0	1	16	0	3	5	5	4	17

Table D.10: Damaged trabeculae in each of 20 fatigue tests tested to a normalized stress of $\Delta\sigma/E_0 = 0.007$, classified by pattern of damage and by extent of damage across the trabeculae, rounded to the nearest quarter.

	Diffuse	Single	Parallel	Cross-Hatch	Fracture	25%	50%	75%	100%	Total
109C2	0	1	0	0	0	1	0	0	0	1
96D1	0	0	1	0	0	1	0	0	0	1
83B2	0	5	0	20	0	8	5	6	6	25
103A2	0	3	2	0	0	0	3	1	1	5
112C3	0	5	1	64	0	15	15	11	29	70
95C2	0	5	2	31	0	16	8	5	9	38
111B1	1	9	3	101	0	21	32	13	48	114
120B1	2	8	0	36	0	11	13	7	15	46
93A1	1	3	0	7	0	1	2	2	6	11
76B2	1	11	3	120	0	35	22	15	63	135
102C2	1	4	0	28	0	18	5	3	7	33
121B2	0	0	0	0	0	0	0	0	0	0
92D1	1	1	2	44	0	10	13	5	20	48
67E1	1	5	0	57	0	14	9	10	30	63
69A1	0	6	0	32	0	14	5	4	15	38
94A1	1	5	9	88	3	13	20	16	57	106
115A2	3	10	0	105	0	24	21	16	57	118
78C1	0	2	3	144	0	31	27	12	79	149
118C2	3	19	11	199	0	44	59	32	97	232
88A1	1	3	0	58	0	20	8	6	28	60
99A1	3	22	16	170	5	30	51	32	103	216
107B2	3	11	11	135	0	34	33	19	74	160
119B2	5	6	10	170	6	38	40	20	99	197
81F1	3	11	5	93	0	19	15	9	69	112
84A1	12	16	2	147	0	48	24	19	86	177
100C1	1	6	2	35	0	14	12	3	15	44
116C1	0	8	4	167	16	36	37	18	104	195
113D2	0	8	7	187	18	42	53	21	104	220
117C1	0	0	0	0	0	0	0	0	0	0
86A2	2	4	3	114	3	31	25	8	62	126

Table D.11: Damaged trabeculae in each of 20 fatigue tests tested to a normalized stress of $\Delta\sigma/E_0 = 0.006$, classified by pattern of damage and by extent of damage across the trabeculae, rounded to the nearest quarter.

	Diffuse	Single	Parallel	Cross-Hatch	Fracture	25%	50%	75%	100%	Total
97B1	0	4	1	16	0	3	1	3	14	21
95D2	2	2	0	12	0	2	2	4	8	16
94A2	0	0	0	0	0	0	0	0	0	0
98A1	1	6	1	46	3	13	11	4	29	57
82E1	0	5	1	32	1	8	6	5	20	39
100A1	0	0	0	1	1	1	0	0	1	2
107D2	0	7	1	77	2	24	22	9	32	87
102B1	1	2	3	78	1	10	21	8	46	85
109B2	0	2	0	26	3	8	8	2	13	31
92C1	0	2	3	36	8	11	11	6	21	49
103B1	1	9	1	69	8	16	22	4	46	88
105C2	0	1	0	24	1	5	5	5	11	26
117B1	0	1	0	0	0	1	0	0	0	1
118B1	0	2	0	3	1	2	1	0	3	6
116B1	1	11	2	102	8	24	30	11	59	124
111D1	0	2	2	84	0	26	26	9	27	88
121C1	1	7	1	38	0	9	15	5	18	47
120C2	1	6	2	53	1	14	14	4	31	63
89A1	5	19	13	136	7	26	43	22	89	180
112C1	0	5	5	84	9	15	12	10	66	103
79C1	2	5	4	62	2	11	17	7	40	75
91F1	3	10	13	69	4	22	21	7	49	99
86A1	1	7	5	82	10	14	19	14	58	105
113A1	0	3	2	20	2	7	7	1	12	27
114C2	1	7	4	64	19	3	23	14	55	95
119B1	1	6	4	93	8	26	21	19	46	112
93A2	1	14	16	146	14	19	40	23	109	191
87D2	1	1	4	60	8	13	18	10	33	74
88A2	1	8	7	118	13	20	31	6	90	147
76B1	2	4	4	60	19	5	19	6	59	89

Table D.12: Damaged trabeculae in each of 30 fatigue tests tested to a normalized stress of $\Delta\sigma/E_0 = 0.005$, classified by pattern of damage and by extent of damage across the trabeculae, rounded to the nearest quarter.